# Transversely isotropic thin film flows

by

Matthew Hopwood

A thesis submitted to
The University of Birmingham and
The University of Adelaide
for the degree of
DOCTOR OF PHILOSOPHY

Supervisor: Dr. Rosemary Dyson (Birmingham)
Co-Supervisor: Dr. Edward Green (Adelaide)
School of Mathematics
College of Engineering and Physical Sciences
University of Birmingham
May 2021

**Abstract**

Many industrial and biological fluids such as cervical mucus have an underlying fibrous microstructure; fibres embedded within a ground matrix give directionally dependent, or anisotropic, material properties. These properties in turn can be critical to ensure key biological functionality. For example, changes in the fibrous reinforcement of cervical mucus during the menstrual cycle regulates the passage of spermatozoa; these rheological properties are typically investigated by attempting to stretch a thread of mucus to determine the current level of fertility.

This thesis aims to understand how the presence of fibres alters the mechanical behaviour of such materials by considering three canonical examples of thin film flows: the squeezing of a film, and the extensional flows of a sheet or a thread. The effect of fibres is incorporated via a transversely isotropic fluid stress tensor which models the suspension as a continuum with an evolving single preferred direction, alongside conservation of mass and momentum. Exploiting the small aspect ratio in each situation, we derive governing equations which we solve via analytical and numerical means. We find throughout that the behaviours of a transversely isotropic fluid are markedly different to that of a Newtonian fluid.

# ACKNOWLEDGMENTS

I would like to sincerely thank my supervisors, Dr. Rosemary Dyson and Dr. Edward Green, for their encouragement and thorough patience throughout the last four years. I am very grateful to Dr. Brendan Harding for sharing his numerical expertise, Dan Theuns for help with proof-reading, and to Jessica Crawshaw for keeping me sane throughout the write-up.

Finally, I would like to thank the many friends at the University of Birmingham, the University of Adelaide, the members of the pub quiz teams, and those who peered into the life of a PhD student with gentle concern. You have ensured that the last few years have been enjoyable ones and there are too many of you to list. You know who you are.

# CONTENTS

# LIST OF FIGURES

# CHAPTER 1

# INTRODUCTION

Fibre-reinforced fluids arise in numerous contexts in industry and biology. Many familiar materials and fluids such as water and glass are termed isotropic, which means they have a structure that behaves the same in every direction. However, some common materials are *anisotropic*, meaning that their properties are different when measured in different directions. For example, wood is easier to split along the direction of the grain, rather than across the grain. This anisotropy causes them to exhibit interesting mechanical behaviours and possess unusual properties, which influence the material's ability to perform its particular function.

Two examples of anisotropic fibre-reinforced fluids are collagen gel and cervical mucus. In the context of tissue engineering, collagen gels are a common media in which cells are seeded when grown in vitro. A number of experimental studies suggest that the alignment of the fibres and distribution of stresses may influence the architecture adopted by the cells [88]. Cervical mucus possesses a fibrous reinforcement that changes orientation throughout the menstrual cycle. Around ovulation, the mucus has a lower pH, a higher concentration of water (which has the effect of lowering the viscosity of the mucus), and the fibrous reinforcement takes a more parallel alignment that allows sperm to migrate. At this point the mucus can be spun out into a thread. Conversely, during the most infertile parts of the menstrual cycle, the fibrous reinforcement does not take a parallel alignment, and the mucus does not stretch and simply breaks [64, 106]. The ability for a fluid to be spun out

into a thread is termed the 'spinnability' or 'spinnbarkeit' of a material, and is applied to cervical mucus as a means of assessing fertility [34]. Given that the fibrous reinforcement appears to play a role in the unusual behaviour of these fluids, it is therefore of interest to study the effects of the presence of fibres within a material.

## 1.1 Models of suspensions

Early work in the modelling of the behaviour of suspensions began with studying the behaviour of individual particles suspended in Newtonian fluid. A Newtonian fluid is isotropic, and satisfies the relation

$$\boldsymbol{\sigma} = -p\boldsymbol{I} + 2\mu\boldsymbol{e}, \tag{1.1}$$

where $\boldsymbol{\sigma}$ is the total stress, $p$ is the pressure, $\mu$ is the viscosity of the fluid, and $\boldsymbol{e} = \frac{1}{2}\left(\nabla\boldsymbol{u} + (\nabla\boldsymbol{u})^T\right)$ is the rate of strain tensor, where $\boldsymbol{u}$ is the fluid velocity. Any fluid that does not satisfy this relation is known as a non-Newtonian fluid. Non-Newtonian fluids may be isotropic, such as generalised Newtonian fluids including Carreau fluids (where the viscosity depends upon the rate of shear), or anisotropic, such as transversely isotropic fluids.

Jeffrey [53], analysed the motion of a rigid, infinitely small, ellipsoidal particle suspended in an incompressible Newtonian fluid. He solved the flow field around the particle and was able to determine the orientation of the particle, using a no-slip boundary condition on the surface on the particle and imposed a far field condition requiring that the velocity field matches the bulk flow far from the particle. This work assumes that the suspension is *dilute*. Dilute is the term used to describe suspensions where only the fluid affects the behaviour of the suspended particle. In semi-dilute (or semi-concentrated) regimes, the interactions between the particles are restricted to being hydrodynamic, and the fluid surrounding the particles must move in the gaps between the particles [35]. Concentrated regimes refer to

suspensions where particles may interact directly and give rise to a significant increase in complexity due to the need to quantify these interactions.

The development of a general constitutive equation for the suspensions of particles of any shape in Newtonian fluids at arbitrary concentrations (but still within the bounds of being at most semi-dilute) was done by Batchelor [12, 13], who considered the suspension of rigid elongated particles suspended in Newtonian fluid, undergoing a pure straining motion in the $x$ direction in order to relax the assumption of being dilute. The orientations of the fibres were described using a probability density function. The bulk stress for a suspension of particles in a Newtonian fluid given by Batchelor [13, 25] is

$$\boldsymbol{\tau} = -\eta_s \boldsymbol{e} + \frac{1}{V} \sum_{i=1}^{nV} \int_{A_i} (\boldsymbol{\sigma}_s \cdot \boldsymbol{n}) \, \boldsymbol{r} \mathrm{d}A_i. \tag{1.2}$$

where $\boldsymbol{\tau}$ is the macroscopic stress, $\eta_s$ is the viscosity of the solvent, $V$ is the volume of the suspension, $n$ is the number of fibres per unit volume, $\boldsymbol{\sigma}_s$, is the local total stress tensor for the solvent, $\boldsymbol{n}$ is the outward unit normal to each area element $\mathrm{d}A_i$ on the surface of the particle, and $\boldsymbol{r}$ is a vector from a fixed coordinate system to $\mathrm{d}A_i$. The assumption that a suspended particle has a much smaller diameter than its length permits the use of asymptotic techniques to simplify the equations, and was used by Batchelor [11, 13] and Hinch & Leal [44] to study the behaviour of suspended particles.

The work of Batchelor was extended by Dinh and Armstrong [25] who constructed a model for a semi-dilute suspension of fibres. Their work focuses upon a single test fibre, replacing the matrix of surrounding fluid and fibres with a continuum. They assumed that the drag upon the fibre surface could be modelled as a force along the major axis of the particle, which leads to a model where the fibre rotates as if it were a line. In this case the fibres may attain a steady state, whereas the ellipsoidal particles in the Jeffery model exhibit periodic behaviour and do not achieve a steady state [53]. The Dinh-Armstrong

rheological equation of state for a fibre suspension is [25]

$$\boldsymbol{\tau} = -\eta_s \boldsymbol{e} \left( 1 + \frac{1}{48} \frac{nL^3}{\ln(2h/D)} : \int \frac{\boldsymbol{PPPP} \mathrm{d}\boldsymbol{P}}{(1 + \boldsymbol{e} : \boldsymbol{PP})^{3/2}} \right), \tag{1.3}$$

where $L, D$ are the length and diameter of the test fibre, $h$ is the average (lateral) spacing between the fibres, and $\boldsymbol{P}$ is the orientation vector of the fibre. The key difference between the Dinh-Armstrong and Jeffrey models is that the Dinh-Armstrong model allows particles to rotate in shear flow towards an equilibrium orientation. This model has been used to model injection and compression moulding [2, 4].

Instead of considering a force balance on a test fibre, Folgar and Tucker [35] advanced a theory for concentrated fibre suspensions by choosing a general form for their theory that satisfied basic physical requirements such as invariance with respect to choice of co-ordinates, and then testing their theory against experiment. Common to this work, and those discussed above, is the use of distribution functions to describe the orientation of the fibres. These provide a full description of the orientations of the fibres within the suspension, however, the initial orientation distribution function is difficult to measure experimentally [59]. In an effort to overcome this difficulty, some works attempted to reconstruct the initial orientation and evolution of the fibres by performing experiment and working backwards [24, 39].

Later works favoured the use of tensors to describe the orientation of fibres, whose components are coefficients in a truncated expansion of the distribution function. This approach was popularised by Lipscomb, who investigated contraction flow of semi-dilute fibre suspensions [58] and Advani [1], who derived evolution equations for second and fourth order tensors to predict the orientation of fibres affected by flow. These tensors are defined to be

$$a_{ij} = \int P_i P_j \psi(\boldsymbol{P}, t) \mathrm{d}\boldsymbol{P}, \tag{1.4}$$

$$a_{ijkl} = \int P_i P_j P_k P_l \psi(\boldsymbol{P}, t) \mathrm{d}\boldsymbol{P}, \tag{1.5}$$

where $\psi$ is the orientation distribution function and $\boldsymbol{P}$ the fibre orientation. Using tensors bypasses a direct calculation of the change in $\psi$ and saves a large amount of computation [1].

Ericsson et al [33], incorporated anisotropic effects into a squeezing flow by considering a test fibre undergoing only affine motion in a similar approach to Dinh-Armstrong, with the use of tensors to describe the orientation of the fibre via the introduction of an anisotropic viscosity tensor into the stress for a Newtonian fluid

$$\boldsymbol{\sigma} = \boldsymbol{\eta} : \boldsymbol{e} - p\boldsymbol{I}, \tag{1.6}$$

where $\boldsymbol{\eta}$ is a fourth-rank anisotropic viscosity tensor, giving rise to a 'quasi-Newtonian' total stress tensor. The operation : is defined to be a contraction over the last two indices so that $\boldsymbol{\eta} : \boldsymbol{e} = \eta_{ijkl} e_{kl}$.

A key difficulty that must be overcome with the tensor-based approach for coupling the flow with fibre direction is that the rate of change of the orientation tensor for the fibre directions presents a closure problem as the evolution equation for a second-order tensor contains a fourth-order tensor (and so on to higher orders). At some order a closure approximation must be taken, which entails approximating a higher order tensor. There are a host of potential choices with varied advantages and disadvantages, for details see [17, 18, 103]. We now introduce our transversely isotropic model for a suspension of fibres.

## 1.2 Transversely isotropic fluids

In this thesis, we model fibre-reinforced fluids as a class of anisotropic materials that are known as 'transversely isotropic'. This class of materials is, non-Newtonian, anisotropic, and possesses a single preferred direction, which may vary both spatially and temporally. The physical properties of such materials are symmetric in all directions normal to this preferred direction. Previous applications include the construction of reinforced composites

[93], primary plant cell wall growth [29], the mechanical behaviour of collagen gels [41], the influence of extracellular matrix anisotropy and cell-matrix interaction on tissue architecture [28], suspensions of biomolecules [46, 48], and propulsion in aligned cervical mucus [23].

We start with the dimensional Stokes equations

$$\nabla^* \cdot \boldsymbol{u}^* = 0, \tag{1.7}$$

$$\nabla^* \cdot \boldsymbol{\sigma}^* = 0, \tag{1.8}$$

where $\boldsymbol{u}^*(\boldsymbol{x}^*, t^*)$ is the velocity vector, $t^*$ is time, $\boldsymbol{x}^*$ represents the position within the co-ordinate system we choose to employ, which will be either Cartesian or cylindrical polar and will be specified in the appropriate places. Henceforth asterisks will denote dimensional variables. In order to incorporate the effects of the fibrous microstructure, we first assume the material possesses a preferred direction induced by the fibres, which is given by the unit vector $\boldsymbol{a}$, and varies with position and time. We use the transversely isotropic constitutive law for a viscous fluid proposed by Ericksen [32]. This is the most general form of a stress tensor that is linearly dependent upon the rate of strain and invariant under translation, rigid body rotation, and the transformation $\boldsymbol{a} \Rightarrow -\boldsymbol{a}$. The constitutive law for $\boldsymbol{\sigma}^*$ is

$$\sigma^*_{ij} = -p^*\delta_{ij} + 2\mu^* e^*_{ij} + \mu^*_1 a_i a_j + \mu^*_2 a_i a_j a_k a_l e^*_{kl} + 2\mu^*_3 (a_i a_l e^*_{jl} + a_j a_m e^*_{mi}), \tag{1.9}$$

where $p^*$ is the pressure, and $\boldsymbol{e}^*$ is the rate of strain tensor. The constants $\mu^*, \mu^*_1, \mu^*_2, \mu^*_3$, are all viscosity-like parameters, which are the familiar dynamic (shear) viscosity for a Newtonian fluid, the contributions to the stress caused by active behaviour of the suspension, and anisotropic extensional and shear viscosities respectively. The reasons for the interpretations of the key parameters $\mu^*_1, \mu^*_2, \mu^*_3$ are as follows. We note first that by setting $\mu^*_1 = \mu^*_2 = \mu^*_3 = 0$, one immediately recovers the stress tensor for an incompressible and isotropic Newtonian fluid. We observe that there is no velocity component to the $\mu^*_1$

term, indicating that the presence of fibres in the fluid generates stress in the fluid even when instantaneously at rest. This term has been interpreted as a tension acting in the fibre direction [41, 93]. In this case there exists a non-zero bulk stress in the fluid despite the fluid being at rest. Spencer interprets this as the fibres in a reinforced composite providing support to the fluid [94]. In the context of suspensions, $\mu_1^*$ has been interpreted to model the contributions to stress caused by the active behaviour of suspended particles [47].

We interpret $\mu_2$ and $\mu_3$ as the anisotropic extensional and shear viscosities respectively, which we demonstrate by considering three deformations of a $2D$ sheet of fibres in a Cartesian plane $(x^*, y^*)$ [41, 46, 85], as illustrated in Figure 1.1. First we fix the fibre alignment to be parallel to the $x$-direction, so we set $\boldsymbol{a} = (1, 0)$. Now, consider an extensional flow parallel to the fibres, $\boldsymbol{u}^* = (u^*(x^*), 0)$, as in Figure 1.1a, direct substitution of $\boldsymbol{a}, \boldsymbol{u}^*$ into the stress tensor immediately yields an extensional viscosity in the fibre direction of $\mu_{||}^* = \mu^* + \dfrac{(\mu_2^* + 4\mu_3^*)}{2}$. Similarly, consideration of extensional flow orthogonal to the fibres given by $\boldsymbol{u}^* = (0, v^*(y^*))$ as in Figure 1.1b gives the extensional viscosity orthogonal the fibre direction, $\mu_\perp^* = \mu^*$. Finally, consideration of shear flow over the fibres $\boldsymbol{u}^* = (u^*(y^*), v^*(x^*))$ as in Figure 1.1c yields a shear viscosity of $\mu_s^* = \mu^* + \mu_3^*$.

We remark that $\mu_2^*$ contributes only to $\mu_{||}^*$ whilst $\mu_3^*$ distinguishes the orthogonal viscosity $\mu_\perp^*$ from the shear viscosity $\mu_s^*$. We therefore call $\mu_2^*$ the anisotropic extensional viscosity, and $\mu_3^*$ the anisotropic shear viscosity [29, 41, 46]. We must also include an equation describing the orientation of the preferred direction within the fluid, $\boldsymbol{a}$, which we discuss in the next subsection.

### 1.2.1 Evolution of the fibre direction

In order to close the model, we require a governing equation for the evolution of the preferred direction of the fluid, $\boldsymbol{a}$. We follow the derivation given in [41, 56], and give an argument based upon the kinematics of the flow. As shown in Figure 1.2, we take a fibre, $\boldsymbol{l}^*$, with $|\boldsymbol{l}^*| \ll 1$ which is advected over by velocity field $\boldsymbol{u}^*$ for a short time $\delta t^*$. Then,

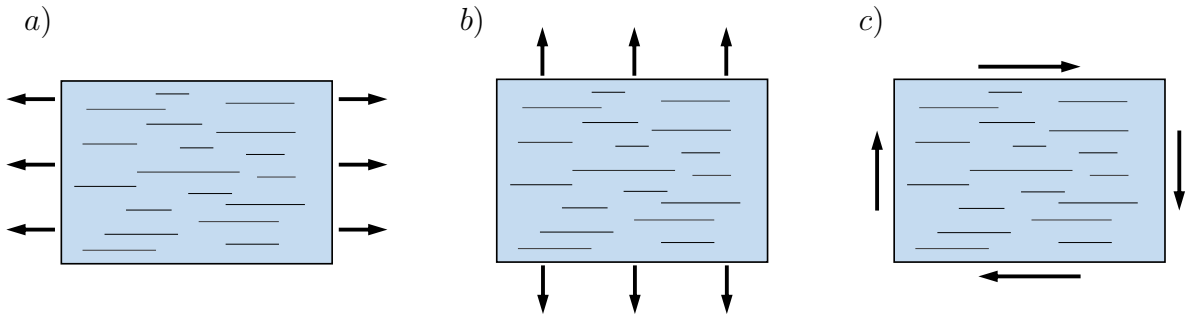


Figure 1.1: A diagram of a $2D$ sheet of fluid with fibres fixed to be aligned in the $x$-direction, undergoing deformation due to a) an extensional flow parallel to the fibres, b) an extensional flow orthogonal to the fibres, and c) a shear flow over the fibres.

the new length of the fibre, $\boldsymbol{l'}^*$ is given by

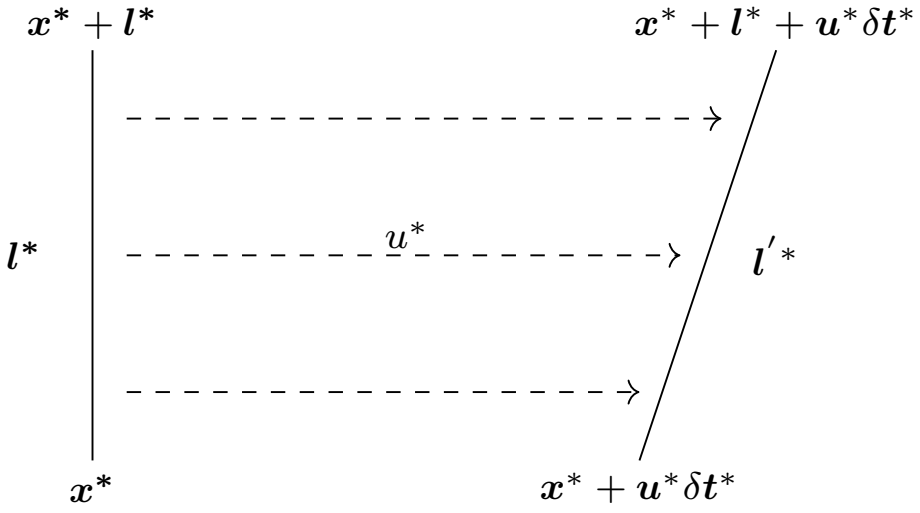


Figure 1.2: Advection of $\boldsymbol{u}^*$ over a single fibre of initial length $\boldsymbol{l}^*$.

$$\boldsymbol{l'}^* = \boldsymbol{l}^* + \underbrace{\boldsymbol{u}^* \left(\boldsymbol{x}^* + \boldsymbol{l}^*\right) \delta t^* - \boldsymbol{u}^* \left(\boldsymbol{x}^*\right) \delta t^*}_{\text{stretching of the fibre}} . \tag{1.10}$$

Applying a Taylor expansion to the second term yields

$$\boldsymbol{l'}^* = \boldsymbol{l}^* + \left(\boldsymbol{l}^* \cdot \nabla^*\right) \boldsymbol{u}^* \delta t^* + \mathcal{O}\left(\boldsymbol{l}^{*^2} \delta t^*\right), \tag{1.11}$$

then taking the limit as $\delta t^* \to 0$

$$\frac{D\boldsymbol{l}^*}{Dt^*} = (\boldsymbol{l}^* \cdot \nabla^*)\, \boldsymbol{u}^*. \tag{1.12}$$

We set $\boldsymbol{l}^* = s^* \boldsymbol{a}$, where $\boldsymbol{a}$ is the unit vector describing the direction of the fibre, and $s^*$ the length of the fibre under consideration. Then we may write

$$\frac{\partial \boldsymbol{a}}{\partial t^*} + (\boldsymbol{u}^* \cdot \nabla^*)\boldsymbol{a} + \frac{\dot{s^*}}{s^*}\boldsymbol{a} = (\boldsymbol{a} \cdot \nabla^*)\boldsymbol{u}^*, \tag{1.13}$$

where $\dfrac{\dot{s^*}}{s^*}$ is the fractional rate of extension of the fibre in the direction of the fibre. We can eliminate $\dfrac{\dot{s^*}}{s^*}$ from (1.13) by multiplying by $\boldsymbol{a}$ and using the fact that $\boldsymbol{a}$ is a unit vector obtain

$$\zeta^* := \frac{\dot{s^*}}{s^*} = \boldsymbol{a} \cdot ((\boldsymbol{a} \cdot \nabla^*)\boldsymbol{u}^*), \tag{1.14}$$

so that equation (1.13) becomes

$$\frac{\partial \boldsymbol{a}}{\partial t^*} + (\boldsymbol{u}^* \cdot \nabla^*)\boldsymbol{a} + \zeta^* \boldsymbol{a} = (\boldsymbol{a} \cdot \nabla^*)\boldsymbol{u}^*. \tag{1.15}$$

Equation (1.15) is the required kinematic equation for the evolution of $\boldsymbol{a}$. We remark that this evolution equation corresponds to the case where the ratio of the the fibre length to thickness approaches infinity. We also note that since $\boldsymbol{a}$ is a unit vector, the model depends only upon the local alignment of the fibres and not their length.

The theory of transversely isotropic fluid flows has been used by a number of studies in other geometries to gain insight into how their behaviour is affected by a microstructure. These include the stability of a transversely isotropic fluid in a Taylor-Couette device with the aim of understanding the behaviour of suspensions of bio-molecules, as well as treating the problem of Rayleigh-Bernard convection [46, 48]. It was found in both works that transversely isotropic effects delay the onset of instabilities, primarily through the

incorporation of an anisotropic shear viscosity. In the context of modifying transversely isotropic fluid models to incorporate active swimming suspensions as [47], transversely isotropic effects are also capable of increasing the size of a developing instability, in particular where translation diffusion is neglected. Other studies have focused upon prototypical flows, to give more generic insights into fluid-fibre interactions. For example, Phan-Thien and Graham studied both the flow of a transversely isotropic fluid around a sphere [74], and the squeezing flow of a layer of fluid between two fixed plates [75] (this latter problem was studied independently by [85] for the case of a fibre-reinforced fluid without fibre extensibility).

We have now introduced the transversely isotropic stress tensor we use to describe the flow, and the coupled kinematic condition governing the evolution of the preferred direction of the fluid induced by the fibres. In this thesis, we study the behaviour of a transversely isotropic fluid in three contexts: the squeezing flow of a thin film, and the extensional flows of a thin sheet and a thread, flows which arise naturally from applications in biology and industry. By comparison with their Newtonian equivalents, we investigate the rheological changes induced by the interplay of the macroscopic flow and fibres within the material, and the resulting effects upon the mechanical behaviours the fluid.

## 1.3 Thin film flows

The fluid mechanics of thin films has been studied for over 100 years. In thin films, the flow exists in a geometry in which the depth is significantly smaller than the length or width of the fluid. The lubrication approximation allows for exploitation of this separation of scales to substantially reduce the complexity of the model, for more efficient examination. This approach has been utilised to examine thin films in a number of areas, for example, the propagation of gravity driven currents [52], flows of films with a free surface over varied topography [45], the stretching and buckling of liquid jets [15, 16, 30] and sheets [49, 104].

The motivation of early studies of thin films included the lubrication of ball bearings

[81] and experimental determination of viscosity [101]. Modern applications are wide ranging, with the study of thin films being of interest in numerous contexts, including compression moulding [100] and rheological testing of materials [31], lava flow [38], drawing of optical fibres and glass tubes [22, 42, 98], the mechanical behaviour of collagen gels [41], and flows in lung airways and linings [43]. The foundation of lubrication theory can be traced to Reynolds, who by application of the theory of creeping flow to a thin film, derived the Reynolds equation, which describes the pressure distribution of a thin film of incompressible fluid without inertia or body forces [81].

Although thin film flows were first studied in the context of Newtonian fluids, some fluids of interest possess non-Newtonian properties such as shear thinning (where the viscosity of the fluid decreases under shear strain). To this end, lubrication theory has also been used to incorporate non-Newtonian effects. In particular, a number of isotropic non-Newtonian fluid models have been studied such as generalised Newtonian fluids [67, 76], fluids exhibiting time-dependent shear thinning (thixotropy) [77], fluids possessing both viscous and elastic characteristics under deformation (viscoelastic) [89] and fluids that resist movement until a critical stress is reached (a yield-stress or viscoplastic fluid) [8, 86]. Use of the lubrication approximation in non-Newtonian settings is unsurprisingly more complex due to the need to account for a wider range of behaviours. For example, in flows involving yield-stress fluids, the leading order terms may not be sufficient to give a good description of the flow, and either regularisation techniques must be employed [37], or higher order terms must be obtained [7]. This is the 'lubrication paradox' as described by Lipscomb and Denn [59].

Some work has incorporated anisotropic effects within thin films, primarily focused upon the behaviour of nematic liquid crystals (NLC). Much like transversely isotropic fluids, NLCs possess a preferred direction, given by the local average orientation of molecules [14, 21]. As one might expect, the anisotropy of NLCs causes the fluid to behave differently to a Newtonian fluid, for example, in [54] a flow of a NLC film down an incline becomes unstable due to the elastic properties of the material. A common approach to modelling

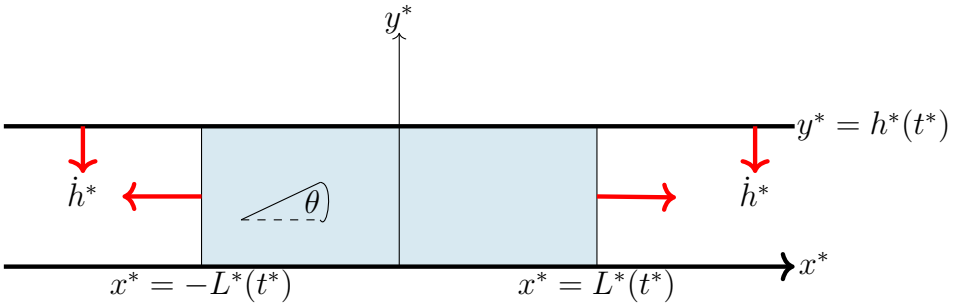


Figure 1.3: Schematic of the squeeze film geometry considered in Chapter 2. The fluid is contained between two plates, at $y^* = 0, h^*$. The lower plate remains fixed, whilst the upper plate is pushed down on the fluid at a prescribed speed $\dot{h}^*$. We prescribe a no-slip boundary condition on the upper and lower plates, and the fluid possesses no-stress free boundaries at $x^* = \pm L^*$. The fibres suspended within the fluid are characterised by their angle from the $x^*$-axis, given by $\theta$.

flows of NLCs is the use of the Ericksen-Leslie equations (see, for example, Ref. [97]), which arise from the Navier-Stokes equations with an anisotropic stress tensor as proposed by Leslie [57], coupled to an equation governing the average orientation of the liquid crystals, which comes from a torque balance on the direction of the molecules. As we saw in section 1.2, the incorporation of an anisotropic stress tensor is similar to our approach. However, the Ericksen-Leslie equations include effects of elasticity, which is not included in our model, and our preferred direction is given by an advection argument.

In this thesis, we consider two types of thin film flow: the squeezing of a fluid between two infinitely long plates, and extensional flow. We thus give greater detail on the progress in these areas.

### 1.3.1 Squeezing flows

Squeezing flows are flows in which a fluid undergoes deformation as two parallel plates are brought towards each other. The classical fluid mechanics problem of squeezing flow has received considerable attention, as evidenced in the review, Ref. [31]. This review has compiled over 200 references, largely upon the behaviours of Newtonian and isotropic non-Newtonian media, e.g. power law, viscoelastic, and viscoplastic fluids. Applications include the rheological testing of materials [31], and compression molding [100] of fibre-

reinforced polymers and composites.

Suspensions of fibres within squeeze flows have been modelled as isotropic non-Newtonian flows, such as Carreau [55], and as viscoelastic [91] fluids. A sizeable amount of work has been undertaken upon understanding the rheological properties of a fluid possessing fibres by using squeezing flow to study the non-Newtonian properties of a composite, including [10, 61, 63, 105]. However, in the context of molding of fibre-reinforced materials, the final fibre orientation of the fluid is intended to enhance the strength of the composite. To this end, the final orientation of fibres in a squeezing flow has been studied, including [35, 56, 72, 85, 95]. Understanding the anisotropic effects induced by the interplay between the fluid and the fibres is therefore crucial in order to predict the final orientation of the reinforcement.

There has been some work in the realm of incorporating anisotropy into the squeezing flow of thin films. Sommer [92] applied the fourth-order viscosity tensor approach similar to Ericsson [33], with fibre movement based upon Jeffery's equation for dilute suspensions to incorporate anisotropic behaviours in a lubricated squeezing flow in a cylindrical geometry. Cousins et al [20] used the Ericksen–Leslie equations to describe the squeezing of a drop of nematic liquid crystal, applicable to the one drop filling process, suggesting that defects in the molecule orientation gave rise to irregularities in the structure of the material, degrading the performance of liquid crystal devices.

The theory of transversely isotropic fluids has previously been applied by Spencer [94, 95] in modelling the forming stage in the production of fibre-reinforced composite materials, which takes place at a temperature above the melting point of the matrix. Indeed, a squeezing flow problem similar to that studied here has been investigated by Rogers [85] in connection with the manufacture of fibre-reinforced resins. The latter paper considers a three-dimensional geometry, which is more realistic than the two-dimensional case studied in chapter 2. However, an assumption common to these previous works is that the material is inextensible in the fibre direction. In Rogers' study, he further assumes the fibres are initially parallel to the plates compressing the fluid, with the result that

there is no change in alignment of the fibres due to the flow. In chapter 2 we consider the behaviour of the fluid when the assumption of material inextensibility in the fibre direction is relaxed. This problem is similar to that treated by Phan-Thien and Graham [75], however, our use of systematic perturbation techniques allows us to gain additional information about the important time- and length-scales.

### 1.3.2 Extensional flows

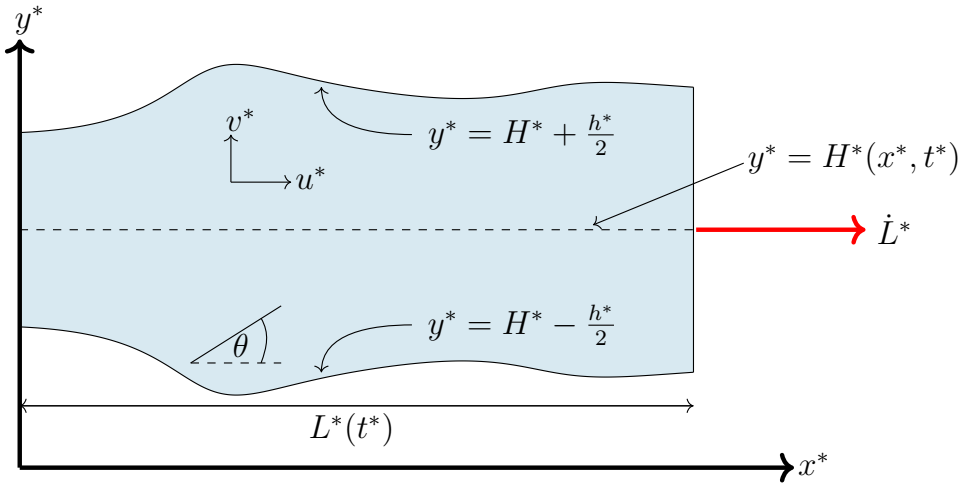


Figure 1.4: Schematic of the extensional flow of the sheet considered in chapter 3. The fluid is fixed to two plates at $x^* = 0, L$, by a no-slip boundary condition. The plate at $x^* = L^*$ is moved at a prescribed speed $\dot{L}^*$. The centre-line of the fluid is given by $H^*(x^*, t^*)$ and the thickness of the film by $h^*(x^*, t^*)$, so that the free boundaries of the film are located at $y^* = H^* \pm \frac{h^*}{2}$.

Extensional flows are flows under which the leading-order fluid velocity in the direction of extension is independent of vertical position. In this thesis, this will be the longitudinal velocity. These problems include the difficulty that they possess free boundaries, which must be solved for. Extensional flows of thin sheets and threads arise in a number of industrial and biological applications, such as the manufacture of optical fibres [98], glass tubes [42] and microelectrodes [51], the experimental determination of the extensional viscosity of non-Newtonian materials using filament-stretching rheometers [62], and biological contexts, such as the modelling of biofilm expansion [99] and the mechanical behaviour of collagen gels [41].

Newtonian extensional thin film problems have been extensively studied (see, the review, Ref. [30]). The first study of extensional flow was by Trouton, [101], who gives his name to the simplest model of extensional flow, which involves only the leading order longitudinal fluid velocity and sheet thickness. The problem of a two-dimensional thin sheet and thread was considered by Howell [49], who demonstrated that the Trouton model may be derived from the Navier-Stokes equations by using an asymptotic expansion in powers of the inverse aspect ratio of the film, and included the roles of inertia and surface tension. As given by Howell, for a two-dimensional sheet undergoing extension, the Trouton model in dimensionless form is

$$\frac{\partial h}{\partial t} + \frac{\partial}{\partial x}\left(uh\right) = 0, \tag{1.16}$$

$$\frac{\partial}{\partial x}\left(4h\frac{\partial u}{\partial x}\right) = 0, \tag{1.17}$$

where $h, u$ are the leading order thickness and longitudinal velocity of the film, which is defined to be the line connecting the centre of mass of each cross section of the film, $x$ is the longitudinal coordinate, and $t$ is time. The constant 4 in equation (1.17) is the Trouton ratio between the shear viscosity and the extensional viscosity for a two-dimensional Newtonian sheet [49]. A first integral of (1.17) yields

$$4h\frac{\partial u}{\partial x} = T(t), \tag{1.18}$$

where $T$ is the resistance of the sheet to the extension, which throughout this thesis we refer to as the tension applied to the film. It is noted by Howell that so long as the tension in the sheet is nonzero, the centre–line of the sheet, defined to be the line connecting the centre of mass of each cross section, is straight to leading–order.

In chapters 3 and 5, our transversely isotropic model will reduce to the Trouton model with appropriate choice of parameters. The Trouton model is only valid for films that are being pulled apart and is not valid for sheets and threads undergoing deformation by bending as the assumption that the centre-line is nearly straight is violated. In order to

capture the full behaviours of the centre-line of the fluid in the sheet, a short timescale analysis is carried out in [16, 49, 50]. This allows for a description of the evolution of the centre-line for sheets that are initially slightly curved, and examination of buckling behaviours of the sheet.

The development of a general theory for thin viscous sheets that undergo deformation by bending, stretching, or an arbitrary combination of both, was published by Ribe [82, 84]. This work was able to quantify relations between bending and stretching of the sheet and these techniques have also been employed to study the coiling of a viscous jet [83]. A complementary study considered sheets with an inhomogenous viscosity, [73]. One of their main results was that 'necking' of the sheet, where regions of the sheet thinned faster than others, could be induced by in-plane variations of viscosity throughout the fluid.

Some works have also studied non-Newtonian effects, motivated by applications such as ink-jet printing [65], fibre-spinning and molding processes [71], where a (typically viscoelastic) fluid undergoes extensional flow. Experimental determination of extensional viscosity in these contexts has been studied, [60, 62, 96] and similarly to Newtonian fluids, asymptotic approaches have been employed to model slender viscoelastic jets [90] and liquid bridges [70], and it has been shown that viscoelastic effects can delay the breakup of a jet [40]. In [78, 80], using a one-dimensional model neglecting curvature and inertia, it is shown that no finite-time breakup occurs at all for Maxwell and Oldroyd-B fluids. However, break up can occur and has been described using similarity solutions for Giesekus fluids [36, 79] and power-law fluids [27].

Viscoplastic effects have also seen some consideration. Extension under gravity has been studied including inertia and surface tension [3, 6] and a general model for extensional dynamics of a viscoplastic sheet and thread has been constructed [9].

For a transversely isotropic fluid, we are aware of two studies of extensional flow. The first of which is Dyson & Jensen [29], who modelled the primary plant cell wall as a thin axisymmetric fibre-reinforced viscous sheet supported between rigid end plates. The other study is that of Green & Friedman [41], who used a similar approach to that of Howell to

derive a generalised version of the Trouton model for the extensional flow of a transversely isotropic sheet. They presented some analytical results for cases in which the equations simplify, but did not tackle the general case - which we do in chapter 3.

## 1.4 Thesis overview

In this chapter we have given an overview of the literature on anisotropic thin film flows and have introduced the equations describing the the fluid flow and evolution of the preferred direction for a transversely isotropic fluid, consisting of the Stokes equations (1.7)-(1.8), along with the constitutive law (1.9), and a kinematic condition governing the fibre direction, (1.15).

In chapter 2 we consider the squeezing flow of a transversely isotropic fluid. This provides a setting where some of the parameter values for a transversely isotropic fluid might be determined experimentally. We introduce the asymptotic and numerical techniques that we employ throughout this thesis, and investigate the behaviour of the film on both a flow- and short- timescale. The advantage of approaching the squeezing flow of a thin film first is that we do not have a free boundary that must be accounted for as we prescribe the movement of the plates.

In chapter 3 we consider the extensional flow of a transversely isotropic sheet, a problem first considered by Green and Friedman [41]. This work presented some analytical results under conditions where the equations are simplified. We expand on this by tackling the general problem, and examine the effect of the fibre direction on the flow. We will see that, though a Newtonian fluid will always have a straight centre-line on the flow timescale, for a transversely isotropic fluid this is not always the case. We then examine the behaviour of the centre-line over a short timescale in chapter 4.

In chapter 5 we consider the extensional flow of an axisymmetric transversely isotropic thread. This is an extension of the work of chapter 3 by including a second fibre angle, which allows us to examine the behaviours of the fibre within the cross section of the

thread. Finally, in chapter 6 we draw conclusions and discuss avenues for potential future work.

CHAPTER 2

# SQUEEZING OF A TRANSVERSELY ISOTROPIC FILM

## 2.1 Introduction

The first model we discuss in this thesis is the squeezing flow of a thin film of viscous transversely isotropic fluid. In doing so we aim to both illustrate the techniques which will be utilised throughout this thesis and to provide a setting in which some of the parameter values discussed in the previous chapter may be determined by laboratory experiment.

In section 2.2 we introduce the governing equations and boundary conditions, applying the equations given in chapter 1 to the geometry of squeezing flow, before applying a thin film approximation in section 2.3 to exploit the slender geometry we consider. We employ asymptotic techniques to study the behaviour of the flow on a short time-scale, for a small anisotropic extensional viscosity in section 2.5, before discussing the results from the short timescale flow in section 2.7 and giving concluding remarks for the chapter in section 2.8.

## 2.2 Governing Equations

We consider the problem of a thin layer of viscous transversely isotropic fluid between two plates, neglecting inertia, gravity and surface tension, with the lower plate being fixed, and the upper plate forced down onto the fluid with prescribed velocity $\dot{h}^*$. We take the

fluid velocities to be $\boldsymbol{u}^* = (u^*, v^*)$ in the $x^*, y^*$ directions respectively, and the direction of the fibres to be $\boldsymbol{a} = (\cos\theta, \sin\theta)$, where $\theta$ is the angle the fibres make with the $x^*$-axis. Dimensional quantities are denoted with an asterisk (see Figure 1.3). We begin with equations for incompressibility of the fluid, and momentum balance

$$\nabla^* \cdot \boldsymbol{u}^* = 0, \tag{2.1}$$

$$\nabla^* \cdot \boldsymbol{\sigma}^* = 0. \tag{2.2}$$

We use the now familiar constitutive law for $\boldsymbol{\sigma}^*$ as given in (1.9), and the fibre direction evolution equation (1.15) is

$$\frac{\partial \theta}{\partial t^*} + u^* \frac{\partial \theta}{\partial x^*} + v^* \frac{\partial \theta}{\partial y^*} = -\sin\theta\cos\theta \frac{\partial u^*}{\partial x^*} - \sin^2\theta \frac{\partial u^*}{\partial y^*} + \cos^2\theta \frac{\partial v^*}{\partial x^*} + \sin\theta\cos\theta \frac{\partial v^*}{\partial y^*}. \tag{2.3}$$

We assume that the lower plate is static at $y^* = 0$, whilst the position of the upper plate, $y^* = h^*(t^*)$, is prescribed. On these two boundaries we apply a no-slip condition:

$$u^* = 0, v^* = 0, \text{on } y^* = 0; \tag{2.4}$$

$$u^* = 0, v^* = \dot{h^*}, \text{on } y^* = h^*, \tag{2.5}$$

where the notation $\dot{h}^*$ is used to represent $\dfrac{\mathrm{d}h^*}{\mathrm{d}t}$. Additionally, we assume the fluid film extends from $x^* = -L^*(t^*)$ to $x^* = L^*(t^*)$ and impose zero stress on these boundaries:

$$\boldsymbol{\sigma}^* \cdot \hat{\boldsymbol{n}} = 0; \text{ on } x^* = \pm L^*. \tag{2.6}$$

We note that we are assuming $L = L(t)$. In reality, one might expect the free boundaries at $x = \pm L$ to be curved, with a radius of curvature $\mathcal{O}(\varepsilon)$. Finally, we must also supply initial conditions for the fibre direction and length of the fluid:

$$\theta(x^*, y^*, 0) = \theta_i^*, L^*(0) = L_0^*. \tag{2.7}$$

### 2.2.1 Nondimensionalisation

We nondimensionalise the governing equations with the following variables:

$$(x^*, y^*) = (xL_0, \varepsilon y L_0), \quad (u^*, v^*) = (uU, \varepsilon v U), \quad p^* = \frac{\mu^* U}{\varepsilon L_0} p, \quad t^* = \frac{L_0}{U} t,$$
$$(L, h) = (L_0 L^*, \varepsilon L_0 h^*),$$

where $U \sim \varepsilon^{-1}\dot{h}$ is a typical horizontal velocity, $L_0$ is the initial half-length of the fluid sheet, and $\varepsilon \ll 1$ is the initial inverse aspect ratio of the sheet. We also recall the dimensionless quantities

$$\mu_1 = \frac{\mu_1^* L}{\mu^* U}, \quad \mu_2 = \frac{\mu_2^*}{\mu^*}, \quad \mu_3 = \frac{\mu_3^*}{\mu^*}.$$

After this process, we have the incompressiblity condition

$$\frac{\partial u}{\partial x} + \frac{\partial v}{\partial y} = 0, \tag{2.8}$$

with the momentum equation in the $x$-direction

$$\begin{aligned} &-\varepsilon^{-2}\frac{\partial p}{\partial x} + \varepsilon^{-2}\frac{\partial^2 u}{\partial y^2} + \frac{\partial^2 u}{\partial x^2} + \mu_1 \frac{\partial}{\partial x}\left(\cos^2\theta\right) + \varepsilon^{-1}\mu_1 \frac{\partial}{\partial y}\left(\cos\theta \sin\theta\right) \\ &\quad + \mu_2 \frac{\partial}{\partial x}\left[\cos^4\theta \frac{\partial u}{\partial x} + \cos^3\theta \sin\theta \left(\varepsilon^{-1}\frac{\partial u}{\partial y} + \varepsilon \frac{\partial v}{\partial x}\right) + \cos^2\theta \sin^2\theta \frac{\partial v}{\partial y}\right] \\ &\quad + \varepsilon^{-1}\mu_2 \frac{\partial}{\partial y}\left[\cos^3\theta \sin\theta \frac{\partial u}{\partial x} + \cos^2\theta \sin^2\theta \left(\varepsilon^{-1}\frac{\partial u}{\partial y} + \varepsilon \frac{\partial v}{\partial x}\right) + \cos\theta \sin^3\theta \frac{\partial v}{\partial y}\right] \\ &+ 2\mu_3 \frac{\partial}{\partial x}\left[2\cos^2\theta \frac{\partial u}{\partial x} + \cos\theta \sin\theta \left(\varepsilon^{-1}\frac{\partial u}{\partial y} + \varepsilon \frac{\partial v}{\partial x}\right)\right] + \mu_3 \frac{\partial}{\partial y}\left[\varepsilon^{-2}\frac{\partial u}{\partial y} + \frac{\partial v}{\partial x}\right] = 0, \end{aligned} \tag{2.9}$$

whilst in the $y$-direction we have

$$
\begin{aligned}
&-\varepsilon^{-3}\frac{\partial p}{\partial y}+\varepsilon\frac{\partial^2 v}{\partial x^2}+\varepsilon^{-1}\frac{\partial^2 v}{\partial y^2}+\varepsilon^{-1}\mu_1\frac{\partial}{\partial x}\left(\sin^2\theta\right)+\mu_1\frac{\partial}{\partial x}\left(\cos\theta\sin\theta\right)\\
&\quad+\varepsilon^{-1}\mu_2\frac{\partial}{\partial y}\left[\cos^2\theta\sin^2\theta\frac{\partial u}{\partial x}+\cos\theta\sin^3\theta\left(\varepsilon^{-1}\frac{\partial u}{\partial y}+\varepsilon\frac{\partial v}{\partial x}\right)+\sin^4\theta\frac{\partial v}{\partial y}\right]\\
&\quad+\mu_2\frac{\partial}{\partial y}\left[\cos^3\theta\sin\theta\frac{\partial u}{\partial x}+\cos^2\theta\sin^2\theta\left(\varepsilon^{-1}\frac{\partial u}{\partial y}+\varepsilon\frac{\partial v}{\partial x}\right)+\cos\theta\sin^3\theta\frac{\partial v}{\partial y}\right]\\
&+2\varepsilon^{-1}\mu_3\frac{\partial}{\partial y}\left[2\sin^2\theta\frac{\partial v}{\partial y}+\cos\theta\sin\theta\left(\varepsilon^{-1}\frac{\partial u}{\partial y}+\varepsilon\frac{\partial v}{\partial x}\right)\right]+\mu_3\frac{\partial}{\partial x}\left[\varepsilon^{-1}\frac{\partial u}{\partial y}+\varepsilon\frac{\partial v}{\partial x}\right]=0,
\end{aligned}
\tag{2.10}
$$

and the fibre equation (2.3)

$$
\frac{\partial\theta}{\partial t}+u\frac{\partial\theta}{\partial x}+v\frac{\partial\theta}{\partial y}=-\sin\theta\cos\theta\frac{\partial u}{\partial x}-\varepsilon^{-1}\sin^2\theta\frac{\partial u}{\partial y}+\varepsilon\cos^2\theta\frac{\partial v}{\partial x}+\sin\theta\cos\theta\frac{\partial v}{\partial y}. \tag{2.11}
$$

Finally, the dimensionless no-slip and zero-stress conditions are

$$u=0, v=0, \text{on } y=0, \tag{2.12}$$

$$u=0, v=\dot{h}, \text{on } y=h, \tag{2.13}$$

$$\sigma_{xx}=0, \text{on } x=\pm L, \tag{2.14}$$

$$\sigma_{xy}=0, \text{on } x=\pm L. \tag{2.15}$$

## 2.3 Thin film approximation

We exploit the slender geometry of the fluid to simplify the governing equations. Expanding the dependent variables as power series of $\varepsilon$,

$$u=u^{(0)}+\varepsilon u^{(1)}+\varepsilon^2 u^{(2)}+..., \text{ etc }, \tag{2.16}$$

equation (2.10) yields at leading order,

$$\frac{\partial p^{(0)}}{\partial y} = 0, \tag{2.17}$$

and hence pressure is uniform throughout the thickness of the film. The $x$-momentum equation supplies

$$-\frac{\partial p^{(0)}}{\partial x} + (1+\mu_3)\frac{\partial^2 u^{(0)}}{\partial y^2} + \mu_2 \frac{\partial}{\partial y}\left(\sin^2\theta^{(0)}\cos^2\theta^{(0)}\frac{\partial u^{(0)}}{\partial y}\right) = 0, \tag{2.18}$$

and the contribution from the fibre equation (2.11) is

$$\sin^2\theta^{(0)}\frac{\partial u^{(0)}}{\partial y} = 0. \tag{2.19}$$

Using this result to integrate equation (2.18), and using the boundary conditions on $u^{(0)}$ at $y = 0, h^{(0)}$, we obtain

$$u^{(0)} = \frac{y\left(y - h^{(0)}\right)}{2\left(1+\mu_3\right)}\frac{\partial p^{(0)}}{\partial x}. \tag{2.20}$$

Substitution of equation (2.20) into conservation of mass, (2.8), together with the boundary condition $v^{(0)} = 0$ on $y = 0$, yields a result for $v^{(0)}$:

$$v^{(0)} = \frac{1}{2\left(1+\mu_3\right)}\left(\frac{h^{(0)}y^2}{2} - \frac{y^3}{3}\right)\frac{\partial^2 p^{(0)}}{\partial x^2}. \tag{2.21}$$

Applying the boundary condition $v^{(0)} = \dot{h}^{(0)}$ on $y = h^{(0)}$ to equation (2.21) gives us an equation for pressure:

$$\frac{2\dot{h}^{(0)}\left(1+\mu_3\right)}{h^{(0)^3}} = \frac{\partial^2 p^{(0)}}{\partial x^2}, \tag{2.22}$$

which, combined with the no-stress boundary condition (2.14) at leading order ($p^{(0)} = 0, \text{ on } x = \pm L^{(0)}$), yields

$$p^{(0)} = \frac{6\left(1+\mu_3\right)}{h^{(0)^3}}\left(x^2 - L_0^2\right)\dot{h}^{(0)}. \tag{2.23}$$

We note that the equation for pressure is only consistent with equation (2.17) if $L_0 = L_0(t)$, that is, the free boundary at $x = \pm L$ is not curved. As previously discussed, we might expect the free boundary to have a radius of curvature $\mathcal{O}(\varepsilon)$. However, since this effect is confined to the two edges of the sheet, we neglect it here. Instead, we determine $L_0$ from conservation of volume:

$$L_0(t) = \frac{A_i}{2h^{(0)}(t)} = \frac{1}{h^{(0)}(t)}, \tag{2.24}$$

where, without loss of generality, we have set the initial area of the fluid sheet, $A_i$, to be two. We now return to the equation for the fibre director angle, equation (2.11). At leading order, we have (2.19), whilst $u^{(0)}$ is given by (2.20). This implies that we must have $\theta^{(0)} = 0$ for the solution developed to be valid. That is, the fibres are almost exactly aligned with the $x$-axis except along the lines $x = 0, y = \dfrac{h^{(0)}}{2}$, where $\dfrac{\partial u^{(0)}}{\partial y} = 0$. Hence, we are unable to satisfy an arbitrary initial condition for $\theta^{(0)}$. This suggests that the solution for $\theta^{(0)}$ is a singular perturbation problem in $t$, the long-time solution of which is $\theta^{(0)}$. Therefore, in order to study the evolution of the fibre alignment for an arbitrary choice of initial condition for $\theta^{(0)}$, we must consider behaviour on a timescale shorter than $\dfrac{L_0}{U}$. We turn to such a short time-scale analysis in Section 2.5.

## 2.4 Experimental determination of the anisotropic shear viscosity

One of the aims of this chapter was to determine how the parameter values for a transversely isotropic fluid might be determined experimentally. We note from section 2.3 that, on the flow timescale, the behaviour of the pressure of the fluid depends upon only one dimensionless parameter, $\mu_3$. One may compute

$$F = \int_{-L}^{L} p^{(0)}|_{y=h_0} \mathrm{d}x = -\frac{8\dot{h}^{(0)}(1+\mu_3)}{h^{(0)^6}}, \tag{2.25}$$

as the leading order force exerted on the upper plate by the fluid. Hence, if the force on the upper plate may be measured, and $\dot{h}^{(0)}$ is known, $\mu_3$ may be determined. Alternatively, if the force exerted on the fluid by the plate is known, we can integrate (2.25) to give

$$\frac{1}{h^{(0)^5}} = \frac{1}{h_i^5} + \frac{5}{8(1+\mu_3)} \int_0^t F(t)\mathrm{d}t. \tag{2.26}$$

We can then determine $\mu_3$ from measurements of the film height. Throughout the rest of the chapter, we examine a short time-scale analysis in order to study the early-time evolution of the fibres.

## 2.5 Short time behaviour

In this section, we examine the short time-scale evolution of the fibres from the initially prescribed orientation to the uniform $\theta^{(0)} \equiv 0$ solution found above. We introduce the short timescale, $\tau$, defined by:

$$t = \varepsilon\tau. \tag{2.27}$$

On this timescale, the distance moved by the plates will be negligible, and hence we set $h^{(0)}(\tau) = h_i = 1$, $L^{(0)}(\tau) = L_i = 1$. Note that we have not rescaled velocities, and therefore the scaling of $\dot{h}^{(0)}$ is unchanged. To leading order, the equations (2.17), (2.18), remain unchanged, whilst the fibre direction equation (2.11) now yields

$$\frac{\partial\theta^{(0)}}{\partial\tau} = -\sin^2\theta^{(0)}\frac{\partial u^{(0)}}{\partial y}. \tag{2.28}$$

At this point it is difficult to make further analytical progress, and we turn to numerical techniques. To this end, we rewrite the incompressibility condition as

$$\frac{\partial}{\partial x}\int_0^{h_i} u\mathrm{d}y = -\dot{h}^{(0)}. \tag{2.29}$$

Writing (2.29) in this way allows us to remove $v^{(0)}$ from the model, and hence we now need only solve for $p^{(0)}, u^{(0)}, \theta^{(0)}$. Our strategy is as follows. Given initial conditions $\theta_i(x,y), h_i, \dot{h}_i$, we simultaneously solve (2.18) and (2.29) for $p^{(0)}$ and $u^{(0)}$ subject to the no-stress boundary conditions using a centered space finite difference scheme. We then use a forward Euler method upon equation (2.28) to update $\theta^{(0)}$ to the next time step. We repeat this process until we reach the desired time. Details of the discretisation and matrix construction can be found in Appendix A.1.

## 2.6 Early time solution for small $\mu_2$

In this subsection, we consider the evolution of the fibre alignment for $\hat{\mu}_2 \ll 1$, remaining in the short time-scale. In this regime, we construct analytical results to compare with the output of the solver detailed above. We write $\hat{\mu}_2 = \delta\mu_2$, where $\delta$ is a small dimensionless parameter. In order to remain consistent with the thin film approximations already made, we require $\varepsilon \ll \delta \ll 1$. We then expand

$$u^{(0)} = u_0^{(0)} + \delta u_1^{(0)} + \delta^2 u_2^{(0)} \text{ etc}, \tag{2.30}$$

with similar expansions for $p^{(0)}, \theta^{(0)}, \dot{h}^{(0)}$. For the sake of simplicity, we take $\dot{h}^{(0)} = -1 + \delta\dot{h}_1^{(0)}$, with $\dot{h}_1^{(0)}$ being prescribed. The solutions for $u_0^{(0)}, v_0^{(0)}, p_0^{(0)}$ are obtained directly from (2.20),(2.21) and (2.23):

$$p_0^{(0)} = 6\left(1+\mu_3\right)\left(1-x^2\right), \quad u_0^{(0)} = -6xy\left(y-1\right), \quad v_0^{(0)} = -6\left(\frac{y^2}{2} - \frac{y^3}{3}\right). \tag{2.31}$$

Next, the equation for the fibre angle gives

$$\frac{\partial\theta_0^{(0)}}{\partial\tau} = 6x\left(1-2y\right)\sin^2\theta_0^{(0)}, \tag{2.32}$$

which, upon integration, yields

$$\cot\theta_0^{(0)} = \cot\theta_i + 6\,(1-2y)\,x\tau, \tag{2.33}$$

We note that from the above, $\theta_0^{(0)} \to 0$ as $\tau \to \infty$, which is consistent with the solution on the $\dfrac{L_0}{U}$ timescale, except along the lines $y = \dfrac{1}{2}$ and $x = 0$. The latter effect is because the leading order vorticity, $\omega_0^{(0)} = 6x\,(2y-1)$, is zero along those lines. We may use these analytical results to provide some validation for our numerical approach. For the choice of $\hat{\mu}_2 = 0.5, \theta_i = \dfrac{\pi}{2}$, we plot results for the leading order fibre direction in Figure 2.1. Despite the relatively large choice of $\hat{\mu}_2$, the numerical techniques show good agreement with the analytical solution with the greatest errors around the line $y = \dfrac{1}{2}$.

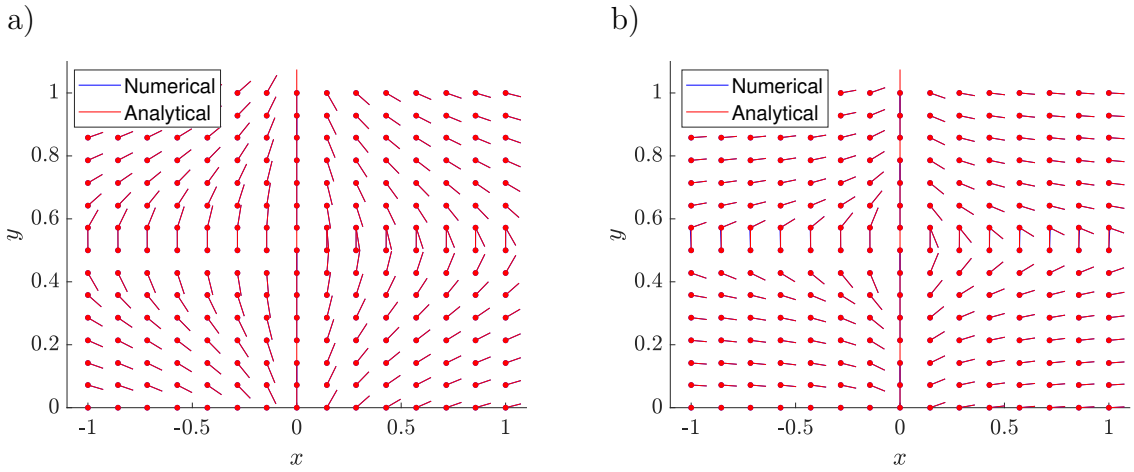


Figure 2.1: Comparison of the analytical result for the fibre direction for the choices of $\hat{\mu}_2 = 0.5, \mu_3 = 0.5, h_i = 1, L_i = 1, \theta_i = \dfrac{\pi}{2}$ against the numerical results at a) $\tau = 1$, and b) $\tau = 5$. The dots correspond to the base of the fibres.

### 2.6.1 Higher order terms for small $\mu_2$

Since the leading-order behaviour of the flow for $\hat{\mu}_2 \ll 1$ is essentially Newtonian, we now wish to determine the next-order terms in the solution for the velocity, to gain some insight into how the presence of the fibres affects the flow, and provide further validation for the numerical techniques detailed above. From (2.17) we have that $p_1^{(0)} = p_1^{(0)}(x,\tau)$,

and the $x$-momentum equation (2.18) then yields

$$\frac{\partial p_1^{(0)}}{\partial x} + (1+\mu_3)\frac{\partial^2 u_1^{(0)}}{\partial y^2} + \frac{\hat{\mu}_2}{4}\frac{\partial}{\partial y}\left(\sin^2 2\theta_0^{(0)}\frac{\partial u_0^{(0)}}{\partial y}\right) = 0. \tag{2.34}$$

Rearrangement of equation (2.33), yields

$$\frac{\sin^2 2\theta_0^{(0)}}{4} = \frac{\tan^2\theta_0^{(0)}}{\left(1+\tan^2\theta_0^{(0)}\right)^2} = \frac{\tan^2\theta_i\left[1+6\left(1-2y\right)x\tau\tan\theta_i\right]^2}{\left(\left[1+6\left(1-2y\right)x\tau\tan\theta_i\right]^2 1+\tan^2\theta_i\right)^2}. \tag{2.35}$$

Substituting this result into equation (2.34), and integrating with respect to $y$ and applying $u_1^{(0)}$ on $y = 0, 1$,

$$u_1^{(0)} = \frac{y\left(y-1\right)}{2\left(1+\mu_3\right)}\frac{\partial p_1^{(0)}}{\partial x} + \frac{\hat{\mu}_2\tan^2\theta_i}{2\left(1+\mu_3\right)^2}\frac{\partial p_0^{(0)}}{\partial x}\left(\mathcal{W}\left(x,y,\tau,\theta_i\right) - y\mathcal{W}\left(x,1,\tau,\theta_i\right)\right), \tag{2.36}$$

where the introduced function $\mathcal{W}$ is given by

$$\mathcal{W}(x,y,\tau,\theta_i) = \int_0^y \frac{\left(1-2\xi\right)\left(1+6\left(1-2\xi\right)x\tau\tan\theta_i\right)^2}{\left(\left[1+6\left(1-2\xi\right)x\tau\tan\theta_i\right]^2+\tan^2\theta_i\right)^2}. \tag{2.37}$$

This integral may be evaluated in a closed form, but the result is unwieldy and is thus given in Appendix A.2 for convenience. Using (2.8), and applying $v_1^{(0)} = 0$ on $y = 0$, we obtain

$$v_1^{(0)} = -\frac{\left(2y^3-3y^2\right)}{12\left(1+\mu_3\right)}\frac{\partial^2 p_1^{(0)}}{\partial x^2} - \frac{\hat{\mu}_2\tan^2\theta_i}{2\left(1+\mu_3\right)^2}\frac{\partial}{\partial x}\left(\frac{\partial p_0^{(0)}}{\partial x}\left[\mathcal{Z}\left(x,y,\tau,\theta_i\right) - \frac{y^2}{2}\mathcal{W}\left(x,1,\tau,\theta_i\right)\right]\right), \tag{2.38}$$

where

$$\mathcal{Z}\left(x,y,\tau,\theta_i\right) = \int_0^y \mathcal{W}\left(x,\xi,\tau,\theta_i\right)\mathrm{d}\xi. \tag{2.39}$$

Again, this integral may be evaluated in closed form, and the result is given in Appendix A.2. Applying the condition $v_1^{(0)} = \dot{h}_1^{(0)}$ on $y = 1$ gives an equation for $p^{(0)}$. Upon

integrating and applying $p_1^{(0)} = 0$ on $x = \pm 1$, we find that

$$p_1^{(0)} = 6\left(1+\mu_3\right)\left(x^2-1\right)\dot{h}_1^{(0)} - 72\hat{\mu}_2 \tan^2\theta_i \left[\int_{-1}^{x} \mathcal{G}\left(\xi,\tau,\theta_i\right)\mathrm{d}\xi - \frac{(1+x)}{2}\int_{-1}^{1} \mathcal{G}\left(\xi,\tau,\theta_i\right)\mathrm{d}\xi\right], \tag{2.40}$$

where we have substituted for $p_0^{(0)}$, and defined $\mathcal{G}$ to be

$$\mathcal{G}\left(x,\tau,\theta_i\right) = x\left(\mathcal{Z}\left(x,1,\tau,\theta_i\right) - \frac{1}{2}\mathcal{W}\left(x,1,\tau,\theta_i\right)\right). \tag{2.41}$$

We begin by setting the speed of the plates at this order, $\dot{h}_1^{(0)} = 0$, and examine the correction term to the pressure induced by the presence of the fibres. In Figure 2.2a, we plot a comparison between the result obtained by computing $p_1^{(0)}$ from (2.40) directly, against the result from the numerical solver as described in section 2.5. The numerical result is obtained by subtracting the analytical result for $p_0^{(0)}$ as given in (2.31). We see good agreement between the asymptotic result and the numerical solution.

In Figure 2.2b we show the correction to the pressure gradient induced by the fibres. We notice that it is non-monotonic, and that as time increases the extrema of the function move from the edges of the fluid domain towards $x = 0$. This is in strong contrast to the purely Newtonian case, where the pressure gradient is linear. Generally the size of the small $\delta$ correction to the pressure gradient decreases with time as the fibre angle tends to zero (in which limit, the behaviour of the fluid is Newtonian).

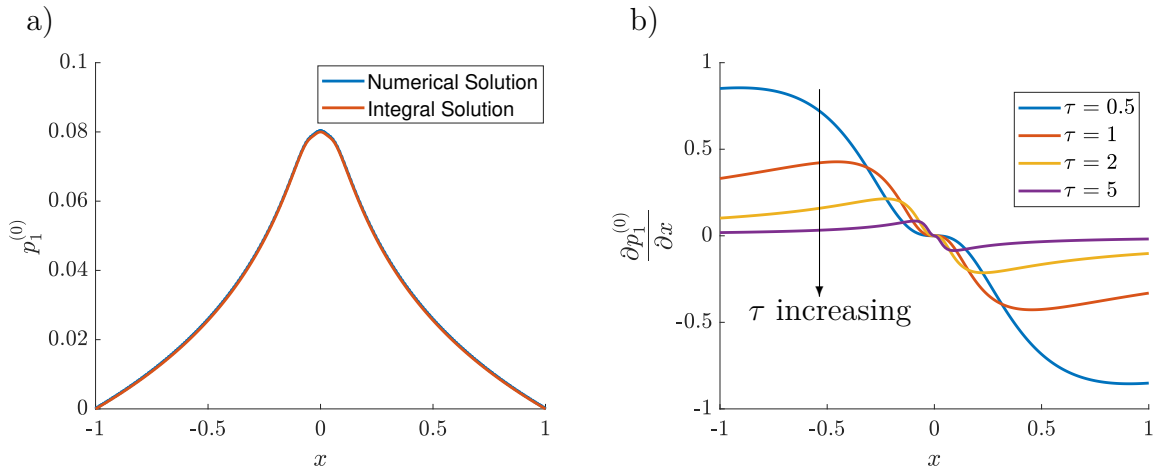


Figure 2.2: Second order correction to pressure a) at $\tau = 5$, as given by the output of the numerical solver detailed in section 2.5 (blue) and the asymptotic result given by equation (2.40) (red), and b) the evolution of the correction to the derivative of pressure with $\mu_2 = \mu_3 = 0.5, \theta_i = \dfrac{\pi}{2}, L_i = 1, h_i = 1, \dot{h}_1^{(0)} = -1$.

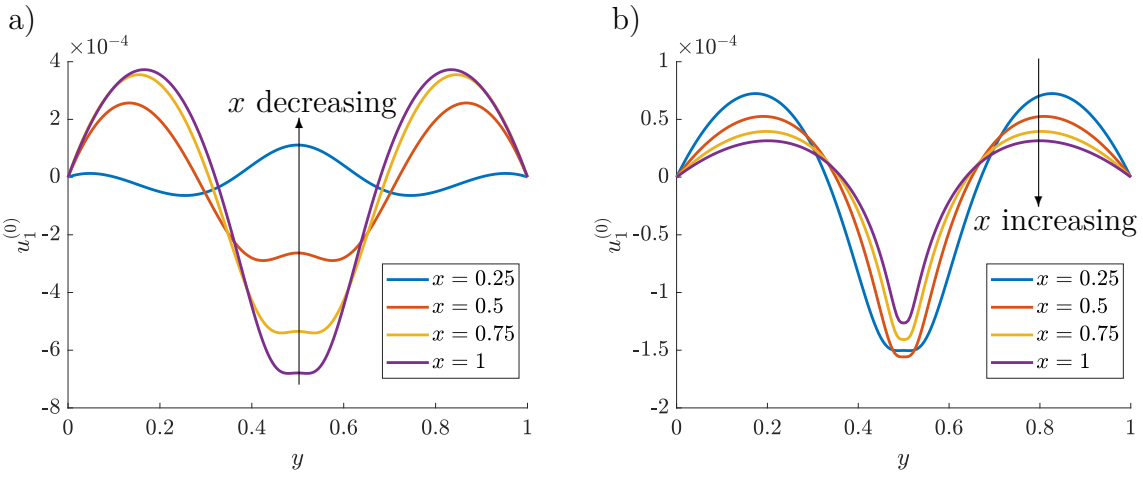


Figure 2.3: Plots of $u_1^{(0)}$ at a) $\tau = 1$, b) $\tau = 5$, at $x = 0.25, 0.5, 0.75, 1$ for $\mu_2 = \mu_3 = 0.5, \theta_i = \frac{\pi}{2}, h_i = L_i = 1$.

The correction to the horizontal velocity, $u_1^{(0)}$, is plotted in Figure 2.3. The velocity profile is very complicated. We note from equation (2.34) that in regions where $\theta \approx 0, \pm\frac{\pi}{2}$ the $\hat{\mu}_2$ term is negligible, whilst it is largest where $\theta \approx \frac{\pi}{4}$. Comparing Figures 2.1 and 2.3, we note that the regions of enhanced flow $\left(u_1^{(0)} > 0\right)$ appear to correlate with $\theta = \pm\frac{\pi}{4}$, whilst the regions of inhibited flow $\left(u_1^{(0)} < 0\right)$ appear to correlate with $\theta = 0, \frac{\pi}{2}$.

In this section we have derived the equations relevant on a short timescale, examined a regime for which $\mu_2 \ll 1$, and shown that in this regime, the numerical techniques we employ are able to recover higher order correction terms to good accuracy as compared

with the asymptotics, providing validation to the numerical approach. We have also seen how the direction of the fibres can cause changes to the pressure and velocity to exhibit non-Newtonian behaviours. We now return to the short timescale, without the restriction of a small $\mu_2$, and discuss the results obtained from the numerics.

## 2.7 Results

In this section we discuss the results obtained from the numerical solver detailed in section 2.5. The results we discuss are on the short timescale, however we relax the assumption that $\mu_2 \ll 1$.

### 2.7.1 Movement of the fibres

We note immediately from equation (2.28) that the rotation of the fibres is controlled wholly by the sign of $\dfrac{\partial u^{(0)}}{\partial y}$ (which is also the leading order vorticity). A counter-intuitive consequence of this is that fibres which are lying nearly aligned with the positive (or negative) $x$-axis may rotate away from the axis to realign with the negative (or positive) $x$-axis. In Figure 2.4 we give a plot of fibre directions initially and at $\tau = 10$, and a heatmap of $\dfrac{\partial u^{(0)}}{\partial y}$ for the initial choices of $\theta(x, y, 0) = \sin(x)\sin^2(\pi y), \mu_2 = 10, \mu_3 = 0, \dot{h} = -1$. We make this choice of $\theta(x, y, 0)$ to ensure both that the fibres are flat against the plates at both boundaries, and there is a wide range of initial fibre directions. Whilst $\dfrac{\partial u^{(0)}}{\partial y}$ itself undergoes some evolution as $u^{(0)}$ evolves to the long time solution, the sign remains consistent throughout. The fibres on the top-right quadrant of the domain are initially nearly flat, and rotate counter-clockwise towards the negative $x$-direction. Similarly, in the top-left quadrant of the domain, fibres that begin almost aligned with the positive $x$-direction rotate clockwise. Fibres within the lower half of the domain rotate towards the closest $x$-axis, as one might expect.

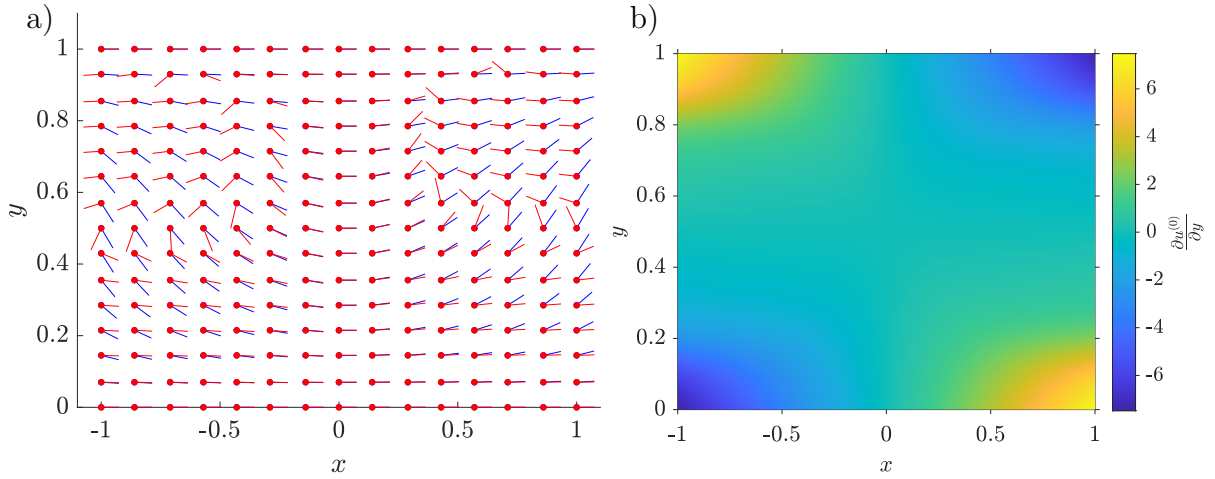


Figure 2.4: Depiction of the direction of the fibres a) in their initial configuration (blue) and at $\tau = 10$ (red), and b) the initial state of $\dfrac{\partial u^{(0)}}{\partial y}$, with the choices of $\theta(x, y, 0) = \sin(x)\sin^2(\pi y)$, $\mu_2 = 10, \mu_3 = 0, h_i = L_i = 1$. The sign of the derivative controls the direction of rotation of the fibres, which is counter-clockwise in the north-east and south-west quadrants.

### 2.7.2 Effect of varying the extensional and shear viscosities

First, we note that we must choose $\mu_2 \neq 0$ in this section. Otherwise, the results obtained for $p^{(0)}, u^{(0)}, v^{(0)}$ are given by the equations for the flow timescale as given in section 2.3.

Increasing $\mu_2$ has the effect of causing the pressure and velocity profiles to exhibit greater deviation from the expected quadratic shape. In Figures 2.5 and 2.6, we give the evolution of leading order pressure and velocity respectively for the choices of $\mu_3 = 0, \theta(x, y, 0) = xy, \dot{h} = -1, h_i = L_i = 1$, for various values of $\mu_2$. We recall from equation (2.17) that $p^{(0)}$ does not vary throughout the thickness of the film. Notice that an increase in $\mu_2$ causes the pressure profile to deviate further from a quadratic, with the initial pressure for the choice of $\mu_2 = 1$ being similar to the profile for a Newtonian fluid, whilst the choices of $\mu_2 = 10$, $\mu_2 = 50$ produces significant deviation from the pressure for a Newtonian fluid. Additionally, choices of large $\mu_2$ delay the convergence of the pressure to the result obtained from the $\dfrac{L_0}{U}$ timescale problem. We also see, in Figure 2.6, that an increase in $\mu_2$ has the effect of inhibiting the flow in some regions and enhancing it in others, similar to section 2.5, with this effect being stronger for an increased $\mu_2$. Fibres oriented vertically appear to have the effect of inhibiting the flow, leading to the

appearance of 'kinks' in Figure 2.6. This behaviour is clearest in Figure 2.6b, where we see that kinks exist at $x = 1, 0.8, 0.6, 0.4$ for $\mu_2 = 50$. The kinks are largest at around $x = 0.4$, and have not yet occurred at $x = 0.2$. Comparing these to Figure 2.7b we see that there are regions across the sheet at $x = 1, 0.8, 0.6, 0.4$ where fibres are pointing vertically. There is a larger region of fibres with this orientation around $x = 0.4$, and there are none at $x = 0.2$. We suggest that the rotation of the fibres is causing the kinks in the velocity to appear; specifically that fibres pointed vertically have a locally inhibiting effect on the longitudinal velocity.

We see significant asymmetry in the velocity profiles in Figure 2.6. The velocity appears to be greatest in regions where the fibres are nearest to parallel with the $x$-axis. We note that the effect is initially most pronounced near the edge of the fluid at $x = 1$, and later near $x = 0$. This is due to the rotation of the fibres - we see in Figure 2.7 that the fibres closest to $x = \pm 1$ rotate before fibres closer to $x = 0$.

The deviations from the pressure profiles for the cases of $\mu_2 = 10, 50$ appear to correlate well with the fibre directions. In Figure 2.7, we include snapshots of the evolution of the fibre director field for the choices $\mu_2 = 10, 50$. The regions where the fibres are pointed vertically (or near-vertically) also appear to correspond well with the perturbations to the pressure profiles given in Figure 2.5.

Turning to varying $\mu_3$, we see that increasing $\mu_3$ has the effect of reducing the non-Newtonian effects caused by $\mu_2$. In Figure 2.8, we give plots of the evolution of pressure for the conditions of $\theta(x, y, 0) = xy$, $\mu_2 = 50, h_i = L_i = 1$. We see that increasing $\mu_3$ is responsible for a significantly larger increase in pressure, compared to $\mu_2$, which one might expect from equation (2.23). This effect, which is clearly observable for $\mu_2 = 50$ in Figure 2.5d is still visible in Figure 2.8 for $\mu_3 = 1, 3$, but has been eliminated when $\mu_3 = 10$.

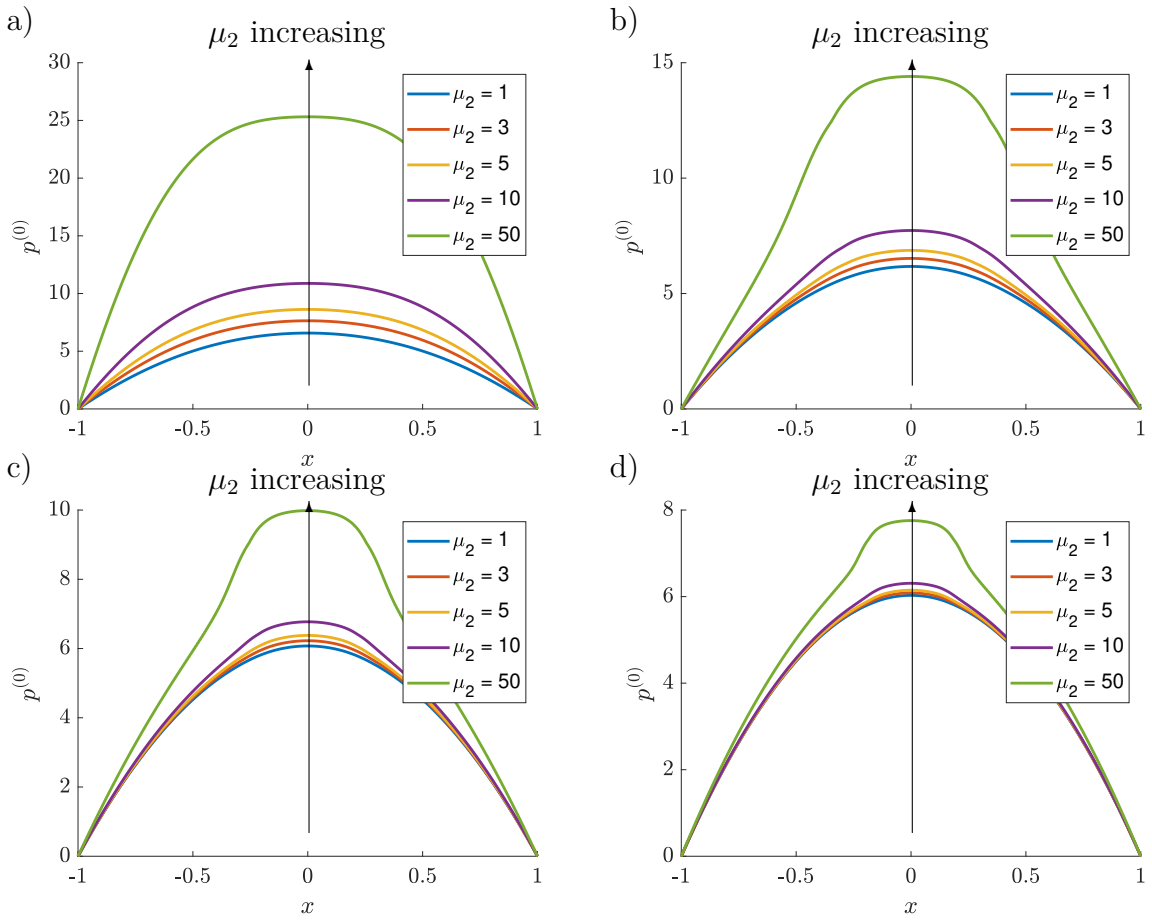


Figure 2.5: Short time evolution of $p^{(0)}$ across the fluid at a) $\tau = 0$, b) $\tau = 2.5$, c) $\tau = 5$, d) $\tau = 10$, for varied $\mu_2$, fixed $\mu_3 = 0$, and $\theta^{(0)}(x, y, 0) = xy, \dot{h}^{(0)} = -1, h_i = L_i = 1$.

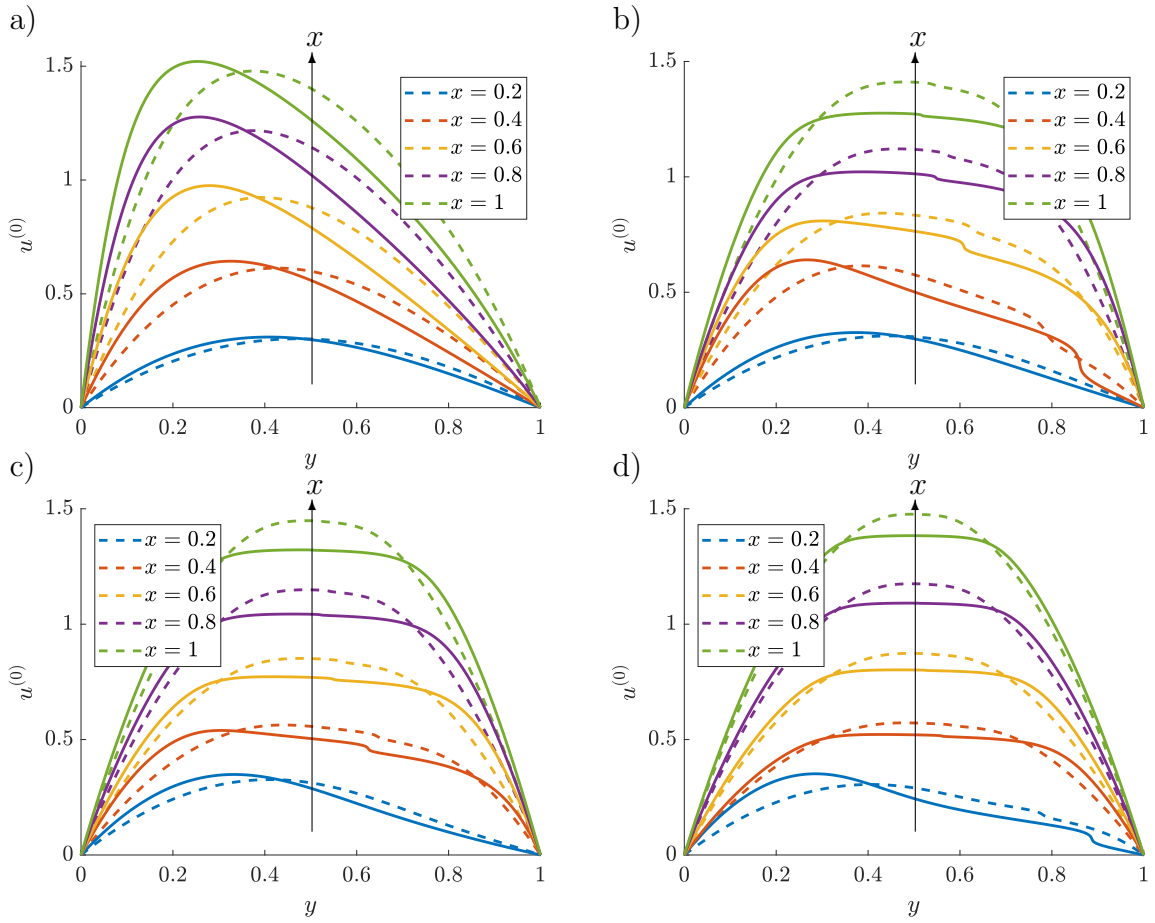


Figure 2.6: Evolution of the horizontal velocity $u^{(0)}$ for $\mu_2 = 10$ (dashed) and $\mu_2 = 50$ (solid) at a) $\tau = 0$, b) $\tau = 2.5$, c) $\tau = 5$, d) $\tau = 10$, for $x = 0.2, 0.4, 0.6, 0.8, 1$ with the prescribed conditions $\theta^{(0)}(x, y, 0) = xy, \dot{h}^{(0)} = -1, h_i = L_i = 1, \mu_3 = 0$.

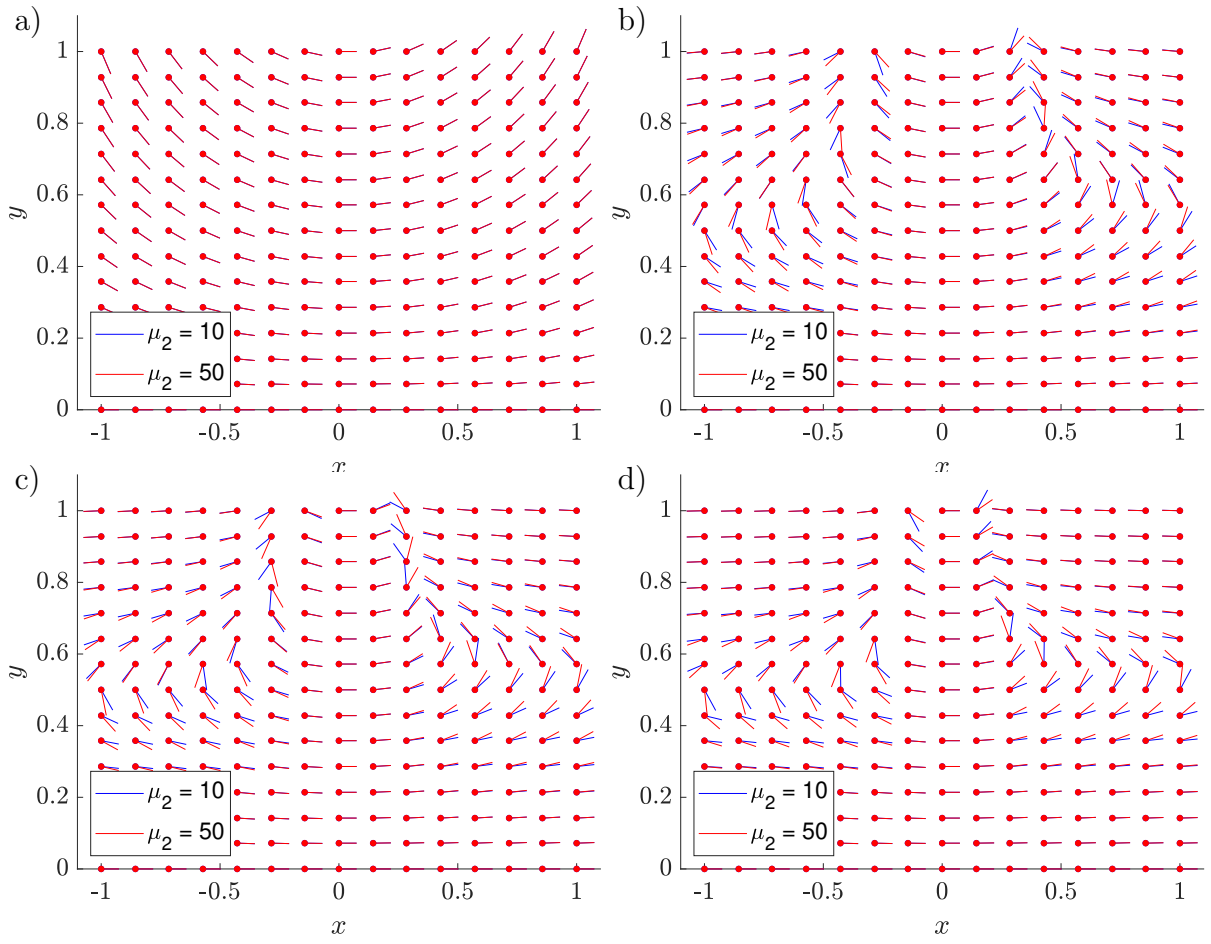


Figure 2.7: Evolution of the fibre director field at a) $\tau = 0$, b) $\tau = 2.5$, c) $\tau = 5$, d) $\tau = 10$, for the conditions $\theta^{(0)}(x, y, 0) = xy, \dot{h}^{(0)} = -1, h_i = L_i = 1, \mu_3 = 0, \mu_2 = 10, 50$.

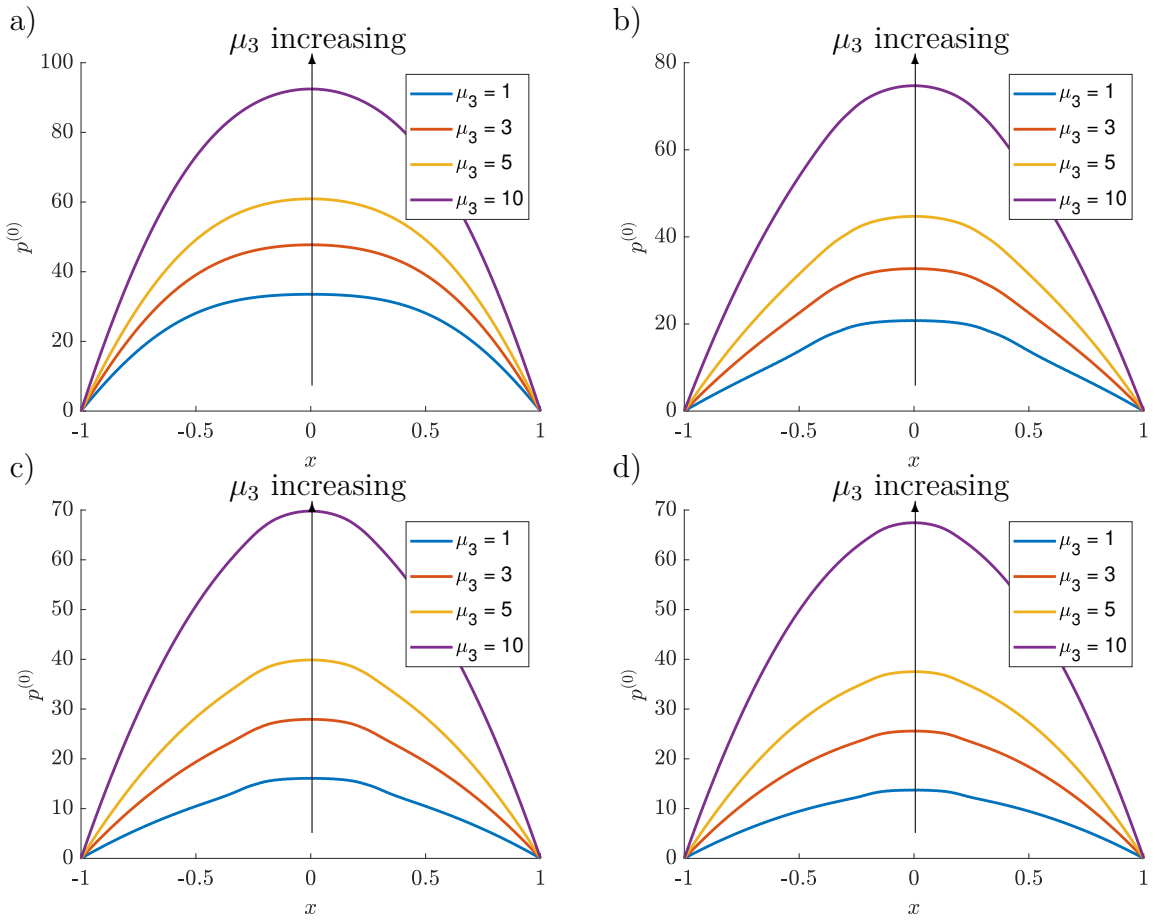


Figure 2.8: Short time evolution of $p^{(0)}$ at a) $\tau = 0$, b) $\tau = 2.5$, c) $\tau = 5$, d) $\tau = 10$, for the conditions $\theta^{(0)}(x, y, 0) = xy, \dot{h}^{(0)} = -1, h_i = L_i = 1, \mu_2 = 50$ and varied $\mu_3$.

## 2.8 Discussion

In this chapter, we have derived the leading-order equations describing the squeezing flow of a thin two-dimensional sheet of incompressible, transversely isotropic viscous fluid. We determined that on the timescale of the flow $\left(\frac{L_0}{U}\right)$ the majority of the fibres are aligned parallel to the $x$-axis and that the flow is essentially the same as for a Newtonian fluid. However, the initial realignment of the fibres takes place on a much shorter timescale $\left(\varepsilon\frac{L_0}{U}\right)$.

The most similar previous study to the work presented here is the work of Phan-Thien and Graham [75], who apply both analytical and numerical methods to the squeezing flow problem for a disc of Ericksen fluid. They derive an approximate solution, equivalent to our $\mathcal{O}\left(\frac{L_0}{U}\right)$ time-scale result, by making an ansatz based on the Newtonian solution. Our approach using systematic perturbation methods has allowed us to identify the short timescale of fibre alignment, which demonstrates the ansatz was reasonable as the fibres had already aligned on the flow timescale, and gives a greater physical picture of the behaviour of this flow. Phan-Thien and Graham observed from their numerical results that the fibres rapidly align parallel to the plates; however, their analytical approach was not able to provide insight into this phenomenon.

We investigated the early time behaviour of the model, validating our numerical techniques against a small time, small $\mu_2$ asymptotic analysis. We found that the presence of the fibres gave rise to more complicated flow patterns than the parabolic velocity profile expected for a Newtonian fluid. The flow appears to be enhanced locally in regions where the fibre angle is smallest, and diminished in regions where the fibre direction is less aligned to the plates, as illustrated in Figure 2.3. Additionally, the pressure profiles exhibit significant deviation from a quadratic profile in regions where the fibres are nearly orthogonal to the plates. If sufficiently accurate measurements of the velocity and pressure could be obtained experimentally, it might be possible to determine $\mu_2$ from the early-time flow, whilst determining $\mu_3$ from the longer-time behaviours. However, whilst the short timescale behaviours are interesting from a theoretical standpoint, it probably has limited

practical significance. There may be viscoelastic effects to contend with, arising from the cross-linking or entanglement of fibres within the gel, which we have neglected, before the practical difficulties of obtaining accurate experimental measurements.

There are additional assumptions in this work that could be relaxed. Firstly, an unrealistic two-dimensional geometry has been assumed. If squeezing flow experiments are to be used to determine some of the parameter values for transversely isotropic fluids then the model must be extended to three dimensions. This extension would require two angles to define the direction of the fibres, and would represent a significant increase in complexity. In addition, we assume perfect fibre alignment. This work could be extended to take account of the degree of fibre alignment, and entanglement, by introducing an order parameter and entanglement variable as considered by Lee & Ockendon [56]. Another issue is the neglect of yield stress, which arises in concentrated isotropic suspensions such as polymer melts [87], which may be significant, particularly if the fibres are cross-linked. However, we note that including yield stress may not change the results for the force on the plates for sufficiently thin films [87].

# CHAPTER 3

# THE EXTENSIONAL FLOW OF A TRANSVERSELY ISOTROPIC SHEET

In this chapter we consider the extensional flow of a thin sheet of an incompressible, transversely isotropic, viscous fluid. This chapter uses a combination of asymptotic analysis, similar to those introduced in the previous chapter, and numerical simulations to extend the work of Green and Friedman [41] to include cases where all of the anisotropic terms in the fluid stress are non-negligible, and the fibre alignment within the sheet may vary with depth. One issue of particular interest is to verify their conjecture that, unlike for a Newtonian fluid, the centre-line of a transversely isotropic sheet need not always be straight.

The biological motivation for studying this problem in Ref. [41] was to provide a description of the mechanical behaviours of collagen gel in vitro in the context of tissue engineering. Collagen gel is a commonly used media in which cells are seeded during the growth of tissue in vitro, and it has been suggested by experiment that the alignment of the fibres and distribution of stresses may influence cell behaviour. For example, in the context of engineering neural tissue, oriented collagen hydrogels are used to provide support and guidance to regenerating neurons through areas of damage [5]. The alignment of collagen fibres has been shown to direct the growth of neurons derived from human stem cells [68]. One method of creating an anisotropic gel with the desired stability that is relevant to the model considered in this chapter involves setting cell-seeded gels within

rectangular moulds and allowing the cells to integrate with fixed tethering points at each end. The build-up of tension within the gel causes the fibres to align longitudinally within the gel. The orientation of the fibres then provide contact guidance for the cells, the active behaviour of these cells then cause them to self-align with the fibres [69]. Understanding how the anisotropy induced by the fibrous microstructure affects the mechanical properties of the gel, and how the fibres reorient under tension, before considering the effects arising from the inclusion of cells is therefore a good first step. Indeed, collagen gel has since been modelled as a transversely isotropic fluid in a multiphase model of the extracellular matrix [28].

This chapter is organised as follows. In section 3.1 we briefly recap the governing equations and thin film approach employed by Green and Friedman in order to keep this thesis self-contained. The Green and Friedman model is then manipulated to become more amenable to our numerical strategies. In section 3.2 we introduce Arbitrary Lagrangian-Eulerian (ALE) techniques and present the model in ALE form. We then solve the model and present a validation of the numerical techniques by comparison with the analytical results for short time, and further present new results primarily for a passive transversely isotropic fluid in section 3.3. We conclude with a discussion and suggestions for future work in section 3.4.

## 3.1 Governing equations

We consider the extensional flow of a thin sheet of an incompressible, transversely isotropic, viscous fluid. As shown in Figure 1.4, we use the 2D Cartesian coordinates $(x^*, y^*)$, with $t^*$ denoting time. The upper and lower boundaries of the fluid are denoted by $y^* = H^{\pm^*} = H^* \pm \frac{h^*}{2}$, where $H^*(x^*, t^*)$ is the position of the centre-line and $h^*(x^*, t^*)$ is the thickness of the fluid sheet. Additionally, the left- and right- hand side boundaries are located at $x^* = 0, L^*(t^*)$. The right-hand end of the sheet, at $x^* = L^*$, is pulled in the $x^*$ direction; we prescribed either the speed of pulling, $\dot{L}^*$, or the tension $T^*$ applied to the

sheet.

We let $\boldsymbol{u}^* = (u^*, v^*)$ be the fluid velocities in the $x^*, y^*$ directions respectively, and denote the stress tensor by $\boldsymbol{\sigma}^*$, which is given in (1.9). The equations of conservation of fluid mass and momentum are thus

$$\nabla^* \cdot \boldsymbol{u}^* = 0, \tag{3.1}$$

$$\nabla^* \cdot \boldsymbol{\sigma}^* = 0. \tag{3.2}$$

We give equations (3.1)-(3.2) in dimensionless form in Appendix B.1. Since our model is two dimensional, We choose $\boldsymbol{a} = (\cos\theta, \sin\theta)$, where $\theta(x^*, y^*, t^*)$ is the angle the fibres make with the $x$-axis and from (1.15) we obtain an equation for the evolution of the angle of the fibres:

$$\frac{\partial\theta}{\partial t^*} + u^*\frac{\partial\theta}{\partial x^*} + v^*\frac{\partial\theta}{\partial y^*} = -\sin\theta\cos\theta\frac{\partial u^*}{\partial x^*} - \sin^2\theta\frac{\partial u^*}{\partial y^*} + \cos^2\theta\frac{\partial v^*}{\partial x^*} + \sin\theta\cos\theta\frac{\partial v^*}{\partial y^*}. \tag{3.3}$$

In order to close our model, we must impose suitable boundary and initial conditions. At the ends of the sheet, we set

$$u^*(0, y^*, t^*) = 0, \qquad u^*(L^*, y^*, t^*) = \dot{L}^*, \tag{3.4}$$

$$H^*(0, t^*) = 0, \qquad H^*(L^*, t^*) = 0. \tag{3.5}$$

On the upper and lower free surfaces, we apply a no-stress boundary condition

$$\boldsymbol{\sigma^*} \cdot \hat{\boldsymbol{n}} = 0; \text{ on } y = H^* \pm \frac{1}{2}h^*, \tag{3.6}$$

together with the usual kinematic condition

$$v^* = \frac{\partial H^*}{\partial t^*} \pm \frac{1}{2}\frac{\partial h^*}{\partial t^*} + u^*\left(\frac{\partial H^*}{\partial x^*} \pm \frac{1}{2}\frac{\partial h^*}{\partial x^*}\right); \text{ on } y = H^* \pm \frac{1}{2}h^*. \tag{3.7}$$

Initial conditions must also be prescribed, for $\theta, h$ and $L$, which we discuss later.

### 3.1.1 The Green and Friedman model

We now introduce the assumption that the sheet is thin, which allows considerable simplification of the governing equations. Full details of the derivation can be found in [41], but for the sake of completeness we recapitulate the main points here. We let $L_0$ and $h_0$ be the initial length and typical initial thickness of the fluid sheet, respectively, and let $U$ be a typical value for the velocity of the fluid at the pulled boundary. We then introduce the parameter $\varepsilon = h_0/L_0 \ll 1$, which is the initial inverse aspect ratio of the sheet. We are interested in the behaviour of the sheet as it undergoes significant changes in length, and so consider the timescale $t \sim L_0/U$. Following [41, 49] we nondimensionalise as follows

$$(x^*, y^*) = (xL_0, \varepsilon y L_0)\,, \quad (u^*, v^*) = (uU, \varepsilon v U)\,, \quad p^* = \frac{\mu^* U}{L_0} p, \quad t^* = \frac{L_0}{U} t,$$
$$(H^*, L^*, h^*) = (\varepsilon L_0 H, L_0 L, \varepsilon L_0 h)\,.$$

These scalings introduce the dimensionless quantities

$$\mu_1 = \frac{\mu_1^* L}{\mu^* U}, \quad \mu_2 = \frac{\mu_2^*}{\mu^*}, \quad \mu_3 = \frac{\mu_3^*}{\mu^*}.$$

At this point, we exploit the thin geometry of the sheet by expanding all of the dependent variables as power series in terms of the inverse aspect ratio $\varepsilon$, that is

$$u = u^{(0)} + \varepsilon u^{(1)} + ...$$

with similar expressions for the other dependent variables. Notice here that unlike Howell, we encounter terms involving odd powers of $\varepsilon$. After some lengthy algebra, full details of which are given in [41], we obtain a system of one dimensional equations for the quantities $h^{(0)}, H^{(0)}, u^{(0)}, u^{(1)}, v^{(0)}, \theta^{(0)}$. As a consequence of the analysis, it is found that the leading order longitudinal velocity satisfies $u^{(0)} = u^{(0)}(x,t)$ only [41] (i.e. the flow is extensional).

Conservation of mass yields:

$$\frac{\partial h^{(0)}}{\partial t}+\frac{\partial}{\partial x}\left(h^{(0)}u^{(0)}\right)=0, \tag{3.8}$$

taking a depth-averaged force balance over the sheet leads to the following equation for $u$

$$\frac{\partial}{\partial x}\int_{H^{(0)-}}^{H^{(0)+}} 4\left(1+\mu_3\right)\frac{\partial u^{(0)}}{\partial x}+\mu_1\cos 2\theta^{(0)}+\mu_2\left(\cos^2 2\theta^{(0)}\frac{\partial u^{(0)}}{\partial x}+\frac{1}{4}\sin 4\theta^{(0)}\frac{\partial u^{(1)}}{\partial y}\right)\mathrm{d}y=0. \tag{3.9}$$

Consideration of the momentum equations and associated no-stress boundary conditions on the upper and lower boundaries of the fluid at higher order gives an equation governing the centre-line of the fluid, $H^{(0)}$

$$\frac{\partial}{\partial x}\int_{H^{(0)-}}^{H^{(0)+}}\frac{\partial}{\partial x}\int_{H^{(0)-}}^{y} 4\left(1+\mu_3\right)\frac{\partial u^{(0)}}{\partial x}+\mu_1\cos 2\theta^{(0)} + \mu_2\left(\cos^2 2\theta^{(0)}\frac{\partial u^{(0)}}{\partial x}+\frac{1}{4}\sin 4\theta^{(0)}\frac{\partial u^{(1)}}{\partial y}\right)\mathrm{d}s\mathrm{d}y=0. \tag{3.10}$$

We note first that $s$ is a dummy variable, we are integrating over the second argument of the functions in the integrand twice, so that the quantities in the integrand of equation (3.10) are $\theta^{(0)}\left(x,s,t\right), u^{(1)}\left(x,s,t\right)$ (to emphasise this, the dummy variable is not used in [41]). Additionally, we note that equation (3.10) is a particularly unusual form of an integro-differential equation, wherein one of the variables of integration appears in the limit of one of the integrals. The equation for the evolution of the fibre angle yields

$$\frac{\partial\theta^{(0)}}{\partial t}+u^{(0)}\frac{\partial\theta^{(0)}}{\partial x}+v^{(0)}\frac{\partial\theta^{(0)}}{\partial y}=-2\sin\theta^{(0)}\cos\theta^{(0)}\frac{\partial u^{(0)}}{\partial x}-\sin^2\theta^{(0)}\frac{\partial u^{(1)}}{\partial y}, \tag{3.11}$$

as an evolution equation governing the behaviour of the fibre director field. The leading order transverse velocity is

$$v^{(0)} = \frac{\partial H^{(0)}}{\partial t} + \frac{\partial}{\partial x}\left(H^{(0)}u^{(0)}\right) - y\frac{\partial u^{(0)}}{\partial x}, \tag{3.12}$$

with

$$\frac{\partial u^{(1)}}{\partial y} = -\mu_1 \frac{2\sin 2\theta^{(0)}}{4 + 4\mu_3 + \mu_2 \sin^2 2\theta^{(0)}} - \mu_2 \frac{\sin 4\theta^{(0)}}{4 + 4\mu_3 + \mu_2 \sin^2 2\theta^{(0)}} \frac{\partial u^{(0)}}{\partial x}, \tag{3.13}$$

being the next-order correction term for $u$. In this form, one can observe that in the case of $\mu_1 = \mu_2 = \mu_3 = 0$, we return to the Trouton model for a Newtonian fluid. In the case of $\mu_1 = \mu_2 = 0$, the fluid behaves very similarly to a Newtonian fluid. In these cases, the model can be solved by means of a Lagrangian transformation, as detailed by Refs. [41, 49].

At this point, we begin to extend the work of Green and Friedman. We note that $\dfrac{\partial u^{(1)}}{\partial y}$ can be readily eliminated from the Green and Friedman model by direct substitution. Dropping the superscript notation on the leading order terms, the equations (3.9) - (3.11) become:

$$\frac{\partial}{\partial x}\int_{H-\frac{h}{2}}^{H+\frac{h}{2}} \frac{\mu_1 \cos 2\theta + (4 + 4\mu_3 + \mu_2)\frac{\partial u}{\partial x}}{4 + 4\mu_3 + \mu_2 \sin^2 2\theta} \mathrm{d}y = 0, \tag{3.14}$$

$$\frac{\partial}{\partial x}\int_{H-\frac{h}{2}}^{H+\frac{h}{2}} \frac{\partial}{\partial x}\int_{H-\frac{h}{2}}^{y} \frac{\mu_1 \cos 2\theta + (4 + 4\mu_3 + \mu_2)\frac{\partial u}{\partial x}}{4 + 4\mu_3 + \mu_2 \sin^2 2\theta} \mathrm{d}s\mathrm{d}y = 0, \tag{3.15}$$

$$\frac{\partial \theta}{\partial t} + u\frac{\partial \theta}{\partial x} + v\frac{\partial \theta}{\partial y} = \frac{\sin 2\theta\left(2\mu_1 \sin^2\theta - (4 + 4\mu_3 + 2\mu_2 \sin^2\theta)\frac{\partial u}{\partial x}\right)}{4 + 4\mu_3 + \mu_2 \sin^2 2\theta}. \tag{3.16}$$

The boundary conditions for the longitudinal velocity are

$$u(0,t) = 0, \quad u(L,t) = \dot{L}. \tag{3.17}$$

We assume that the sheet is being extended in the $x$ direction and assume that the end points of the centre-line remain upon $y = 0$, thus

$$H(0,t) = H(L,t) = 0. \tag{3.18}$$

The kinematic boundary condition yields

$$v = \frac{\partial H}{\partial t} \pm \frac{1}{2}\frac{\partial h}{\partial t} + u\left(\frac{\partial H}{\partial x} \pm \frac{1}{2}\frac{\partial h}{\partial x}\right); \text{ on } y = H^{\pm}. \tag{3.19}$$

We will need to prescribe initial conditions for the thickness $h$ and the fibre direction $\theta$ in the sheet. Henceforth, unless otherwise stated, we prescribe $L(t) = 1 + t$.

As in the Newtonian problem, we do not need to prescribe an initial condition for $H$ as we are unable to satisfy an arbitrary initial condition for $H$ [41, 49]. We anticipate that in order to study the behaviour of sheets that initially obey (3.15), we must consider a shorter timescale than $\frac{L_0}{U}$. To this end, in chapter 4 we follow a similar path to work by Howell [49], and consider the behaviour of a sheet on a timescale of $\varepsilon^2\frac{L_0}{U}$.

## 3.2 ALE formulation of the model

Although the thin film system, (3.8), (3.14)-(3.16) is a significant simplification compared to the full two-dimensional problem, it is too complex to allow significant analytical progress, and so must be solved numerically in general. In this section, we reformulate the mathematical model into an Arbitrary Lagrangian-Eulerian (ALE) formulation. ALE methods involve the construction of a reference domain with mappings to both the Lagrangian and Eulerian descriptions of the flow. Unlike numerical techniques based on either a purely Lagrangian description, where the nodes of the computational mesh follow an associated material particle throughout the motion, or upon a purely Eulerian description, where the computational mesh is fixed and the motion of the continuum is with respect to the grid, ALE methods allow freedom in moving the mesh in a way

that is not necessarily fixed to a material particle. This can provide accurate solutions when modelling greater distortions of a flow problem than can ordinarily be handled by numerical techniques upon a Lagrangian description, with more resolution than is often attainable by a purely Eulerian description [26].

Our approach largely follows Donea et al [26], but we outline the details here for completeness. We introduce Lagrangian, Eulerian, and reference domain variables which we denote by $\boldsymbol{X} = (X, Y)$, $\boldsymbol{x} = (x, y)$ and $\boldsymbol{x'} = (x', y')$, respectively. Converting between Eulerian and Lagrangian descriptions of flow fields is well established, and has been employed in Newtonian extensional flow problems several times in the past [41, 49, 107]. We define the map $\boldsymbol{\varphi}$ from the Lagrangian to the Eulerian descriptions such that

$$(\boldsymbol{x}, t) = (\boldsymbol{\varphi}(\boldsymbol{X}, t), t),$$

where the material velocity $\boldsymbol{v}$ is given by

$$\frac{\partial \boldsymbol{\varphi}}{\partial t} = \boldsymbol{v}(\boldsymbol{X}, t), \tag{3.20}$$

so that the familiar material time derivative of an arbitrary scalar field $f$ (e.g pressure) is

$$\frac{Df(\boldsymbol{X}, t)}{Dt} = \frac{\partial f(\boldsymbol{x}, t)}{\partial t} + \frac{\partial f(\boldsymbol{x}, t)}{\partial \boldsymbol{x}} \frac{\partial \boldsymbol{\varphi}}{\partial t} = \frac{\partial f}{\partial t} + (\boldsymbol{v} \cdot \nabla_{\boldsymbol{x}}) f. \tag{3.21}$$

Now, it remains only to define the map from the reference domain to the Eulerian domain, which we denote by $\boldsymbol{\Phi}$. This satisfies

$$(\boldsymbol{x}, t) = (\boldsymbol{\Phi}(\boldsymbol{x'}, t), t).$$

The mesh velocity, $\boldsymbol{u}_{\text{mesh}}$, is given by

$$\boldsymbol{u}_{\text{mesh}}(\boldsymbol{x'}, t) = \frac{\partial \boldsymbol{\Phi}}{\partial t}.$$

We obtain the relations between physical quantities, such as pressure, in the reference and Eulerian descriptions in the same way we do between Lagrangian and Eulerian descriptions. In particular, the time derivative of an arbitrary scalar field $f$ is

$$\frac{\partial f\left(\boldsymbol{x}', t\right)}{\partial t} = \frac{\partial f\left(\boldsymbol{x}, t\right)}{\partial t} + \left(\boldsymbol{u}_{\text{mesh}} \cdot \nabla_{\boldsymbol{x}}\right) f(\boldsymbol{x}, t), \tag{3.22}$$

so that the transformation from the reference to the Eulerian description behaves very much like the familiar transformation between Lagrangian and Eulerian frames. For convenience, we rewrite (3.22) as

$$\frac{\partial f\left(\boldsymbol{x}', t\right)}{\partial t} - \left(\boldsymbol{u}_{\text{mesh}} \cdot \frac{\partial \boldsymbol{x}'}{\partial \boldsymbol{x}} \nabla_{\boldsymbol{x}'}\right) f(\boldsymbol{x}', t) = \frac{\partial f\left(\boldsymbol{x}, t\right)}{\partial t}. \tag{3.23}$$

As a final note, if $\boldsymbol{\Phi} = \boldsymbol{\varphi}$, then the reference description is the same as the Lagrangian description and thus $\boldsymbol{u}_{\text{mesh}} = \boldsymbol{v}$. If $\boldsymbol{\Phi} = \boldsymbol{I}$, then the reference description is the same as the Eulerian description, and $\boldsymbol{u}_{\text{mesh}} = \boldsymbol{0}$. For further explanation of ALE techniques, we direct the reader to Ref. [26].

### 3.2.1 Employing ALE

We define the reference domain, $D_{\text{ref}}$, to be

$$(x', y') \in D_{\text{ref}} = [0, 1] \times \left[-\frac{1}{2}, \frac{1}{2}\right], \tag{3.24}$$

and define the mapping from the reference variables to the Eulerian variables $\boldsymbol{\Phi} : D_{\text{ref}} \to [0, L] \times [H^-, H^+]$ such that

$$(x, y) = \boldsymbol{\Phi}\left(x', y'\right) = \left(Lx', H\left(\frac{Lx'}{L(0)}, t\right) + h\left(\frac{Lx'}{L(0)}, t\right) y'\right). \tag{3.25}$$

This choice of map maintains equidistant spacing in the mesh in both horizontal and vertical directions. Therefore, our discretisation of $D_{ref}$ can be a simple equidistant grid. As already discussed, the mesh velocity is readily obtained by differentiating the mapping $\mathbf{\Phi}$ with respect to time. Written in terms of Eulerian variables, we have

$$\frac{\partial \mathbf{\Phi}}{\partial t} = \mathbf{u}_{\text{mesh}} = \left( \dot{L}\frac{x}{L}, \dot{L}\frac{x}{L}\left(\frac{\partial H}{\partial x}(x,t) + \frac{y - H(x,t)}{h(x,t)}\frac{\partial h}{\partial x}(x,t)\right) + \frac{\partial H}{\partial t}(x,t) \right. \\ \left. + \frac{y - H(x,t)}{h(x,t)}\frac{\partial h}{\partial t}(x,t)\right). \quad (3.26)$$

We now account for the introduction of the moving mesh by using (3.23) and (3.25). We first modify the equation for $\theta$, (3.16). This equation becomes

$$\frac{\partial \theta}{\partial t} + \left(\frac{u - u_{\text{mesh}}}{L}\right)\frac{\partial \theta}{\partial x'} + \left(\frac{v - v_{\text{mesh}}}{h}\right)\frac{\partial \theta}{\partial y'} = \frac{\sin 2\theta \left(2\mu_1 \sin^2\theta - \frac{1}{L}\left(1 + 2\mu_2 \sin^2\theta\right)\frac{\partial u}{\partial x'}\right)}{4 + 4\mu_3 + \mu_2 \sin^2 2\theta}. \quad (3.27)$$

This form of (3.27) allows us yet further simplification. As explicitly demonstrated in Appendix B.2, this equation corresponds to advection purely in a horizontal direction on the reference domain, which significantly eases implementation. We note that this also decouples $\theta$ from $H$, and since $v$ does not arise in any other equation, we need not prescribe an initial $H$ and can simply compute the transverse velocity on demand. To

summarise the model in the ALE form, we have

$$\frac{\partial h}{\partial t}+\left(\frac{u-u_{\text{mesh}}}{L}\right)\frac{\partial h}{\partial x'}+\frac{1}{L}\frac{\partial u}{\partial x'}=0, \tag{3.28}$$

$$\frac{\partial \theta}{\partial t}+\left(\frac{u-u_{\text{mesh}}}{L}\right)\frac{\partial \theta}{\partial x'}=\frac{\sin 2\theta\left(2\mu_1\sin^2\theta-\frac{1}{L}\left(4+4\mu_3+2\mu_2\sin^2\theta\right)\frac{\partial u}{\partial x'}\right)}{4+4\mu_3+\mu_2\sin^2 2\theta}, \tag{3.29}$$

$$\frac{\partial}{\partial x'}\int_{-\frac{1}{2}}^{\frac{1}{2}}\frac{\mu_1\cos 2\theta+\frac{1}{L}\left(4+4\mu_3+\mu_2\right)\frac{\partial u}{\partial x'}}{4+4\mu_3+\mu_2\sin^2 2\theta}h\mathrm{d}y'=0, \tag{3.30}$$

$$\begin{aligned}\frac{\partial^2}{\partial x'^2}\int_{-\frac{1}{2}}^{\frac{1}{2}}\int_{-\frac{1}{2}}^{y'}&\frac{\mu_1\cos 2\theta+\frac{1}{L}\left(4+4\mu_3+\mu_2\right)\frac{\partial u}{\partial x'}}{4+4\mu_3+\mu_2\sin^2 2\theta}h^2\mathrm{d}s'\mathrm{d}y'\\ &=\left(\frac{\partial^2 H}{\partial x'^2}+\frac{1}{2}\frac{\partial^2 h}{\partial x'^2}\right)\int_{-\frac{1}{2}}^{\frac{1}{2}}\frac{\mu_1\cos 2\theta+\frac{1}{L}\left(4+4\mu_3+\mu_2\right)\frac{\partial u}{\partial x'}}{4+4\mu_3+\mu_2\sin^2 2\theta}h\mathrm{d}y',\end{aligned} \tag{3.31}$$

for $(x',y')\in D_{\text{ref}}$, and equation (3.31) arose via application of the Leibniz rule to (3.15). The associated boundary and initial conditions now become

$$u(0,t)=0, \qquad u(1,t)=1, \tag{3.32}$$

$$H(0,t)=0, \qquad H(1,t)=0, \tag{3.33}$$

$$h(x',0)=h_i\left(x'\right), \qquad \theta\left(x',y',0\right)=\theta_i\left(x',y'\right). \tag{3.34}$$

We exclude the equation for the transverse velocity $v$, since this quantity is readily calculated from (3.12) at any $(x',y',t)$ once the model (3.28)-(3.31) is solved.

In order to solve this model we use the following algorithm. Given initial conditions, equation (3.30) is solved to obtain $u\left(x',0\right)$. This can be achieved by using the trapezoidal rule and a centred finite difference approximation. We note that this particular equation can be approached in either ALE or Eulerian variables, since applying the trapezoidal rule to solve the integral (3.30) effectively decouples $H$ from the system (see appendix). Once solved, equations (3.28) and (3.29) can be used to update $h,\theta$ to the next time-step, at which point the process is repeated until the required end time is reached. The quantities $v,H$ can then be computed at any time using (3.12) and (3.15) (or (3.31)) respectively, as

well as any other quantities of interest. In our implementation, we solved equations (3.28) - (3.31) in the ALE form given above. We use a centred finite difference approximation upon equations (3.30), (3.31) and an upwind scheme upon equations (3.28), (3.29). Upwind finite difference schemes are commonly utilized and were developed to solve systems of hyperbolic partial differential equations [19]. Upwind schemes are designed to capture the flow of information in a system, which is done by using finite differences that are biased in the same direction as the characteristic speeds of the system. Suppose a quantity is travelling with positive velocity, at some earlier time this quantity would have been 'downstream' of where it is now. Hence, only points in the stencil in that direction have relevant information about what has happened to that quantity in the previous time-step. Information from points in the stencil 'upstream' of the current position is irrelevant in determining how the quantity reached its current position. Upwind schemes have the advantages that they are stable and accurate when used upon PDEs containing advection terms where using centred finite difference schemes is inappropriate. An analysis of the errors and behaviours of using an upwind scheme on an advection problem is described in Ref. [66].

Since the ALE framework acts like a simple substitution on the integral equations, it is equally possible to discretise and solve equations (3.14) and (3.15) in their Eulerian forms, and indeed the discretisation is similar. We include the discretisations of equations (3.30), (3.31) in Appendix B.3.

In this section we have reformulated the Green and Friedman model equations in an Arbitrary Lagrangian-Eulerian setting and proposed a numerical strategy to solve these equations. We now present validation of the numerical approach and go on to present results.

## 3.3 Results

### 3.3.1 Validation of numerical method

In order to validate our approach, we consider the early-time behaviour of the sheet, for which an analytical expression is available [41]. Introducing the short timescale $t' = \delta^{-1}t$, where $\varepsilon \ll \delta \ll 1$, assuming constant initial film thickness, $h_i$, and alignment angle, $\theta_i$, and performing a Taylor expansion on the variables so that

$$h = h_i + \hat{h}t'\delta + \mathcal{O}\left(\delta^2\right)...,$$
$$\theta = \theta_i + \hat{\theta}t'\delta + \mathcal{O}\left(\delta^2\right)...,$$

where $\hat{h}, \hat{\theta}$ are the changes in thickness and fibre direction respectively, it is possible to derive an analytical expression for the evolution of the fibre angle in the sheet for constant initial conditions for thickness and fibre direction, see Ref. [41]. The result is:

$$\hat{\theta} = -2\sin 2\theta_i + \frac{2\sin^2\theta_i}{4 + 4\mu_3 + \mu_2\sin^2 2\theta_i}\left[\mu_1 \sin 2\theta_i + \frac{\mu_2}{2}\sin 4\theta_i\right], \tag{3.35}$$

where $t'\hat{\theta}$ is the total change in the fibre angle over the short time $t'$, and $\theta_i$ is the constant initial condition. In [41], the authors note that a consequence of this analysis is that so long as $\mu_1, \mu_2$ and the tension in the sheet are all sufficiently small, the fibres will align with the direction of pulling as long as $\theta_i \neq \frac{\pi}{2}, \frac{3\pi}{2}$. In Figure 3.1 we plot the results from using our code to solve the system as detailed in Section 3.2 up to $t = 0.05$ against the analytical result. The maximum absolute error on Figure 3.1a is 0.002, located at $\theta_i = 0.5027, 2.6389$ for $\mu_1 = 10$. The relative error increases significantly where $\hat{\theta} \approx 0$, being undefined when $\hat{\theta} = 0$. The maximum absolute error in Figure 3.1b is 0.0033, and occurs at $\theta_i = 1.4556, 1.6860$, for $\mu_2 = 10$.

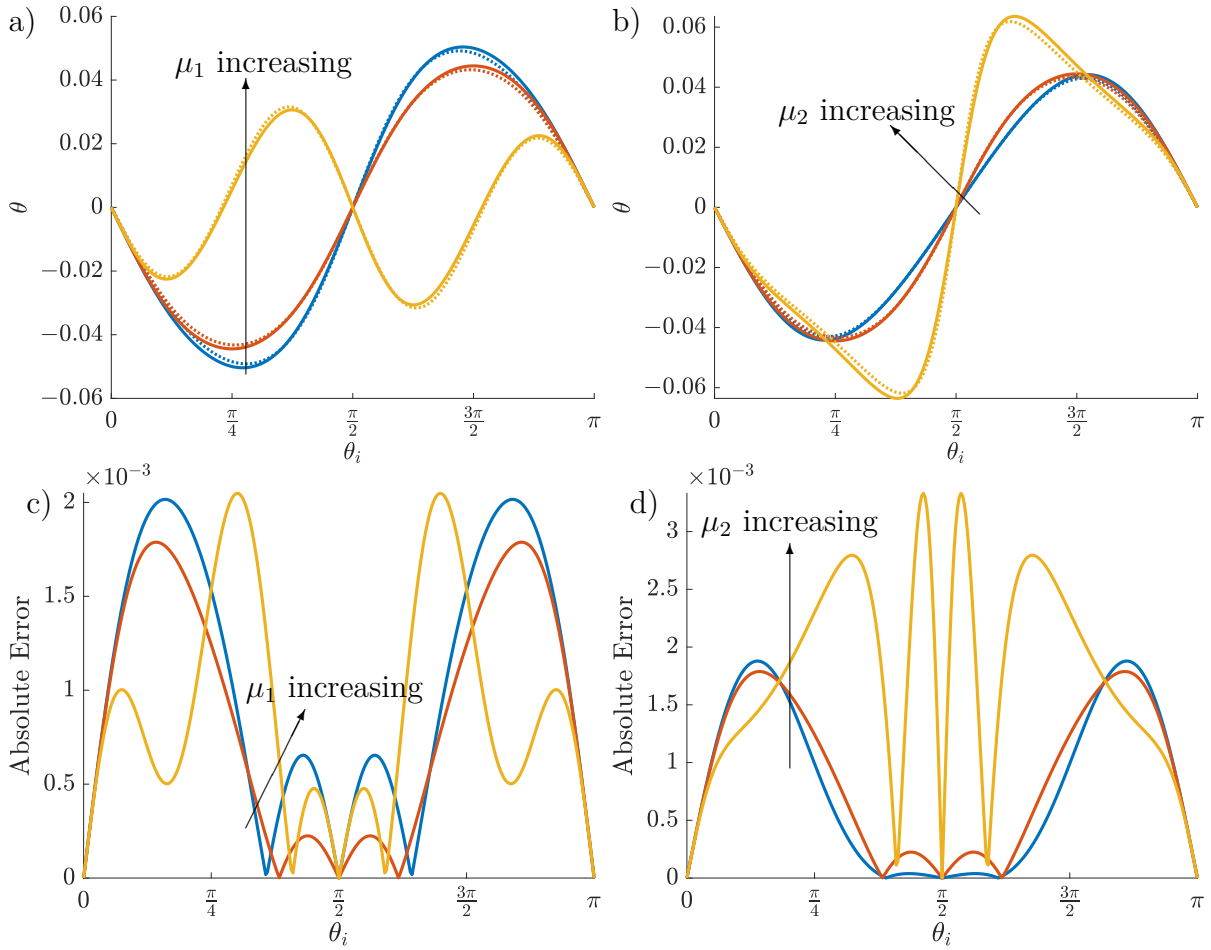


Figure 3.1: Comparison of the analytical result for $\hat{\theta}$ at $t' = 0.05$, with $\theta_i \in [0, \pi]$ for a) $\mu_1 = 0, 1, 10$ (blue, red, yellow respectively) with $\mu_2 = \mu_3 = 1$ fixed and b) $\mu_2 = 0, 1, 10$ (blue, red, yellow respectively) with $\mu_1 = \mu_3 = 1$ fixed. The analytical results from (3.35) are solid lines, the dotted lines are the numerical results obtained by solving (3.28)-(3.31). The absolute errors between the numerical and analytical results are given for c) varied $\mu_1$ and d) varied $\mu_2$.

### 3.3.2 Solutions for initially uniform transversely isotropic sheets with $\mu_1 = 0$.

We now extend the work of Green & Friedman by studying the effect of the viscosities $\mu_2, \mu_3$, and the fibres, upon the fluid as the sheet is stretched. Green & Friedman considered the cases where $\mu_1 = \mu_2 = 0$. Throughout this section, we study sheets without tension in the fibre direction, i.e. $\mu_1 = 0$, but with $\mu_2 \neq 0$ . We first turn our attention to transversely isotropic sheets that have an initially constant thickness. For clarity of exposition, we

introduce the quantity

$$G_2(x', y', t) = \int_{-\frac{1}{2}}^{y'} \frac{(4 + 4\mu_3 + \mu_2)}{4 + 4\mu_3 + \mu_2 \sin^2 2\theta} \mathrm{d}y', \tag{3.36}$$

the definition of $G_2$ is readily obtained in the spatial form by performing the inverse of the transformation $\mathbf{\Phi}$. In the case where the sheet has no tension in the fibre direction the equation for $u$ in ALE variables, (3.30), becomes

$$\frac{\partial}{\partial x'} \left( h \frac{\partial u}{\partial x'} G_2 \left( x', \frac{1}{2}, t \right) \right) = 0. \tag{3.37}$$

This is of the same form as the longitudinal momentum equation in the Trouton model, with $G_2$ playing the role of a spatially-varying viscosity (setting $\mu_1 = \mu_2 = \mu_3 = 0$ gives $G_2 = 4$, the Trouton ratio for a Newtonian thin sheet [49]). We interpret $G_2$ as a heterogeneous, time-dependent, 'effective viscosity'. As we shall show, we see the effect of $G_2$ is to induce 'necking' in the sheet (the sheet undergoes thinning at a greater rate in some areas of the sheet than others, generating a 'neck'). This behaviour has been observed in Newtonian fluids which possess an inhomogenous viscosity [73].

We also note that if the fibre angle is independent of $x'$, or if $\mu_1 = \mu_2 = 0$ [41], then $G_2$ as it appears in equation (3.37) does not possess $x'$ dependence. Hence a fluid that does not possess tension in the fibre direction when at rest, and has a uniform fibre direction will behave like a Newtonian fluid, with a modified viscosity. In this case, the centre-line of the fluid is always a straight line, and the model can be solved by transforming to Lagrangian variables, as detailed in [41, 49].

A first integral of (3.37) yields,

$$h \frac{\partial u}{\partial x'} G_2 = T(t), \tag{3.38}$$

where $T$ is the tension applied to the sheet. Directly from (3.38) we see that $G_2$ may induce non-linear behaviours in $u$. For a Newtonian fluid or a transversely isotropic fluid

where only $\mu_3 \neq 0$, choosing an initial condition of constant thickness across the sheet yields that $u$ must be linear in $x'$. In that case, as shown by Howell, $u = \dot{L}x$ for all time, and $h$ is a function of $t$ only [49] (using a similar approach, the same result was shown for a fluid with $\mu_1 = \mu_2 = 0$, [41]). However, for a transversely isotropic sheet with $\mu_2 \neq 0$, the existence of the trigonometric terms inside $G_2$ changes this. When $\mu_2 > 0$, even if $h(x', 0)$ is constant, if $\theta(x', y, 0)$ depends upon $x'$, this will result in $u$ becoming nonlinear in $x'$, and by (3.28), this will cause $h$ to become spatially non-uniform. In Figure 3.2, we illustrate the early evolution of the thickness of the sheet and the behaviour of $\frac{1}{G_2}$, for $h(x', 0) = 1, \theta(x', y', 0) = \cos(4\pi x'y') - 0.1, \mu_1 = \mu_3 = 0, \mu_2 = 5$. Notice that the sheet thickness immediately becomes non-uniform, and the location of the peaks and troughs in $\frac{1}{G_2}$ correlates with the locations of local minima and maxima of the thickness of the sheet.

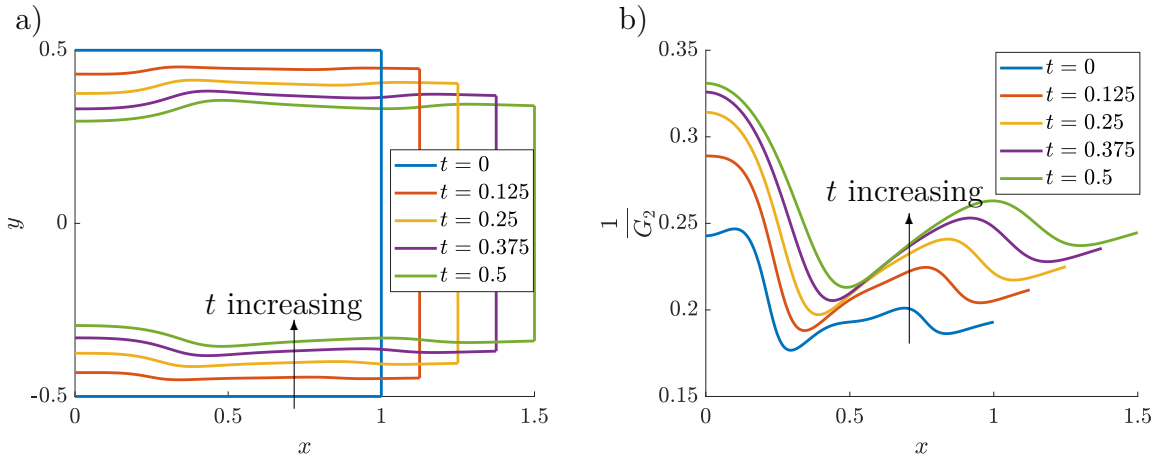


Figure 3.2: The evolution of a) the thickness of the sheet and b) the function $\frac{1}{G_2}$ up to the time $t = 0.5$, pulling at $L(t) = 1 + t$, with the initial conditions $h(x', 0) = 1, \theta(x', y', 0) = \cos(4\pi x'y') - 0.1, \mu_1 = \mu_3 = 0, \mu_2 = 5$.

### 3.3.3 Effect of varying the extensional and shear viscosities $\mu_2, \mu_3$, with $\mu_1 = 0$.

In this subsection, we continue to use the initial conditions $h(x', 0) = 1, \theta(x', y', 0) = \cos(4\pi x'y') - 0.1, \mu_1 = 0$, but now vary $\mu_2$ and $\mu_3$ and compare the state of the sheet at $t = 5$. First, we note that setting $\mu_2 = 0$ yields $G_2 = 4$ regardless of the value of $\mu_3$. We

plot in Figure 3.3 the thickness and velocity $u$ in the sheet for varied $\mu_2$ and notice that for these choices of $\theta(x', y', 0)$ and $h(x', 0)$ that we see a global increase in the longitudinal velocity for increasing $\mu_2$. Additionally, we see that there are regions of the sheet that thin more quickly for increasing $\mu_2$, and other regions that thin more slowly. Intuition based upon the behaviour of a pipe flow would lead one to expect that in regions where the sheet is thicker, the velocity would be lower. This is not true here, and as in the previous subsection, this behaviour is linked to the behaviour of $G_2$ as we shall now demonstrate. Taking $\mu_3 = 0$, we have

$$G_2\left(x', \frac{1}{2}, t\right) = \int_{-\frac{1}{2}}^{\frac{1}{2}} \frac{4\left(4+\mu_2\right)}{4+\mu_2 \sin^2 2\theta} \mathrm{d}y'. \tag{3.39}$$

Integrating (3.38) and using $u(1) = 1$, we may write

$$1 = T \int_0^1 \frac{1}{hG_2(x', \frac{1}{2}, t)} \mathrm{d}x', \tag{3.40}$$

and so

$$u = \frac{\int_0^{x'} \frac{1}{hG_2} \mathrm{d}s}{\int_0^1 \frac{1}{hG_2} \mathrm{d}x'}. \tag{3.41}$$

From equation (3.41), we see that $u$ behaves as a normalised cumulative integral. If $G_2$ is fixed, the longitudinal velocity does behave like a pipe flow. Where $h$ is small, $1/h$ is larger than the averaged value of $1/h$ across the domain, and hence $u^{(0)}$ will increase in this region. In Figure 3.3, we see that for increasing $\mu_2$, whilst $G_2$ increases, $hG_2$ decreases, leading to an enhanced velocity on the left hand side of the domain. Where $hG_2$ is larger, around $x = 3$, we see the gradient of $u^{(0)}$ decrease below that of $\mu_2 = 0$.

We note that by (3.40), as the fibres within the fluid sheet flatten out and $G_2$ increases everywhere and hence so does the tension, $T$, and that the tension will increase with

increasing $\mu_2$.

If we allow $\mu_2, \mu_3 \neq 0$, we now find that

$$G_2\left(x', \frac{1}{2}, t\right) = \int_{-\frac{1}{2}}^{\frac{1}{2}} \frac{4 + \mu_2 + 4\mu_3}{4 + 4\mu_3 + \mu_2 \sin^2 2\theta} \mathrm{d}y'. \tag{3.42}$$

We find that increasing $\mu_3$ has the effect of globally increasing the value of $G_2$ and hence the tension applied to the ends of the sheet, and the effect of damping the uniformity-breaking behaviour of $\mu_2$. That is, increasing the term $\mu_3$ drives the fluid to behave as 'more Newtonian', whilst increasing $\mu_2$ drives the non-Newtonian behaviour of breaking the uniformity of the sheet previously discussed. As an illustrative example, we include Figure 3.4. The figure represents the state of the sheet at $t = 5$, with initial conditions $h(x', 0) = 1, \theta(x', y', 0) = \cos(4\pi x' y') - 0.1$ for varied $\mu_3$ and fixed $\mu_2 = 5$. Notice that increasing $\mu_3$ causes the thickness of the sheet to exhibit less deviation from uniformity, and the longitudinal velocity to tend towards $u = \dot{L}x'$, the solution for a Newtonian fluid.

### 3.3.4 Behaviour of the fibres

We now turn our attention to the behaviour of the fibres within the sheet. Green and Friedman found that for the special case of not extending the sheet ($\dot{L} = 0$), that the fibres tend to align parallel to the $y$-axis, and that for the case of an extensional flow with $\mu_1, \mu_2 = 0$ that the fibres align with the direction of extension (i.e parallel to the $x$-axis) [41].

For $\mu_1 = 0$, we start by extending the results in section 6 of Ref. [41], for early time with a constant initial fibre direction. If $h_i, \theta_i$ are uniform, then we can see from equations (3.14) and (3.16) that $\dfrac{\partial u}{\partial x'} = 1$, and $\theta$ and $h$ must be functions of time only. Moreover, (3.16) yields

$$\frac{\partial \theta}{\partial t} = \frac{-\sin 2\theta \left(4 + 4\mu_3 + 2\mu_2 \sin^2 \theta\right) \frac{1}{L}}{4 + 4\mu_3 + \mu_2 \sin^2 2\theta}, \tag{3.43}$$

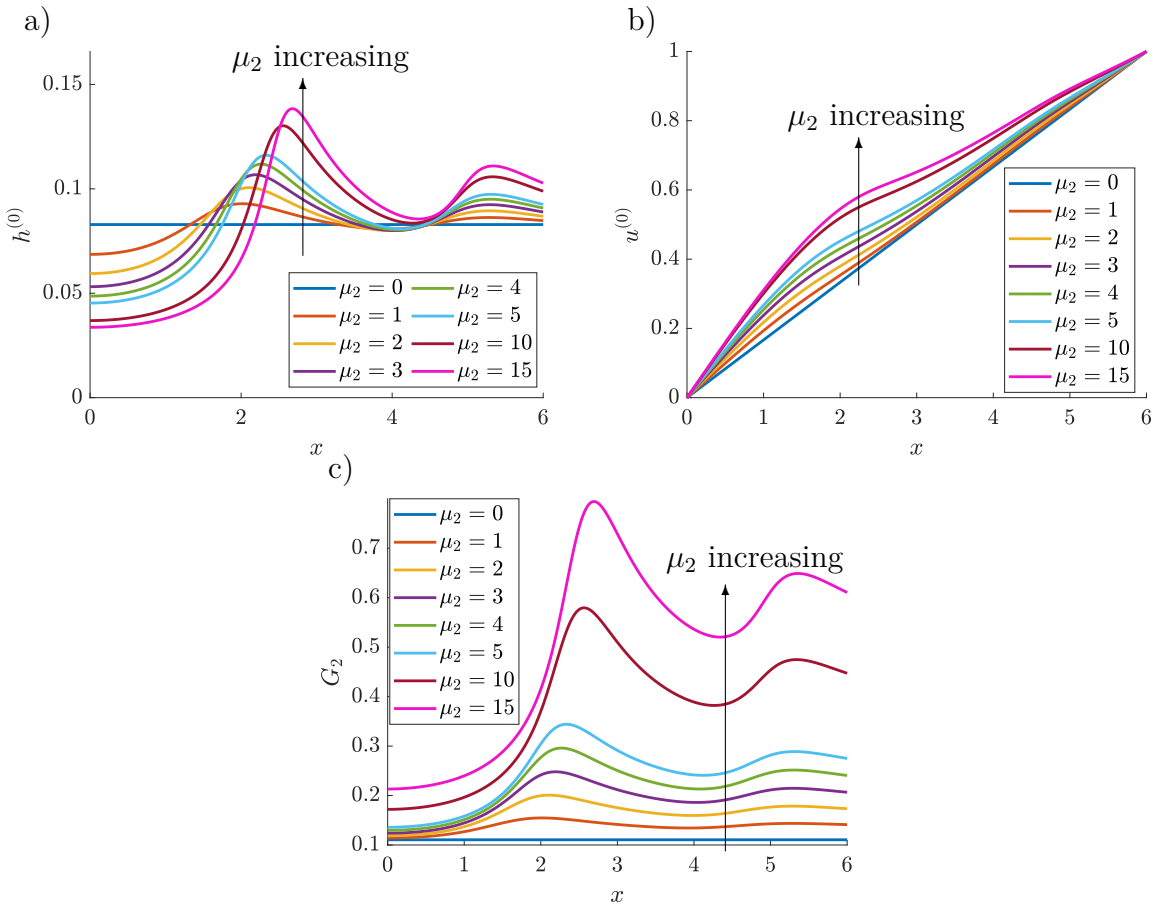


Figure 3.3: Comparison of the a) thickness, b) longitudinal velocity and c) $G_2$ at $t = 5$, pulling at $L(t) = 1 + t$, for varied $\mu_2$, with the conditions $h(x', 0) = 1, \theta(x', y', 0) = \cos(4\pi x' y') - 0.1, \mu_1 = \mu_3 = 0$. Note that more extreme behaviour in $G_2$ correlates with greater change in the thickness and velocity profile across the sheet.

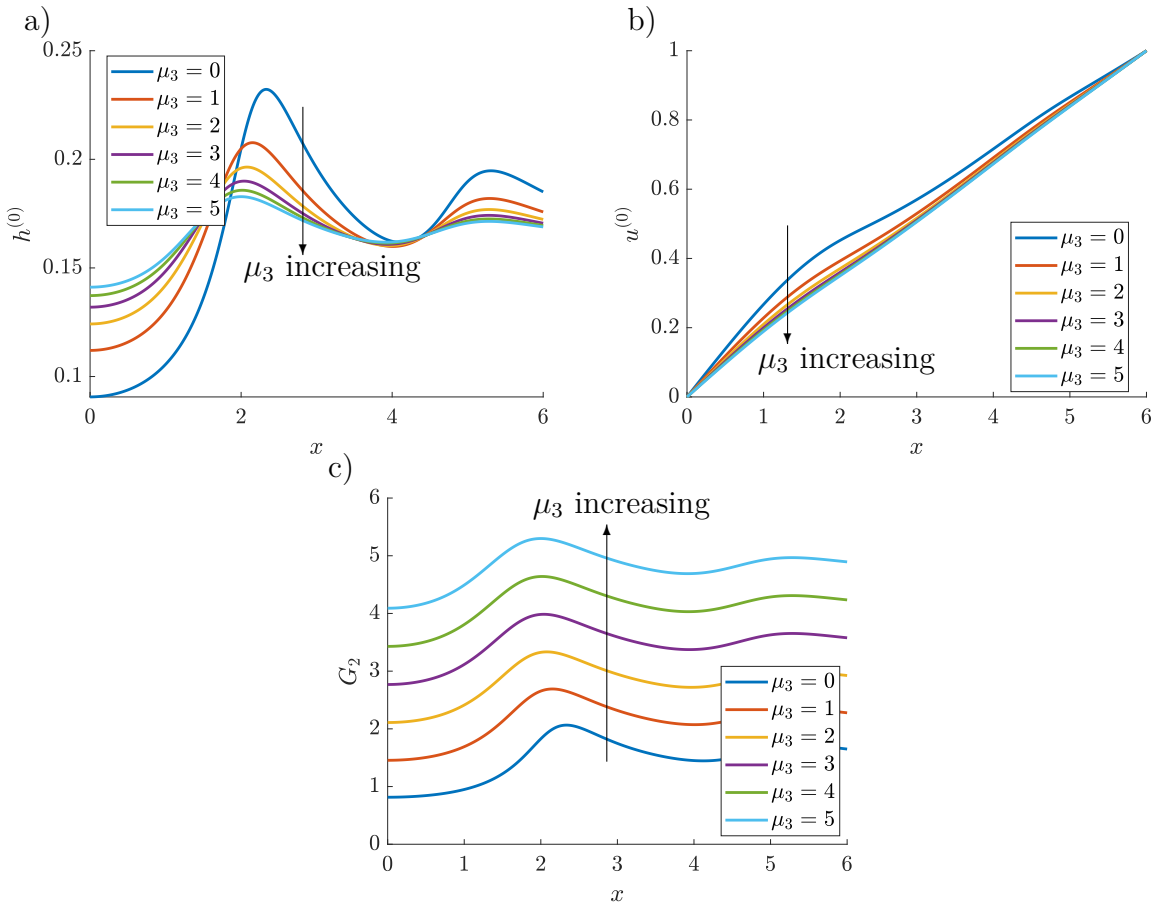


Figure 3.4: Comparison of a) thickness of the sheet, and b) longitudinal velocity of the sheet at $t = 5$ and c) $G_2$ at $t = 5$, $\theta(x', y', 0) = \cos(4\pi x' y') - 0.1$, for $\mu_1 = 0, \mu_2 = 5$, and varied values of $\mu_3$.

which implies that the behaviour of the fibres is determined by the sign of $\sin 2\theta$. For $0 < \theta < \frac{\pi}{2}$, we have $\frac{\partial \theta}{\partial t} < 0$, whilst for $\frac{\pi}{2} < \theta < \pi$, $\frac{\partial \theta}{\partial t} > 0$. Therefore, much like the case $\mu_1 = \mu_2 = 0$, studied by Green and Friedman, the fibres tend to orient themselves with the direction of extension, regardless of the value of $\mu_2$, given uniform initial conditions for $h$ and $\theta$. Additionally, we note that $\theta = \pm\frac{\pi}{2}$ is an unstable fixed point of equation (3.43), whilst $\theta = 0, \pi$ are stable fixed points.

We now consider the case $\mu_1 > 0$, for an initially constant $h_i$ and $\theta_i$. We again have that $\frac{\partial u}{\partial x'} = 1$ and $h, \theta$ remain uniform for all time. Equation (3.16) now yields

$$\frac{\partial \theta}{\partial t} = \frac{\sin 2\theta \left(2\mu_1 \sin^2\theta - (4 + 4\mu_3 + 2\mu_2 \sin^2\theta)\,\frac{1}{L}\right)}{4 + 4\mu_3 + \mu_2 \sin^2 2\theta}, \tag{3.44}$$

and so the evolution of the fibre direction is less clear. By again considering the cases $0 < \theta < \frac{\pi}{2}$, $\frac{\pi}{2} < \theta < \pi$, $-\frac{\pi}{2} < \theta < 0$, $-\pi < \theta < -\frac{\pi}{2}$ we find that in order for the fibres to align along $x$-axis over time, we require

$$\sin^2\theta\,(L\mu_1 - \mu_2) < 2 + 2\mu_3. \tag{3.45}$$

If this condition is satisfied, fibres with angles between $-\frac{\pi}{2} < \theta < \frac{\pi}{2}$ will rotate towards the positive $x$-axis, with fibres outside of this range rotating towards the negative $x$-axis, similarly to the above. However, since this expression includes $L(t)$, it is possible for fibres that initially rotate towards the longitudinal orientation to reverse their evolution as $L\mu_1$ grows with time to violate equation (3.45). We illustrate this behaviour in Figure 3.5. For the choices of $\theta_i = \frac{\pi}{4}, L_i = h_i = 1, \mu_1 = 5, \mu_2 = 0, \mu_3 = 1$, we give the evolution of the fibre angle and evolution of the left hand side (3.45). Initially, the fibres rotate towards the $x$-axis, until the inequality (3.45) is violated, at which time the fibres reverse their rotation and begin to rotate towards $\theta = \frac{\pi}{2}$.

Finally, we consider a choice of initial fibre angle distribution that is non-uniform. We choose $\theta(x', y', 0) = \cos(4\pi x' y') - 0.1$, $h(x', 0) = 1$ with $\mu_1 = \mu_3 = 0, \mu_2 = 5$. With a

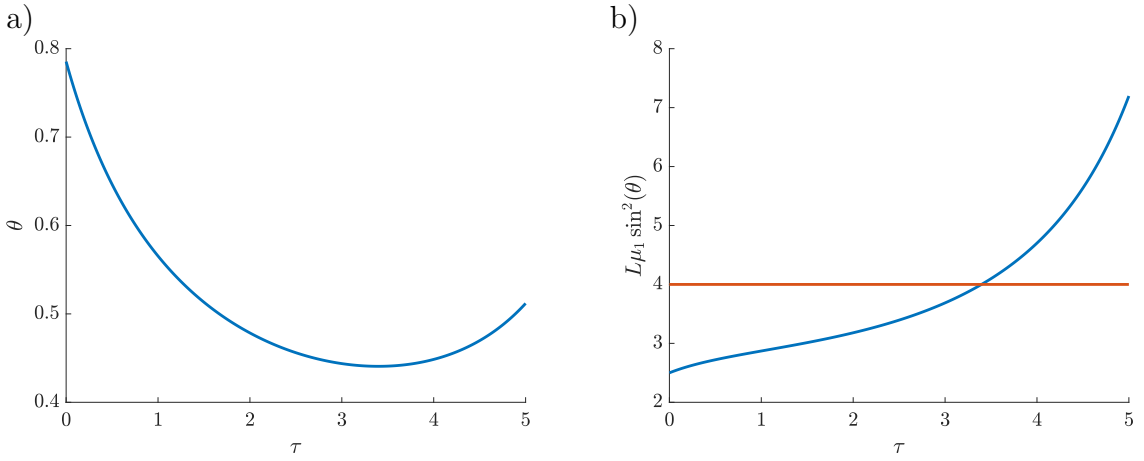


Figure 3.5: Evolution of a) the fibre angle $\theta$, and b) the left hand side of (3.45), $L\mu_1 \sin^2\theta$, (blue), with the threshold $2 + 2\mu_3$, (red), for the choices of $\theta_i = \frac{\pi}{4}, L_i = h_i = 1, \mu_1 = 5, \mu_2 = 0, \mu_3 = 1$. Note the reversal in the direction of rotation when $L\mu_1 \sin^2\theta \geq 2 + 2\mu_3$.

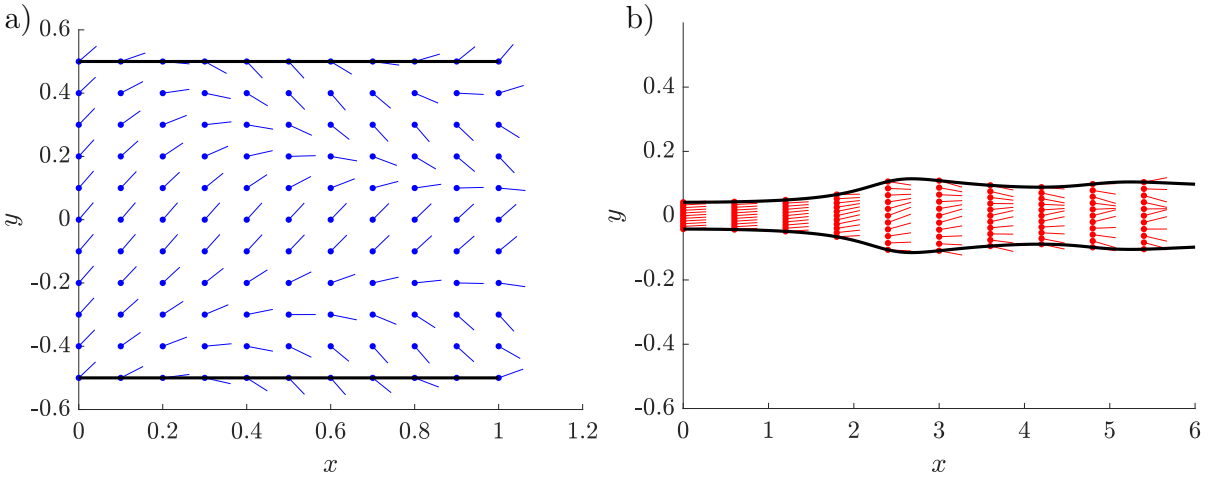


Figure 3.6: a) The initial thickness of the sheet and orientation of the fibres, and b) the thickness of the sheet and orientation of the fibres at $t = 5$, for the initial conditions $h(x', 0) = 1, \theta(x', y', 0) = \cos(4\pi x' y') - 0.1$ and choices of $\mu_1 = \mu_3 = 0, \mu_2 = 5$.

non-uniform choice of initial fibre distribution, we cannot make analytical progress with (3.16). However, we see in Figure 3.6 that the fibres have a tendency to align in the direction of the sheet when $\mu_1 = 0$. We also note that the rate at which the fibres align in this direction is enhanced in the regions of the sheet that undergoes fastest thinning of the fluid.

### 3.3.5 Centre-line of the fluid: When is it flat?

In the Newtonian problem, it was shown by Howell that the centre-line of the sheet straightens on a timescale shorter than $\frac{L_0}{U}$ (and is therefore generally taken to simply be $H = 0$ [16, 49]). This is not necessarily true for a transversely isotropic fluid. It is noted by Green & Friedman that should $\theta = \theta(x', t)$ and $\mu_1 = \mu_2 = 0$, then equations (3.14) and (3.15) with the requirement that $H(0, t) = H(L(t), t) = 0$, yields that the centre-line must be flat [41]. We extend this result to include $\mu_1, \mu_2 \neq 0$ by taking a similar approach. Supposing $\theta = \theta(x', t)$, then the integrand of equations (3.30) and (3.31) can be evaluated explicitly, yielding

$$\frac{\partial}{\partial x'}(hf) = 0, \tag{3.46}$$

$$\frac{\partial^2}{\partial x'^2}\left(\frac{1}{2}h^2 f\right) = \left(\frac{\partial^2 H}{\partial x'^2} + \frac{1}{2}\frac{\partial^2 h}{\partial x'^2}\right) hf, \tag{3.47}$$

where

$$f(x', t) = \frac{\mu_1 \cos 2\theta + \frac{1}{L}\left(4 + 4\mu_3 + \mu_2\right)\frac{\partial u}{\partial x'}}{4 + 4\mu_3 + \mu_2 \sin^2 2\theta}. \tag{3.48}$$

Expanding the second derivative on the LHS of equation (3.47) and using (3.46) yields that

$$\frac{\partial^2 H}{\partial x'^2} = 0, \tag{3.49}$$

and therefore $H(x', t) \equiv 0$. Turning our attention to the choice of $\theta(x', y', 0) = \theta_i(y')$, and now making the assumption that $\mu_1 = 0$ we have that the equation for the centre-line can be written as,

$$\left(\frac{\partial^2 H}{\partial x'^2} + \frac{1}{2}\frac{\partial^2 h}{\partial x'^2}\right) hG_2\left(\frac{1}{2}, t\right) = \frac{\partial^2}{\partial x'^2}\left(h^2 \int_{-\frac{1}{2}}^{\frac{1}{2}} G_2(y', t)\mathrm{d}y'\right). \tag{3.50}$$

We recall that, as noted in section 3.3.2, if we choose $\theta_i = \theta_i(y')$ only and the initial thickness $h_i$ to be uniform, then $G_2$ will not possess $x'$-dependence and $h$ will also remain

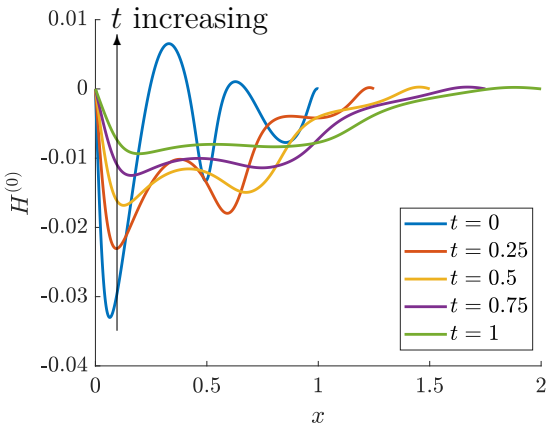


Figure 3.7: Evolution of the centre-line of the sheet under the initial conditions $h(x', 0) = 1, \theta(x', y', 0) = \sin(4\pi x' y') - 0.1$ with $\mu_2 = 5, \mu_1 = \mu_3 = 0$.

uniform for all time. As a result we once again obtain (3.49), so that asymmetry in the fibre angles over the centre-line is not sufficient to cause an initially uniform sheet with $\mu_1 = 0$ to deflect.

If $\mu_1 = 0$ and $h_i$ is uniform, we must choose $\theta(x', y', 0) = \theta(x', y')$ with $\frac{\partial \theta}{\partial y'}|_{y'=0} \neq 0$ to obtain centre-line deflection. In Figure 3.7 we plot the centre-line evolution for the initial conditions $\theta(x', y', 0) = \sin(4\pi x' y') - 0.1$ with $\mu_2 = 5, \mu_1 = \mu_3 = 0$. Since the centre-line does not instantaneously collapse to 0, this suggests that considering the behaviour of the fluid on a short timescale may reveal interesting behaviour that is markedly different from a Newtonian fluid.

If we consider a condition for $h(x', 0)$ that is not uniform, we find that there will exist a small deflection when $\theta(x', y', 0) = \theta_i(y')$, since a non-uniform $h$ will induce $x$-dependence in $u_x$ via (3.30). Hence, $\theta$ will gain $x'$-dependence through its evolution equation (3.29). As an illustrative example, we give the evolution of the centre-line in Figure 3.8 for the choices of $h(x', 0') = 1 + x'^2, \theta(y', 0) = \sin(4\pi y'), \mu_2 = 5, \mu_1 = \mu_3 = 0$.

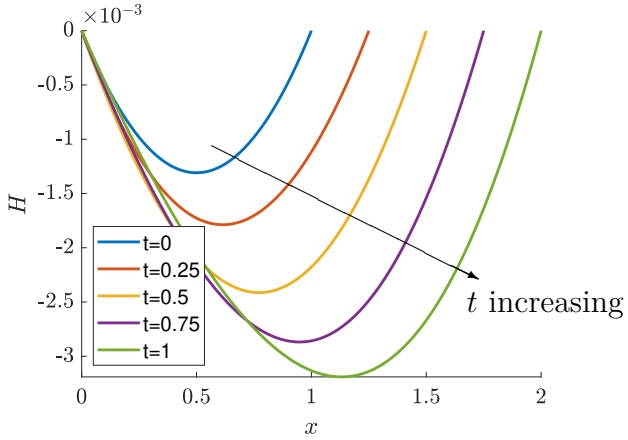


Figure 3.8: Evolution of the centre-line of the sheet for the choices of $h(x',0') = 1 + x'^2, \theta(y',0) = \sin(4\pi y'), \mu_2 = 5, \mu_1 = \mu_3 = 0$.

### 3.3.6 Behaviour of sheets possessing tension in the fibre direction, $\mu_1 > 0$.

Here, we briefly examine two special cases for the sheet for which $\mu_1 > 0$. We start by prescribing $L(t) = 1 + t$, $h_i = 1$, $\mu_1 = 5$, $\mu_2 = \mu_3 = 0$, and we test two initial choices of $\theta$, $\theta_i = 0$, corresponding to the fibres being aligned in the direction of extension, and $\theta_i = \dfrac{\pi}{2}$, corresponding to the fibres being aligned in the transverse direction in the sheet. In Figure 3.9 we plot the tension required to be applied to the sheet to achieve the prescribed rate of pulling for these two initial choices of $\theta$. First, we note that for these choices of $\theta_i$, there is no evolution in $\theta$ with time as $\theta = 0, \dfrac{\pi}{2}$ are fixed points of equation (3.29). Next, we notice that for fibres arranged in the transverse direction of the sheet, that the tension applied to the sheet is negative. To explain this we begin with the equation for $u$ in spatial variables,

$$T = \int_{H^-}^{H^+} \frac{\mu_1 \cos 2\theta + (4 + 4\mu_3 + \mu_2)\frac{\partial u}{\partial x}}{4 + 4\mu_3 + \mu_2 \sin^2 2\theta} \mathrm{d}y, \tag{3.51}$$

now since $\theta$ has no evolution for these particular choices of $\theta_i$ (as they are fixed points of equation (3.27)), then

$$T = \frac{1}{4\,(1 + \mu_3)} \left( (4 + 4\mu_3 + \mu_2)\frac{\partial u}{\partial x} \pm \mu_1 \right) h, \tag{3.52}$$

where the positive sign corresponds to $\theta_i = 0$, and the negative to $\theta_i = \frac{\pi}{2}$. We note that the active behaviour of fibres aligned in the longitudinal direction enhances the tension in the sheet. This is similar to the behaviour of cell-seeded hydrogels, where the active behaviour of the suspended self-aligning cells cause an increase in tension across the sheet [69]. In the case of $\theta_i = \frac{\pi}{2}$, it is possible that $\mu_1 > (4 + 4\mu_3 + \mu_2)\, u_x$ and hence $T < 0$. We interpret this as being due to the fibres in the transverse direction attempting to contract the sheet, which due to mass conversation, would generate a compression in the longitudinal direction, as the sheet attempts to extend longitudinally. If we define the total tension required to move the sheet at the prescribed speed as $T_L$, the tension caused by the fibres as $T_f$ and the tension applied to the sheet as $T$, then we expect that

$$T_L = T + T_f. \tag{3.53}$$

The rate of extension is too slow to compensate for the compression generated by the fibres pulling in the transverse direction, hence $T < 0$. As discussed by Howell for the Newtonian case, [49], when the sheet is in compression we expect buckling to occur, and that the curvature of the centre-line will in time become significant. Thus, in this case, the nearly-straight centre-line scaling assumed in the Green and Friedman model will be violated, and the model will fail to predict the behaviour of the sheet.

## 3.4 Discussion

In this chapter we have constructed a numerical strategy to solve the model proposed by Green & Friedman for the extensional flow of a thin two-dimensional sheet of a fibre-reinforced fluid, first reducing the model by eliminating $u^{(1)}$ and then employing a Arbitrary Lagrangian-Eulerian method. We have shown how the distribution of fibres within the fluid can cause interesting non-Newtonian behaviours such as driving non-uniformity in the development of the thickness of an initially uniformly thick sheet and the generation

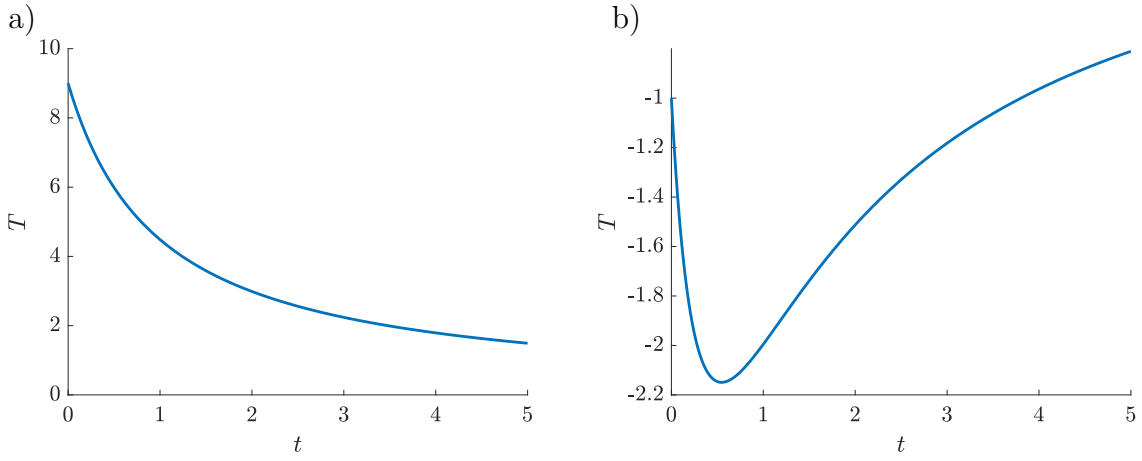


Figure 3.9: Evolution of the tension applied to the sheet for two initial choices of fibre direction, a) $\theta_i = 0$, and b) $\theta_i = \dfrac{\pi}{2}$ up to $t = 5$ with $h(x', 0) = 1, \mu_1 = 5, \mu_2 = \mu_3 = 0$, and prescribed pulling $L = 1 + t$.

of a non-zero centre-line even with the implicit assumption that the centre-line is nearly straight. Additionally, we are unaware of any existing mathematical models that possess a coupled pair of integro-differential equations with a double integral having limits involving a variable like (3.31). Furthermore, we have investigated the short time behaviour of the model, to create a framework for the examination of sheets with an initially curved centre-line.

Similar to previous work, we see that the fibres of a transversely isotropic fluid generally align in the direction of extension, provided $\mu_1 = 0$, as long as the fibres are not initially pointing in the transverse direction of the sheet. As far as the behaviour of an active transversely isotropic fluid is concerned, preliminarily we have seen that allowing $\mu_1 \neq 0$ allows the fibres to develop towards alignments that are not in the direction of extension of the fluid. However, if the fibres are aligned in the longitudinal direction of the sheet and possess active behaviour, the tension within the sheet is increased. Active behaviour giving rise to greater tension has been observed in the seeding of hydrogels with a suspension of self-aligning cells [5]. Future work in this area could include constructing more biologically realistic multiphase model that incorporates the work in this chapter as a fibrous extracellular matrix or hydrogel, with the cells exhibiting active behaviour instead of the fibres. This could result in a model of how different experimental setups

lead to different alignment patterns of cells and could determine the best conditions to grow neural tissue.

Our results also show that the behaviour of a passive transversely isotropic fluid sheet is controlled largely by the behaviour of the function $G_2$, through which the fibre orientation acts upon the longitudinal velocity and centre-line of the fluid. We interpret this function as the 'effective viscosity' throughout the sheet. In places, this viscosity induces necking in the sheet, as has been seen in Newtonian fluids with an inhomogenous viscosity [73] and is the direct cause of the longitudinal velocity not behaving as a pipe flow intuition would expect. That is, where the sheet is thicker does not necessarily correspond to a decrease in the longitudinal velocity, but rather a change in the gradient $\dfrac{\partial u}{\partial x}$ driven by $G_2$.

There are a number of avenues for further work related to this chapter. We model sheets that are nearly straight, with the employment of a Cartesian co-ordinate system restricting the model to examining sheets which are initially slightly curved, i.e $\dfrac{H}{L_0}$ is small. Where this is not the case, future work could entail the use of a curvilinear co-ordinate system to approach sheets with curvature in the centre-line, in works similar to Ribe [82].

As the thread starts to become very thin, there may be a new regime where the $\mu_1$ term in (3.30) dominates the $\dfrac{\partial u}{\partial x'}$ term. Perhaps the behaviour of the sheet in this regime may shed light upon how the active behaviour of the fluid may drive breakup of the sheet. Simpler modifications could include prescribing the tension applied to the ends of the sheet, rather than prescribing the length. Furthermore we could also modify the model to include the effects of surface tension, inertia, and body forces.

# CHAPTER 4

# SHORT TIMESCALE ANALYSIS OF THE EXTENSIONAL FLOW OF A SHEET

We extend the work of the previous chapter by examining the extensional flow a two-dimensional transversely isotropic viscous sheet, over a timescale shorter than the $\frac{L_0}{U}$ timescale we employed in chapter 3. In Ref. [49], it is demonstrated that the leading order equations for the extensional flow of a slender, viscous, Newtonian sheet predict that the centre-line of the sheet is straight. Hence, the model cannot satisfy an initial condition for the case when the centre-line that is not straight. In order to study the behaviour of initially curved sheets, a short timescale analysis is performed. It is demonstrated that the required timescale must be $\varepsilon^2 \frac{L_0}{U}$ by Buckmaster et al [16], where $L, U$ are the characteristic length and velocity scales respectively. As discussed in the previous chapter, in the transversely isotropic problem, it is similarly impossible to satisfy an arbitrary initial condition for the centre-line, and there exist possible choices for the key parameters and initial distribution fibre angles, that give rise to a centre-line that is not identically zero on the flow timescale. This indicates that there may exist interesting behaviours, different from the Newtonian case, on this short timescale.

We begin by giving the governing equations on this timescale in section 4.1. Next, we derive a reduced model using a now familiar lubrication approximation in section 4.2. This derivation is lengthy, and a summary is given in section 4.2.1, before yet further reductions to the model are made. The numerical strategy is briefly detailed in section 4.2.2. We

compare the results from the short timescale to the initial results from the Green and Friedman model and discuss the effect of changing parameter values in section 4.3.

## 4.1 Governing equations on the short timescale

We seek a short timescale in order to describe the evolution of the centre-line and fibres. As before, we define $L_0, h_0, U$ to be the initial length, typical initial thickness, and typical value for the velocity for the fluid at the pulled boundary respectively and reintroduce the parameter $\varepsilon = h_0/L_0 \ll 1$, which is the initial inverse aspect ratio of the sheet. Unlike chapter 3, we are interested in the behaviour of the sheet on a short timescale in order to study the movement of the centre-line. We use the same scaling as Buckmaster et al [16] and Howell [49], and re-scale the equations and boundary conditions by setting

$$\tau = \frac{t}{\varepsilon^2}. \tag{4.1}$$

Except for the new timescale, we use the same scalings as in chapter 3. The dimensionless equations for the sheet are given in (B.1)-(B.3). Immediately from the kinematic boundary condition (3.19) we see that we must re-scale the vertical velocity $v$ to be small. Hence, we set

$$v = \frac{V}{\varepsilon^2}.$$

Applying this scaling to the dimensionless equations for the sheet (B.1)-(B.3), yields

$$\varepsilon^2 \frac{\partial u}{\partial x} + \frac{\partial V}{\partial y} = 0, \tag{4.2}$$

from continuity, whilst the $x$-momentum equation becomes

$$
\begin{aligned}
&-\varepsilon^3\frac{\partial p}{\partial x}+\varepsilon\frac{\partial^2 u}{\partial y^2}+\varepsilon^3\frac{\partial^2 u}{\partial x^2}+\varepsilon^3\mu_1\frac{\partial}{\partial x}(\cos^2\theta)+\varepsilon^2\mu_1\frac{\partial}{\partial y}(\cos\theta\sin\theta)\\
&\quad+\mu_2\frac{\partial}{\partial x}\left[\varepsilon^3\cos^4\theta\frac{\partial u}{\partial x}+\cos^3\theta\sin\theta\left(\varepsilon^2\frac{\partial u}{\partial y}+\varepsilon^2\frac{\partial V}{\partial x}\right)+\varepsilon\cos^2\theta\sin^2\theta\frac{\partial V}{\partial y}\right]\\
&\quad+2\mu_3\frac{\partial}{\partial x}\left[2\varepsilon^3\cos^2\theta\frac{\partial u}{\partial x}+\cos\theta\sin\theta\left(\varepsilon^2\frac{\partial u}{\partial y}+\varepsilon^2\frac{\partial V}{\partial x}\right)\right]\\
&\quad+\mu_2\frac{\partial}{\partial y}\left[\cos\theta\sin\theta\left(\varepsilon^2\cos^2\theta\frac{\partial u}{\partial x}+\varepsilon\cos\theta\sin\theta\left(\frac{\partial u}{\partial y}+\frac{\partial V}{\partial x}\right)+\sin^2\theta\frac{\partial V}{\partial y}\right)\right]\\
&\quad+\mu_3\frac{\partial}{\partial y}\left[\varepsilon\frac{\partial u}{\partial y}+\varepsilon\frac{\partial V}{\partial x}\right]=0,
\end{aligned}
\tag{4.3}
$$

and in the $y$ direction we have:

$$
\begin{aligned}
&-\varepsilon^2\frac{\partial p}{\partial y}+\epsilon^2\frac{\partial^2 V}{\partial x^2}+\frac{\partial^2 V}{\partial y^2}+\varepsilon^2\mu_1\frac{\partial}{\partial y}(\sin^2\theta)+\varepsilon^3\mu_1\frac{\partial}{\partial x}(\cos\theta\sin\theta)\\
&\quad+\mu_2\frac{\partial}{\partial y}\left[\varepsilon^2\sin^2\theta\cos^2\theta\frac{\partial u}{\partial x}+\varepsilon\cos\theta\sin^3\theta\left(\frac{\partial u}{\partial y}+\frac{\partial V}{\partial x}\right)+\sin^4\theta\frac{\partial V}{\partial y}\right]\\
&\quad+2\mu_3\frac{\partial}{\partial y}\left[2\sin^2\theta\frac{\partial V}{\partial y}+\varepsilon\cos\theta\sin\theta\left(\frac{\partial u}{\partial y}+\frac{\partial V}{\partial x}\right)\right]\\
&\quad+\mu_2\frac{\partial}{\partial x}\left[\varepsilon^3\sin\theta\cos^3\theta\frac{\partial u}{\partial x}+\varepsilon^2\cos^2\theta\sin^2\theta\left(\frac{\partial u}{\partial y}+\frac{\partial V}{\partial x}\right)+\varepsilon\cos\theta\sin^3\theta\frac{\partial V}{\partial y}\right]\\
&\quad+\mu_3\frac{\partial}{\partial x}\left[\varepsilon^2\frac{\partial u}{\partial y}+\varepsilon^2\frac{\partial V}{\partial x}\right]=0.
\end{aligned}
\tag{4.4}
$$

The equation for the evolution of the fibre angles, (3.3), becomes

$$
\frac{\partial\theta}{\partial\tau}+\varepsilon^2 u\frac{\partial\theta}{\partial x}+V\frac{\partial\theta}{\partial y}=-\varepsilon^2\sin\theta\cos\theta\frac{\partial u}{\partial x}-\varepsilon\sin^2\theta\frac{\partial u}{\partial y}+\varepsilon\cos^2\theta\frac{\partial V}{\partial x}+\sin\theta\cos\theta\frac{\partial V}{\partial y}. \tag{4.5}
$$

We must also apply the scaling to the boundary conditions. The no stress boundary conditions give us

$$\varepsilon\frac{\partial u}{\partial y}+\varepsilon\frac{\partial V}{\partial x}+\varepsilon^2\mu_1\cos\theta\sin\theta+\mu_2\cos\theta\sin\theta\left(\varepsilon^2\cos^2\theta\frac{\partial u}{\partial x}+\cos\theta\sin\theta\left(\varepsilon\frac{\partial u}{\partial y}+\varepsilon\frac{\partial V}{\partial x}\right)+\sin^2\theta\frac{\partial V}{\partial y}\right)+\mu_3\left(\varepsilon\frac{\partial V}{\partial x}+\varepsilon\frac{\partial u}{\partial y}\right)=\varepsilon\left[\frac{\partial H}{\partial x}\pm\frac{1}{2}\frac{\partial h}{\partial x}\right]\left[-\varepsilon^2p+2\varepsilon^2\frac{\partial u}{\partial x}+\varepsilon^2\mu_1\cos^2\theta+\mu_2\cos^2\theta\left(\varepsilon^2\cos^2\theta\frac{\partial u}{\partial x}+\cos\theta\sin\theta\left(\varepsilon\frac{\partial u}{\partial y}+\varepsilon\frac{\partial V}{\partial x}\right)+\sin^2\theta\frac{\partial V}{\partial y}\right)+2\mu_3\cos\theta\left(2\varepsilon^2\cos\theta\frac{\partial u}{\partial x}+\sin\theta\left(\varepsilon\frac{\partial u}{\partial y}+\varepsilon\frac{\partial V}{\partial x}\right)\right)\right],\ \text{on } y=H^{\pm}, \quad (4.6)$$

$$-\varepsilon^2p+2\frac{\partial V}{\partial y}+\varepsilon^2\mu_1\sin^2\theta+\mu_2\sin^2\theta\left(\varepsilon^2\cos^2\theta\frac{\partial u}{\partial x}+\cos\theta\sin\theta\left(\varepsilon\frac{\partial u}{\partial y}+\varepsilon\frac{\partial V}{\partial x}\right)+\sin^2\theta\frac{\partial V}{\partial y}\right)+2\mu_3\left(2\sin^2\theta\frac{\partial V}{\partial y}+\sin\theta\cos\theta\left(\varepsilon\frac{\partial u}{\partial y}+\varepsilon\frac{\partial V}{\partial x}\right)\right)=\varepsilon\left[\frac{\partial H}{\partial x}\pm\frac{1}{2}\frac{\partial h}{\partial x}\right]\left[\varepsilon\frac{\partial u}{\partial y}+\varepsilon\frac{\partial V}{\partial x}+\varepsilon^2\mu_1\cos\theta\sin\theta+\mu_2\cos\theta\sin\theta\left(\varepsilon^2\cos^2\theta\frac{\partial u}{\partial x}+\cos\theta\sin\theta\left(\varepsilon\frac{\partial u}{\partial y}+\varepsilon\frac{\partial V}{\partial x}\right)+\sin^2\theta\frac{\partial V}{\partial y}\right)+\mu_3\left(\varepsilon\frac{\partial V}{\partial x}+\varepsilon\frac{\partial u}{\partial y}\right)\right]\ \text{on } y=H^{\pm}, \quad (4.7)$$

in the $x$ and $y$ directions respectively. We also will have the boundary conditions

$$u(0,\tau)=0,\quad u(L,\tau)=\dot{L}, \quad (4.8)$$

$$H(0,\tau)=H(L,\tau)=0, \quad (4.9)$$

$$\frac{\partial H}{\partial x}(0,\tau)=\frac{\partial H}{\partial x}(L,\tau)=0, \quad (4.10)$$

and will need to prescribe initial conditions for $\theta^{(0)}$ and $h^{(0)}$. Throughout this chapter, we will continue to use $L(t)=1+t$ unless otherwise stated, which gives the right hand boundary condition $u(L,\tau)=1$.

## 4.2 Thin film approximation

Once again, we introduce the assumption that the sheet is thin. We reduce the model by exploiting the slender geometry of the sheet by expanding our variables as a power series of the inverse aspect ratio of the sheet, $\varepsilon$:

$$u \sim u^{(0)} + \varepsilon u^{(1)} + ..., \text{ etc.}$$

As before, we see that the modification to transverse isotropy requires that we include odd powers in our expansion. At leading order the continuity equation gives

$$\frac{\partial V^{(0)}}{\partial y} = 0, \tag{4.11}$$

with the kinematic condition

$$V^{(0)} = \frac{\partial H^{(0)}}{\partial \tau} \pm \frac{1}{2}\frac{\partial h^{(0)}}{\partial \tau}; \text{ on } y = H^{(0)^{\pm}}, \tag{4.12}$$

where, as in the previous chapter, $H^{(0)^{\pm}} = H^{(0)} \pm \dfrac{h^{(0)}}{2}$. Integrating (4.11) with the kinematic condition yields

$$V^{(0)} = \frac{\partial H^{(0)}}{\partial \tau}, \qquad \frac{\partial h^{(0)}}{\partial \tau} = 0. \tag{4.13}$$

Much like the Newtonian problem [49], the transverse velocity is independent of depth, and there is no thinning of the sheet on this timescale. Additionally, we obtain an equation for $\theta^{(0)}$ at this order, which is

$$\frac{\partial \theta^{(0)}}{\partial \tau} + \frac{\partial H^{(0)}}{\partial \tau}\frac{\partial \theta^{(0)}}{\partial y} = 0. \tag{4.14}$$

An immediate consequence of (4.14) is that movement of the centre-line of the fluid is required in order to have rotation of the fibres. To obtain equations for $u^{(0)}, p^{(0)}$ and $H^{(0)}$

we must proceed to higher orders. At $\mathcal{O}(\varepsilon)$ we obtain

$$\frac{\partial^2 u^{(0)}}{\partial y^2} + \mu_2 \frac{\partial}{\partial y}\left(\cos^2\theta^{(0)} \sin^2\theta^{(0)} \left(\frac{\partial u^{(0)}}{\partial y} + \frac{\partial V^{(0)}}{\partial x}\right)\right) + \mu_3 \frac{\partial}{\partial y}\left(\frac{\partial u^{(0)}}{\partial y} + \frac{\partial V^{(0)}}{\partial x}\right) = 0, \tag{4.15}$$

from the $x$-momentum equation, with the corresponding boundary condition

$$\frac{\partial u^{(0)}}{\partial y} + \frac{\partial V^{(0)}}{\partial x} + \mu_2 \cos^2\theta^{(0)} \sin^2\theta^{(0)} \left(\frac{\partial u^{(0)}}{\partial y} + \frac{\partial V^{(0)}}{\partial x}\right) + \mu_3 \left(\frac{\partial u^{(0)}}{\partial y} + \frac{\partial V^{(0)}}{\partial x}\right) = 0; \text{ on } y = H^{(0)^{\pm}}. \tag{4.16}$$

Integration of (4.15) and application of (4.16) yields

$$\left(\frac{\partial u^{(0)}}{\partial y} + \frac{\partial V^{(0)}}{\partial x}\right)\left(1 + \mu_2 \cos^2\theta \sin^2\theta + \mu_3\right) = 0, \tag{4.17}$$

hence, we recover the statement for $u^{(0)}$

$$u^{(0)} = \bar{u}(x,\tau) + \left(H^{(0)} - y\right)\frac{\partial^2 H^{(0)}}{\partial\tau\partial x}, \tag{4.18}$$

where $\bar{u}(x,t)$ is a function arising from the integration of (4.17). This is precisely the same result one obtains for a Newtonian fluid [49], although the result appears in our analysis at $\mathcal{O}(\varepsilon)$ instead of $\mathcal{O}(\varepsilon^2)$. As $u^{(0)}$ possesses $y$-dependence, the flow is not extensional on this timescale. As noted by Howell [49], dependence of $u^{(0)}$ on $y$ leads to bending stresses within the sheet.

Consideration of equations at $\mathcal{O}(\varepsilon^2)$ allow us to obtain an expression for $p^{(0)}$. First, the continuity equation at this order yields

$$\frac{\partial u^{(0)}}{\partial x} + \frac{\partial V^{(2)}}{\partial y} = 0, \tag{4.19}$$

then the $y$-momentum equation at $\mathcal{O}(\varepsilon^2)$ is

$$
\begin{aligned}
-\frac{\partial p^{(0)}}{\partial y}+\frac{\partial^2 V^{(0)}}{\partial x^2}+\frac{\partial^2 V^{(2)}}{\partial y^2}+\mu_1\frac{\partial}{\partial y}\left(\sin^2\theta^{(0)}\right)+\mu_2\frac{\partial}{\partial y}\Bigg(&\cos^2\theta^{(0)}\sin^2\theta^{(0)}\frac{\partial u^{(0)}}{\partial x}+\\
&+\cos\theta^{(0)}\sin^3\theta^{(0)}\left(\frac{\partial u^{(1)}}{\partial y}+\frac{\partial V^{(1)}}{\partial x}\right)+\sin^4\theta\frac{\partial V^{(2)}}{\partial y}\Bigg)\\
&+2\mu_3\frac{\partial}{\partial y}\left(2\sin^2\theta^{(0)}\frac{\partial V^{(2)}}{\partial y}+\cos\theta^{(0)}\sin\theta^{(0)}\left(\frac{\partial u^{(1)}}{\partial y}+\frac{\partial V^{(1)}}{\partial x}\right)\right)=0, \quad (4.20)
\end{aligned}
$$

with the associated boundary condition

$$
\begin{aligned}
-p^{(0)}+2\frac{\partial V^{(2)}}{\partial y}+\mu_1\sin^2\theta^{(0)}+\mu_2\Bigg(&\cos^2\theta^{(0)}\sin^2\theta^{(0)}\frac{\partial u^{(0)}}{\partial x}\\
&+\cos\theta^{(0)}\sin^3\theta^{(0)}\left(\frac{\partial u^{(1)}}{\partial y}+\frac{\partial V^{(1)}}{\partial x}\right)+\sin^4\theta\frac{\partial V^{(2)}}{\partial y}\Bigg)\\
+2\mu_3\left(2\sin^2\theta^{(0)}\frac{\partial V^{(2)}}{\partial y}+\cos\theta^{(0)}\sin\theta^{(0)}\left(\frac{\partial u^{(1)}}{\partial y}+\frac{\partial V^{(1)}}{\partial x}\right)\right)&=0;\ \text{on } y=H^{(0)^{\pm}}. \quad (4.21)
\end{aligned}
$$

There are a number of terms involving $H^{(1)}$ that arise in the calculation of (4.21). These terms are multiplied by $\dfrac{\partial u^{(0)}}{\partial y}+\dfrac{\partial V^{(0)}}{\partial x}$ and are thus omitted. Noting that $V^{(0)}$ must be a function of $x,t$ only, we can directly integrate (4.20)

$$
\begin{aligned}
-p^{(0)}+y\frac{\partial^2 V^{(0)}}{\partial x^2}+\frac{\partial V^{(2)}}{\partial y}+\mu_1\sin^2\theta^{(0)}+\mu_2\Bigg(&\cos^2\theta^{(0)}\sin^2\theta^{(0)}\frac{\partial u^{(0)}}{\partial x}\\
&+\cos\theta^{(0)}\sin^3\theta^{(0)}\left(\frac{\partial u^{(1)}}{\partial y}+\frac{\partial V^{(1)}}{\partial x}\right)+\sin^4\theta\frac{\partial V^{(2)}}{\partial y}\Bigg)\\
+2\mu_3\left(2\sin^2\theta^{(0)}\frac{\partial V^{(2)}}{\partial y}+\cos\theta^{(0)}\sin\theta^{(0)}\left(\frac{\partial u^{(1)}}{\partial y}+\frac{\partial V^{(1)}}{\partial x}\right)\right)&+c(x,\tau)=0. \quad (4.22)
\end{aligned}
$$

Applying the boundary conditions (4.21) and using (4.19) allows us to directly obtain the function $c$,

$$
c(x,\tau)=-\frac{\partial\bar{u}}{\partial x}-\frac{\partial H^{(0)}}{\partial x}\frac{\partial^2 H^{(0)}}{\partial x\partial\tau}-H\frac{\partial^3 H^{(0)}}{\partial^2 x\partial\tau},
$$

and hence the fibre-enhanced leading order pressure is

$$p^{(0)} = -2\frac{\partial u^{(0)}}{\partial x} + \mu_1 \sin^2\theta^{(0)} + \mu_2 \left( \cos^2\theta^{(0)} \sin^2\theta^{(0)} \frac{\partial u^{(0)}}{\partial x} + \cos\theta^{(0)} \sin^3\theta^{(0)} \left( \frac{\partial u^{(1)}}{\partial y} + \frac{\partial V^{(1)}}{\partial x} \right) + \sin^4\theta \frac{\partial V^{(2)}}{\partial y} \right) + 2\mu_3 \left( 2\sin^2\theta^{(0)} \frac{\partial V^{(2)}}{\partial y} + \cos\theta^{(0)} \sin\theta^{(0)} \left( \frac{\partial u^{(1)}}{\partial y} + \frac{\partial V^{(1)}}{\partial x} \right) \right) = 0. \quad (4.23)$$

We note here that setting $\mu_1 = \mu_2 = \mu_3 = 0$ recovers the expected Newtonian pressure. Now, the $x$-momentum equation is

$$\frac{\partial^2 u^{(1)}}{\partial y^2} + \mu_1 \frac{\partial}{\partial y} \left( \cos\theta^{(0)} \sin\theta^{(0)} \right) + \mu_2 \frac{\partial}{\partial y} \left( \cos^3\theta^{(0)} \sin^2\theta^{(0)} \frac{\partial u^{(0)}}{\partial x} + \cos^2\theta^{(0)} \sin^2\theta^{(0)} \left( \frac{\partial u^{(1)}}{\partial y} + \frac{\partial V^{(1)}}{\partial x} \right) + \cos\theta^{(0)} \sin^3\theta^{(0)} \frac{\partial V^{(2)}}{\partial y} \right) + \mu_3 \frac{\partial}{\partial y} \left( \frac{\partial u^{(1)}}{\partial y} + \frac{\partial V^{(1)}}{\partial x} \right) = 0, \quad (4.24)$$

with the associated boundary condition

$$\frac{\partial u^{(1)}}{\partial y} + \frac{\partial V^{(1)}}{\partial x} + \mu_1 \cos\theta^{(0)} \sin\theta^{(0)} + \mu_2 \left( \cos^3\theta^{(0)} \sin^2\theta^{(0)} \frac{\partial u^{(0)}}{\partial x} + \cos^2\theta^{(0)} \sin^2\theta^{(0)} \left( \frac{\partial u^{(1)}}{\partial y} + \frac{\partial V^{(1)}}{\partial x} \right) + \cos\theta^{(0)} \sin^3\theta^{(0)} \frac{\partial V^{(2)}}{\partial y} \right) + \mu_3 \left( \frac{\partial u^{(1)}}{\partial y} + \frac{\partial V^{(1)}}{\partial x} \right) = 0, \text{ on } y = H^{(0)^{\pm}}, \quad (4.25)$$

combining these yields a compatibility condition

$$\left( \frac{\partial u^{(1)}}{\partial y} + \frac{\partial V^{(1)}}{\partial x} \right) \left( 1 + \mu_2 \cos^2\theta^{(0)} \sin^2\theta^{(0)} + \mu_3 \right) + \mu_1 \cos\theta^{(0)} \sin\theta^{(0)} + \mu_2 \frac{\partial u^{(0)}}{\partial x} \left( \cos^3\theta^{(0)} \sin\theta^{(0)} - \cos\theta^{(0)} \sin^3\theta^{(0)} \right) = 0. \quad (4.26)$$

We note that in our analysis, $V^{(1)}$ never appears without $u^{(1)}$. We can thus view this compatibility condition as an equation to eliminate both $V^{(1)}$ and $u^{(1)}$.

In order to close the model, we must go to yet higher orders in order to obtain equations for $u^{(0)}, H^{(0)}$. Our approach is similar to the Newtonian case: we integrate the relevant equations over the depth of the sheet and apply the no-stress boundary conditions at $y = H^{(0)^{\pm}}$. In our approach, a number of higher order terms in the boundary conditions will be eliminated by substitution of previously obtained quantities. At next order, equation (4.26) also appears as part of the boundary conditions. Using this equation to cancel out numerous terms greatly simplifies those conditions. Following this process, we may write the $\mathcal{O}(\varepsilon^3)$ $x$-momentum equation as

$$\begin{aligned}
\frac{\partial}{\partial x}\Bigg[-p^{(0)} + 2\frac{\partial u^{(0)}}{\partial x} + \mu_1 \cos^2\theta^{(0)} + \mu_2 \Bigg(\cos^4\theta^{(0)}\frac{\partial u^{(0)}}{\partial x} \\
+ \cos^3\theta^{(0)}\sin\theta^{(0)}\left(\frac{\partial u^{(1)}}{\partial y} + \frac{\partial V^{(1)}}{\partial x}\right) + \cos^2\theta^{(0)}\sin^2\theta^{(0)}\frac{\partial V^{(2)}}{\partial y}\Bigg) \\
+2\mu_3\left(2\cos^2\theta^{(0)}\frac{\partial u^{(0)}}{\partial x} + \cos\theta^{(0)}\sin\theta^{(0)}\left(\frac{\partial u^{(1)}}{\partial y} + \frac{\partial V^{(1)}}{\partial x}\right)\right)\Bigg] - \frac{\partial^2 u^{(0)}}{\partial x^2} \\
= -\frac{\partial}{\partial y}\Bigg[\frac{\partial u^{(2)}}{\partial y} + \frac{\partial V^{(2)}}{\partial x} + \mu_1\left(\theta^{(1)}\cos 2\theta^{(0)}\right) + \mu_2\Bigg(\cos^3\theta^{(0)}\sin\theta^{(0)}\frac{\partial u^{(1)}}{\partial x} \\
+\theta^{(1)}\left(\cos^4\theta^{(0)} - 3\cos^2\theta^{(0)}\sin^2\theta^{(0)}\right)\frac{\partial u^{(0)}}{\partial x} + \cos^2\theta^{(0)}\sin^2\theta^{(0)}\left(\frac{\partial u^{(2)}}{\partial y} + \frac{\partial V^{(2)}}{\partial x}\right) \\
+\frac{1}{2}\theta^{(1)}\sin 4\theta^{(0)}\left(\frac{\partial u^{(1)}}{\partial y} + \frac{\partial V^{(1)}}{\partial x}\right) + \cos\theta^{(0)}\sin^3\theta^{(0)}\frac{\partial V^{(3)}}{\partial y} \\
+\theta^{(1)}\left(3\cos^2\theta^{(0)}\sin^2\theta^{(0)} - \sin^4\theta^{(0)}\right)\frac{\partial V^{(2)}}{\partial y}\Bigg) + \mu_3\left(\frac{\partial u^{(2)}}{\partial y} + \frac{\partial V^{(2)}}{\partial x}\right)\Bigg] + \frac{\partial^2 V^{(2)}}{\partial x \partial y}, \quad (4.27)
\end{aligned}$$

where we have 'added 0' to both sides of the equation so that (4.27) takes a similar form to the boundary condition

$$\begin{aligned}
&\frac{\partial u^{(2)}}{\partial y}+\frac{\partial V^{(2)}}{\partial x}+\mu_1\theta^{(1)}\cos 2\theta^{(0)}+\mu_2\left(\cos^3\theta^{(0)}\sin\theta^{(0)}\frac{\partial u^{(1)}}{\partial x}\right.\\
&\qquad+\theta^{(1)}\left(\cos^4\theta^{(0)}-3\cos^2\theta^{(0)}\sin^2\theta^{(0)}\right)\frac{\partial u^{(0)}}{\partial x}\\
&\qquad+\cos^2\theta^{(0)}\sin^2\theta^{(0)}\left(\frac{\partial u^{(2)}}{\partial y}+\frac{\partial V^{(2)}}{\partial x}\right)+\frac{1}{2}\theta^{(1)}\sin 4\theta^{(0)}\left(\frac{\partial u^{(1)}}{\partial y}+\frac{\partial V^{(1)}}{\partial x}\right)\\
&\qquad\left.+\cos\theta^{(0)}\sin^3\theta^{(0)}\frac{\partial V^{(3)}}{\partial y}+\theta^{(1)}\left(3\cos^2\theta^{(0)}\sin^2\theta^{(0)}-\sin^4\theta^{(0)}\right)\frac{\partial V^{(2)}}{\partial y}\right)\\
&\qquad+\mu_3\left(\frac{\partial V^{(2)}}{\partial x}+\frac{\partial u^{(2)}}{\partial y}\right)\\
&=\left(\frac{\partial H^{(0)}}{\partial x}\pm\frac{1}{2}\frac{\partial h^{(0)}}{\partial x}\right)\left[-p^{(0)}+2\frac{\partial u^{(0)}}{\partial x}+\mu_1\cos^2\theta^{(0)}\right.\\
&+\mu_2\left(\cos^4\theta^{(0)}\frac{\partial u^{(0)}}{\partial x}+\cos^3\theta^{(0)}\sin\theta^{(0)}\left(\frac{\partial u^{(1)}}{\partial y}+\frac{\partial V^{(1)}}{\partial x}\right)+\cos^2\theta^{(0)}\sin^2\theta^{(0)}\frac{\partial V^{(2)}}{\partial y}\right)\\
&\left.2\mu_3\left(2\cos^2\theta^{(0)}\frac{\partial u^{(0)}}{\partial x}+\cos\theta^{(0)}\sin\theta^{(0)}\left(\frac{\partial u^{(1)}}{\partial y}+\frac{\partial V^{(1)}}{\partial x}\right)\right)\right];\ \text{on } y=H^{(0)}\pm\frac{h^{(0)}}{2}. \quad (4.28)
\end{aligned}$$

We note that the remainder terms outside of the derivatives in (4.27) cancel due to $\mathcal{O}(\varepsilon^2)$ continuity equation (4.19). Additionally, a number of terms involving $H^{(1)}$ appear in the computation of (4.28). These terms reduce to zero as a result of lower order results, and are omitted. Integrating equation (4.27) over the depth of the sheet yields

$$\int_{H^{(0)-}}^{H^{(0)+}}\frac{\partial}{\partial x}\left(-p^{(0)}+g_1(x,\tau)\right)\mathrm{d}y=-\left[\frac{\partial u^{(2)}}{\partial y}+\frac{\partial V^{(2)}}{\partial x}+g_2(x,\tau)\right]_{y=H^{(0)-}}^{y=H^{(0)+}}, \quad (4.29)$$

where

$$\begin{aligned}
g_1=&-p^{(0)}+2\frac{\partial u^{(0)}}{\partial x}+\mu_1\cos^2\theta^{(0)}+\mu_2\left(\cos^4\theta^{(0)}\frac{\partial u^{(0)}}{\partial x}\right.\\
&+\cos^3\theta^{(0)}\sin\theta^{(0)}\left(\frac{\partial u^{(1)}}{\partial y}+\frac{\partial V^{(1)}}{\partial x}\right)+\cos^2\theta^{(0)}\sin^2\theta^{(0)}\frac{\partial V^{(2)}}{\partial y}\\
&\left.+2\mu_3\left(2\cos^2\theta^{(0)}\frac{\partial u^{(0)}}{\partial x}+\cos\theta^{(0)}\sin\theta^{(0)}\left(\frac{\partial u^{(1)}}{\partial y}+\frac{\partial V^{(1)}}{\partial x}\right)\right)\right), \quad (4.30)
\end{aligned}$$

$$g_2 = \mu_1\theta^{(1)}\cos 2\theta^{(0)} + \mu_2\left(\cos^3\theta^{(0)}\sin\theta^{(0)}\frac{\partial u^{(1)}}{\partial x}\right.$$
$$+\theta^{(1)}\left(\cos^4\theta^{(0)} - 3\cos^2\theta^{(0)}\sin^2\theta^{(0)}\right)\frac{\partial u^{(0)}}{\partial x}$$
$$+\cos^2\theta^{(0)}\sin^2\theta^{(0)}\left(\frac{\partial u^{(2)}}{\partial y} + \frac{\partial V^{(2)}}{\partial x}\right) + \frac{1}{2}\theta^{(1)}\sin 4\theta^{(0)}\left(\frac{\partial u^{(1)}}{\partial y} + \frac{\partial V^{(1)}}{\partial x}\right)$$
$$\left.+\cos\theta^{(0)}\sin^3\theta^{(0)}\frac{\partial V^{(3)}}{\partial y} + \theta^{(1)}\left(3\cos^2\theta^{(0)}\sin^2\theta^{(0)} - \sin^4\theta^{(0)}\right)\frac{\partial V^{(2)}}{\partial y}\right)$$
$$+\mu_3\left(\frac{\partial V^{(2)}}{\partial x} + \frac{\partial u^{(2)}}{\partial y}\right), \quad (4.31)$$

are functions containing the collected $\mu_1, \mu_2, \mu_3$ terms from (4.27) and are readily obtained by inspection. Application of (4.28) to (4.29) now yields

$$\int_{H^{(0)^-}}^{H^{(0)^+}} \frac{\partial}{\partial x}\left(-p^{(0)} + g_1\right)\mathrm{d}y = \left(\frac{\partial H^{(0)}}{\partial x} - \frac{1}{2}\frac{\partial h^{(0)}}{\partial x}\right)\left(-p^{(0)} + g_1\right)_{y=H^{(0)^-}}$$
$$-\left(\frac{\partial H^{(0)}}{\partial x} + \frac{1}{2}\frac{\partial h^{(0)}}{\partial x}\right)\left(-p^{(0)} + g_1\right)_{y=H^{(0)^+}}. \quad (4.32)$$

Use of the Leibniz rule, (4.19), and substitution of (4.23), we now obtain an equation for $\bar{u}$ (as defined in equation (4.18))

$$\int_{H^{(0)^-}}^{H^{(0)^+}} \left(4\frac{\partial u^{(0)}}{\partial x} + \mu_1\cos 2\theta^{(0)} + \mu_2\left(\cos^2 2\theta^{(0)}\frac{\partial u^{(0)}}{\partial x} + \frac{1}{4}\sin 4\theta^{(0)}\left(\frac{\partial u^{(1)}}{\partial y} + \frac{\partial V^{(1)}}{\partial x}\right)\right)\right.$$
$$\left.+4\mu_3\frac{\partial u^{(0)}}{\partial x}\right)\mathrm{d}y = T(\tau). \quad (4.33)$$

A similar, albeit significantly more involved, process at $\mathcal{O}(\varepsilon^4)$ yields an equation for $H^{(0)}$, the details of which we provide in appendix C.1.

$$\frac{\partial}{\partial x}\int_{H^{(0)^-}}^{H^{(0)^+}}\frac{\partial}{\partial x}\int_{H^{(0)^-}}^{y}\left(4\frac{\partial u^{(0)}}{\partial x} + \mu_1\cos 2\theta^{(0)} + \mu_2\cos^2 2\theta^{(0)}\frac{\partial u^{(0)}}{\partial x}\right.$$
$$\left.+\frac{\mu_2}{4}\sin 4\theta^{(0)}\left(\frac{\partial u^{(1)}}{\partial y} + \frac{\partial V^{(1)}}{\partial x}\right) + 4\mu_3\frac{\partial u^{(0)}}{\partial x}\right)\mathrm{d}s\mathrm{d}y = 0. \quad (4.34)$$

At this point, using equation (4.26) to eliminate the $u^{(1)}$ and $V^{(1)}$ terms, the equations (4.33) and (4.34) can be written in the familiar form

$$\frac{\partial}{\partial x}\int_{H^-}^{H^+}\frac{\mu_1\cos 2\theta+(4+4\mu_3+\mu_2)\frac{\partial u}{\partial x}}{4+4\mu_3+\mu_2\sin^2 2\theta}\mathrm{d}y=0, \tag{4.35}$$

$$\frac{\partial}{\partial x}\int_{H^-}^{H^+}\frac{\partial}{\partial x}\int_{H^-}^{y}\frac{\mu_1\cos 2\theta+(4+4\mu_3+\mu_2)\frac{\partial u}{\partial x}}{4+4\mu_3+\mu_2\sin^2 2\theta}\mathrm{d}s\mathrm{d}y=0. \tag{4.36}$$

Application of the Leibniz rule to (4.36) and use of (4.35) yields

$$\frac{\partial^2}{\partial x^2}\int_{H^-}^{H^+}\int_{H^-}^{y}\frac{\mu_1\cos 2\theta+(4+4\mu_3+\mu_2)\frac{\partial u}{\partial x}}{4+4\mu_3+\mu_2\sin^2 2\theta}\mathrm{d}y\mathrm{d}y = \left(\frac{\partial^2 H}{\partial x^2}+\frac{1}{2}\frac{\partial^2 h}{\partial x^2}\right)\int_{H^-}^{H^+}\frac{\mu_1\cos 2\theta+(4+4\mu_3+\mu_2)\frac{\partial u}{\partial x}}{4+4\mu_3+\mu_2\sin^2 2\theta}\mathrm{d}y. \tag{4.37}$$

We note that these equations are of the same form as (3.14), (3.15), with the difference being that $u^{(0)}$ now possesses $y$-dependence.

### 4.2.1 Summary

- At $O(1)$ we obtained equations for $V^{(0)}$ and $\theta^{(0)}$ that were the same for a Newtonian fluid, and demonstrate that on this timescale the sheet is not thinning to leading order.
- Next, at $\mathcal{O}(\varepsilon)$ we obtain an equation for $u^{(0)}$ in terms of $H^{(0)}$ and introduce $\bar{u}$.
- At $\mathcal{O}(\varepsilon^2)$ we obtain $V^{(2)}$ in terms of $u^{(0)}$ from continuity, and leading order pressure, $p^{(0)}$, by integrating the $y$-momentum equation. From the $x$-momentum equation we obtain an equation for $u_y^{(1)}+V_x^{(1)}$ in terms of $u^{(0)}$. Since $u^{(1)}$ and $V^{(1)}$ appear together everywhere, this equation allows us to eliminate all $u^{(1)}$ and $V^{(1)}$ terms from the equation for pressure, and the integral equations we obtain at higher orders.
- At $\mathcal{O}(\varepsilon^3)$ we obtain an equation for $\bar{u}$ by integrating the $x$-momentum equation

at this order with its associated boundary condition, and use $\mathcal{O}(\varepsilon^2)$ continuity to collect the extra terms.

- In a similar way, at $\mathcal{O}(\varepsilon^4)$ we integrate the $y$-momentum equation across the sheet to obtain an equation for the centre-line $H^{(0)}$.

We now have derived a closed system of equations for the variables $\theta^{(0)}, u^{(0)}, \bar{u}, H^{(0)}$, namely equations (4.14),(4.18),(4.35),(4.37) respectively. Additionally, $v^{(0)}, p^{(0)}$ may be computed via (4.13) and (4.23) respectively, and there is no thinning on this timescale, hence we simply specify $h^{(0)}$. Our system of equations may be reduced to three equations in three variables by substitution of the result for $u^{(0)}$ into the integral equations, which we discuss in the next subsection. Finally, for completeness, we also state the boundary conditions here:

$$\bar{u}(0,\tau) = 0, \quad \bar{u}(1,\tau) = 1, \tag{4.38}$$

$$H(0,\tau) = H(1,\tau) = 0, \tag{4.39}$$

$$\frac{\partial H}{\partial x}(0,\tau) = \frac{\partial H}{\partial x}(1,\tau) = 0, \tag{4.40}$$

with initial conditions prescribed for $\theta, h$. The new boundary conditions given for $\bar{u}$ are equivalent to those given for $u^{(0)}$ in (4.8).

### 4.2.2 Further reduction of model

In this subsection, we go yet further in reducing the number of variables and equations in our model, and give some details of our numerical strategy. In order to numerically solve the coupled pair of integro-differential equations, we continue by substituting the

expression for $u^{(0)}$, equation (4.18) into (4.35), (4.37).

$$\frac{\partial}{\partial x}\int_{-\frac{1}{2}}^{\frac{1}{2}}\frac{\mu_1\cos 2\theta+(4+4\mu_3+\mu_2)\frac{\partial\bar{u}}{\partial x}}{4+4\mu_3+\mu_2\sin^2 2\theta}h\mathrm{d}\tilde{y}+\frac{\partial}{\partial x}\left(\frac{\partial H}{\partial x}\frac{\partial^2 H}{\partial x\partial\tau}\int_{-\frac{1}{2}}^{\frac{1}{2}}\frac{(4+4\mu_3+\mu_2)}{4+4\mu_3+\mu_2\sin^2 2\theta}h\mathrm{d}\tilde{y}\right.$$
$$\left.-\frac{\partial^3 H}{\partial x^2\partial\tau}\int_{-\frac{1}{2}}^{\frac{1}{2}}\frac{(4+4\mu_3+\mu_2)\,\tilde{y}}{4+4\mu_3+\mu_2\sin^2 2\theta}h^2\mathrm{d}\tilde{y}\right)=0, \quad (4.41)$$

where we have used the the substitution $y = H + h\tilde{y}$ to simplify the limits of the integrals. Similarly, (4.37) gives

$$\frac{\partial^2}{\partial x^2}\left(\int_{-\frac{1}{2}}^{\frac{1}{2}}\int_{-\frac{1}{2}}^{\tilde{y}}\frac{\mu_1\cos 2\theta+(4+4\mu_3+\mu_2)\frac{\partial\bar{u}}{\partial x}}{4+4\mu_3+\mu_2\sin^2 2\theta}h^2\mathrm{d}\tilde{y}'\mathrm{d}\tilde{y}\right.$$
$$+\frac{\partial H}{\partial x}\frac{\partial^2 H}{\partial x\partial\tau}\int_{-\frac{1}{2}}^{\frac{1}{2}}\int_{-\frac{1}{2}}^{\tilde{y}}\frac{4+4\mu_3+\mu_2}{4+\mu_3+\mu_2\sin^2 2\theta}h^2\mathrm{d}\tilde{y}'\mathrm{d}\tilde{y}$$
$$\left.-\frac{\partial^3 H}{\partial x^2\partial\tau}\int_{-\frac{1}{2}}^{\frac{1}{2}}\int_{-\frac{1}{2}}^{\tilde{y}}\frac{(4+4\mu_3+\mu_2)\tilde{y}'}{4+4\mu_3+\mu_2\sin^2 2\theta}h^3\mathrm{d}\tilde{y}'\mathrm{d}\tilde{y}\right)$$
$$=\left(\frac{\partial^2 H}{\partial x^2}+\frac{1}{2}\frac{\partial^2 h}{\partial x^2}\right)\left(\int_{-\frac{1}{2}}^{\frac{1}{2}}\frac{\mu_1\cos 2\theta+(4+4\mu_3+\mu_2)\frac{\partial\bar{u}}{\partial x}}{4+4\mu_3+\mu_2\sin^2 2\theta}h\mathrm{d}\tilde{y}\right.$$
$$+\frac{\partial H}{\partial x}\frac{\partial^2 H}{\partial x\partial\tau}\int_{-\frac{1}{2}}^{\frac{1}{2}}\frac{4+4\mu_3+\mu_2}{4+4\mu_2+\mu_2\sin^2 2\theta}h\mathrm{d}\tilde{y}$$
$$\left.-\frac{\partial^3 H}{\partial x^2\partial\tau}\int_{-\frac{1}{2}}^{\frac{1}{2}}\frac{(4+4\mu_3+\mu_2)\,\tilde{y}}{4+4\mu_3+\mu_2\sin^2 2\theta}h^2\mathrm{d}\tilde{y}\right), \quad (4.42)$$

Where we have simplified the limits of the double integrals by first using the transformation $y' = H + h\tilde{y}'$ to transmute the limits of the inner integral, followed by using $y = H + h\tilde{y}$ on the outer integral.

Equations (4.41), (4.42) appear significantly more complex than (4.35), (4.36), however there are several benefits to this form of the equations. Firstly, substituting (4.18) into our

integral equations has reduced the model to three equations in three variables. We now need to solve for $\theta^{(0)}, \bar{u}, H^{(0)}$ using equations (4.14),(4.41),(4.42) respectively. Moreover, as we will choose an upwinding scheme to discretise (4.14), and $\dfrac{\partial \bar{u}}{\partial x}$ depends on only $x, \tau$ and can be removed from the integral, the integrals are pre-computable at each time step, which significantly eases the numerical solution.

The strategy is as follows: given an initial condition for $\theta, H$, we simultaneously solve for $\bar{u}$ at the current time step, and $H$ at the next time step using a FTCS finite difference discretisation. Then we use equation (4.14) to update $\theta$ to the next time step using an upwinding method. We repeat this until we reach the desired time. We give the discretisations of equations (4.14),(4.41),(4.42) and details of the construction of the resulting linear system in appendix C.2.

## 4.3 Results

In the previous chapter, we established that a nonzero centre-line can exist on the $\dfrac{L_0}{U}$ timescale. In order to capture the full behaviour of the centre-line, we turned our attention to the $\varepsilon^2 \dfrac{L_0}{U}$ timescale. In Figure 4.1a, we give the evolution of the centre-line over $\tau$, for the initial conditions of $\mu_1 = \mu_3 = 0, \mu_2 = 5$, $L(0) = 1$, $\theta(x, y, 0) = \sin(4\pi xy) - 0.1$, $H(x, 0) = 0$, up to $\tau = 200000$, and then compare the values of $H(x, \tau = 200000)$ with $H(x, t = 0)$. Note that there is a more pronounced trough around $x = 0.5$ than in Figure 3.7. This is due to some evolution in $\theta$ throughout the short timescale by equation (4.14), which changes the initial condition of $\theta$ on the $\dfrac{L_0}{U}$ timescale.

In Figure 4.1b, we plot the position of the centre-line at $\tau = 200000$, together with the initial $H^{(0)}$ produced by solving the Green and Friedman model ($t = 0$). We see that the long time behaviour of the short timescale model closely matches the result produced by the Green and Friedman model, which provides validation for the numerical techniques employed in both chapters 3 and 4. We also, in Figure 4.1c, give the maximum of the absolute difference across the sheet between the initial centre-line given by solving

the Green and Friedman model, and the centre-line given by solving the short timescale problem. We note that the initial delay in the change in absolute difference is caused by the centre-line initially rising from flat to assume a similar shape to the final centre-line, before decaying. We show this behaviour in Figure 4.1c and Figure 4.1d. The formation of the peaks and troughs clear in Figure4.1a at $\tau = 100$ can be observed in Figure 4.1b at $\tau = 25$, after the centre-line has risen from the initial condition of $H = 0$.

For a Newtonian fluid, Howell was able to obtain an analytical expression for the decay of the centre-line of an initially curved sheet undergoing tension by use of eigenfunction expansions [49], assuming the same boundary conditions we use in this chapter, $H(0,\tau) = H(1,\tau) = \dfrac{\partial H}{\partial x}(0,\tau) = \dfrac{\partial H}{\partial x}(1,\tau) = 0$. It is found that the centre-line decays exponentially to $H = 0$. The behaviour for a transversely isotropic fluid is more complex. The results plotted in Figure 4.1 began with the initial condition $H(x, \tau = 0) = 0$, and we immediately see that the convergence to the Green and Friedman centre-line is not exponential for all time.

### 4.3.1 Effect of key parameters upon convergence

In this subsection we discuss the effect of increasing $\mu_2, \mu_3$ upon the convergence of the short timescale centre-line to the result from the Green and Friedman model. First we note that if $\mu_2 = 0$, $\mu_3$ has no effect upon convergence. In Figure 4.2 we give a plot of the decay of the maximum value of $H(x,\tau)$ for the initial conditions of $H(x,0) = \frac{1}{20}e^{-\frac{(x-0.5)^2}{0.01}}, \theta(x,y,0) = \sin(4\pi xy), h(x,0) = 1, L = 1$. There is no difference in the decay of the centre-line to flat between the Newtonian case and $\mu_3 = 10$ and by equation (4.14), there is also no difference in the rotation of the fibres.

Now choosing $\mu_2 > 0$, in Figure 4.3 we plot the maximum absolute difference across the sheet between the centre-line on the short timescale and the result obtained by solving equation (3.31) for varied values of $\mu_2, \mu_3$ with the conditions $h(x,0) = 1, \theta(x,y,0) = \sin(4\pi xy) - 0.1, \mu_1 = 0, \mu_2 = 5, L(0) = 1$. First, in Figure 4.3a, we fix $\mu_3 = 0$ and vary $\mu_2$ (note the case of $\mu_2 = 5$ corresponds to the example given above). Similarly to chapter 3,

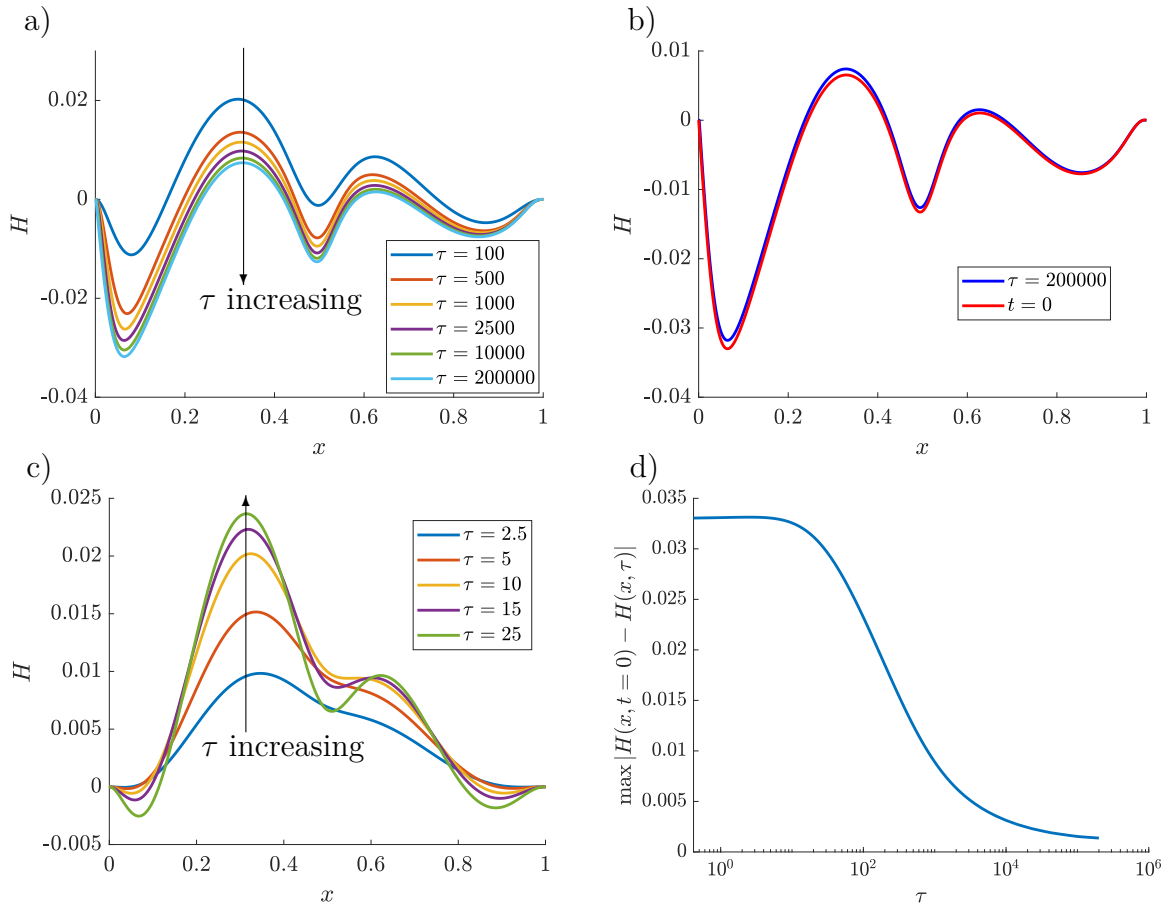


Figure 4.1: Behaviour of the centre-line a) up to $\tau = 200000$ (short timescale), where $\tau = 0$ is omitted as $H(x, 0) = 0$, and b) comparison of the centre-line of the fluid plotted in the physical variables at $\tau = 200000$ (short timescale) and $t = 0$ (Green and Friedman). In c) we give the behaviour of the centre-line from $\tau = 0$ to $\tau = 100$, and in d) we plot the maximum of the absolute difference between the evolving centre-line on the short timescale and the Green and Friedman result. The conditions for all of the above are $H(x, 0) = 0, h(x, 0) = 1, \theta(x, y, 0) = \sin(4\pi xy) - 0.1, \mu_1 = \mu_3 = 0, \mu_2 = 5,\ L(0) = 1$.

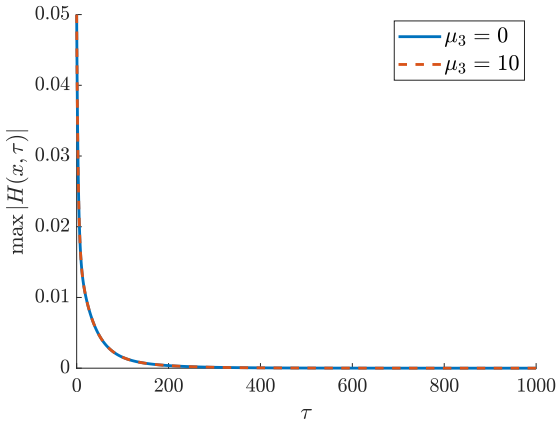


Figure 4.2: The decay of the maximum value of $H(x, \tau)$ for the conditions $H(x, 0) = \frac{1}{20} e^{-\frac{(x-0.5)^2}{0.01}}, \mu_1 = \mu_2 = 0, h(x, 0) = 1, L = 1$.

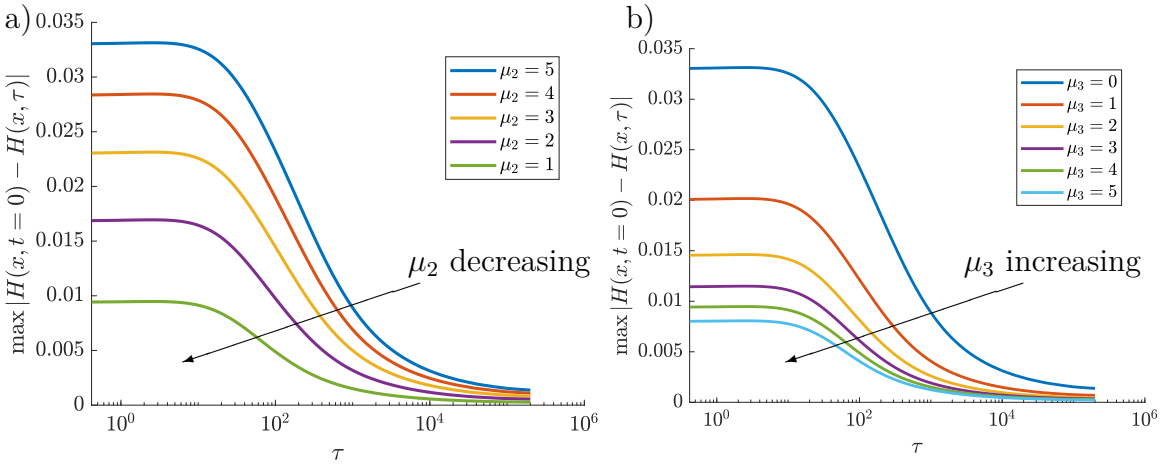


Figure 4.3: Maximum absolute difference across the sheet between the centre-line on the short timescale and the result obtained by solving equation (3.31) for a) $\mu_3 = 0$, $\mu_2 = 1, 2, 3, 4, 5$ and b) $\mu_2 = 5$, $\mu_3 = 1, 2, 3, 4, 5$, with the conditions $H(x, 0) = 0, h(x, 0) = 1, \theta(x, y, 0) = \sin(4\pi xy) - 0.1, \mu_1 = 0, L(0) = 1$.

increasing $\mu_2$ gives rise to stronger non-Newtonian effects within the sheet. As $\mu_2$ increases, the maximum error in Figure 4.3a also increases - this corresponds to the deepening of the trough around $x = 0.5$ seen in Figure 4.1a. In Figure 4.3b, we fix $\mu_2 = 5$ and vary $\mu_3$ (as before, the case of $\mu_3 = 0$ corresponds to the example given above). Once again, we see that the effect of increasing $\mu_3$ is to moderate the effects of $\mu_2$ and force the sheet to behave in a 'more Newtonian' manner.

## 4.4 Discussion

In this chapter, we have developed a short timescale analysis for the extensional flow of an inertia-less viscous transversely isotropic sheet. Combined with the model from chapter 3, we have a complete description of the movement of the centre-line. To summarise, a sheet of $\mathcal{O}(\varepsilon L_0)$ thickness that is 'nearly flat' (i.e the displacement of the centre-line is at most $\mathcal{O}(\varepsilon^2 L_0)$) is put under a tension by moving its ends at a prescribed speed, will begin to straighten on the timescale $\mathcal{O}(\varepsilon^2 \frac{L_0}{U})$, without stretching, with the displacement of the centre-line being given by (4.42), which must be simultaneously solved with (4.41). Unlike a Newtonian fluid [49, 16], the straightening of the sheet does not complete on this

timescale, and further straightening of the sheet occurs on the $\mathcal{O}(\frac{L_0}{U})$ timescale, where the sheet is now stretching and the motion of the fluid is given by the equations (3.28)-(3.31).

We also considered the effects of varying the anisotropic extensional and shear viscosities. Similarly to the $\mathcal{O}(\frac{L_0}{U})$ timescale, increasing the anisotropic extensional viscosity, $\mu_2$, gives rise to greater non-Newtonian effects. The convergence of the centre-line to the result from the Green and Friedman model takes longer, and there is a greater degree of fibre rotation, whilst increasing the anisotropic shear viscosity, $\mu_3$, moderates these effects. Future work could involve increasing the range of values examined for $\mu_2$. In our simulations, we found that increasing $\mu_2$ significantly increased $\frac{\partial H}{\partial \tau}$, which resulted in the requirement to choose an extremely small step size in order not to violate the Courant–Friedrichs–Lewy condition when solving (4.14). A remedy for this could include using an adaptive step size.

CHAPTER 5

# THE EXTENSIONAL FLOW OF AN AXISYMMETRIC TRANSVERSELY ISOTROPIC THREAD

## 5.1 Introduction

We consider the extensional flow of a thin thread of an incompressible, transversely isotropic, viscous fluid. We use the same asymptotic and numerical techniques as discussed in previous chapters.

A biological motivation for studying this problem is that it provides a simplified representation of the 'spinnbarkeit' or 'spinnability' test, which is applied to cervical mucus as a means of assessing fertility [34]. The test entails taking a sample of mucus and stretching it. Around ovulation, the mucus has a lower pH, a higher concentration of water (which has the effect of lowering the viscosity of the mucus), and the fibrous reinforcement takes a more parallel alignment that allows sperm to migrate. At this point the mucus can be stretched the furthest, i.e. the fluid exhibits maximum spinnbarkeit. Conversely, during the most infertile parts of the menstrual cycle, the mucus does not stretch and simply breaks [64, 106]. Understanding the dynamics of stretching a transversely isotropic thread can provide some basic insights into how factors such as fibre concentration and alignment influence spinnbarkeit. This extends the work of chapter 3 by considering a geometry that allows us to include a second angle in the description of the direction of

the fibres, which will allow us to investigate the importance of the fibre alignment in the cross-section of the fluid thread. Comparison between the sheet and the thread, which both reduce to the Trouton model in a Newtonian context, may provide insight into the mechanical behaviour of anisotropic fluids.

We derive a system of governing equations for a transversely isotropic viscous fluid thread under the assumptions that the thread is axisymmetric, and is free of both inertia and body forces in section 5.2. We exploit the slender geometry of the thread using a similar thin film approach as previous chapters, we reduce the governing equations to a leading-order model (section 5.3) which is then solved numerically alongside a small-angle system for the purposes of validation (section 5.5), and results are discussed in section 5.6.

## 5.2 Governing equations

We consider an axisymmetric, inertialess, viscous thread. Here, we allow the azimuthal velocity to be non-zero in order to account for azimuthal velocities induced by the fibres, but maintain axisymmetry. We use the cylindrical coordinate system $(r^*, \theta, x^*)$ and the flow field is given by $\boldsymbol{u}^* = (v^*, w^*, u^*)$. The thread is bounded by a curve $r^* = R^*(x^*, t^*)$. Throughout, asterisks are used to denote dimensional quantities. A schematic of the problem is given in Figure 5.1, where $\hat{\boldsymbol{n}}$ is the outward pointing normal on the boundary of the thread and $L^*(t^*)$ is the half length of the thread, which we will later prescribe in dimensionless form. The ends of the sheet, at $x^* = \pm L^*$, are pulled apart at speed $\dot{L}^*$.

The mass and momentum balances are,

$$\nabla^* \cdot \boldsymbol{u}^* = 0, \tag{5.1}$$

$$\nabla^* \cdot \boldsymbol{\sigma}^* = 0. \tag{5.2}$$

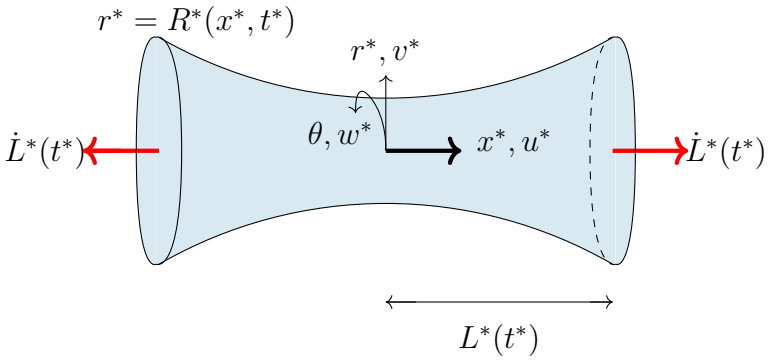


Figure 5.1: Schematic of the extensional flow of a thread. The fluid is fixed between two plates at $x^* = \pm L$, by a no slip boundary condition. The plates are then pulled apart at a prescribed speed $\dot{L}^*$. Here dot represents $\mathrm{d}/\mathrm{d}t$. The free boundary of the thread, given by a no-stress boundary condition, is located at $R^*(x^*, t^*)$.

We use the familiar constitutive law for a transversely isotropic fluid as given in (1.9).

These equations are solved subject to a kinematic boundary condition for a free surface

$$\frac{\partial R^*}{\partial t^*} + u^* \frac{\partial R^*}{\partial x^*} = v^*; \text{ on } r^* = R^*(x^*, t^*), \tag{5.3}$$

and a no-stress condition on the free boundary

$$\boldsymbol{\sigma}^* \cdot \hat{\boldsymbol{n}} = \mathbf{0}; \text{ on } r^* = R^*(x^*, t^*). \tag{5.4}$$

In component form, the mass and momentum conservation equations yield

$$\frac{\partial u^*}{\partial x^*} + \frac{\partial v^*}{\partial r^*} + \frac{v^*}{r^*} = 0, \tag{5.5}$$

$$\frac{\partial \sigma^*_{rr}}{\partial r^*} + \frac{\partial \sigma^*_{rx}}{\partial x^*} + \frac{1}{r^*}(\sigma^*_{rr} - \sigma^*_{\theta\theta}) = 0, \tag{5.6}$$

$$\frac{\partial \sigma^*_{r\theta}}{\partial r^*} + \frac{\partial \sigma^*_{\theta x}}{\partial x^*} + \frac{2\sigma^*_{r\theta}}{r^*} = 0, \tag{5.7}$$

$$\frac{\partial \sigma^*_{rx}}{\partial r^*} + \frac{\partial \sigma^*_{xx}}{\partial x^*} + \frac{\sigma^*_{rx}}{r^*} = 0, \tag{5.8}$$

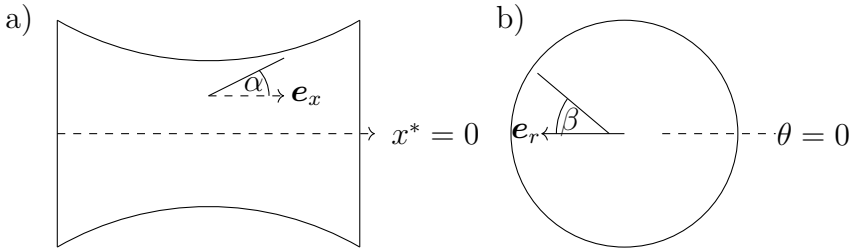


Figure 5.2: Characterisation of a fibre in terms of the angles $\alpha, \beta$. a) shows the cross-section along the length of the thread, whilst b) shows the cross section of the fibre taken at an arbitrary $x^*$.

whilst the kinematic condition and no-stress boundary conditions (5.3) and (5.4) give:

$$\frac{\partial R^*}{\partial t^*} + u^* \frac{\partial R^*}{\partial x^*} = v^*; \text{ on } r^* = R^*(x^*, t^*), \tag{5.9}$$

$$\frac{\partial R^*}{\partial x^*} \sigma^*_{rx} = \sigma^*_{rr}; \text{ on } r^* = R^*(x^*, t^*), \tag{5.10}$$

$$\frac{\partial R^*}{\partial x^*} \sigma^*_{\theta x} = \sigma^*_{\theta r}; \text{ on } r^* = R^*(x^*, t^*), \tag{5.11}$$

$$\frac{\partial R^*}{\partial x^*} \sigma^*_{xx} = \sigma^*_{xr}; \text{ on } r^* = R^*(x^*, t^*). \tag{5.12}$$

In order to describe the evolution of the fibre alignment, we introduce a unit vector $\boldsymbol{a}$ as defined in chapter 1. For a cylindrical fluid thread, we use

$$\boldsymbol{a} = (a_r, a_\theta, a_x) = (\sin\alpha\cos\beta, \sin\alpha\sin\beta, \cos\alpha),$$

where $\alpha$ and $\beta$ are the angles the fibre makes with the unit vectors $\boldsymbol{e}^*_x$ and $\boldsymbol{e}^*_r$ respectively, a visualisation is given in Figure 5.2. The three components of the fibre direction equation (1.15) in the $r^*, \theta, x^*$ directions are,

$$\cos\alpha\cos\beta\frac{D\alpha}{Dt^*} - \sin\alpha\sin\beta\frac{D\beta}{Dt^*} + \sin\alpha\cos\beta\zeta^* = \sin\alpha\cos\beta\frac{\partial v^*}{\partial r^*} + \cos\alpha\frac{\partial v^*}{\partial x^*}, \tag{5.13}$$

$$\begin{aligned}\cos\alpha\sin\beta\frac{D\alpha}{Dt^*} + \sin\alpha\cos\beta\frac{D\beta}{Dt^*} + \sin\alpha\sin\beta\zeta^* &= \sin\alpha\cos\beta\left(\frac{\partial w^*}{\partial r^*} - \frac{w^*}{r^*}\right) \\ &\quad + \cos\alpha\frac{\partial w^*}{\partial x^*} + \sin\alpha\sin\beta\frac{v^*}{r^*},\end{aligned} \tag{5.14}$$

$$-\sin\alpha\frac{D\alpha}{Dt^*} + \cos\alpha\zeta^* = \sin\alpha\cos\beta\frac{\partial u^*}{\partial r^*} + \cos\alpha\frac{\partial u^*}{\partial x^*}, \tag{5.15}$$

where $\dfrac{D}{Dt^*} = \dfrac{\partial}{\partial t^*} + u^* \dfrac{\partial}{\partial x^*} + v^* \dfrac{\partial}{\partial r^*}$ is the convective derivative. As we have three equations in two variables we must perform a consistency check upon the equations. To do this we first construct an evolution equation for $\beta$ by combining equations (5.13) and (5.14), yielding

$$\frac{D\beta}{Dt^*} = \cos^2\beta\left(\frac{\partial w^*}{\partial r^*} - \frac{w^*}{r^*}\right) + \sin\beta\cos\beta\left(\frac{v^*}{r^*} - \frac{\partial v^*}{\partial r^*}\right) + \cot\alpha\left(\cos\beta\frac{\partial w^*}{\partial x^*} - \sin\beta\frac{\partial v^*}{\partial x^*}\right), \quad (5.16)$$

Similarly, one can eliminate the derivatives of $\beta$ by again combining (5.13),(5.14), which yields a more complicated equation for $\alpha$:

$$\cos\alpha\frac{D\alpha}{Dt^*} + \sin\alpha\zeta^* = \sin\alpha\left(\cos^2\beta\frac{\partial v^*}{\partial r^*} + \sin^2\beta\frac{v^*}{r^*}\right) + \sin\alpha\sin\beta\cos\beta\left(\frac{\partial w^*}{\partial r^*} - \frac{w^*}{r^*}\right) + \cos\alpha\left(\cos\beta\frac{\partial v^*}{\partial x^*} + \sin\beta\frac{\partial w^*}{\partial x^*}\right). \quad (5.17)$$

Finally, substitution of equation (5.15) allows us to calculate the fractional rate of extension of the fibre, $\zeta^*$:

$$\zeta^* = \sin^2\alpha\left(\cos^2\beta\frac{\partial v^*}{\partial r^*} + \sin^2\beta\frac{v^*}{r^*}\right) + \sin^2\alpha\sin\beta\cos\beta\left(\frac{\partial w^*}{\partial r^*} - \frac{w^*}{r^*}\right) + \sin\alpha\cos\alpha\left(\cos\beta\frac{\partial v^*}{\partial x^*} + \sin\beta\frac{\partial w^*}{\partial x^*}\right) + \sin\alpha\cos\alpha\cos\beta\frac{\partial u^*}{\partial r^*} + \cos^2\alpha\frac{\partial u^*}{\partial x^*}. \quad (5.18)$$

Since we can also calculate $\zeta^*$ directly via (1.14), which provides the same result, this provides a check on the consistency of the equations. An alternative combination of (5.15) and (5.17) yields

$$\frac{D\alpha}{Dt^*} = \sin\alpha\cos\alpha\left(\cos^2\beta\frac{\partial v^*}{\partial r^*} + \sin^2\alpha\frac{v^*}{r^*}\right) + \sin\alpha\sin\beta\cos\alpha\cos\beta\left(\frac{\partial w^*}{\partial r^*} - \frac{w^*}{r^*}\right) + \cos^2\alpha\left(\cos\beta\frac{\partial v^*}{\partial x} + \sin\beta\frac{\partial w^*}{\partial x}\right) - \sin\alpha\left(\sin\alpha\cos\beta\frac{\partial u^*}{\partial r} + \cos\alpha\frac{\partial u^*}{\partial x}\right). \quad (5.19)$$

Finally, we require boundary conditions for $\alpha$ and $\beta$. We choose

$$\frac{\partial \alpha}{\partial x^*} = 0; \text{ on } x^* = 0, \tag{5.20}$$

$$\frac{\partial \beta}{\partial x^*} = 0; \text{ on } x^* = 0, \tag{5.21}$$

to ensure symmetry about the mid-point of the thread. Together with equations (5.5)-(5.8), their associated boundary conditions (5.9)-(5.12), and the constitutive law (1.9), equations (5.19) and (5.16) with boundary conditions for $\alpha$ and $\beta$ given by (5.20) and (5.21) provide a complete set of governing equations and boundary conditions. We choose to use (5.19) and (5.16) as the equations for $\alpha$ and $\beta$ as these expressions later yield the leading-order equations most amenable to the numerical methods we later employ. We will also need initial conditions for $\alpha, \beta$ and $R$ in addition to a prescribed pulling speed $\dot{L}$. We shall prescribe these later in dimensionless form.

### 5.2.1 Nondimensionalisation

We nondimensionalise with the following scalings

$$\begin{aligned}
&(u^*, v^*, w^*) = U^*(u, \varepsilon v, \varepsilon w), (x^*, r^*) = L_0^*(x, \varepsilon r), R^* = \varepsilon L_0^* R, t^* = \frac{L_0^*}{U^*} t, \\
&(\sigma_{xx}^*, \sigma_{\theta\theta}^*, \sigma_{rr}^*) = \frac{\mu^* U^*}{L_0^*}(\sigma_{xx}, \sigma_{\theta\theta}, \sigma_{rr}), (\sigma_{xr}^*, \sigma_{x\theta}^*, \sigma_{\theta r}^*) = \frac{\mu^* U^*}{\varepsilon L_0^*}(\sigma_{xr}, \sigma_{x\theta}, \sigma_{\theta r}), \\
&\zeta^* = \frac{U^*}{\varepsilon L_0^*}\zeta, p^* = \frac{\mu^* U^*}{L_0^*} p,
\end{aligned}$$

where $\varepsilon = \dfrac{R_0^*}{L_0^*}$ is the inverse aspect ratio of the thread, $L_0^*$ is the initial half length of the fibre, and $R_0^*$ is the maximum value of $R^*(x^*, 0)$ over the thread. $U^* = \dot{L}^*$ is the characteristic velocity for the problem. We make a particular choice of the length of the fibre, which we define in dimensionless form as $L(t) = 1 + t$. This choice is equivalent to prescribing $\dot{L} = 1$. In general, one may choose to specify a tension upon the fibre instead of prescribing the length. The continuity equation (5.5) and $r$-momentum balance

(5.6) remain unchanged by these transformations, whilst rescaling the $\theta$ and $x$-momentum balances respectively become

$$\varepsilon\frac{\partial\sigma_{x\theta}}{\partial x}+\frac{\partial\sigma_{r\theta}}{\partial r}+\frac{2}{r}\sigma_{r\theta}=0, \tag{5.22}$$

$$\varepsilon^2\frac{\partial\sigma_{xx}}{\partial x}+\frac{\partial\sigma_{rx}}{\partial r}+\frac{\sigma_{rx}}{r}=0. \tag{5.23}$$

Similarly, the kinematic boundary condition (5.9) and $r$-direction no-stress condition (5.10) remain unchanged, with the other no-stress boundary conditions (5.11) and (5.12) yielding

$$\varepsilon\frac{\partial R}{\partial x}\sigma_{\theta x}=\sigma_{\theta r};\ \text{on } r=R(x,t), \tag{5.24}$$

$$\varepsilon^2\frac{\partial R}{\partial x}\sigma_{xx}=\sigma_{xr};\ \text{on } r=R(x,t). \tag{5.25}$$

The equation governing the evolution of the fibre angle $\alpha$, equation (5.19), supplies

$$\begin{aligned}\varepsilon\frac{D\alpha}{Dt}=&\,\varepsilon\sin\alpha\cos\alpha\left(\cos^2\beta\frac{\partial v}{\partial r}+\sin^2\alpha\frac{v}{r}\right)+\varepsilon\sin\alpha\sin\beta\cos\alpha\cos\beta\left(\frac{\partial w}{\partial r}-\frac{w}{r}\right)\\&+\varepsilon^2\cos^2\alpha\left(\cos\beta\frac{\partial v}{\partial x}+\sin\beta\frac{\partial w}{\partial x}\right)-\sin\alpha\left(\sin\alpha\cos\beta\frac{\partial u}{\partial r}+\varepsilon\cos\alpha\frac{\partial u}{\partial x}\right),\end{aligned} \tag{5.26}$$

with the equation governing $\beta$, (5.16), giving

$$\begin{aligned}\sin\alpha\frac{D\beta}{Dt}=&\,\sin^2\alpha\cos\beta\left(\frac{\partial w}{\partial r}-\frac{w}{r}\right)\\&+\sin\alpha\sin\beta\cos\beta\left(\frac{v}{r}-\frac{\partial v}{\partial r}\right)-\varepsilon\cos\alpha\sin\beta\frac{\partial v}{\partial x}+\varepsilon\cos\alpha\cos\beta\frac{\partial w}{\partial x},\end{aligned} \tag{5.27}$$

with the dimensionless fractional rate of extension of the fibre in the fibre direction, $\zeta$, given by

$$\begin{aligned}\zeta=&\,\varepsilon\sin^2\alpha\left(\cos^2\beta\frac{\partial v}{\partial r}+\sin^2\beta\frac{v}{r}\right)+\varepsilon\sin^2\alpha\sin\beta\cos\beta\left(\frac{\partial w}{\partial r}-\frac{w}{r}\right)+\varepsilon\cos^2\alpha\frac{\partial u}{\partial x}\\&+\varepsilon^2\sin\alpha\cos\alpha\left(\cos\beta\frac{\partial v}{\partial x}+\sin\beta\frac{\partial w}{\partial x}\right)+\sin\alpha\cos\alpha\cos\beta\frac{\partial u}{\partial r}.\end{aligned} \tag{5.28}$$

## 5.3 Thin film approximation

We exploit the slender geometry of the thread to simplify the governing equations in precisely the same way as in previous chapters. We expand the dependent variables as power series of $\varepsilon$,

$$u \sim u^{(0)} + \varepsilon u^{(1)} + \varepsilon^2 u^{(2)} + ..., \text{ etc},$$

with similar expressions for $v, p, R, \alpha, \beta$ and the components of the stress tensor. Unlike the Newtonian problem studied by Howell [49], odd powers of $\varepsilon$ appear in the governing equations and so must be included in the asymptotic expansions.

### 5.3.1 Leading Order

At leading order, the mass and momentum balances yield

$$\frac{v^{(0)}}{r} + \frac{\partial v^{(0)}}{\partial r} + \frac{\partial u^{(0)}}{\partial x} = 0, \tag{5.29}$$

$$\frac{\partial \sigma_{rr}^{(0)}}{\partial r} + \frac{\partial \sigma_{rx}^{(0)}}{\partial x} + \frac{1}{r}(\sigma_{rr}^{(0)} - \sigma_{\theta\theta}^{(0)}) = 0, \tag{5.30}$$

$$\frac{\partial \sigma_{r\theta}^{(0)}}{\partial r} + \frac{2}{r}\sigma_{r\theta}^{(0)} = 0, \tag{5.31}$$

$$\frac{\partial \sigma_{rx}^{(0)}}{\partial r} + \frac{\sigma_{rx}^{(0)}}{r} = 0, \tag{5.32}$$

with the kinematic and no-stress boundary conditions

$$\frac{\partial R^{(0)}}{\partial t} + u^{(0)}\frac{\partial R^{(0)}}{\partial x} = v^{(0)}; \text{ on } r = R^{(0)}(x,t), \tag{5.33}$$

$$\sigma_{rr}^{(0)} = \frac{\partial R^{(0)}}{\partial x}\sigma_{rx}^{(0)}; \text{ on } r = R^{(0)}, \tag{5.34}$$

$$\sigma_{\theta r}^{(0)} = 0; \text{ on } r = R^{(0)}, \tag{5.35}$$

$$\sigma_{xr}^{(0)} = 0; \text{ on } r = R^{(0)}. \tag{5.36}$$

Considering the $x$-momentum equation (5.32) with the associated boundary condition (5.36) yields

$$\sigma_{rx}^{(0)} = \frac{\partial u^{(0)}}{\partial r}\left(1 + \mu_2 \cos^2\alpha^{(0)} \sin^2\alpha^{(0)} \cos^2\beta^{(0)} + \mu_3 \sin^4\alpha^{(0)} \sin^2\beta^{(0)} \cos^2\beta^{(0)}\right) = 0, \tag{5.37}$$

hence,

$$\frac{\partial u^{(0)}}{\partial r} = 0, \tag{5.38}$$

so we conclude $u^{(0)} = u^{(0)}(x,t)$. Therefore, the modification to include transverse isotropy does not change the fact that the flow is extensional. We note that this result yields $\zeta^{(0)} = 0$, from (5.28), and that equation (5.26) gives an identity at this order. Similarly, we have that

$$\sigma_{r\theta}^{(0)} = \sigma_{x\theta}^{(0)} = \sigma_{rx}^{(0)} = 0, \tag{5.39}$$

hence the $\theta$-momentum equation (5.31) and the $r$-momentum equation (5.32) also reduce to identities. We can integrate the continuity equation (5.29) and noting that the axisymmetry of the problem demands that $v^{(0)} = 0$ at $r = 0$, we may conclude

$$v^{(0)} = -\frac{r}{2}\frac{\partial u^{(0)}}{\partial x}. \tag{5.40}$$

Direct substitution of $v^{(0)}$ into (5.33) and rearrangement yields

$$\frac{\partial R^{(0)}}{\partial t} + u^{(0)}\frac{\partial R^{(0)}}{\partial x} + \frac{R^{(0)}}{2}\frac{\partial u^{(0)}}{\partial x} = 0. \tag{5.41}$$

Now, the $r$-momentum equation (5.30) leads directly to an equation for the leading order pressure in terms of the velocities and the fibre angles

$$\begin{aligned}\frac{\partial}{\partial r}\Bigg[-p^{(0)} - \frac{\partial u^{(0)}}{\partial x}\left(1+2\mu_3\sin^2\alpha^{(0)}\cos^2\beta^{(0)}\right) + \sin^2\alpha^{(0)}\cos^2\beta^{(0)}\left(\mu_1+\mu_2\zeta^{(1)}\right) \\ +2\mu_3\sin^2\alpha^{(0)}\sin\beta^{(0)}\cos\beta^{(0)}\left(\frac{\partial w^{(0)}}{\partial r}-\frac{w^{(0)}}{r}\right) + 2\mu_3\sin\alpha^{(0)}\cos\alpha^{(0)}\cos\beta^{(0)}\frac{\partial u^{(1)}}{\partial r}\Bigg] \\ +\frac{1}{r}\Bigg[-2\mu_3\frac{\partial u^{(0)}}{\partial x}\sin^2\alpha^{(0)}\cos 2\beta^{(0)} + \sin^2\alpha^{(0)}\cos 2\beta^{(0)}\left(\mu_1+\mu_2\zeta^{(1)}\right) \\ +2\mu_3\sin\alpha^{(0)}\cos\alpha^{(0)}\cos\beta^{(0)}\frac{\partial u^{(1)}}{\partial r}\Bigg] = 0. \quad (5.42)\end{aligned}$$

We note that this equation requires

$$\alpha^{(0)} = 0; \text{ on } r = 0, \tag{5.43}$$

in order to prevent the second term in the (5.42) from becoming unbounded. Finally, equation (5.27) yields an equation for $\beta$,

$$\frac{D\beta^{(0)}}{Dt} = \cos^2\beta^{(0)}\left(\frac{\partial w^{(0)}}{\partial r}-\frac{w^{(0)}}{r}\right), \tag{5.44}$$

where we have used (5.40) in order to eliminate terms involving $v^{(0)}$.

To briefly summarise, at leading order we have used the $x$-momentum equation to determine that we do indeed have extensional flow, and from continuity we obtained $v^{(0)}$ in terms of $u^{(0)}$ and used this along with the kinematic condition to derive an equation for conservation of mass (5.41). Additionally, we obtained an equation for pressure in terms of $u^{(0)}, u^{(1)}, w^{(0)}, \alpha^{(0)}$ and $\beta^{(0)}$ from the leading order $r$-momentum equation, (5.30). Equations (5.38),(5.40),(5.41) all arise in precisely the same form as for a Newtonian fluid [49]. Unlike in the Newtonian case, the equation for pressure is not analytically tractable as $u^{(1)}, \alpha^{(0)}, \beta^{(0)}$ all depend upon $r$.

It remains to obtain equations for $u^{(0)}, u^{(1)}, w^{(0)}, \alpha^{(0)}$ in order to close the model. To this end, we continue to higher orders.

### 5.3.2 Obtaining $u^{(1)}$, $w^{(0)}$ and $\alpha^{(0)}$

In order to obtain equations for $u^{(1)}, w^{(0)}$ and $\alpha^{(0)}$, we now consider the governing equations at $\mathcal{O}(\varepsilon)$. From the $\theta$ and $x$-momentum equations (5.22) and (5.23) and their associated boundary conditions (5.24) and (5.25) respectively, we have

$$\frac{\partial \sigma_{rx}^{(1)}}{\partial r} + \frac{\sigma_{rx}^{(1)}}{r} = 0, \tag{5.45}$$

$$\frac{\partial \sigma_{r\theta}^{(1)}}{\partial r} + \frac{2}{r}\sigma_{r\theta}^{(1)} = 0, \tag{5.46}$$

subject to

$$\sigma_{rx}^{(1)} = 0; \text{ on } r = R^{(0)}(x,t), \tag{5.47}$$

$$\sigma_{\theta r}^{(1)} = 0; \text{ on } r = R^{(0)}(x,t). \tag{5.48}$$

Both equations integrate easily; applying the boundary conditions (5.47)-(5.48) yields

$$\sigma_{rx}^{(1)} = 0, \tag{5.49}$$

$$\sigma_{r\theta}^{(1)} = 0. \tag{5.50}$$

Equations (5.49),(5.50) provide two simultaneous equations for $\dfrac{\partial w^{(0)}}{\partial r} - \dfrac{w^{(0)}}{r}$ and $\dfrac{\partial u^{(1)}}{\partial r}$, namely

$$\begin{aligned}
&\frac{\partial u^{(1)}}{\partial r}\left[1 + \mu_2 \sin^2\alpha^{(0)} \cos^2\alpha^{(0)} \cos^2\beta^{(0)} + \mu_3\left(\sin^2\alpha^{(0)}\cos^2\beta^{(0)} + \cos^2\alpha^{(0)}\right)\right] \\
&+\left(\frac{\partial w^{(0)}}{\partial r} - \frac{w^{(0)}}{r}\right)\left[\mu_2 \sin^3\alpha^{(0)}\cos\alpha^{(0)}\sin\beta^{(0)}\cos^2\beta^{(0)} + \mu_3 \sin\alpha^{(0)}\cos\alpha^{(0)}\sin\beta^{(0)}\right] \\
&+\frac{\partial u^{(0)}}{\partial x}\left[\frac{\mu_2}{2}\sin\alpha^{(0)}\cos\alpha^{(0)}\cos\beta^{(0)}\left(3\cos^2\alpha^{(0)} - 1\right) + \mu_3 \sin\alpha^{(0)}\cos\alpha^{(0)}\cos\beta^{(0)}\right] \\
&+\mu_1 \sin\alpha^{(0)}\cos\alpha^{(0)}\cos\beta^{(0)} = 0,
\end{aligned} \tag{5.51}$$

and

$$\begin{aligned}
&\frac{\partial u^{(1)}}{\partial r}\left[\mu_2 \sin^3\alpha^{(0)}\cos\alpha^{(0)}\sin\beta^{(0)}\cos^2\beta^{(0)}+\mu_3\sin\alpha^{(0)}\cos\alpha^{(0)}\sin\beta^{(0)}\right]\\
&\quad+\left(\frac{\partial w^{(0)}}{\partial r}-\frac{w^{(0)}}{r}\right)\left[1+\mu_2\sin^4\alpha^{(0)}\sin^2\beta^{(0)}\cos^2\beta^{(0)}+\mu_3\sin^2\alpha^{(0)}\right]\\
+\frac{\partial u^{(0)}}{\partial x}&\left[\frac{\mu_2}{2}\sin^2\alpha^{(0)}\sin\beta^{(0)}\cos\beta^{(0)}\left(3\cos^2\alpha^{(0)}-1\right)-2\mu_3\sin^2\alpha^{(0)}\sin^2\beta^{(0)}\cos^2\alpha^{(0)}\right]\\
&\quad+\mu_1\sin^2\alpha^{(0)}\sin\beta^{(0)}\cos\beta^{(0)}=0.
\end{aligned}\tag{5.52}$$

Solving (5.51) and (5.52) gives

$$\frac{\partial u^{(1)}}{\partial r}=\mathcal{F}_1\left(\alpha^{(0)},\beta^{(0)}\right)\frac{\partial u^{(0)}}{\partial x}+\mu_1\mathcal{F}_2\left(\alpha^{(0)},\beta^{(0)}\right),\tag{5.53}$$

$$\frac{\partial w^{(0)}}{\partial r}-\frac{w^{(0)}}{r}=\mathcal{G}_1\left(\alpha^{(0)},\beta^{(0)}\right)\frac{\partial u^{(0)}}{\partial x}+\mu_1\mathcal{G}_2\left(\alpha^{(0)},\beta^{(0)}\right),\tag{5.54}$$

where $\mathcal{F}_1,\mathcal{F}_2,\mathcal{G}_1,\mathcal{G}_2$ are lengthy functions given in appendix D.1 as equations (D.3)-(D.6). These expressions identify $u^{(1)}$ and $w^{(0)}$ in terms of only $\alpha^{(0)}$, $\beta^{(0)}$ and $u^{(0)}$. Also at $\mathcal{O}(\varepsilon)$, (5.26) yields an equation for $\alpha^{(0)}$:

$$\begin{aligned}
\frac{D\alpha^{(0)}}{Dt}=&-\frac{3}{2}\sin\alpha^{(0)}\cos\alpha^{(0)}\frac{\partial u^{(0)}}{\partial x}+\sin\alpha^{(0)}\cos\alpha^{(0)}\sin\beta^{(0)}\cos\beta^{(0)}\left(\frac{\partial w^{(0)}}{\partial r}-\frac{w^{(0)}}{r}\right)\\
&-\sin^2\alpha^{(0)}\cos\beta^{(0)}\frac{\partial u^{(1)}}{\partial r}.
\end{aligned}\tag{5.55}$$

Finally, we obtain a statement for $\zeta^{(1)}$ at this order:

$$\begin{aligned}
\zeta^{(1)}=&\sin^2\alpha^{(0)}\sin\beta^{(0)}\cos\beta^{(0)}\left(\frac{\partial w^{(0)}}{\partial r}-\frac{w^{(0)}}{r}\right)+\sin\alpha^{(0)}\cos\alpha^{(0)}\cos\beta^{(0)}\frac{\partial u^{(1)}}{\partial r}\\
&+\frac{1}{2}\frac{\partial u^{(0)}}{\partial x}\left(3\cos^2\alpha^{(0)}-1\right).
\end{aligned}\tag{5.56}$$

An equation for $u^{(0)}$ is still required in order to close the model. We must go to higher orders again in order to obtain this.

### 5.3.3 Closing the model

At $O(\varepsilon^2)$ the momentum balance in the $x$-direction is given by

$$\frac{\partial(\sigma_{xr}^{(2)})}{\partial r} + \frac{\sigma_{xr}^{(2)}}{r} + \frac{\partial \sigma_{xx}^{(0)}}{\partial x} = 0, \tag{5.57}$$

$$\sigma_{rx}^{(2)} = \sigma_{xx}^{(0)} \frac{\partial R^{(0)}}{\partial x}; \text{ on } r = R^{(0)}. \tag{5.58}$$

We integrate (5.57) over the thread to obtain

$$\int_0^{R^{(0)}} \frac{\partial}{\partial r}\left(r\sigma_{xr}^{(2)}\right) \mathrm{d}r + \int_0^{R^{(0)}} \frac{\partial}{\partial x}\left(r\sigma_{xx}^{(0)}\right) \mathrm{d}r = 0. \tag{5.59}$$

Use of the Leibniz rule and application of the boundary condition (5.58), yields

$$\frac{\partial}{\partial x}(\bar{\sigma}_{xx}^{(0)}) = 0, \tag{5.60}$$

where

$$\bar{\sigma}_{xx}^{(0)} = \int_0^{R^{(0)}} r\sigma_{xx}^{(0)} \mathrm{d}r, \tag{5.61}$$

which is the axial tension of the thread, and is the analogue of equation (3.14) for a sheet, and

$$\sigma_{xx}^{(0)} = -p^{(0)} + 2\frac{\partial u^{(0)}}{\partial x}\left(1 + 2\mu_3 \cos^2\alpha^{(0)}\right) + \cos^2\alpha^{(0)}\left(\mu_1 + \mu_2\zeta^{(1)}\right) + 2\mu_3 \sin\alpha^{(0)} \cos\alpha^{(0)} \cos\beta^{(0)} \frac{\partial u^{(1)}}{\partial r}. \tag{5.62}$$

To summarise, we may use equations (5.53) and (5.54) to eliminate $u^{(1)}$ and $w^{(0)}$ from equations (5.42), (5.44), (5.55), and (5.60). At this point, we have now derived a system of five equations for $R^{(0)}$, $u^{(0)}$, $p^{(0)}$, $\alpha^{(0)}$, and $\beta^{(0)}$, namely (5.41), (5.42), (5.44), (5.55), and (5.60). In order to solve this problem numerically given initial conditions for $R^{(0)}, \alpha^{(0)}, \beta^{(0)}$,

we proceed as follows: First, we simultaneously solve (5.42) and (5.60) using centered finite differences, in order to obtain $p^{(0)}$ and $u^{(0)}$ at $t = 0$. Once obtained, we update $R^{(0)}, \alpha^{(0)}, \beta^{(0)}$ to the next time step using equations (5.41),(5.55),(5.44) respectively, by employing a upwinding finite difference scheme. With the updated values of $R^{(0)}, \alpha^{(0)}, \beta^{(0)}$, we calculate $u^{(0)}$ and $p^{(0)}$ at this new time step, and we repeat this process until the desired time is reached.

### 5.3.4 Twisting of the fibre

In general, a two-dimensional Stokes flow with a stress-free boundary allows an arbitrary translation and rigid body rotation to be added to the flow. To eliminate this rotation and determine $w^{(0)}$ uniquely we consider the twist of the thread. Following Cummings and Howell [22], we take moments about the $x$-axis at $\mathcal{O}(\varepsilon^2)$. At this order the $\theta$-momentum equation and associated boundary condition gives

$$\frac{\partial \sigma_{r\theta}^{(2)}}{\partial r} + \frac{2}{r}\sigma_{r\theta}^{(2)} + \frac{\partial \sigma_{\theta x}^{(1)}}{\partial x} = 0, \tag{5.63}$$

$$\sigma_{r\theta}^{(2)} = \frac{\partial R^{(0)}}{\partial x}\sigma_{x\theta}^{(1)}; \text{ on } r = R^{(0)}. \tag{5.64}$$

Taking moments about the centre-line of the thread, $r = 0$ and integrating over the thread, we obtain

$$\int_0^{2\pi}\int_0^{R^{(0)}} \left( \frac{\partial(\sigma_{r\theta}^{(2)})}{\partial r} + \frac{2\sigma_{r\theta}^{(2)}}{r} + \frac{\partial \sigma_{\theta x}^{(1)}}{\partial x} \right) r^2 \mathrm{d}r\mathrm{d}\theta = 0. \tag{5.65}$$

As the thread is axisymmetric, we may eliminate the integral in $\theta$, and rewrite (5.65) as

$$\int_0^{R^{(0)}} \frac{\partial}{\partial r}(r^2\sigma_{r\theta}^{(2)})\mathrm{d}r + \int_0^{R^{(0)}} \frac{\partial}{\partial x}(r^2\sigma_{\theta x}^{(1)})\mathrm{d}r = 0, \tag{5.66}$$

Integrating (5.66) with the boundary condition (5.64) and applying the Leibniz rule, we have

$$\frac{\partial}{\partial x}\int_0^{R^{(0)}} r^2\sigma_{\theta x}^{(1)}\mathrm{d}r = 0. \tag{5.67}$$

where

$$\begin{aligned}\sigma_{\theta x}^{(1)} = \sin\alpha^{(0)}\cos\alpha^{(0)}\sin\beta^{(0)}\left(\mu_1+\mu_2\zeta^{(1)}\right)+\mu_3\Bigg(\sin^2\alpha^{(0)}\sin\beta^{(0)}\cos\beta^{(0)}\frac{\partial u^{(1)}}{\partial r}\\ +\sin\alpha^{(0)}\cos\alpha^{(0)}\cos\beta^{(0)}\left(\frac{\partial w^{(0)}}{\partial r}-\frac{w^{(0)}}{r}\right)+\sin\alpha^{(0)}\cos\alpha^{(0)}\sin\beta^{(0)}\frac{\partial u^{(0)}}{\partial x}\Bigg).\end{aligned} \tag{5.68}$$

We note that integrating (5.67) allows us to remove all spatial dependencies

$$\int_0^{R^{(0)}} r^2\sigma_{\theta x}^{(1)}\mathrm{d}r = k(t), \tag{5.69}$$

since $k$ is a function of only $t$, there can be no twist across the thread. If there is rotation at the boundary, this rotation must be uniform across the thread. Once the system of equations in the previous section has been solved, $w^{(0)}$ can be obtained using equation (5.54). Then, use of the equation (5.69) accounts for any rigid body rotation imposed at the boundary.

## 5.4 Transformation to fixed boundary problem

Although the system of equations derived in the previous section are a significant simplification compared to the full system, they are still too complex to permit further analytical progress. In order to solve the system numerically, we transform the problem from a moving boundary problem to a fixed boundary problem by using the transformation:

$$\lambda = \frac{x}{L(t)}, \quad \gamma = \frac{r}{R^{(0)}(x,t)}, \quad t = \tau. \tag{5.70}$$

In all that follows, we have eliminated all terms involving $u^{(1)}$ and $w^{(0)}$ by employing equations (5.53) and (5.54), and used trigonometric identities where possible to condense the equations. We now write

$$R^{(0)}(x,t) = R^{(0)}(\lambda,\tau), \quad \hat{\alpha}^{(0)}(x,r,t) = \hat{\alpha}^{(0)}(\lambda,\gamma,\tau), \text{ etc.}$$

Applying the transformation to equation (5.41), we have

$$\frac{\partial R^{(0)}}{\partial \tau} + \left(\frac{u^{(0)} - \dot{L}\lambda}{L}\right)\frac{\partial R^{(0)}}{\partial \lambda} + \frac{R^{(0)}}{2L}\frac{\partial u^{(0)}}{\partial \lambda} = 0, \tag{5.71}$$

for conservation of mass. The equation for the fibre angle $\alpha^{(0)}$, (5.55) becomes

$$\begin{aligned}\frac{\partial \alpha^{(0)}}{\partial \tau} + \frac{u^{(0)} - \lambda\dot{L}}{L}\frac{\partial \alpha^{(0)}}{\partial \lambda} = \frac{1}{L}\Bigg( &-\frac{3}{2}\sin\alpha^{(0)}\cos\alpha^{(0)} + \sin\alpha^{(0)}\cos\alpha^{(0)}\sin\beta^{(0)}\cos\beta^{(0)}\mathcal{G}_1 + \\ &- \sin^2\alpha^{(0)}\cos\beta^{(0)}\mathcal{F}_1\Bigg)\frac{\partial u^{(0)}}{\partial \lambda} \\ &+ \mu_1\left(\frac{1}{4}\sin 2\alpha^{(0)}\sin 2\beta^{(0)}\mathcal{G}_2 - \sin^2\alpha^{(0)}\cos\beta^{(0)}\mathcal{F}_2\right),\end{aligned} \tag{5.72}$$

where we have eliminated the $u^{(1)}$ and $w^{(0)}$ terms using equations (5.53) and (5.54). From equation (5.44) we obtain a transformed equation for $\beta^{(0)}$

$$\frac{\partial \beta^{(0)}}{\partial \tau} + \frac{u^{(0)} - \lambda\dot{L}}{L}\frac{\partial \beta^{(0)}}{\partial \lambda} = \frac{1}{L}\cos^2\beta^{(0)}\mathcal{G}_1\frac{\partial u^{(0)}}{\partial \lambda} + \mu_1\cos^2\beta^{(0)}\mathcal{G}_2. \tag{5.73}$$

We note that the expected derivatives with respect to $\gamma$ in equations (5.72),(5.73) do not appear as their coefficients cancel out during the transformation. The equation for pressure, (5.42) becomes:

$$\frac{\partial}{\partial \gamma}\left[-p^{(0)} + \mathcal{H}_0\frac{\partial u^{(0)}}{\partial \lambda} + \mu_1\mathcal{H}_1\right] + \frac{1}{\gamma}\left[\mathcal{H}_2\frac{\partial u^{(0)}}{\partial \lambda} + \mu_1\mathcal{H}_3\right] = 0, \tag{5.74}$$

where the functions $\mathcal{H}_i$ are also lengthy trigonometric functions of $\alpha^{(0)}, \beta^{(0)}$, and are given in the Appendix as (D.12)-(D.15). We note that in the numerics, every $\mathcal{H}_i$ is precomputable

at each timestep. Similarly, we may write the equation for $u^{(0)}$ in a similarly condensed form, by using equations (5.53) and (5.56) to eliminate $\dfrac{\partial u^{(1)}}{\partial r}$ and $\zeta^{(1)}$ in (5.62), before again substituting the resulting expression for $\sigma_{xx}^{(0)}$ into (5.60), using (5.61), and expanding. The result is

$$\frac{\partial}{\partial \lambda}\left(R^{(0)^2}\left(\frac{1}{L}\mathcal{J}_0\frac{\partial u^{(0)}}{\partial \lambda}+\mu_1\mathcal{J}_1-\int_0^1 p^{(0)}\gamma \mathrm{d}\gamma\right)\right)=0. \tag{5.75}$$

Much like the functions $\mathcal{H}_i$, the pair of functions $\mathcal{J}_0, \mathcal{J}_1$ are lengthy, precomputable functions of $\alpha^{(0)}, \beta^{(0)}$ terms and are given in the appendix as (D.17)-(D.18). Our numerical approach is as follows. Given initial conditions in $R^{(0)}, \alpha^{(0)}, \beta^{(0)}$, we first pre-compute the functions $\mathcal{H}_0, \mathcal{H}_1, \mathcal{H}_2, \mathcal{H}_3, \mathcal{J}_0, \mathcal{J}_1$ using equations (D.12)-(D.15) and (D.17)-(D.18). We then simultaneously solve equations (5.74) and (5.75) using a FTCS finite difference scheme for $u^{(0)}$ and $p^{(0)}$ at the first time step. We then use a upwinding scheme upon equations (5.71),(5.72),(5.73) to update $R^{(0)}, \alpha^{(0)}, \beta^{(0)}$ respectively to the next time step whereupon the process is repeated until a desired time is reached. We note that the construction of the linear system given by equations (5.74) and (5.75) is similar to that given by the short timescale squeezing flow problem studied in chapter 2, with the major differences being greater pre-compuation of coefficients, and that $p^{(0)}$ depends upon two variables, with $u^{(0)}$ depending on one, which is the opposite to the problem considered in chapter 2. The construction for the squeeze flow solver is given in Appendix A.1, and we omit the details of the construction of the solver for equations (5.74)-(5.75) from this thesis.

## 5.5 Validation of numerical methods in a small angle regime

Before describing the numerical scheme, we first consider a small $\alpha$ limit, such that the fibres are lying "nearly flat" along the axis of the thread. This gives a simplified set of governing equations which may be separately solved and used to validate the numerical solutions. As we will subsequently show, a special case arises when $\mu_1 = 0$ that allows for analytical progress using a Lagrangian transformation. Comparing the analytical solution

of the special case with the solutions to the small $\alpha$ system and the full model will provide validation for both sets of numerics.

### 5.5.1 Governing equations of the small angle regime

We begin by writing

$$\alpha^{(0)} = \eta\hat{\alpha}, \tag{5.76}$$

where $\eta$ is a small parameter. Similarly to the small $\mu_2$ analysis in chapter 2, we require $\varepsilon \ll \eta \ll 1$ in order for this simplification to be consistent with the thin film expansion that has been performed. We have

$$\sin\alpha^{(0)} = \eta\hat{\alpha} - \frac{1}{6}\eta^3\hat{\alpha}^3 + ...,$$
$$\cos\alpha^{(0)} = 1 - \frac{1}{2}\eta^2\hat{\alpha}^2 + ....$$

We start by applying the approximation to equations (5.51)-(5.52) for $u^{(1)}$ and $w^{(0)}$:

$$\frac{\partial u^{(1)}}{\partial r} = \frac{-\eta\hat{\alpha}}{1+\mu_3}\cos\beta^{(0)}\left(\mu_1 + \frac{\partial u^{(0)}}{\partial x}\left(\mu_2+\mu_3\right)\right) + \mathcal{O}\left(\eta^2\right), \tag{5.77}$$

and

$$\frac{\partial w^{(0)}}{\partial r} - \frac{w^{(0)}}{r} = \frac{-\eta\hat{\alpha}\mu_3\sin\beta^{(0)}\cos\beta^{(0)}}{1+\mu_3}\left(\mu_1 + \frac{\partial u^{(0)}}{\partial x}\left(\mu_2+\mu_3\right)\right) + \mathcal{O}\left(\eta^2\right). \tag{5.78}$$

Hence, upon substitution into other equations in the model, the lowest order contribution from $u^{(1)}$ and $w^{(0)}$ terms is at $\mathcal{O}(\eta)$. Along with (5.56), these results reduce equation (5.42) to

$$\frac{\partial}{\partial r}\left(-p^{(0)} - \frac{\partial u^{(0)}}{\partial x}\right) + \mathcal{O}(\eta) = 0, \tag{5.79}$$

which, to leading order, is the result obtained for the Newtonian problem [49]. Direct integration and use of (5.34) in precisely the same way as the Newtonian case yields pressure directly

$$p^{(0)} = -\frac{\partial u^{(0)}}{\partial x} + \mathcal{O}\left(\eta^2\right). \tag{5.80}$$

Substituting these expressions into $\sigma_{xx}^{(0)}$, we obtain

$$\sigma_{xx}^{(0)} = 3\frac{\partial u^{(0)}}{\partial x} + \mu_1 + \mu_2\frac{\partial u^{(0)}}{\partial x} + 4\mu_3\frac{\partial u^{(0)}}{\partial x} + \mathcal{O}\left(\eta^2\right). \tag{5.81}$$

This allows us to eliminate pressure from the momentum balance, which allows us to reduce equation (5.60) from an integro-differential equation to a partial differential equation:

$$\frac{\partial}{\partial x}\left(\frac{R^{(0)^2}}{2}\left(\frac{\partial u^{(0)}}{\partial x}\left(3+\mu_2+4\mu_3\right)+\mu_1\right)\right) + \mathcal{O}\left(\eta\right) = 0. \tag{5.82}$$

Additionally, at leading order, the fibre equations simplify to

$$\frac{D\hat{\alpha}}{Dt} = -\frac{3\hat{\alpha}}{2}\frac{\partial u^{(0)}}{\partial x} + \mathcal{O}\left(\eta\right), \tag{5.83}$$

$$\frac{D\beta^{(0)}}{Dt} = 0 + \mathcal{O}\left(\eta\right), \tag{5.84}$$

and conservation of mass remains unchanged. Upon applying the co-ordinate transformation defined in (5.70), we obtain the following system of equations

$$\frac{\partial R^{(0)}}{\partial \tau} + \frac{1}{L}\frac{\partial R^{(0)}}{\partial \lambda}\left(u^{(0)} - \lambda\dot{L}\right) + \frac{R}{2L}\frac{\partial u^{(0)}}{\partial \lambda} = 0, \tag{5.85}$$

$$\frac{\partial}{\partial \lambda}\left(\frac{R^{(0)^2}}{2}\left(\frac{\partial u^{(0)}}{\partial \lambda}\left(3+\mu_2+4\mu_3\right)+L\mu_1\right)\right) = 0, \tag{5.86}$$

$$\frac{\partial \hat{\alpha}}{\partial \tau} + \frac{\left(u^{(0)} - \lambda\dot{L}\right)}{L}\frac{\partial \hat{\alpha}}{\partial \lambda} = -\frac{3\hat{\alpha}}{2L}\frac{\partial u^{(0)}}{\partial \lambda}, \tag{5.87}$$

$$\frac{\partial \beta^{(0)}}{\partial \tau} + \frac{\left(u^{(0)} - \lambda\dot{L}\right)}{L}\frac{\partial \beta^{(0)}}{\partial \lambda} = 0, \tag{5.88}$$

with

$$u(0,\tau)=0, \quad u(1,\tau)=1, \quad L(\tau)=1+\tau, R(\lambda,0)=R_0(\lambda)$$
$$\frac{\partial R}{\partial \lambda}|_{\lambda=0}=0, \quad \hat{\alpha}(\lambda,\gamma,0)=\hat{\alpha}_0(\lambda,\gamma), \quad \beta(\lambda,\gamma,0)=\beta_0(\lambda,\gamma). \tag{5.89}$$

We note that the absence of a $\gamma$ derivative in equations (5.87) and (5.88) implies that each $r-\theta$ cross section evolves as a whole as the cross section evolves along the thread.

To briefly summarise, equations (5.85)-(5.88) give four partial differential equations as conservation laws for mass and momentum with two conditions governing the fibre angles. We note that the mass and momentum conservation laws decouple from the fibre equations, and that equation (5.82) contains an 'enhanced' Trouton ratio, which is 3 for a Newtonian axisymmetric thread [49], with additional terms related to the anisotropic extensional and shear viscosities.

To solve this system numerically for given initial $R, \hat{\alpha}, \beta$, we first use equation (5.85) to obtain $u^{(0)}$ at the initial time, using a centred space finite difference scheme. We then use an upwind finite difference scheme upon equations (5.85), (5.87), (5.88) to update $R, \hat{\alpha}, \beta^{(0)}$ respectively to the next time step. At this point, we return to (5.86) to update $u^{(0)}$ to the next time step and repeat this process until the desired time is reached.

### 5.5.2 Special case: Analytical solution for $\mu_1 = 0$

It is possible to make further analytical progress under the assumption that $\mu_1 = 0$. The equations (5.41) and (5.82) are analytically tractable by use of a Lagrangian coordinate transformation similar to the approach used by Howell in two dimensions [49]. We employ the Lagrangian coordinates $\tau, \psi, \rho$ as defined by

$$\frac{\partial x}{\partial \tau}=u\left(x\left(\rho,\tau\right),\tau\right), \frac{\partial r}{\partial \tau}=v\left(r\left(\psi,\tau\right),\tau\right), x\left(\rho,0\right)=\rho, r\left(\psi,0\right)=\psi, t=\tau.$$

Applying the transformation, equations (5.41), (5.82)-(5.84) give

$$\frac{\partial R^{(0)^2}}{\partial \tau} + R^{(0)^2}\frac{\partial u^{(0)}}{\partial \rho}\left(\frac{\partial x}{\partial \rho}\right)^{-1} = 0, \tag{5.90}$$

$$(3 + \mu_2 + 4\mu_3)\, R^{(0)^2}\frac{\partial u^{(0)}}{\partial \rho}\left(\frac{\partial x}{\partial \rho}\right)^{-1} = T_0(\tau), \tag{5.91}$$

$$\frac{\partial \hat{\alpha}}{\partial \tau} = -\frac{3\hat{\alpha}}{2}\frac{\partial u^{(0)}}{\partial \rho}\left(\frac{\partial x}{\partial \rho}\right)^{-1}, \tag{5.92}$$

$$\frac{\partial \beta^{(0)}}{\partial \tau} = 0, \tag{5.93}$$

where we have multiplied (5.90) by $2R^{(0)}$, and we have obtained equation (5.91) by taking the first integral of (5.82) before applying the transformation. The function $T_0(\tau)$ represents the tension applied to the ends of the fluid thread. At this point, it is clear that equations (5.90)-(5.91) are very similar to the Trouton model studied by Howell [49], and for the purposes of validating the full model we follow the same approach to constructing their solution. We may immediately integrate equation (5.90) to obtain a statement for $x$:

$$\frac{\partial x}{\partial \rho} = \frac{R_0^{(0)^2}(\rho)}{R^{(0)^2}(\rho, \tau)}. \tag{5.94}$$

Direct substitution of (5.90) into (5.91) gives

$$\frac{\partial R^{(0)^2}}{\partial \tau} + \frac{T_0}{3 + \mu_2 + 4\mu_3} = 0, \tag{5.95}$$

which is a very similar result to that for a Newtonian thread, with a modified tension term [49]. Upon integration, we obtain

$$R^{(0)^2} = R_0^{(0)^2} - g(\tau), \tag{5.96}$$

where, $\dot{g}(\tau) = \dfrac{T_0(\tau)}{3 + \mu_2 + 4\mu_3}, g(0) = 0$. As with a Newtonian thread, there are two methods to determine $g$: we may specify either the half-length of the fibre, or the tension applied to

the thread. If we specify the half-length of the fibre, $L(\tau)$, then $g$ is given by the relation

$$L(\tau) = \int_0^1 \frac{R^{(0)^2}(\rho,0)}{R^{(0)^2}(\rho,\tau)}\mathrm{d}\rho = \int_0^1 \frac{R^{(0)^2}(\rho,0)}{R^{(0)^2}(\rho,0) - g(\tau)}\mathrm{d}\rho. \tag{5.97}$$

We choose to prescribe an initial radius $R_0^{(0)}$ that is uniform, which allows us to obtain

$$g = R_0^{(0)^2}\left(\frac{L-1}{L}\right), \tag{5.98}$$

$$T_0 = (3+\mu_2+4\mu_3)R_0^{(0)^2}\left(1+\frac{\dot{L}}{L^2}\right), \tag{5.99}$$

$$R^{(0)} = \frac{R_0^{(0)}}{\sqrt{L}}, \tag{5.100}$$

$$x = \rho L, \tag{5.101}$$

$$u = \rho\dot{L}, \tag{5.102}$$

which gives the same solution for $R^{(0)}, u^{(0)}$ as the Newtonian problem, with the exception that the tension contains the 'enhanced Trouton ratio' found in equation (5.91). Physically, this simply means that one must apply a greater tension to a fluid thread containing fibre reinforcement with a nearly flat fibre alignment to induce precisely the same result as a Newtonian fluid thread. We note that the equations for the bulk properties of the flow, (5.90)-(5.91), do not possess terms involving the fibre-angles. In this regime, there is a one way coupling such that the flow is influencing the fibres, but the fibres do not influence the flow. We can exploit this by using (5.92) and (5.93) to calculate the fibre behaviour directly. Equation (5.93) immediately gives us that a uniform initial $\beta^{(0)}$ would remain constant and uniform. Equation (5.92) gives

$$\hat{\alpha} = \frac{\hat{\alpha}_0}{L^{3/2}}. \tag{5.103}$$

Choosing $L = 1+\tau$, we present in Figure 5.3 a direct comparison between the analytical results, the small angle-equations (5.85)-(5.88) and the full system (5.71)-(5.75) for the initial choices of $R_0^{(0)} = 1, \hat{\alpha}_0 = 0.01\pi$, with $\mu_2 = 50, \mu_3 = 25$. We note first that choosing

initial conditions that are uniform remain so, hence the values of $R^{(0)}$ and $\hat{\alpha}$ presented in Figure 5.3 represents the angle at every point in the domain. We see that as the thread thins, the angle of the fibres decays to zero, representing the fibres aligning in the direction of extension. This is similar behaviour to the sheet when $\mu_1 = 0$ as described in Chapter 3. We see that the errors are small - in Figure 5.4 we give the relative errors between the analytical result, and the numerical solutions of the small angle system of equations and the full model. In Figure 5.4a we see that the maximum relative error for $\hat{\alpha}$ between the analytical results and the output of the full system of equations is 0.3%, and Figure 5.4b show that the relative error between the small angle equations and the full model is 0.1%. Figures 5.4c and 5.4d show that the relative error for $R^{(0)}$ between the analytical results and the output of the full system of equations is 0.09% respectively.

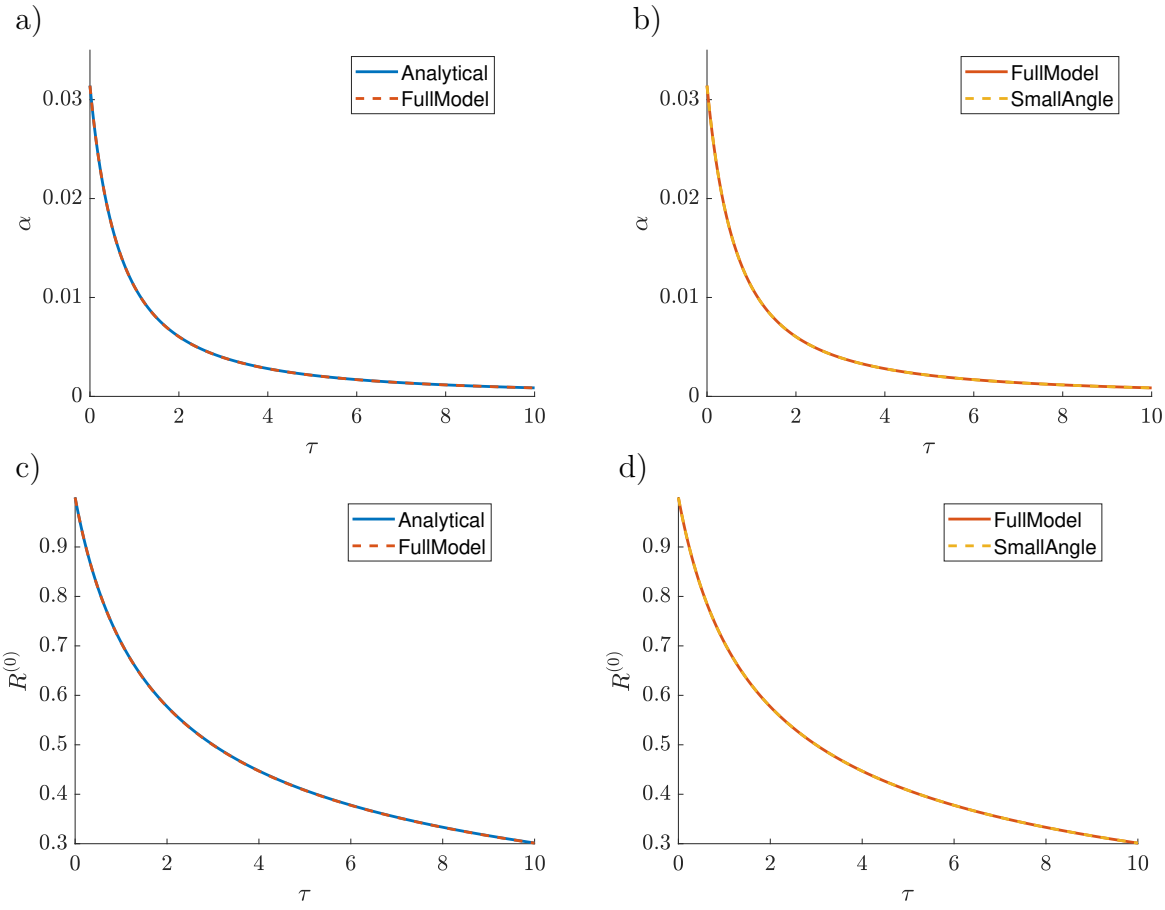


Figure 5.3: Comparison of the evolution of a) $\hat{\alpha}$ between the full system of equations and the analytical result, b) $\hat{\alpha}$ between the full system of equations and the small angle equations, c) $R^{(0)}$ between the full system of equations and the analytical result and d) $R^{(0)}$ between the full system of equations and the small angle equations for the initial conditions $\alpha = 0.01\pi$,$R_0^{(0)} = 1$ with $\mu_2 = 50, \mu_3 = 25$.

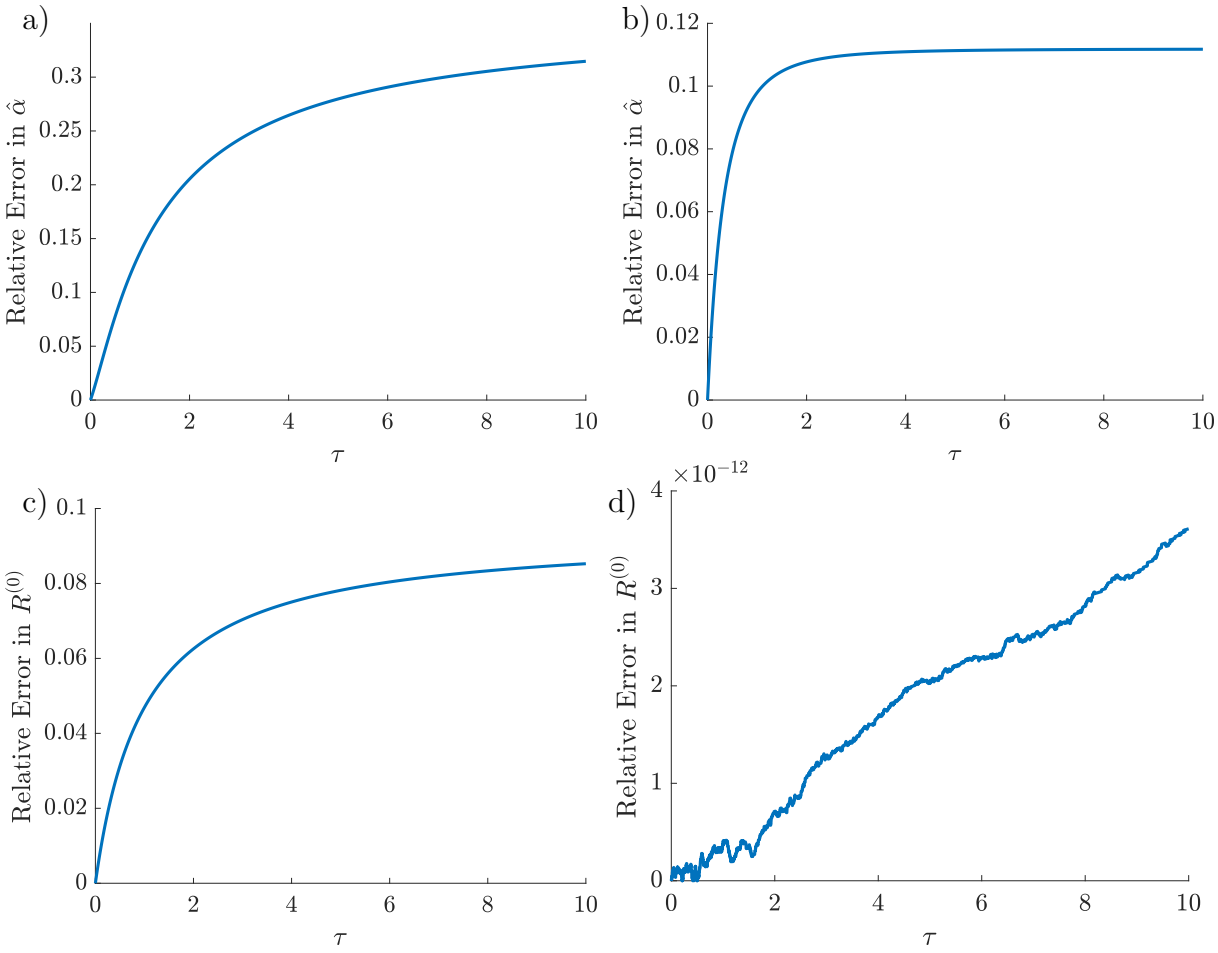


Figure 5.4: Figures showing the relative error in the results presented in Figure 5.3. The relative errors are a) between the analytical result and numerical solution of the full model for $\hat{\alpha}$, b) between the solutions of the small-angle equations and the full model for $\hat{\alpha}$, c) between the analytical result and numerical solution of the full model for $R^{(0)}$, and d) between the solutions of the small-angle equations and the full model for $R^{(0)}$.

### 5.5.3 Comparison between small-$\alpha$ and full system

Here, we compare the numerical results of the full model (5.71)-(5.75) with the output of the small $\alpha$ equations, (5.85)-(5.88), with two sets of initial conditions that we cannot make further analytical progress with. First, in Figure 5.5, we present a comparison between the small angle system and full model for a thread without active behaviour ($\mu_1 = 0$). We make the initial choices of $R_0^{0)} = 1 + \lambda^2, \hat{\alpha}_0 = 0.01\pi, \mu_1 = 0, \mu_2 = 50, \mu_3 = 25$. We plot in Figure 5.5a the maximum relative error between the small angle equations and the full system across the thread for each of the quantities $\hat{\alpha}, u^{(0)}, R^{(0)}$. We see that for these initial conditions and parameter choices that the errors are small, with the error for $u^{(0)}$ in particular being 0.0032% at $\tau = 10$. Moreover, the errors appear to have converged by $\tau = 10$. We also give plots for the evolution of $R^{(0)}$ and $u^{(0)}$ and note that this choice of initial condition for $R^{(0)}$ induces $\lambda$-dependence in $\hat{\alpha}$, as $u^{(0)}$ is no longer linear, as we would expect from equation (5.94).

The second comparison involves the activation of $\mu_1$ terms. We choose $\hat{\alpha}_0 = 0.01\lambda\gamma, \mu_1 = 1, \mu_2 = 25, \mu_3 = 100$. The activation of the $\mu_1$ term introduces error, and we change the initial radius of the thread to possess less curvature. We choose $R_0^{(0)} = 1 + \frac{1}{10}\sqrt{(1+\lambda^2)}$. We see that the relative errors are larger than the previous case, but remain under 1% up to $\tau = 0$. We see in Figures 5.6a that unlike the previous comparisons with $\mu_1 = 0$ above, the errors continue to grow with time. We note that the velocity profile in Figure 5.6b adopts a concave down shape, which is markedly different to the behaviour of both the sheet discussed in Chapter 3 and the analytical solutions for $\mu_1 = 0$. The globally increased velocity appears to have led to a greater rate of thinning, see Figure 5.6c compared to the analytical case shown in Figure 5.3. As we shall show in the next section, activation of $\mu_1$ can cause $\alpha^{(0)}$ to grow in the full model, which may lead to a small-$\alpha$ approximation becoming invalid.

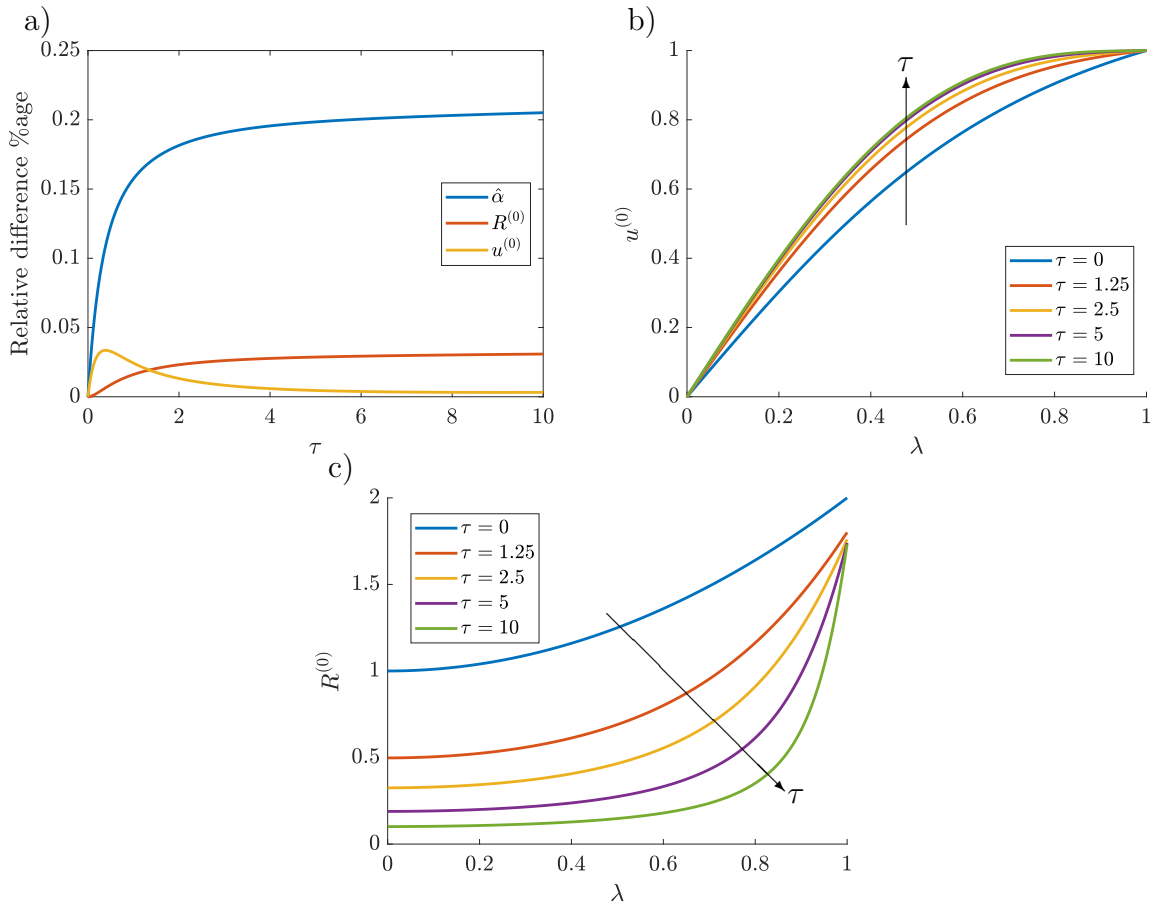


Figure 5.5: Evolution of a) the relative error between the full system of equations and the small angle equations, b) of $u^{(0)}$ and c) $R^{(0)}$ for initial conditions $\alpha = 0.01\pi$,$R_0^{(0)} = 1 + \lambda^2, \mu_2 = 50, \mu_3 = 25$.

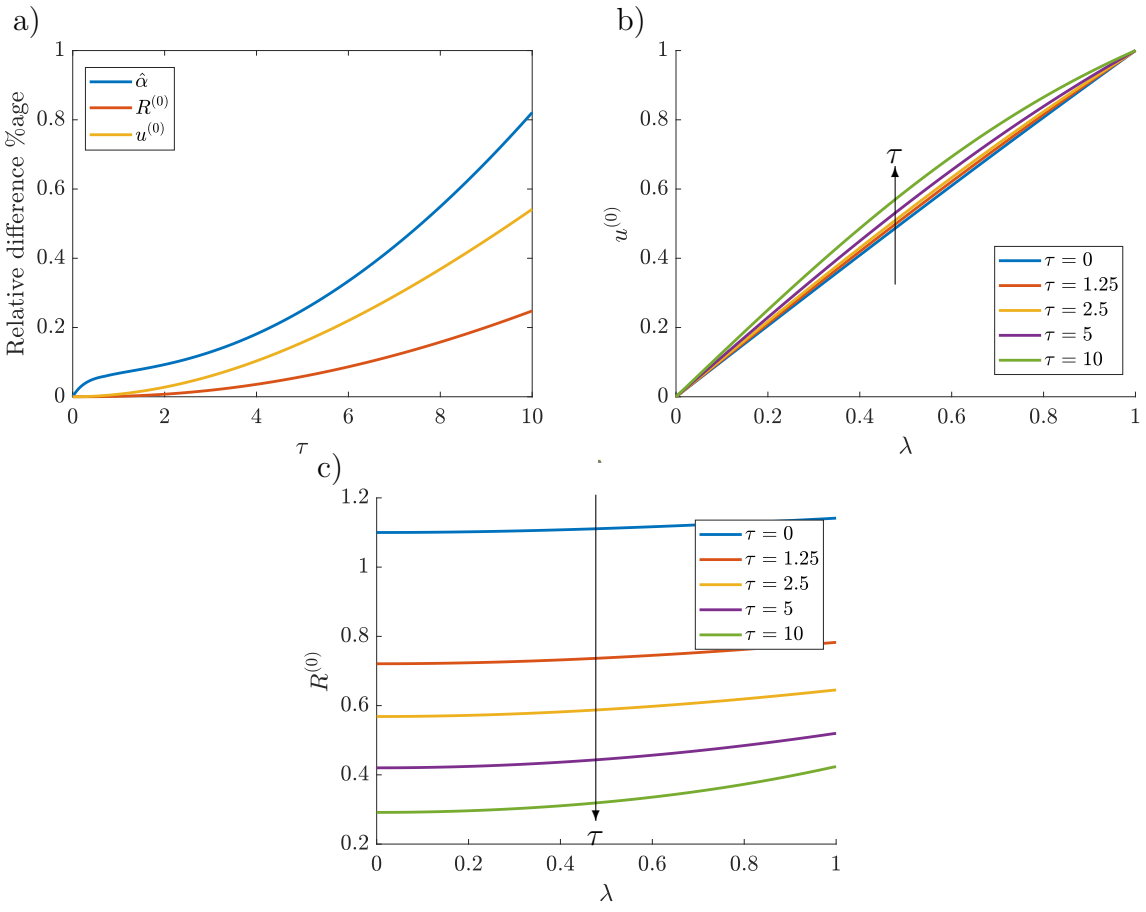


Figure 5.6: Evolution of a) the relative error between the full system of equations and the small angle equations, b) of $u^{(0)}$ and c) $R^{(0)}$ for initial conditions $\alpha = 0.01\lambda\gamma, R_0^{(0)} = 1 + \frac{1}{10}\sqrt{1+x^2}, \mu_1 = 1, \mu_2 = 25, \mu_3 = 100$.

## 5.6 Results

### 5.6.1 Solutions for $\mu_1 = 0$

Having now validated the numerical methods, we study the effect of varying the viscosities $\mu_2, \mu_3$ with $\mu_1 = 0$ fixed . To this end, we first turn our attention to consider the behaviour of transversely isotropic sheets that have an initially constant thickness, which for simplicity we set $R^{(0)}(\lambda, 0) = 1$. We start by setting $\beta^{(0)}(\lambda, \gamma, 0) = 0$, and we note that this choice of $\beta$ has the effect of fixing the fibres into a spoke-like arrangement for all time, as $\beta^{(0)} = 0$ is a fixed point of equation (5.73). We then give plots of the longitudinal velocity $u^{(0)}$ and radius $R^{(0)}$ in the physical variables, both initially and at $\tau = 10$, for the choices $\mu_1 = 0, \mu_2 = 0, \alpha^{(0)}(\lambda, \gamma, 0) = \lambda\gamma, \beta^{(0)}(\lambda, \gamma, 0) = 0$, with varied $\mu_3$ in Figure 5.7. We see that similarly to the extensional flow of the sheet in chapter 3, increasing $\mu_3$ has the effect of reducing the (qualitative) non-Newtonian behaviour of the thread - both the velocity and radius deviate less from the Newtonian solution for an initially uniform thread and that the fibres align with the direction of extension of the fluid.

If we now choose a $\beta^{(0)}(\lambda, \gamma, 0) \neq 0$, the behaviour of the thread is significantly more complex. In Figure 5.8 we give similar plots, but with the initial choice of $\beta^{(0)}(\lambda, \gamma, 0) = \frac{\pi}{4}$ and we see that the effect of increasing $\mu_3$ is much more complex than that of the sheet. We see, in Figure 5.8c that increasing $\mu_3$ allows $\alpha^{(0)}$ to grow, representing the fibres rotating to orient in the transverse direction of the thread, against the motion of the fluid. In the same regions, $\beta^{(0)}$ grows towards $\frac{\pi}{2}$, which represents the components of the fibres in the cross-section of the thread evolving from a spiral arrangement to a hoop orientation. This is in contrast to the behaviour of the fibres within a transversely isotropic sheet, which rotate to align with the direction of extension when $\mu_1 = 0$, and gives rise to more complicated flow profiles than the sheet (Figure 5.8a).

We also see that near $\gamma = 0$, where $\alpha^{(0)}$ is initially relatively small, that the fibres do align with the direction of extension and that there is little evolution in $\beta^{(0)}$, which is consistent with the small-$\alpha$ equations.

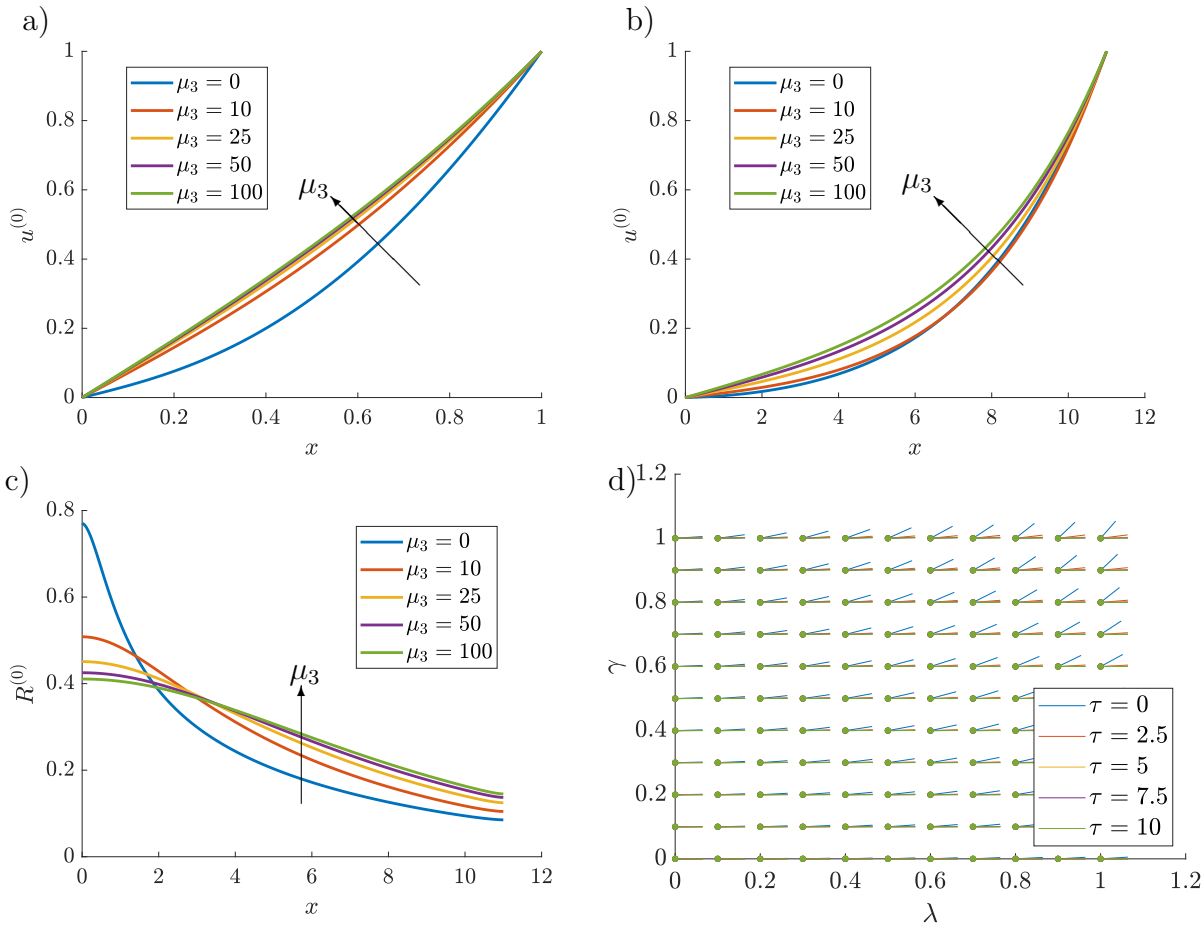


Figure 5.7: Plots of a) initial $u^{(0)}$ and b) $u^{(0)}$ at $\tau = 10$, c) $R^{(0)}$ at $\tau = 10$, for $\mu_3 = 0, 10, 25, 50, 100$, with initial conditions $\alpha(\lambda, \gamma, 0) = \lambda\gamma, \beta(\lambda, \gamma, 0) = 0, R_0^{(0)} = 1, \mu_1 = 0, \mu_2 = 25$. d) Evolution of the fibre angle for $\mu_3 = 100$.

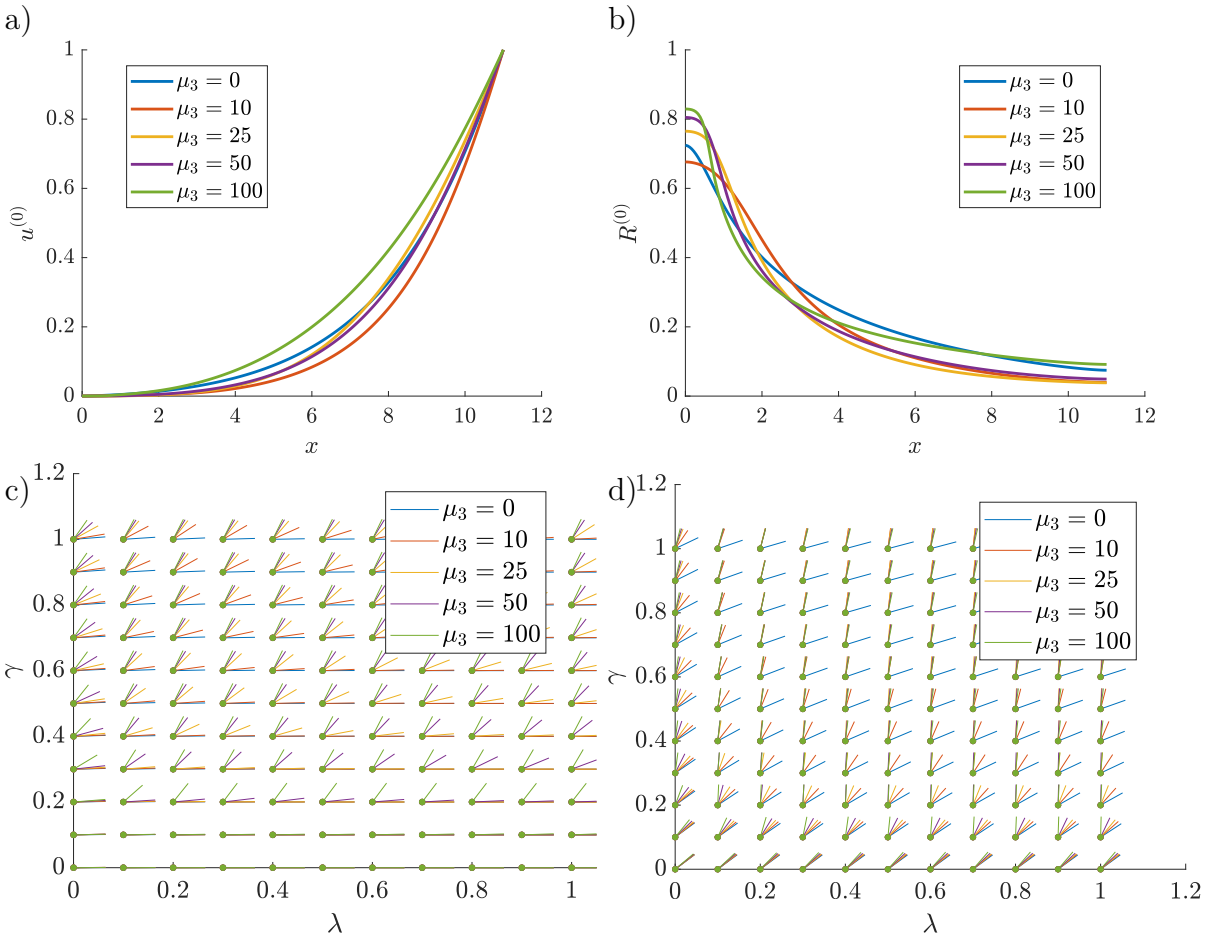


Figure 5.8: The a) longitudinal velocity, $u^{(0)}$, b) radius of the thread, $R^{(0)}$, c) fibre angles $\alpha^{(0)}$ and d) $\beta^{(0)}$, at $\tau = 10$, for varied $\mu_3 = 0, 10, 25, 50, 100$ for initial conditions $\alpha(\lambda, \gamma, 0) = \lambda\gamma, \beta(\lambda, \gamma, 0) = \frac{\pi}{4}, R_0^{(0)} = 1, \mu_1 = 0, \mu_2 = 25$. $u^{(0)}$ and $R^{(0)}$ are plotted in the physical variables, whilst the fibre angles $\alpha^{(0)}$ and $\beta^{(0)}$ are plotted in the transformed variables for ease of comparison.

We now turn to examining the behaviour of the thread with varied $\mu_2$. We fix $\mu_3$ with $\mu_1 = 0$. Similarly to the sheet, increasing $\mu_2$ has the effect of causing the thread to behave in a more non-Newtonian manner. In Figure 5.9 we give plots of the longitudinal velocity, radius of the thread and fibre angles $\alpha^{(0)}, \beta^{(0)}$, at $\tau = 10$, for varied $\mu_2$ and conditions of $\alpha(\lambda, \gamma, 0) = \lambda\gamma, \beta(\lambda, \gamma, 0) = \frac{\pi}{4}, R_0^{(0)} = 1, \mu_1 = 0, \mu_3 = 25$. We see that increasing $\mu_2$ has the effect of inhibiting the longitudinal velocity and increasing the rate of thinning of the thread. In the regions where the thread is thinner, one might expect the velocity to be enhanced. However, if we compare between different values of $\mu_2$, we see that although the rate of thinning has been increased, the velocity across the whole of the thread has been inhibited. We expect an expression, similar to $G_2$, for an inhomogeneous viscosity exists, but it is difficult to observe from equations (5.74) and (5.75).

We also note that increasing $\mu_2$ appears to have a significantly lesser effect upon the rotation of the fibres compared to $\mu_3$. In Figures 5.9c and 5.9d we show the orientation of the fibres for the conditions above and we see that the final positions of the fibres exhibit less variance than Figure 5.8, where we varied $\mu_3$. We note that increasing $\mu_2$ has the effect of increasing $\alpha^{(0)}$ so that the fibres are less oriented towards the direction of extension, whilst there is very little difference between $\mu_2 = 0$ and $\mu_2 = 100$ in the fibre angle within the cross-section of the sheet.

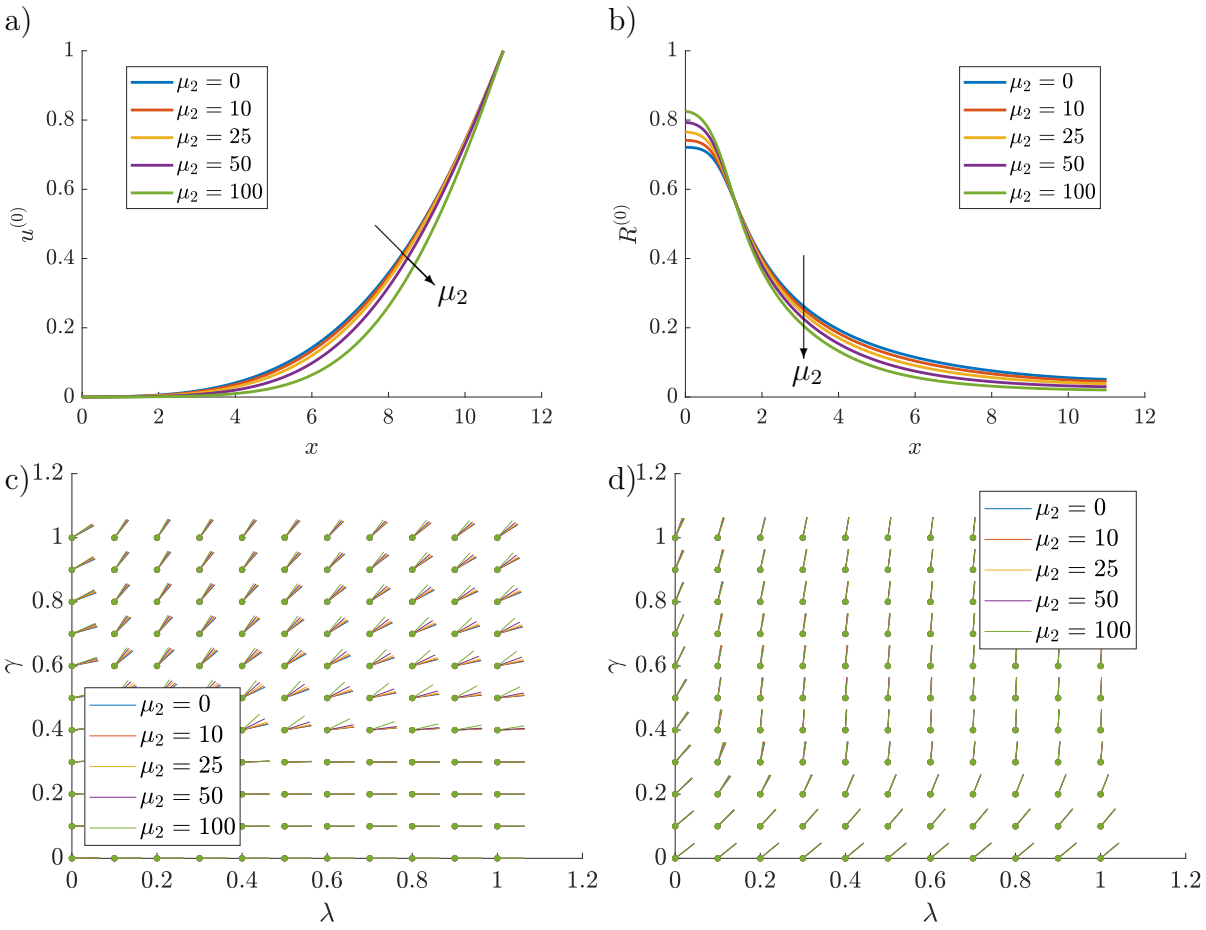


Figure 5.9: The a) longitudinal velocity, $u^{(0)}$, b) radius of the thread, $R^{(0)}$, c) fibre angles $\alpha^{(0)}$ and d) $\beta^{(0)}$, at $\tau = 10$, for varied $\mu_2 = 0, 10, 25, 50, 100$ for initial conditions $\alpha(\lambda, \gamma, 0) = \lambda\gamma, \beta(\lambda, \gamma, 0) = \frac{\pi}{4}, R_0^{(0)} = 1, \mu_1 = 0, \mu_3 = 25$. $u^{(0)}$ and $R^{(0)}$ are plotted in the physical variables, whilst the fibre angles $\alpha^{(0)}$ and $\beta^{(0)}$ are plotted in the transformed variables for ease of comparison.

## 5.7 Conclusion

We investigated a small-angle behaviour of the model, validating the numerical techniques for the full system of equations against a small-$\alpha$ analysis. We found that in this regime the fibres aligned with the direction of extension, and that there was a one-way coupling between the fibres and the fluid, with the fluid affecting the orientation of the fibres. However the orientation of the fibres did not play a role in the evolution of the velocity or radius of the fluid. We found that variations of the parameters $\mu_1, \mu_2, \mu_3$ do affect the behaviour of the flow, with $\mu_2, \mu_3$ forming an enhanced Trouton viscosity. In this regime, the flow is essentially Newtonian with a modified tension provided $\mu_1 = 0$.

In chapter 3, we saw that the fibres of a transversely isotropic fluid align in the direction of extension, provided $\mu_1 = 0$, and that the fibres were not initially pointing in the transverse direction. Here, we require also that $\mu_3 = 0$. We found that for a transversely isotropic thread, $\mu_3$ plays a role in creating non-Newtonian behaviours, unlike in chapters 2-4, and may even be a greater driver of these behaviours than $\mu_2$, as shown in Figures 5.8 and 5.9. There appears to be two regimes of behaviour, one where the extensional viscosity dominates the behaviour of the flow, and one where the shear viscosity is dominant.

Throughout this chapter, we have seen behaviours where varying a parameter led to results which were more complex than expected. For example, we saw, in Figure 5.7 that increasing $\mu_3$ has the effect of reducing the change in the radius over the longitudinal direction. In this figure, we would expect that the thread when $\mu_3 = 0$ to undergo breakup earlier than the thread when $\mu_3 = 100$. In this case, the spinnability of the thread would be increased by an increase of $\mu_3$. However, we saw in Figure 5.8 that the thread is thinner when $\mu_3 = 25$ compared to $\mu_3 = 0, 100$. This implies that the spinnability of the thread is also influenced by the fibre angles, in addition to the key parameters, as we might expect. As a result, we suggest that these behaviours are related to an inhomogenous viscosity similar to $G_2$ in Chapter 3. It may be possible to construct this viscosity numerically from equation (5.75), which is the equivalent of (3.30). This could lead to greater insight into

the mechanical behaviour of the thread, and which components of our model have the greatest affect upon the spinnability of the thread.

There are a number of potential avenues for future work, the most obvious of which is that the results presented here are for $\mu_1 = 0$. We have seen in chapter 3 and in section 5.5 that activation of the $\mu_1$ term can cause issues with tension and the numerical approach.

We could also relax the the requirement of axisymmetry of the thread. This would give rise to a setting wherein we could study the development of the centre-line of the thread in a nearly-straight setting, similar to the work presented in chapter 4. Alternatively, we could construct a curvilinear coordinate system following the centre-line of the thread, similarly to Refs. [29, 102]. Moreover, we would also expect to see short time-scale behaviour in such a setting, and comparison with the sheet may lead to additional insight into the mechanical changes induced by the addition of the second fibre angle. Further work might also include investigations of the effects of inertia, surface tension, body forces or compressibility. Finally, we may include some degree of entanglement and alignment as the fibres in cervical mucus may not always align as assumed in this model, and may also be entangled.

# CHAPTER 6

# CONCLUSION

In this final chapter we summarise the main results of the thesis, and suggest further work which could be carried out.

## 6.1 Summary of findings

We have derived models for the thin film flow of a transversely isotropic fluid in the three contexts of a squeezing flow, the extensional flow of a sheet, and the extensional flow of an axisymmetric thread. In all cases the result was a system of leading-order equations which depended upon the thickness and longitudinal velocity, along with either the pressure (chapters 2, 5) or centre-line (chapters 3, 4). The extensional flow problems studied in chapters 3-5 resulted in models that are a generalisation of the Trouton model for the extensional flow of a Newtonian fluid [49].

In chapter 2 we derived a model describing the squeezing flow of an incompressible, viscous, transversely isotropic fluid. We found that the majority of the fibres reorient themselves to be parallel with the $x$-axis on a shorter timescale than that of the flow, with the exception of a thin layer around half-depth of the film. On the short timescale, we found that

- The orientation of the fibres does have an effect on the flow, inhibiting the longitudinal flow in some regions, whilst enhancing it in others. In particular, when $\mu_2$ is small,

the greatest changes to the flow occur where $\theta \sim \frac{\pi}{4}$.

- Increasing the anisotropic extensional viscosity, $\mu_2$, increased the non-Newtonian behaviours of the sheet, whilst increasing the anisotropic shear viscosity $\mu_3$ inhibited these behaviours. We note that increasing $\mu_3$ causes a significant increase of the magnitude of the pressure, but not the shape.

- By measuring the force of the fluid on the upper plate, that $\mu_3$ can be calculated. This provides a setting where $\mu_3$ may be determined by experiment.

- The tension generated by the fibres in the fibre direction, $\mu_1$, plays no role at leading order.

We then turned to the extensional flow of a transversely isotropic sheet in chapter 3. This problem was studied by Howell [49] for a Newtonian fluid, and some special cases for a transveresly isotropic fluid were examined by Green and Friedman [41]. We manipulated the model of Green and Friedman to eliminate $u^{(1)}$, and constructed a numerical strategy to solve the equations in the general case. As was the case in chapter 2, the presence of the fibres caused interesting non-Newtonian behaviours to appear. We found

- A passive transversely isotropic sheet has a generalised Trouton viscosity, $G_2$, that depends on the fibre angle and could vary both spatially and temporally, controlled the behaviours of the sheet. The behaviours of the thickness and longitudinal velocity of the sheet were linked to $G_2$.

- As per the squeezing flow studied in chapter 2, increasing $\mu_2$ enhanced the non-Newtonian behaviours of the sheet, whilst increasing $\mu_3$ inhibited these behaviours. In particular, increasing $\mu_2$ had the effect of increasing the rate of thinning in some regions of the sheet, whilst inhibiting thinning to a greater degree in others.

- The centre-line need not be straight for a transversely isotropic fluid.

- When $\mu_1 \neq 0$, care must be taken to ensure that the rate of extension is fast enough to compensate for the compression generated by the fibres pulling in the transverse direction. Otherwise, the sheet will buckle and the model is not valid.

We were unable to satisfy an arbitrary initial condition for the centre-line of the fluid, which also occurs in the Newtonian problem [49]. In order to study the behaviour of initially curved sheets, and motivated by the non-Newtonian behaviour of the centre-line, we examined the short timescale behaviour of a transversely isotropic sheet in chapter 4. We derived equations governing the evolution of the flow and fibre angles on this timescale. This flow was not extensional, as there are bending stresses within the sheet on this timescale. Interestingly, the rotation of the fibres depended only upon the movement of the centre-line (equation (4.14)). We also found that the convergence of an arbitrary initial condition for the centre-line to the result predicted by the model in chapter 3 was not exponential. This is in contrast to the Newtonian case, where the centre-line decays exponentially to straight with homogeneous boundary conditions, as shown in [49]. We again considered the effects of varying the anisotropic extensional and shear viscosities and again found that increasing the anisotropic extensional viscosity, $\mu_2$, gives rise to greater non-Newtonian effects. In this problem, increasing $\mu_2$ had the effect of slightly increasing the time taken for the convergence of the centre-line to that predicted by the Green and Friedman model, and induced a greater degree of fibre rotation.

The final problem considered was the extensional flow of an axisymmetric, incompressible, viscous, transversely isotropic thread, in chapter 5. In this setting we included two fibre angles, one describing the angle with the $x$-axis, which was precisely the same as in chapters 2-4, and another angle describing the orientation of the fibres within the cross-section of the fluid. We found that

- When the fibre angle in the cross-section of the thread was fixed such that the fibres had a 'spoke-like' arrangement in the cross section of the thread, increasing $\mu_3$ inhibited the non-Newtonian behaviours of the thread.

- However, when this restriction was removed, $\mu_3$ was responsible for the development of some non-Newtonian behaviours, rather than inhibiting them as in chapters 2-4. These behaviours arose when $\mu_3 \gg \mu_2$, which means that the shear viscosity was dominating the behaviour of the flow.

- The fibres within the thread were able to rotate away from the longitudinal direction when $\mu_1 = 0$, particularly when $\mu_3$ was increased. This is in strong contrast to the sheet, where if $\mu_1 = 0$ the fibres would align in the direction of extension regardless of the values of $\mu_2, \mu_3$.

These complex behaviours throughout chapter 5 may be as a result of an inhomogenous viscosity, similar to the function $G_2$ discovered in chapter 3. As discussed in chapter 5, it may be possible to construct this viscosity numerically from equation (5.75). It may be possible to pick out certain combinations of parameters and fibre angles that cause the thread to quickly thin in a certain region, which would drastically decrease the spinnability of the thread. In this case, we could directly link the model derived in chapter 5 to measurements of spinnability of cervical mucus.

## 6.2 Future work

The work in this thesis was motivated by understanding how the interplay between the fibrous micro-structure and macroscopic flow of fluids such as collagen gel and cervical mucus altered their mechanical properties. Inclusion of effects such as inertia, surface tension and body forces may significantly alter the behaviour of the fluid and would lead to more realistic models. It is also possible that the fibres interact with each other and become entangled. This could be incorporated by using models of entanglement such as those in Ref. [56]. In addition, comparison of these models with experimental data could reveal the values of the key parameters.

The models presented in this thesis are complex coupled systems involving partial differential equations or integro-partial differential equations that do not yield readily

to analytical techniques. Therefore, there are opportunities for improved numerical techniques, or perhaps simplifications of the equations via other arguments. In particular, our numerical strategy in chapter 4 limited the range of values for the key parameters we could select. Large values of $\mu_2$ resulted in a choice of an extremely small time step in order not to violate the Courant–Friedrichs–Lewy condition. This resulted in long computational time. More sophisticated approaches may yield shorter computational times, or a wider range of parameter values to be tested. We also note the following particular areas

- We have not studied the breakup of the extensional flows of sheets and threads in this thesis. Non-Newtonian effects are known to play a role in the breakup of viscoelastic jets, as discussed in chapter 1.

- The squeezing flow in chapter 2 included free boundaries that were straight. In reality, we might expect this to not be the case, and that the boundary has a radius of curvature.

- In addition, the squeezing flow possessed thin layers close to $x = 0$ and $y = \frac{h}{2}$, where fibre alignment appears to take place on a longer timescale. Examining the movement of the fibres in this region on a longer timescale could yield interesting non-Newtonian results.

- An unrealistic two-dimensional geometry was assumed. A three-dimensional geometry would require two angles to define the direction of the fibres, and as we saw in chapter 5, this gave rise to a significant increase in the complexity of the equations.

- The model in chapter 3 models sheets with the employment of a Cartesian co-ordinate system restricting the model to examining sheets which are initially slightly curved. Where this is not the case, future work could entail the use of a curvilinear co-ordinate system to approach sheets with curvature in the centre-line, as in works similar to Ribe [82].

- In chapters 4 and 5, only sheets and threads for which $\mu_1 = 0$ were considered. As

we saw in chapter 3, $\mu_1$ can drive interesting non-Newtonian behaviours and should be considered.

- In chapter 5, there appears to be at least two regimes when $\mu_1 = 0$. Perhaps further asymptotic work could yield simpler equations in an regime where either the extensional or shear viscosities are dominant.

- Removing the assumption of axisymmetry of the thread and employment of a curvilinear co-ordinate system would provide a more realistic model.

Transversely isotropic fluids arise in a variety of contexts in industry and biology and it is therefore important to understand how the anisotropy induced by the fibres affect the underlying mechanics of the material. Throughout this thesis, we have applied systematic perturbation techniques to transversely isotropic thin film flows. This has allowed us to identify key timescales over which the flow and fibre alignment evolves, and uncover the non-Newtonian behaviours exhibited by this class of fluid. Whilst our present theory is not complete and the models presented in this thesis may not be immediately applicable in practice, we believe they represent a useful step towards improving our understanding of the mechanics of materials possessing a fibrous microstructure.

# Appendices

APPENDIX A

# APPENDIX FOR SQUEEZING FLOW

## A.1 Discretisation of the short time squeeze flow equations

In this appendix we give the discretisation and construction of the numerical solver we use to solve the short time squeezing flow problem. To summarise, our equations are

$$\frac{\partial}{\partial x}\int_0^{h_i} u\mathrm{d}y = -\dot{h}^{(0)}, \tag{A.1}$$

$$\frac{\partial \theta^{(0)}}{\partial \tau} = -\sin^2\theta^{(0)}\frac{\partial u^{(0)}}{\partial y}, \tag{A.2}$$

$$-\frac{\partial p^{(0)}}{\partial x} + \left(1+\mu_3+\mu_2\sin^2\theta^{(0)}\cos^2\theta^{(0)}\right)\frac{\partial^2 u^{(0)}}{\partial y^2} + \mu_2\frac{\partial}{\partial y}\left(\sin^2\theta^{(0)}\cos^2\theta^{(0)}\right)\frac{\partial u^{(0)}}{\partial y} = 0, \tag{A.3}$$

where pressure, longitudinal velocity, and fibre direction, $p^{(0)}(x,\tau), u^{(0)}(x,y,\tau), \theta^{(0)}(x,y,\tau)$ are the quantities to be computed. The distance between the plates, $h_i$, the velocity of the upper plate, $\dot{h}^{(0)}$, and an initial condition for the fibre direction $\theta(x,y,0)$ are prescribed. The strategy is as follows. Given $\theta(x,y,0)$, we simultaneously solve (A.1) and (A.3) to obtain $p^{(0)}, u^{(0)}$ at the first time step, before using (A.2) updating $\theta^{(0)}$ to the next time step. We repeat this process until we reach a desired time. We discretise with

$$\theta^{(0)}(x_i,y_j,\tau_k) = \theta^k_{i,j}, \text{ etc} \tag{A.4}$$

where $i = 1 : M+1, j = 1 : N+1, k = 1 : T+1$ where $M, N$ are the number of steps in the $x, y$-directions and $T$ is the number of time steps. The discretisation of equation (A.2) is

$$\theta_{i,j}^{k+1} = \theta_{i,j}^{k} - \frac{\Delta\tau}{2\Delta y}\left(u_{i,j+1}^{k} - u_{i,j-1}^{k}\right)\sin^2\theta_{i,j}^{k}, \tag{A.5}$$

where at the ends of the domain the centred finite differences on the right hand side of (A.5) are replaced by the appropriate one-sided approximations. We next consider equation (A.3). It is first helpful to define $\Gamma(x, y, \tau) = \sin^2\theta^{(0)}\cos^2\theta^{(0)}$. The discretisation is then

$$-\frac{p_{i+1}^{k} - p_{i-1}^{k}}{2\Delta x} + \left(1 + \mu_3 + \mu_2\Gamma_{i,j}^{k}\right)\frac{u_{i,j+1}^{k} - 2u_{i,j}^{k} + u_{i,j-1}^{k}}{\Delta y^2} + \mu_2\frac{\Gamma_{i,j+1}^{k} - \Gamma_{i,j-1}^{k}}{2\Delta y}\frac{u_{i,j+1}^{k} - u_{i,j-1}^{k}}{2\Delta y} = 0, \tag{A.6}$$

where we have already used that $\dfrac{\partial p^{(0)}}{\partial y} = 0$. In order to approach the integral equation (A.1), we define

$$I(x, \tau) = \int_0^{h_i} u \mathrm{d}y, \tag{A.7}$$

then application of the the trapezoidal rule gives

$$I_i^k = \frac{\Delta y}{2}\left(u_{i,1}^{k} + u_{i,N+1}^{k} + 2\sum_{n=2}^{N} u_{i,n}^{k}\right), \tag{A.8}$$

and hence we discretise (A.1) as

$$\frac{\Delta y}{4\Delta x}\left(\left(u_{i+1,1}^{k} + u_{i+1,N+1}^{k} + 2\sum_{n=2}^{N} u_{i+1,n}^{k}\right) - \left(u_{i-1,1}^{k} + u_{i-1,N+1}^{k} + 2\sum_{n=2}^{N} u_{i-1,n}^{k}\right)\right) = -\dot{h}. \tag{A.9}$$

The structure of the implicit solver for $u^{(0)}, p^{(0)}$ will then take the form

$$\begin{pmatrix} \boldsymbol{M}_U & \boldsymbol{M}_P \\ \boldsymbol{M}_{IC} & \mathbf{0} \\ \mathbf{0} & \boldsymbol{M}_{PB} \end{pmatrix}\begin{pmatrix} \boldsymbol{U} \\ \boldsymbol{P} \end{pmatrix} = \begin{pmatrix} \mathbf{0} \\ \boldsymbol{b} \\ \mathbf{0} \end{pmatrix}, \tag{A.10}$$

where $\boldsymbol{P}$ is simply the column vector of $p_i^k$, for all $i$, and $\boldsymbol{U}$ takes the form

$$\boldsymbol{U} = \begin{pmatrix} \boldsymbol{U_1} \\ \boldsymbol{U_2} \\ \vdots \\ \boldsymbol{U_{M+1}} \end{pmatrix} \tag{A.11}$$

where each $\boldsymbol{U_i}$ contains a column vector of the elements $u_{i,j}$ for all $j$. The vector $\boldsymbol{b}$, of length $M-1$, contains the RHS of equation (A.9) which we apply for $i = 2 : M$. At $i = 1, M+1$ we apply the no-stress boundary condition (i.e $p^{(0)} = 0$ on $x = \pm L$), the terms of which are contained in $\boldsymbol{M}_{PB}$. Now, the matricies $\boldsymbol{M}_U, \boldsymbol{M}_P$ contain the terms related to $u^{(0)}, p^{(0)}$ in equation (A.6), as well as the boundary conditions for $u^{(0)}$ on $y = 0, h$. Now, $\boldsymbol{M}_U$ is a $(M+1)(N+1) \times (M+1)(N+1)$ matrix, and is comprised of a collection of smaller matricies. We begin by defining

$$\gamma_{i,j} = \frac{1}{\Delta y^2}\left(1 + \mu_3 + \mu_2 \Gamma_{i,j}^k\right), \tag{A.12}$$

$$\lambda_{i,j} = \frac{\mu_2}{4\Delta y^2}\left(\Gamma_{i,j+1} - \Gamma_{i,j-1}\right), \tag{A.13}$$

to simplify the coefficients of $u_{i,j}^k$. Now, define

$$\boldsymbol{D}_i = \begin{pmatrix} 1 & & & & & & & \\ \gamma_{i,2} - \lambda_{i,2} & -2\lambda_{i,2} & \gamma_{i,2} + \lambda_{i,2} & & & & & \\ 0 & \gamma_{i,3} - \lambda_{i,3} & -2\lambda_{i,3} & \gamma_{i,3} + \lambda_{i,3} & & & & \\ & & \ddots & \ddots & \ddots & & & \\ & & & & & & & \\ & & & & & \gamma_{i,N} - \lambda_{i,N} & -2\lambda_{i,N} & \gamma_{i,N} + \lambda_{i,N} \\ & & & & & & & 1 \end{pmatrix}, \tag{A.14}$$

So that each $D_i$ is a $(N+1)\times(N+1)$ matrix. The first and final rows of $D_i$ correspond to the boundary conditions $u^{(0)}=0$ on $y=0,h$. Now, $\boldsymbol{M}_U$ is

$$\boldsymbol{M}_U=\begin{pmatrix}\boldsymbol{D}_1 & \boldsymbol{0} & & & & \\ \boldsymbol{0} & \boldsymbol{D}_2 & \boldsymbol{0} & & & \\ & \ddots & \ddots & \ddots & & \\ & & & \boldsymbol{D}_M & \boldsymbol{0} & \\ & & & \boldsymbol{0} & \boldsymbol{D}_{M+1} & \end{pmatrix}. \tag{A.15}$$

The matrix $\boldsymbol{M}_P$ is of dimension $(M+1)(N+1)\times(M+1)$ is similarly constructed from smaller block matricies. We begin by defining the matricies $\boldsymbol{J}_i$ to be a $(N+1)\times(M+1)$ matrix for each $i=1:M+1$. For $i=1,M+1$ we must adjust the discretisation (A.6), we simply use a forward (backward) finite difference scheme for the $\frac{\partial p^{(0)}}{\partial x}$ at either ends of the domain respectively. Then,

$$\boldsymbol{J}_1=\begin{pmatrix}0 & 0 & 0 & \dots \\ \frac{1}{\Delta x} & \frac{-1}{\Delta x} & 0 & \\ \vdots & \vdots & \vdots & \\ \frac{1}{\Delta x} & \frac{-1}{\Delta x} & 0 & \\ 0 & 0 & 0 & \dots\end{pmatrix}, \tag{A.16}$$

$$\boldsymbol{J}_i=\begin{pmatrix} & & & i-1^{\text{th}} & & i+1^{\text{th}} & & \\ 0 & \dots & & & & & & 0 \\ 0 & \dots & \frac{1}{2\Delta x} & 0 & \frac{-1}{2\Delta x} & 0 & \dots & \\ & & & \vdots & \vdots & \vdots & & \\ 0 & \dots & \frac{1}{2\Delta x} & 0 & \frac{-1}{2\Delta x} & 0 & \dots & \\ 0 & & & & & & & \end{pmatrix},$$

for $i = 2 : M$. The matrix $\boldsymbol{J}_{M+1}$ is similar to $\boldsymbol{J}_1$, except that the last two columns are filled. Finally, we can write $\boldsymbol{M}_p$:

$$\boldsymbol{M}_p = \begin{pmatrix} \boldsymbol{J}_1 \\ \boldsymbol{J}_2 \\ \vdots \\ \boldsymbol{J}_{M+1} \end{pmatrix}. \tag{A.17}$$

We turn our attention to the construction of $\boldsymbol{M}_{IC}, \boldsymbol{M}_{PB}$. We apply the integral condition (A.1) on $i = 2 : M$, with the no stress boundary condition $p^{(0)} = 0$, on $x = \pm L$ being applied on $i = 1, M + 1$. We define $\boldsymbol{M}_{IC}$ to be

$$\boldsymbol{M}_{IC} = \begin{pmatrix} \overbrace{-\frac{\Delta y}{4\Delta x} & \dots & -\frac{\Delta y}{4\Delta x}}^{N+1 \text{ terms, } I_1^k} & 0 & 0 & 0 & \overbrace{\frac{\Delta y}{4\Delta x} & \dots & \frac{\Delta y}{4\Delta x}}^{I_3^k} & 0 & \dots \\ 0 & 0 & 0 & -\frac{\Delta y}{4\Delta x} & -\frac{\Delta y}{4\Delta x} & -\frac{\Delta y}{4\Delta x} & 0 & 0 & 0 & \frac{\Delta y}{4\Delta x} & \dots \\ \vdots & \vdots & \vdots & & \ddots & \ddots & \ddots & & & & \\ & & & & & & & & & & \end{pmatrix}.$$

Each row of $\boldsymbol{M_{IC}}$ possesses $2\,(N+1)$ non-zero entries, corresponding to the use of the Simpsons rule upon the integral condition (see (A.9)). Finally, the matrix $\boldsymbol{M}_{PB}$ is a $2 \times (M+1)$ matrix. The no-stress boundary conditions supply $p_1^k = p_{M+1}^k = 0$ for all $k$. Hence, we simply have

$$\boldsymbol{M}_{PB} = \begin{pmatrix} 1 & 0 \dots & & \\ 0 & \dots & 0 & 1 \end{pmatrix}. \tag{A.18}$$

## A.2 Functions defined in Section 2.6.1

In this appendix, we present the functions $\mathcal{W}$ and $\mathcal{Z}$, as defined by integrals in Section 2.6.1 for completeness. As these functions are rather lengthy, they were omitted from the main Chapter for the sake of concision. We begin by considering the function $\mathcal{W}$ as

defined in equation (2.37). We may write

$$\mathcal{W} = \mathcal{W}_1\left(x, y, \tau, \theta_i\right) - \mathcal{W}_1\left(x, 0, \tau, \theta_i\right), \tag{A.19}$$

where

$$\begin{aligned}\mathcal{W}_1 = -\frac{\log Q}{144x^2\tau^2\tan^2\theta_i} + \frac{1}{144x^2\tau^2\tan^3\theta_i}\left(\arctan\left(\frac{1+6x\tau\tan\theta_i\left(1-2y\right)}{\tan\theta_i}\right)\right) \\ - \frac{1}{144x^2\tau^2 Q\tan^2\theta_i}\left(6x\tau(1-2y)\tan\theta_i + 1 + \tan^2\theta_i\right),\end{aligned} \tag{A.20}$$

and

$$Q = \left(1 + 6x\tau\tan\theta_i(1-2y)\right)^2 + \tan^2\theta_i. \tag{A.21}$$

Similarly, we may express $\mathcal{Z}$ in closed form, we write

$$\mathcal{Z} = \mathcal{Z}_1\left(x, y, \tau, \theta_i\right) - \mathcal{Z}_1\left(x, 0, \tau, \theta_i\right), \tag{A.22}$$

where

$$\begin{aligned}\mathcal{Z}_1 = \left(\frac{3\tan^2\theta_i - 6(1-2y)x\tau\tan\theta_i - 1}{1728x^3\tau^3\tan^4\theta_i}\right)\arctan\left(\frac{1+6x\tau\tan\theta_i(1-2y)}{\tan\theta_i}\right) \\ + \left(\frac{4+12(1-2y)x\tau\tan\theta_i}{3456x^3\tau^3\tan^3\theta_i}\right)\log Q + \frac{y}{72x^2\tau^2\tan^2\theta_i} - y\mathcal{W}_1\left(x, 0, \tau, \theta_i\right).\end{aligned} \tag{A.23}$$

APPENDIX B

# APPENDIX FOR TI SHEET

## B.1 Model equations in full

For the purposes of convenience, we give the dimensionless forms of (3.1), (3.2) and (3.3) in component form,

$$\frac{\partial u}{\partial x} + \frac{\partial v}{\partial y} = 0, \tag{B.1}$$

for conservation of mass, with the momentum equation (3.2) yielding in the $x$-direction:

$$\begin{aligned}
&-\varepsilon^2\frac{\partial p}{\partial x} + \frac{\partial^2 u}{\partial y^2} + \varepsilon^2\frac{\partial^2 u}{\partial x^2} + \varepsilon^2\mu_1\frac{\partial}{\partial x}(\cos^2\theta) + \varepsilon\mu_1\frac{\partial}{\partial y}(\cos\theta\sin\theta) \\
&\quad + \mu_2\frac{\partial}{\partial x}\left[\varepsilon^2\cos^4\theta\frac{\partial u}{\partial x} + \cos^3\theta\sin\theta\left(\varepsilon\frac{\partial u}{\partial y} + \varepsilon^3\frac{\partial v}{\partial x}\right) + \varepsilon^2\cos^2\theta\sin^2\theta\frac{\partial v}{\partial y}\right] \\
&\quad + 2\mu_3\frac{\partial}{\partial x}\left[2\varepsilon^2\cos^2\theta\frac{\partial u}{\partial x} + \cos\theta\sin\theta\left(\varepsilon\frac{\partial u}{\partial y} + \varepsilon^3\frac{\partial v}{\partial x}\right)\right] \\
&\quad + \mu_2\frac{\partial}{\partial y}\left[\cos\theta\sin\theta\left(\varepsilon\cos^2\theta\frac{\partial u}{\partial x} + \cos\theta\sin\theta\left(\frac{\partial u}{\partial y} + \varepsilon^2\frac{\partial v}{\partial x}\right) + \varepsilon\sin^2\theta\frac{\partial v}{\partial y}\right)\right] \\
&\quad + \mu_3\frac{\partial}{\partial y}\left[\frac{\partial u}{\partial y} + \varepsilon^2\frac{\partial v}{\partial x}\right] = 0,
\end{aligned} \tag{B.2}$$

whilst in the $y$ direction we have:

$$
\begin{aligned}
&-\varepsilon\frac{\partial p}{\partial y}+\varepsilon^3\frac{\partial^2 v}{\partial x^2}+\varepsilon\frac{\partial^2 v}{\partial y^2}+\varepsilon\mu_1\frac{\partial}{\partial y}(\sin^2\theta)+\varepsilon^2\mu_1\frac{\partial}{\partial x}(\cos\theta\sin\theta)\\
&\quad+\mu_2\frac{\partial}{\partial y}\left[\varepsilon\sin^2\theta\cos^2\theta\frac{\partial u}{\partial x}+\cos\theta\sin^3\theta\left(\frac{\partial u}{\partial y}+\varepsilon^2\frac{\partial v}{\partial x}\right)+\varepsilon\sin^4\theta\frac{\partial v}{\partial y}\right]\\
&\quad+2\mu_3\frac{\partial}{\partial y}\left[2\varepsilon\sin^2\theta\frac{\partial v}{\partial y}+\cos\theta\sin\theta\left(\frac{\partial u}{\partial y}+\varepsilon^2\frac{\partial v}{\partial x}\right)\right]\\
&\quad+\mu_2\frac{\partial}{\partial x}\left[\varepsilon^2\sin\theta\cos^3\theta\frac{\partial u}{\partial x}+\cos^2\theta\sin^2\theta\left(\varepsilon\frac{\partial u}{\partial y}+\varepsilon^3\frac{\partial v}{\partial x}\right)+\varepsilon^2\cos\theta\sin^3\theta\frac{\partial v}{\partial y}\right]\\
&\quad+\mu_3\frac{\partial}{\partial x}\left[\varepsilon\frac{\partial u}{\partial y}+\varepsilon^3\frac{\partial v}{\partial x}\right]=0,
\end{aligned}
\tag{B.3}
$$

with the fibre director field being given by

$$
\varepsilon\frac{\partial\theta}{\partial t}+\varepsilon u\frac{\partial\theta}{\partial x}+\varepsilon v\frac{\partial\theta}{\partial y}=-\varepsilon\sin\theta\cos\theta\frac{\partial u}{\partial x}-\sin^2\theta\frac{\partial u}{\partial y}+\varepsilon^2\cos^2\theta\frac{\partial v}{\partial x}+\varepsilon\sin\theta\cos\theta\frac{\partial v}{\partial y}.
\tag{B.4}
$$

## B.2 Simplification of the equation for $\theta$

In the main text, we claimed that equation (3.27) permitted great simplification by noting that the equation corresponded only to advection in a purely horizontal direction the reference domain. To demonstrate this simplification, suppose $\tilde{\theta}\,(x', y', t)$ is a function defined over $D_{\text{ref}}$ that satisfies the advection equation

$$
\frac{\partial\tilde{\theta}}{\partial t}+\tilde{u}\frac{\partial\tilde{\theta}}{\partial x'}=\tilde{f},
\tag{B.5}
$$

where $\tilde{u}(x',t)$ and $\tilde{f}(x',t)$ are a horizontal advection velocity and forcing term respectively. We can relate $\theta(x,y,t) = \tilde{\theta}(x(x',t), y(x',y',t), t)$, and using the mapping $\mathbf{\Phi}$, which gives

$$\frac{\partial \tilde{\theta}}{\partial t} = \frac{\partial \theta}{\partial t} + \frac{\dot{L}x}{L}\frac{\partial \theta}{\partial x} + \left(\frac{\partial H}{\partial t} + \left(\frac{y-H}{h}\right)\frac{\partial h}{\partial t} + \frac{\dot{L}x}{L}\left(\frac{\partial H}{\partial x} + \left(\frac{y-H}{h}\right)\frac{\partial h}{\partial x}\right)\right)\frac{\partial \theta}{\partial y}, \quad \text{(B.6)}$$

$$\frac{\partial \tilde{\theta}}{\partial x'} = L\frac{\partial \theta}{\partial x} + L\left(\frac{\partial H}{\partial x} + \left(\frac{y-H}{h}\right)\frac{\partial h}{\partial x}\right)\frac{\partial \theta}{\partial y}. \quad \text{(B.7)}$$

Substituting (B.6)-(B.7) into (B.5), then yields

$$\frac{\partial \theta}{\partial t} + \frac{\partial \theta}{\partial x}\left(L\tilde{u} + \frac{\dot{L}x}{L}\right) + \frac{\partial \theta}{\partial y}\left(\frac{\partial H}{\partial t} + \left(\frac{y-H}{h}\right)\frac{\partial h}{\partial t} + \left(\frac{\partial H}{\partial x} + \left(\frac{y-H}{h}\right)\frac{\partial h}{\partial x}\right)\left(L\tilde{u} + \frac{\dot{L}x}{L}\right)\right) = \tilde{f}, \quad \text{(B.8)}$$

we now choose $u(x,t) = L\tilde{u} + \dfrac{\dot{L}x}{L}$, in order to recover the correct coefficient of $\dfrac{\partial \theta}{\partial x}$. Examining the coefficient of the $\dfrac{\partial \theta}{\partial y}$ term we note that

$$\frac{\partial H}{\partial t} + \left(\frac{y-H}{h}\right)\frac{\partial h}{\partial t} + u\left(\frac{\partial H}{\partial x} + \left(\frac{y-H}{h}\right)\frac{\partial h}{\partial x}\right) \quad \text{(B.9)}$$

$$= \frac{\partial H}{\partial t} + u\frac{\partial H}{\partial x} + \left(\frac{y-H}{h}\right)\left(-h\frac{\partial u}{\partial x}\right) \quad \text{(B.10)}$$

$$= \frac{\partial H}{\partial t} + \frac{\partial}{\partial x}(uH) - y\frac{\partial u}{\partial x} = v \quad \text{(B.11)}$$

where we have used the equation for conservation of mass, (3.8), to obtain (B.10). Here, we have demonstrated that the coefficient of $\theta_y$ is precisely $v$ when mapping back from $D_{ref}$ to the original domain. Therefore, we have shown that the advection of $\theta$ is purely horizontal upon the reference domain, with velocity $\tilde{u}(x',t) = \dfrac{u - \dot{L}x'}{L} = \dfrac{u - u_{\text{mesh}}}{L}$.

## B.3 Discretisation of the Green and Friedman integral equations

In what follows, the treatment of the integral equations is in the Eulerian framework. With the equation for $u$, the following approach yields precisely the same approximation in either system of variables. The integral equation for $H$ is more convenient to treat in the Eulerian frame. Additionally, we drop the superscript notation for leading-order quantities.

The integral equations (3.30),(3.31) require further treatment before being discretised and solved. Introduce

$$F(x,y,t) = \frac{\mu_1 \cos 2\theta + (4 + 4\mu_3 + \mu_2)\, u_x}{4 + 4\mu_3 + \mu_2 \sin^2 2\theta}, \tag{B.12}$$

it will be convenient now to break this up into $F = F_1 + u_x F_2$, where

$$F_1 = \frac{\mu_1 \cos 2\theta}{4 + 4\mu_3 + \mu_2 \sin^2 2\theta}, \qquad F_2 = \frac{4 + 4\mu_3 + \mu_2}{4 + 4\mu_3 + \mu_2 \sin^2 2\theta}, \tag{B.13}$$

in much the same way, we also introduce notation for the integrals of $F$, by defining $G = G_1 + u_x G_2$, where

$$G_m(x,y,t) = \int_{H^-}^{y} F_m(x,s,t)\,\mathrm{d}s, \tag{B.14}$$

for $m = 1, 2$. Equation (3.30) can now be written as

$$0 = \frac{\partial}{\partial x}\left(G_1\left(x, H^+, t\right) + u_x(x,t)\, G_2\left(x, H^+, t\right)\right), \tag{B.15}$$

using the trapezoidal rule,

$$G_m\left(x, H^+, t\right) = \frac{h(x,t)}{N-1}\left(\frac{F_m(x,y_0,t) + F_m(x,y_{N-1},t)}{2} + \sum_{i=1}^{N-2} F_m(x,y_i,t)\right), \tag{B.16}$$

where $N$ is the number of nodes in the $y$-direction. We note that upon substituting the trapezoidal rule into (B.15), the result does not depend on $H$. That is, its presence in the integration limits is redundant and effectively just describes a vertical translation. Therefore, $H$ is decoupled from the rest of the system and we can easily solve the integral for $u$ in either the Eulerian or ALE frame and then calculate $H$ at a desired time. Choosing to approach the equation for $u$ in the ALE framework, by applying the same approach to equation (3.30) yields precisely the same discretisation as the Eulerian. For completeness, we include the discretisation for equation (B.15). First, introduce the notation

$$[G_m]^k_{i,N-1} = G_m\left(x_i, H^k_i + h^k_i/2, t_k\right), \tag{B.17}$$

now (B.15) gives us, through normal finite differences,

$$\frac{[G_1]^k_{i-1,N-1} - [G_1]^k_{i+1,N-1}}{2L/(M-1)} = \frac{[G_2]^k_{i+1,N-1} - [G_2]^k_{i-1,N-1}}{2L/(M-1)} \frac{u^k_{i+1} - u^k_i}{2L/(M-1)} + \frac{u^k_i - 2u^k_i + u^k_{i-1}}{(L/(M-1))^2} [G_2]^k_{i,N-1}, \tag{B.18}$$

where $N, M$ are the number of nodes in the vertical and horizontal directions respectively so that $i = 0 : M-1, j = 0 : N-1$. Noting that $u^k_0 = 0$, $u^k_{M-1} = \dot{L}(t_k)$, and that $G_m$ is readily precomputed at each time-step $k$, yields a tri-diagonal system for $u^k$. If we now consider the equation for $H$, (3.28), this is the only equation in the model that is indeed easier to treat in the Eulerian framework than the ALE. Using the Leibniz rule one may write equation (3.15) as

$$0 = -\left(H_{xx} + \frac{h_{xx}}{2}\right) G\left(x, H^+, t\right) + \frac{\partial^2}{\partial x^2} \int_{H^-}^{H^+} G(x, y, t) \mathrm{d}y, \tag{B.19}$$

in order to proceed, one must apply the trapezoidal rule twice to each $G_m$. Applying it once yields

$$\int_{H^-}^{H^+} G_m(x,y,t)\,\mathrm{d}y = \frac{h(x,t)}{N-1}\left(\frac{G_m(x,y_0,t)+G_m(x,y_{N-1},t)}{2}+\sum_{j=1}^{N-2} G_m(x,y_j,t)\right), \quad \text{(B.20)}$$

then, for each $j>0$,

$$G_m(x,y_j,t) = \frac{h(x,t)}{N-1}\left(\frac{F_m(x,y_0,t)+F_m(x,y_j,t)}{2}+\sum_{i=1}^{j-1} F_m(x,y_i,t)\right), \quad \text{(B.21)}$$

for the case $j=0$, $G_m(x,y_0,t)=0$. Substitution of (B.21) into (B.20) yields

$$\int_{H^-}^{H^+} G_m(x,y,t)\,\mathrm{d}y = \left(\frac{h}{N-1}\right)^2\left(\frac{2N-3}{4}F_m(x,y_0,t)+\frac{1}{4}F_m(x,y_{N-1},t) + \sum_{j=1}^{N-2}(N-1-j)\,F_m(x,y_j,t)\right). \quad \text{(B.22)}$$

Finally, we require the introduction of the notation

$$[IG_m]_i^k = \int_{H^-}^{H^+} G_m(x_i,y,t_k)\,\mathrm{d}y, \quad \text{(B.23)}$$

for $m=1,2$. Clearly, we use (B.22) to precompute $[IG_m]$ at the required nodes as necessary. The discretisation of equation (B.19) is then

$$\begin{aligned}
&\frac{H_{i-1}^k-2H_i^k+H_{i+1}^k}{\left(L(t_k)/(M-1)\right)^2}\left([G_1]_i^k+\frac{u_{i+1}^k-u_{i-1}^k}{2L(t_k)/(M-1)}[G_2]_i^k\right)\\
&=-\frac{h_{i-1}^k-2h_i^k+h_{i+1}^k}{2\left(L(t_k)/(M-1)\right)^2}\left([G_1]_i^k+\frac{u_{i+1}^k-u_{i-1}^k}{2L(t_k)/(M-1)}[G_2]_i^k\right)+\frac{[IG_1]_{i-1}^k-2[IG_1]_i^k+[IG_1]_{i+1}^k}{\left(L(t_k)/(M-1)\right)^2}\\
&\quad+\frac{u_{i+2}^k-2u_{i+1}^k+2u_{i-1}^k-u_{i-2}^k}{2\left(L(t_k)/(M-1)\right)^3}[IG_2]_i^{k+1}+\frac{u_{i+1}^k-2u_i^k+u_{i-1}^k}{\left(L(t_k)/(M-1)\right)^2}\frac{[IG_2]_{i+1}^k-[IG_2]_{i-1}^k}{2L(t_k)/(M-1)}\\
&\quad+\frac{[IG_2]_{i+1}^k-2[IG_2]_i^k+[IG_2]_{i-1}^k}{\left(L(t_k)/(M-1)\right)^2}\frac{u_{i+1}^k-u_{i-1}^k}{2L(t_k)/(M-1)}. \quad \text{(B.24)}
\end{aligned}$$

Equation (B.24) contains wholly precomputable quantities on the RHS. Therefore, similar to the equation for $u$, this creates a tri-diagonal system to be solved for $H$. For the specific cases of $i = 0, M-1$, we have the boundary condition that $H_0^k = H_{M-1}^k = 0$. For the cases of $i = 1, M-2$, the discretisation must be modified slightly because the stencil for the $u_{xxx}$ is too wide. This can be done in a number of ways and is omitted.

APPENDIX C

# APPENDIX FOR SHORT TIME TI SHEET

## C.1 Derivation of the second integro-differential equation in the short timescale model

The process of deriving the second integro-differential equation is similar to obtaining (4.33), but the equations are at $\mathcal{O}(\varepsilon^4)$ and require numerous earlier results to reduce the equations. We begin with the continuity equations at $\mathcal{O}(\varepsilon^3)$ and $\mathcal{O}(\varepsilon^4)$, which are

$$\frac{\partial u^{(1)}}{\partial x} + \frac{\partial V^{(3)}}{\partial y} = 0, \tag{C.1}$$

$$\frac{\partial u^{(2)}}{\partial x} + \frac{\partial V^{(4)}}{\partial y} = 0, \tag{C.2}$$

We will also require the $\mathcal{O}(\varepsilon^3)$ $x$-momentum equation (4.27), into which we substitute (4.23) to eliminate $p^{(0)}$ and (4.19) to eliminate $V^{(2)}$:

$$\begin{aligned}\frac{\partial}{\partial y}\Bigg[&\left(\frac{\partial V^{(2)}}{\partial x} + \frac{\partial u^{(2)}}{\partial y}\right)\left(1 + \mu_2 \cos^2\theta^{(0)} \sin^2\theta^{(0)} + \mu_3\right) + \mu_1 \theta^{(1)} \cos 2\theta^{(0)} \\ &+ \mu_2 \left(\theta^{(1)} \cos 4\theta^{(0)} \frac{\partial u^{(0)}}{\partial x} + \frac{1}{4}\sin 4\theta^{(0)} \frac{\partial u^{(1)}}{\partial x} + \frac{1}{2}\theta^{(1)} \sin 4\theta^{(0)} \left(\frac{\partial u^{(1)}}{\partial y} + \frac{\partial V^{(1)}}{\partial x}\right)\right)\Bigg] \\ &= -\frac{\partial}{\partial x}\Bigg[4\frac{\partial u^{(0)}}{\partial x} + \mu_1 \cos 2\theta^{(0)} + \mu_2 \cos^2 2\theta^{(0)} \frac{\partial u^{(0)}}{\partial x} \\ &\qquad + \frac{\mu_2}{4}\sin 4\theta^{(0)} \left(\frac{\partial u^{(1)}}{\partial y} + \frac{\partial V^{(1)}}{\partial x}\right) + 4\mu_3 \frac{\partial u^{(0)}}{\partial x}\Bigg].\end{aligned} \tag{C.3}$$

Then, the $y$-momentum equation at this order is,

$$\frac{\partial \mathcal{A}}{\partial y} + \frac{\partial \mathcal{B}}{\partial x} - \frac{\partial^2 V^{(4)}}{\partial y^2} - \frac{\partial^2 u^{(2)}}{\partial x \partial y} = 0, \tag{C.4}$$

with the associated boundary condition,

$$\mathcal{A} = \left( \frac{\partial H^{(0)}}{\partial x} \pm \frac{1}{2} \frac{\partial h^{(0)}}{\partial x} \right) \mathcal{B}; \text{ on } y = H^{(0)^{\pm}}, l \tag{C.5}$$

where

$$\begin{aligned}
\mathcal{A} = -p^{(2)} + 2\frac{\partial V^{(4)}}{\partial y} + \mu_1 \left( \theta^{(1)^2} \cos 2\theta^{(0)} + \theta^{(2)} \sin 2\theta^{(0)} \right) + \mu_2 \Bigg( \sin^2 \theta^{(0)} \cos^2 \theta^{(0)} \frac{\partial u^{(2)}}{\partial x} \\
+ \frac{\theta^{(1)}}{2} \sin 4\theta^{(0)} \frac{\partial u^{(1)}}{\partial x} + \left( \theta^{(1)^2} \cos 4\theta^{(0)} + \frac{\theta^{(1)}}{2} \sin 4\theta^{(0)} \right) \frac{\partial u^{(0)}}{\partial x} + \cos \theta^{(0)} \sin^3 \theta^{(0)} \left( \frac{\partial u^{(3)}}{\partial y} + \frac{\partial V^{(3)}}{\partial x} \right) \\
+ \theta^{(1)} \left( 3 \sin^2 \theta^{(0)} \cos^2 \theta^{(0)} - \sin^4 \theta^{(0)} \right) \left( \frac{\partial u^{(2)}}{\partial y} + \frac{\partial V^{(2)}}{\partial x} \right) \\
+ \Bigg( \theta^{(2)} \left( 3 \sin^2 \theta^{(0)} \cos^2 \theta^{(0)} - \sin^4 \theta^{(0)} \right) \\
+ \theta^{(1)^2} \left( 3 \sin \theta^{(0)} \cos^3 \theta^{(0)} - 5 \sin^3 \theta^{(0)} \cos \theta^{(0)} \right) \Bigg) \left( \frac{\partial u^{(1)}}{\partial y} + \frac{\partial V^{(1)}}{\partial x} \right) \\
+ \sin^4 \theta^{(0)} \frac{\partial V^{(4)}}{\partial y} + 4\theta^{(1)} \cos \theta^{(0)} \sin^3 \theta^{(0)} \frac{\partial V^{(3)}}{\partial y} \\
+ \left( 4\theta^{(2)} \cos \theta^{(0)} \sin^3 \theta^{(0)} + 2\theta^{(1)^2} \left( 3 \sin^2 \theta^{(0)} \cos^2 \theta^{(0)} - \sin^4 \theta^{(0)} \right) \right) \frac{\partial V^{(2)}}{\partial y} \Bigg) \\
+ 2\mu_3 \Bigg( 2 \sin^2 \theta^{(0)} \frac{\partial V^{(4)}}{\partial y} + \left( 4\theta^{(2)} \sin \theta^{(0)} \cos \theta^{(0)} + 2\theta^{(1)^2} \cos 2\theta^{(0)} \right) \frac{\partial V^{(2)}}{\partial y} \\
+ 4\theta^{(1)} \cos \theta^{(0)} \sin \theta^{(0)} \frac{\partial V^{(3)}}{\partial y} \\
+ \cos \theta^{(0)} \sin \theta^{(0)} \left( \frac{\partial u^{(3)}}{\partial y} + \frac{\partial V^{(3)}}{\partial x} \right) + \theta^{(1)} \cos 2\theta^{(0)} \left( \frac{\partial u^{(2)}}{\partial y} + \frac{\partial V^{(2)}}{\partial x} \right) \\
+ \left( \theta^{(2)} \cos 2\theta^{(0)} - \theta^{(1)^2} \sin 2\theta^{(0)} \right) \left( \frac{\partial u^{(1)}}{\partial y} + \frac{\partial V^{(1)}}{\partial x} \right) \Bigg) \Bigg),
\end{aligned} \tag{C.6}$$

$$\mathcal{B} = \frac{\partial V^{(2)}}{\partial x} + \frac{\partial u^{(2)}}{\partial y} + \mu_1\theta^{(1)}\cos 2\theta^{(0)} + \mu_2\left(\theta^{(1)}\left(\cos^4\theta^{(0)} - 3\sin^2\theta^{(0)}\cos^2\theta^{(0)}\right)\frac{\partial u^{(0)}}{\partial x}\right.$$
$$+ \sin\theta^{(0)}\cos^3\theta^{(0)}\frac{\partial u^{(1)}}{\partial x} + \cos^2\theta^{(0)}\sin^2\theta^{(0)}\left(\frac{\partial u^{(2)}}{\partial y} + \frac{\partial V^{(2)}}{\partial x}\right)$$
$$+ \frac{\theta^{(1)}}{2}\sin 4\theta^{(0)}\left(\frac{\partial u^{(1)}}{\partial y} + \frac{\partial V^{(1)}}{\partial x}\right)$$
$$\left.+\cos\theta^{(0)}\sin^3\theta^{(0)}\frac{\partial V^{(3)}}{\partial y} + \theta^{(1)}\left(3\sin^2\theta^{(0)}\cos^2\theta^{(0)} - \sin^4\theta^{(0)}\right)\frac{\partial V^{(2)}}{\partial y}\right) + \mu_3\left(\frac{\partial u^{(2)}}{\partial y} + \frac{\partial V^{(2)}}{\partial x}\right). \tag{C.7}$$

Integrating (C.4) over the depth of the sheet yields

$$\mathcal{A}|_{y=H^{(0)+}} - \mathcal{A}|_{y=H^{(0)-}} + \int_{H^-}^{H^+}\frac{\partial \mathcal{B}}{\partial x}\mathrm{d}y = 0. \tag{C.8}$$

Use of the Liebniz rule, the boundary condition (C.5), the continuity equation at $\mathcal{O}(\varepsilon^3)$, (C.1) and rearranging gives

$$\frac{\partial}{\partial x}\int_{H^{(0)-}}^{H^{(0)+}}\left[\left(\frac{\partial V^{(2)}}{\partial x} + \frac{\partial u^{(2)}}{\partial y}\right)\left(1 + \mu_2\cos^2\theta^{(0)}\sin^2\theta^{(0)} + \mu_3\right) + \mu_1\theta^{(1)}\cos 2\theta^{(0)}\right.$$
$$\left.+ \mu_2\left(\theta^{(1)}\cos 4\theta^{(0)}\frac{\partial u^{(0)}}{\partial x} + \frac{1}{4}\sin 4\theta^{(0)}\frac{\partial u^{(1)}}{\partial x} + \frac{\theta^{(1)}}{2}\sin 4\theta^{(0)}\left(\frac{\partial u^{(1)}}{\partial y} + \frac{\partial V^{(1)}}{\partial x}\right)\right)\right]\mathrm{d}y = 0. \tag{C.9}$$

In order to eliminate $V^{(2)}, u^{(2)}, \theta^{(1)}$, we integrate (C.3), and substitute directly into (C.9),

$$\frac{\partial}{\partial x}\int_{H^{(0)-}}^{H^{(0)+}}\left(\int_{H^{(0)-}}^{y}\frac{\partial}{\partial x}\left[4\frac{\partial u^{(0)}}{\partial x} + \mu_1\cos 2\theta^{(0)} + \mu_2\cos^2 2\theta^{(0)}\frac{\partial u^{(0)}}{\partial x}\right.\right.$$
$$\left. + \frac{\mu_2}{4}\sin 4\theta^{(0)}\left(\frac{\partial u^{(1)}}{\partial y} + \frac{\partial V^{(1)}}{\partial x}\right) + 4\mu_3\frac{\partial u^{(0)}}{\partial x}\right]\mathrm{d}y$$
$$- \left(\frac{\partial H^{(0)}}{\partial x} - \frac{1}{2}\frac{\partial h^{(0)}}{\partial x}\right)\left[4\frac{\partial u^{(0)}}{\partial x} + \mu_1\cos 2\theta^{(0)} + \mu_2\cos^2 2\theta^{(0)}\frac{\partial u^{(0)}}{\partial x}\right.$$
$$\left.\left. + \frac{\mu_2}{4}\sin 4\theta^{(0)}\left(\frac{\partial u^{(1)}}{\partial y} + \frac{\partial V^{(1)}}{\partial x}\right) + 4\mu_3\frac{\partial u^{(0)}}{\partial x}\right]_{y=H^{(0)-}}\right)\mathrm{d}y = 0. \tag{C.10}$$

Evaluating this in the Newtonian case gives the equation of the centre-line from [49]. The second term arises because we have arbitrarily chosen the lower limit of the inner integral and so we need to add that value back on. A final application of the Leibniz rule finally yields

$$\frac{\partial}{\partial x}\int_{H^{(0)-}}^{H^{(0)+}}\frac{\partial}{\partial x}\int_{H^{(0)-}}^{y}4\frac{\partial u^{(0)}}{\partial x}+\mu_1\cos 2\theta^{(0)}+\mu_2\cos^2 2\theta^{(0)}\frac{\partial u^{(0)}}{\partial x} \\ +\frac{\mu_2}{4}\sin 4\theta^{(0)}\left(\frac{\partial u^{(1)}}{\partial y}+\frac{\partial V^{(1)}}{\partial x}\right)+4\mu_3\frac{\partial u^{(0)}}{\partial x}\mathrm{d}y'\mathrm{d}y=0, \quad \text{(C.11)}$$

which is precisely equation (4.36).

## C.2 Discretisation of the short timescale model

In this section, we give the discretisation of the full system of the short timescale equations, namely (4.14),(4.35),(4.37). As before, we drop the superscript notation for leading-order quantities. We discretise with

$$\theta(x_i, y_j, \tau_k) = \theta^k_{i,j}, \text{ etc} \quad \text{(C.12)}$$

and for functions that contain subscripts:

$$Z_1(x_i, y_j, \tau_k) = [Z_1]^k_{i,j}, \text{ etc} \quad \text{(C.13)}$$

where $i = 1 : M-1, j = 1 : N-1$, where $M, N$ are the number of nodes in the $x, y$-directions.

### C.2.1 Theta Equation

We readily write the discretisation for equation (4.14):

$$\frac{\theta_{i,j}^{k+1}-\theta_{i,j}^{k}}{\Delta\tau}+\frac{H_i^{k+1}-H_i^k}{\Delta\tau}\frac{\theta_{i,j+1}^{k}-\theta_{i,j}^{k}}{\Delta y}=0,\ \text{for}\ \frac{\partial H}{\partial\tau}<0, \tag{C.14}$$

$$\frac{\theta_{i,j}^{k+1}-\theta_{i,j}^{k}}{\Delta\tau}+\frac{H_i^{k+1}-H_i^k}{\Delta\tau}\frac{\theta_{i,j}^{k}-\theta_{i,j-1}^{k}}{\Delta y}=0,\ \text{for}\ \frac{\partial H}{\partial\tau}>0, \tag{C.15}$$

we can combine (C.14), (C.15) by defining

$$a_i^+=\max(H_i^{k+1}-H_i^k,0),\qquad a_i^-=\min(H_i^{k+1}-H_i^k,0),$$

we may now write

$$\theta_{i,j}^{k+1}=\theta_{i,j}^{k}-\frac{1}{\Delta y}\left(a_i^+\left(\theta_{i,j}^{k}-\theta_{i,j-1}^{k}\right)+a_i^-\left(\theta_{i,j+1}^{k}-\theta_{i,j}^{k}\right)\right). \tag{C.16}$$

### C.2.2 Equation for $\bar{u}$ and $H$

Equation (4.41) supplies the following equation for $\bar{u}$:

$$\frac{\partial}{\partial x}\int_{-\frac{1}{2}}^{\frac{1}{2}}\frac{\mu_1\cos 2\theta+(4+4\mu_3+\mu_2)\frac{\partial\bar{u}}{\partial x}}{4+4\mu_3+\mu_2\sin^2 2\theta}h\mathrm{d}\tilde{y}+\frac{\partial}{\partial x}\left(\frac{\partial H}{\partial x}\frac{\partial^2 H}{\partial x\partial\tau}\int_{-\frac{1}{2}}^{\frac{1}{2}}\frac{(4+4\mu_3+\mu_2)}{4+4\mu_3+\mu_2\sin^2 2\theta}h\mathrm{d}\tilde{y}\right.$$
$$\left.-\frac{\partial^3 H}{\partial x^2\partial\tau}\int_{-\frac{1}{2}}^{\frac{1}{2}}\frac{(4+4\mu_3+\mu_2)\,\tilde{y}}{4+4\mu_3+\mu_2\sin^2 2\theta}h^2\mathrm{d}\tilde{y}\right)=0. \tag{C.17}$$

Similarly to the discretisation of the Green and Friedman model equations, we define

$$Z_1(x,y,\tau) = \int_{-\frac{1}{2}}^{y} \frac{\mu_1 \cos 2\theta}{4+4\mu_3+\mu_2 \sin^2 2\theta} h \mathrm{d}\tilde{y}, \tag{C.18}$$

$$Z_2(x,y,\tau) = \int_{-\frac{1}{2}}^{y} \frac{4+4\mu_3+\mu_2}{4+4\mu_3+\mu_2 \sin^2 2\theta} h \mathrm{d}\tilde{y}, \tag{C.19}$$

$$J(x,t) = \int_{-\frac{1}{2}}^{\frac{1}{2}} \frac{(4+4\mu_3+\mu_2)\, h^2 y'}{4+4\mu_3+\mu_2 \sin^2 2\theta} \mathrm{d}\tilde{y}, \tag{C.20}$$

we note that the definitions of $Z_1, Z_2$ here are similar to $G_1, G_2$ in appendix B.3, but are not precisely the same. It is possible to obtain $G_1, G_2$ from $Z_1, Z_2$ by undoing both the transformation $y = H + h\tilde{y}$ and the short-timescale. Since the ALE transformation in chapter 3 acts only as a linear transformation on the integral equations, one may treat $Z_1, Z_2$ as the integrals in ALE form on the short-timescale. We did not use the ALE machinery on the short timescale model as the boundaries are fixed, as the sheet does not extend or thin on this timescale, and the equation for $\theta^{(0)}$ is relatively straightforward. We may now rewrite equation (C.17) as

$$\begin{aligned} Z_2(x,\frac{1}{2},\tau)\frac{\partial^2 \bar{u}}{\partial x^2} + \frac{\partial Z_2(x,\frac{1}{2},\tau)}{\partial x}\frac{\partial \bar{u}}{\partial x} + \frac{\partial^2 H}{\partial x \partial \tau}\left(\frac{\partial Z_2(x,\frac{1}{2},\tau)}{\partial x}\frac{\partial H}{\partial x} + Z_2(x,\frac{1}{2},\tau)\frac{\partial^2 H}{\partial x^2}\right) \\ + \frac{\partial^3 H}{\partial x^2 \partial \tau}\left(Z_2(x,\frac{1}{2},\tau)\frac{\partial H}{\partial x} - \frac{\partial J}{\partial x}\right) - J\frac{\partial^4 H}{\partial x^3 \partial \tau} = -\frac{\partial Z_1(x,\frac{1}{2},\tau)}{\partial x}. \end{aligned} \tag{C.21}$$

We choose to use a FTCS finite difference method, hence the discretisation of (C.21) is

$$
\begin{aligned}
[Z_2]^k_{i,N-1}\frac{\bar{u}^k_{i+1}-2\bar{u}^k_i+\bar{u}^k_{i-1}}{\Delta x^2}+\frac{[Z_2]^k_{i+1,N-1}-[Z_2]^k_{i-1,N-1}}{2\Delta x}\frac{\bar{u}^k_{i+1}-\bar{u}^k_{i-1}}{2\Delta x}+\\
\frac{\left(H^{k+1}_{i+1}-H^{k+1}_{i-1}\right)-\left(H^k_{i+1}-H^k_{i-1}\right)}{2\Delta\tau\Delta x}\left(\frac{[Z_2]^k_{i+1,N-1}-[Z_2]^k_{i-1,N-1}}{2\Delta x}\frac{H^k_{i+1}-H^k_{i-1}}{2\Delta x}\right.\\
\left.+[Z_2]^k_{i,N-1}\frac{H^k_{i+1}-2H^k_i+H^k_{i-1}}{\Delta x^2}\right)\\
+\frac{\left(H^{k+1}_{i+1}-2H^{k+1}_i+H^{k+1}_{i-1}\right)-\left(H^k_{i+1}-2H^k_i+H^k_{i-1}\right)}{\Delta\tau\Delta x^2}\left([Z_2]^k_{i,N-1}\frac{H^k_{i+1}-H^k_{i-1}}{2\Delta x}\right.\\
\left.-\frac{J^k_{i+1}-J^k_{i-1}}{2\Delta x}\right)-J^k_i\frac{\left(H^{k+1}_{i+2}-2H^{k+1}_{i+1}+2H^{k+1}_{i-1}-H^{k+1}_{i-2}\right)-\left(H^k_{i+2}-2H^k_{i+1}+2H^k_{i-1}-H^k_{i-2}\right)}{2\Delta\tau\Delta x^3}\\
=-\frac{[Z_1]^k_{i+1,N-1}-[Z_1]^k_{i-1,N-1}}{2\Delta x}, \quad \text{(C.22)}
\end{aligned}
$$

This discretisation can be written in a matrix form

$$\Delta\tau\Delta x^2\mathbf{b}+\mathbf{M_H}\mathbf{H}^k=\mathbf{M_H}\mathbf{H}^{k+1}+\Delta\tau\Delta x\mathbf{M_{\bar{U}}}\bar{\mathbf{u}}^k, \quad \text{(C.23)}$$

where $\boldsymbol{H}^k=\left(H^k_1,H^k_2,\ldots,H^k_{N+1}\right)^T$, $\bar{\boldsymbol{u}}^k=\left(\bar{u}^k_1,\bar{u}^k_2,\ldots,\bar{u}^k_{N+1}\right)^T$, and $\boldsymbol{M_H},\boldsymbol{M_{\bar{U}}}$ are matrices whose entries are the coefficients of the $H^{k+1}$ and $\bar{u}^k$ terms respectively, and are dependent upon the choice of discretisation of the $x$-derivatives of $H,\bar{u}$. We note that the left hand side of (C.23) is known and precomputable at each time step. Due to the $\dfrac{\partial H^4}{\partial x^3\partial\tau}$ term, the stencil must be adjusted at the ends of the domain, by using biased finite differences. Next, the equation for $H$ is where we have used the the substitution $y=H+h\tilde{y}$ to simplify

the limits of the integrals. Similarly, (4.37) gives

$$\begin{aligned}
\frac{\partial^2}{\partial x^2}\Bigg(&\int_{-\frac{1}{2}}^{\frac{1}{2}}\int_{-\frac{1}{2}}^{\tilde{y}}\frac{\mu_1\cos 2\theta+(4+4\mu_3+\mu_2)\,\frac{\partial\bar{u}}{\partial x}}{4+4\mu_3+\mu_2\sin^2 2\theta}h^2\mathrm{d}\tilde{y}'\mathrm{d}\tilde{y}\\
&+\frac{\partial H}{\partial x}\frac{\partial^2 H}{\partial x\partial\tau}\int_{-\frac{1}{2}}^{\frac{1}{2}}\int_{-\frac{1}{2}}^{\tilde{y}}\frac{4+4\mu_3+\mu_2}{4+\mu_3+\mu_2\sin^2 2\theta}h^2\mathrm{d}\tilde{y}'\mathrm{d}\tilde{y}\\
&-\frac{\partial^3 H}{\partial x^2\partial\tau}\int_{-\frac{1}{2}}^{\frac{1}{2}}\int_{-\frac{1}{2}}^{\tilde{y}}\frac{(4+4\mu_3+\mu_2)\tilde{y}'}{4+4\mu_3+\mu_2\sin^2 2\theta}h^3\mathrm{d}\tilde{y}'\mathrm{d}\tilde{y}\Bigg)\\
=&\left(\frac{\partial^2 H}{\partial x^2}+\frac{1}{2}\frac{\partial^2 h}{\partial x^2}\right)\Bigg(\int_{-\frac{1}{2}}^{\frac{1}{2}}\frac{\mu_1\cos 2\theta+(4+4\mu_3+\mu_2)\,\frac{\partial\bar{u}}{\partial x}}{4+4\mu_3+\mu_2\sin^2 2\theta}h\mathrm{d}\tilde{y}\\
&+\frac{\partial H}{\partial x}\frac{\partial^2 H}{\partial x\partial\tau}\int_{-\frac{1}{2}}^{\frac{1}{2}}\frac{4+4\mu_3+\mu_2}{4+4\mu_2+\mu_2\sin^2 2\theta}h\mathrm{d}\tilde{y}\\
&-\frac{\partial^3 H}{\partial x^2\partial\tau}\int_{-\frac{1}{2}}^{\frac{1}{2}}\frac{(4+4\mu_3+\mu_2)\,\tilde{y}}{4+4\mu_3+\mu_2\sin^2 2\theta}h^2\mathrm{d}\tilde{y}\Bigg).
\end{aligned}\tag{C.24}$$

Similarly to the approach to the equation for $\bar{u}$, and appendix B.3, we define some more functions for notational convenience:

$$IZ_1(x,\tau)=\int_{-\frac{1}{2}}^{\frac{1}{2}}\int_{-\frac{1}{2}}^{\tilde{y}}\frac{\mu_1\cos 2\theta}{4+4\mu_3+\mu_2\sin^2 2\theta}h^2\mathrm{d}\tilde{y}'\mathrm{d}\tilde{y},\tag{C.25}$$

$$IZ_2(x,\tau)=\int_{-\frac{1}{2}}^{\frac{1}{2}}\int_{-\frac{1}{2}}^{\tilde{y}}\frac{4+4\mu_3+\mu_2}{4+4\mu_3+\mu_2\sin^2 2\theta}h^2\mathrm{d}\tilde{y}'\mathrm{d}\tilde{y},\tag{C.26}$$

$$K(x,\tau)=\int_{-\frac{1}{2}}^{\frac{1}{2}}\int_{-\frac{1}{2}}^{\tilde{y}}\frac{(4+4\mu_3+\mu_2)\,h^3\tilde{y}'}{4+4\mu_3+\mu_2\sin^2 2\theta}\mathrm{d}\tilde{y}'\mathrm{d}\tilde{y}.\tag{C.27}$$

With the introduced functions, we may express (C.24) as

$$
\begin{aligned}
IZ_2\frac{\partial^3\bar{u}}{\partial x^3} + 2\frac{\partial IZ_2}{\partial x}\frac{\partial^2\bar{u}}{\partial x^2} + \frac{\partial\bar{u}}{\partial x}\left(\frac{\partial^2 IZ_2}{\partial x^2} - Z_2\left(\frac{\partial^2 H}{\partial x^2} + \frac{1}{2}\frac{\partial^2 h}{\partial x^2}\right)\right) \\
- K\frac{\partial^5 H}{\partial x^4\partial\tau} + \frac{\partial^4 H}{\partial x^3\partial\tau}\left(IZ_2\frac{\partial H}{\partial x} - 2\frac{\partial K}{\partial x}\right) \\
+ \frac{\partial^3 H}{\partial x^2\partial\tau}\left(2IZ_2\frac{\partial^2 H}{\partial x^2} + 2\frac{\partial IZ_2}{\partial x}\frac{\partial H}{\partial x} + J\left(\frac{\partial^2 H}{\partial x^2} + \frac{1}{2}\frac{\partial^2 h}{\partial x^2}\right) - \frac{\partial^2 K}{\partial x^2}\right) \\
+ \frac{\partial^2 H}{\partial x\partial\tau}\left(IZ_2\frac{\partial^3 H}{\partial x^3} + 2\frac{\partial IZ_2}{\partial x}\frac{\partial^2 H}{\partial x^2} + \frac{\partial^2 IZ_2}{\partial x^2}\frac{\partial H}{\partial x} - Z_2\frac{\partial H}{\partial x}\left(\frac{\partial^2 H}{\partial x^2} + \frac{1}{2}\frac{\partial^2 h}{\partial x^2}\right)\right) \\
= Z_1\left(\frac{\partial^2 H}{\partial x^2} + \frac{1}{2}\frac{\partial^2 h}{\partial x^2}\right) - \frac{\partial^2 IZ_1}{\partial x^2}. \quad \text{(C.28)}
\end{aligned}
$$

The discretisation of (C.28) is:

$$
\begin{aligned}
&[IZ_2]_i^k \frac{\bar{u}_{i+2}^k - 2\bar{u}_{i+1}^k + 2\bar{u}_{i-1}^k - \bar{u}_{i-2}^k}{2\Delta x^3} + \frac{[IZ_2]_{i+1}^k - [IZ_2]_{i-1}^k}{\Delta x} \frac{\bar{u}_{i+1}^k - 2\bar{u}_i^k + \bar{u}_{i-1}^k}{\Delta x^2} \\
&\quad + \frac{\bar{u}_{i+1}^k - \bar{u}_{i-1}^k}{2\Delta x} \left( \frac{[IZ_2]_{i+1}^k - 2[IZ_2]_i^k + [IZ_2]_{i-1}^k}{\Delta x^2} - Z_{2_i} \left( \frac{H_{i+1}^k - 2H_i^k + H_{i-1}^k}{\Delta x^2} + \frac{1}{2} \frac{h_{i+1}^k - 2h_i^k + h_{i-1}^k}{\Delta x^2} \right) \right) \\
&\quad + \frac{\left(H_{i+1}^{k+1} - H_{i-1}^{k+1}\right) - \left(H_{i+1}^k - H_{i-1}^k\right)}{2\Delta\tau\Delta x} \left( \frac{[IZ_2]_{i+1}^k - 2[IZ_2]_i^k + [IZ_2]_{i-1}^k}{\Delta x^2} \frac{H_{i+1}^k - H_{i-1}^k}{2\Delta x} \right. \\
&\quad \left. + \frac{[IZ_2]_{i+1}^k - [IZ_2]_{i-1}^k}{\Delta x} \frac{H_{i+1}^k - 2H_i^k + H_{i-1}^k}{\Delta x^2} \right. \\
&\quad \left. + [IZ_2]_i^k \frac{H_{i+2}^k - 2H_{i+1}^k + 2H_{i-1}^k - H_{i-2}^k}{2\Delta x^3} - Z_{2_i}^k \frac{H_{i+1}^k - H_{i-1}^k}{2\Delta x} \left( \frac{H_{i+1}^k - 2H_i^k + H_{i-1}^k}{\Delta x^2} + \frac{1}{2} \frac{h_{i+1}^k - 2h_i^k + h_{i-1}^k}{\Delta x^2} \right) \right) \\
&\quad + \frac{\left(H_{i+1}^{k+1} - 2H_i^{k+1} H_{i-1}^{k+1}\right) - \left(H_{i+1}^k - 2H_i^k + H_{i-1}^k\right)}{\Delta\tau\Delta x^2} \left( 2[IZ_2]_i^k \frac{H_{i+1}^k - 2H_i^k + H_{i-1}^k}{\Delta x^2} + \frac{IZ_{2_{i+1}} - IZ_{2_{i-1}}}{\Delta x} \frac{H_{i+1}^k - H_{i-1}^k}{2\Delta x} \right. \\
&\quad \left. - \frac{K_{i+1}^k - 2K_i^k + K_{i-1}^k}{\Delta x^2} + J_i^k \left( \frac{H_{i+1}^k - 2H_i^k + H_{i-1}^k}{\Delta x^2} + \frac{1}{2} \frac{h_{i+1}^k - 2h_i^k + h_{i-1}^k}{\Delta x^2} \right) \right) \\
&\quad + \frac{\left(H_{i+2}^{k+1} - 2H_{i+1}^{k+1} + 2H_{i-1}^{k+1} - H_{i-2}^{k+1}\right) - \left(H_{i+2}^k - 2H_{i+1}^k + 2H_{i-1}^k - H_{i-2}^k\right)}{2\Delta\tau\Delta x^3} \left( IZ_{2_i}^k \frac{H_{i+1}^k - H_{i-1}^k}{2\Delta x} - \frac{K_{i+1}^k - K_{i-1}^k}{2\Delta x} \right) \\
&\quad - K_i^k \frac{\left(H_{i+2}^{k+1} - 4H_{i+1}^{k+1} + 6H_i^{k+1} - 4H_{i-1}^{k+1} + H_{i-2}^{k+1}\right) - \left(H_{i+2}^k - 4H_{i+1}^k + 6H_i^k - 4H_{i-1}^k + H_{i-2}^k\right)}{\Delta\tau\Delta x^4} \\
&\quad = Z_{1_i}^k \left( \frac{H_{i+1}^k - 2H_i^k + H_{i-1}^k}{\Delta x^2} + \frac{1}{2} \frac{h_{i+1}^k - 2h_i^k + h_{i-1}^k}{\Delta x^2} \right) - \frac{IZ_{2_{i+1}}^k - 2IZ_{2_i}^k + IZ_{2_{i-1}}^k}{\Delta x^2}. \quad \text{(C.29)}
\end{aligned}
$$

As before, use of a FTCS finite difference scheme allows us to write this equation in the form

$$\Delta\tau\Delta x^2\mathbf{c} + \mathbf{M'_H}\mathbf{H}^k = \mathbf{M'_H}\mathbf{H}^{k+1} + \Delta\tau\Delta x\mathbf{M'_{\bar{U}}}\bar{\mathbf{u}}^k, \tag{C.30}$$

where the coefficients of all $H^{k+1}, \bar{u}^k$ terms are entries within $\boldsymbol{M'_H}, \boldsymbol{M'_{\bar{U}}}$ respectively.

In our implementation, the matrices $\boldsymbol{M'_{\bar{U}}}, \boldsymbol{M'_H}$ are a quintuple banded matrices. The additional derivative in $H$ does not change the size of the stencil. We include the boundary conditions for $H$ in the first two and final two lines of both matrices, so that it is not necessary to adjust the stencil near the endpoints of the domain. Hence, we can construct the linear system

$$\begin{pmatrix} \mathbf{M_H} & \Delta\tau\Delta x\mathbf{M_{\bar{U}}} \\ \mathbf{M'_H} & \Delta\tau\Delta x\mathbf{M'_{\bar{U}}} \end{pmatrix} \begin{pmatrix} \mathbf{H}^{k+1} \\ \bar{\mathbf{u}}^k \end{pmatrix} = \begin{pmatrix} \Delta\tau\Delta x^2\mathbf{b} + \mathbf{M_H}\mathbf{H}^k \\ \Delta\tau\Delta x^2\mathbf{c} + \mathbf{M'_H}\mathbf{H}^k \end{pmatrix}. \tag{C.31}$$

This linear system is solved at each $k$, with equation (4.14) requring $H^{k+1}$ in order to update $\theta^k \to \theta^{k+1}$.

APPENDIX D

# FUNCTIONS DEFINED IN THE DERIVATION OF THE MODEL FOR A TRANSVERSELY ISOTROPIC THREAD

## D.1 Ancillary functions

In this appendix, we present the ancillary functions defined in Section 5.3.2. All of these expressions are lengthy, and so are omitted from the main text for the sake of concision.

### D.1.1 Elimination of $u^{(1)}$ and $w^{(0)}$ from the model

Here, we present the functions $\mathcal{F}_1, \mathcal{F}_2, \mathcal{G}_1, \mathcal{G}_2$ as defined by (5.53) and (5.54). We obtain the following statements for $u^{(1)}$ and $w^{(0)}$ by combining the equations (5.51) and (5.52),

$$\begin{aligned}
&\frac{\partial u^{(1)}}{\partial r}\Bigg[\left(1+\sin^2\alpha^{(0)}\cos^2\alpha^{(0)}\cos^2\beta^{(0)}\mu_2+\left(\sin^2\alpha^{(0)}\cos^2\beta^{(0)}+\cos^2\alpha^{(0)}\right)\mu_3\right)\\
&\qquad\cdot\left(1+\sin^4\alpha^{(0)}\cos^2\beta^{(0)}\sin^2\beta^{(0)}\mu_2+\sin^2\alpha^{(0)}\mu_3\right)\\
&\qquad-\sin^2\alpha^{(0)}\sin^2\beta^{(0)}\cos^2\alpha^{(0)}\left(\sin^2\alpha^{(0)}\cos^2\beta^{(0)}\mu_2+\mu_3\right)^2\Bigg]\\
&=\frac{\partial u^{(0)}}{\partial x}\Bigg[\sin^3\alpha^{(0)}\cos\alpha^{(0)}\sin^2\beta^{(0)}\left(\cos\beta^{(0)}\left(\frac{3\cos^2\alpha^{(0)}-1}{2}\right)\mu_2-2\mu_3\cos^2\alpha^{(0)}\sin\beta^{(0)}\right)\\
&\qquad\cdot\left(\sin^2\alpha^{(0)}\cos^2\alpha^{(0)}\mu_2+\mu_3\right)\\
&\qquad-\sin\alpha^{(0)}\cos\alpha^{(0)}\cos\beta^{(0)}\left(\left(\frac{3\cos^2\alpha^{(0)}-1}{2}\right)\mu_2+\mu_3\right)\\
&\qquad\cdot\left(1+\sin^4\alpha^{(0)}\cos^2\beta^{(0)}\sin^2\beta^{(0)}\mu_2+\sin^2\alpha^{(0)}\mu_3\right)\Bigg]\\
&\qquad-\mu_1\sin\alpha^{(0)}\cos\alpha^{(0)}\cos\beta^{(0)}\left(1+\mu_3\sin^2\alpha^{(0)}\cos^2\beta^{(0)}\right), \quad \text{(D.1)}
\end{aligned}$$

with

$$\begin{aligned}
&\left(\frac{\partial w^{(0)}}{\partial r}-\frac{w^{(0)}}{r}\right)\Bigg[\sin^2\alpha^{(0)}\sin^2\beta^{(0)}\cos^2\alpha^{(0)}\left(\sin^2\alpha^{(0)}\cos^2\beta^{(0)}\mu_2+\mu_3\right)^2\\
&\quad-\left(1+\sin^4\alpha^{(0)}\cos^2\beta^{(0)}\sin^2\beta^{(0)}\mu_2+\sin^2\alpha^{(0)}\mu_3\right)\left(1+\sin^2\alpha^{(0)}\cos^2\beta^{(0)}\cos^2\alpha^{(0)}\mu_2\right.\\
&\qquad\left.+\left(\sin^2\alpha^{(0)}\cos^2\beta^{(0)}+\cos^2\alpha^{(0)}\right)\mu_3\right)\Bigg]\\
&\quad=\frac{\partial u^{(0)}}{\partial x}\Bigg[\sin^2\alpha^{(0)}\sin\beta^{(0)}\left(\cos\beta^{(0)}\left(\frac{3\cos^2\alpha^{(0)}-1}{2}\right)\mu_2-2\mu_3\cos^2\alpha^{(0)}\sin\beta^{(0)}\right)\\
&\qquad\left(1+\sin^2\alpha^{(0)}\cos^2\alpha^{(0)}\cos^2\beta^{(0)}\mu_2+\left(\sin^2\alpha^{(0)}\cos^2\beta^{(0)}+\cos^2\alpha^{(0)}\right)\mu_3\right)\\
&-\sin^2\alpha^{(0)}\cos^2\alpha^{(0)}\sin\beta^{(0)}\cos\beta^{(0)}\left(\left(\frac{3\cos^2\alpha^{(0)}-1}{2}\right)\mu_2+\mu_3\right)\left(\sin^2\alpha^{(0)}\cos^2\beta^{(0)}\mu_2+\mu_3\right)\Bigg]\\
&\qquad+\mu_1\sin^2\alpha^{(0)}\sin\beta^{(0)}\cos\beta^{(0)}\left(1+\sin^2\alpha^{(0)}\cos^2\beta^{(0)}\mu_3\right). \quad \text{(D.2)}
\end{aligned}$$

We note that the coefficient of $\dfrac{\partial u^{(1)}}{\partial r}$ is the negative of the coefficient of $\dfrac{\partial w^{(0)}}{\partial r} - \dfrac{w^{(0)}}{r}$. After division, we can now write down $\mathcal{F}_1, \mathcal{F}_2, \mathcal{G}_1, \mathcal{G}_2$, which are

$$\mathcal{F}_1 = \frac{c_1}{d}, \tag{D.3}$$

$$\mathcal{F}_2 = \frac{c_2}{d}, \tag{D.4}$$

$$\mathcal{G}_1 = \frac{c_3}{-d}, \tag{D.5}$$

$$\mathcal{G}_2 = \frac{c_4}{-d}, \tag{D.6}$$

where

$$\begin{aligned} c_1 = \sin^3\alpha^{(0)}\cos\alpha^{(0)}\sin^2\beta^{(0)} &\left(\cos\beta^{(0)}\left(\frac{3\cos^2\alpha^{(0)}-1}{2}\right)\mu_2 - 2\mu_3\cos^2\alpha^{(0)}\sin\beta^{(0)}\right) \\ &\cdot\left(\sin^2\alpha^{(0)}\cos^2\alpha^{(0)}\mu_2+\mu_3\right) \\ -\sin\alpha^{(0)}\cos\alpha^{(0)}\cos\beta^{(0)} &\left(\left(\frac{3\cos^2\alpha^{(0)}-1}{2}\right)\mu_2+\mu_3\right) \\ &\cdot\left(1+\sin^4\alpha^{(0)}\cos^2\beta^{(0)}\sin^2\beta^{(0)}\mu_2+\sin^2\alpha^{(0)}\mu_3\right), \end{aligned} \tag{D.7}$$

$$c_2 = -\sin\alpha^{(0)}\cos\alpha^{(0)}\cos\beta^{(0)}\left(\mu_3\sin^2\alpha^{(0)}\cos^2\beta^{(0)}+1\right), \tag{D.8}$$

$$\begin{aligned} c_3 = \sin^2\alpha^{(0)}\sin\beta^{(0)} &\left(\cos\beta^{(0)}\frac{\mu_2}{2}\left(3\cos^2\alpha^{(0)}-1\right) - 2\mu_3\cos^2\alpha^{(0)}\sin\beta^{(0)}\right) \\ &\cdot\left(1+\sin^2\alpha^{(0)}\cos^2\alpha^{(0)}\cos^2\beta^{(0)}\mu_2+\left(\sin^2\alpha^{(0)}\cos^2\beta^{(0)}+\cos^2\alpha^{(0)}\right)\mu_3\right) \\ -\sin^2\alpha^{(0)}\cos^2\alpha^{(0)}\sin\beta^{(0)}\cos\beta^{(0)} &\left(\frac{\mu_2}{2}\left(3\cos^2\alpha^{(0)}-1\right)+\mu_3\right) \\ &\cdot\left(\sin^2\alpha^{(0)}\cos^2\beta^{(0)}\mu_2+\mu_3\right), \end{aligned} \tag{D.9}$$

$$c_4 = \sin^2\alpha^{(0)}\sin\beta^{(0)}\cos\beta^{(0)}\left(1+\sin^2\alpha^{(0)}\cos^2\beta^{(0)}\mu_3\right), \tag{D.10}$$

$$d = \Big(1 + \sin^2\alpha^{(0)}\cos^2\alpha^{(0)}\cos^2\beta^{(0)}\mu_2 + \Big(\sin^2\alpha^{(0)}\cos^2\beta^{(0)} + \cos^2\alpha^{(0)}\Big)\mu_3\Big)$$
$$\cdot\Big(1 + \sin^4\alpha^{(0)}\cos^2\beta^{(0)}\sin^2\beta^{(0)}\mu_2 + \sin^2\alpha^{(0)}\mu_3\Big)$$
$$- \sin^2\alpha^{(0)}\sin^2\beta^{(0)}\cos^2\alpha^{(0)}\Big(\sin^2\alpha^{(0)}\cos^2\beta^{(0)}\mu_2 + \mu_3\Big)^2. \quad \text{(D.11)}$$

### D.1.2 Functions defined in the transformed equation for pressure

The statements of $\mathcal{H}_i$ may be obtained by substitution of $\zeta^{(1)}$ into equation (5.42). For completeness, we list the resulting functions here

$$\mathcal{H}_0 = \frac{1}{L}\Bigg( - 1 - 2\mu_3\sin^2\alpha^{(0)}\cos\beta^{(0)} + \frac{\mu_2}{2}\sin^2\alpha^{(0)}\cos^2\beta^{(0)}\Big(3\cos^2\alpha^{(0)} - 1\Big)$$
$$+ \Big(\mu_2\sin^3\alpha^{(0)}\cos^3\beta^{(0)} + 2\mu_3\sin\alpha^{(0)}\cos\beta^{(0)}\Big)\Big(\sin\alpha^{(0)}\sin\beta^{(0)}\mathcal{G}_1 + \cos\alpha^{(0)}\mathcal{F}_1\Big)\Bigg), \quad \text{(D.12)}$$

$$\mathcal{H}_1 = \sin^2\alpha^{(0)}\cos^2\beta^{(0)} + \sin^3\alpha^{(0)}\cos^3\beta^{(0)}\mu_2\Big(\sin\alpha^{(0)}\sin\beta^{(0)}\mathcal{G}_2 + \cos\alpha^{(0)}\mathcal{F}_2\Big)$$
$$+ 2\mu_3\sin\alpha^{(0)}\cos\beta^{(0)}\Big(\sin\alpha^{(0)}\sin\beta^{(0)}\mathcal{G}_2 + \cos\alpha^{(0)}\mathcal{F}_2\Big), \quad \text{(D.13)}$$

$$\mathcal{H}_2 = \frac{1}{L}\sin^2\alpha^{(0)}\cos 2\beta^{(0)}\Bigg( - 2\mu_3 + \mu_2\Bigg(\sin^2\alpha^{(0)}\sin\beta^{(0)}\cos\beta^{(0)}\mathcal{G}_1 + \sin\alpha\cos\alpha\cos\beta\mathcal{F}_1$$
$$+ \frac{1}{2}(3\cos^2\alpha^{(0)} - 1)\Bigg)\Bigg) + \frac{2\mu_3}{L}\sin\alpha^{(0)}\cos\alpha^{(0)}\cos\beta^{(0)}\mathcal{F}_1, \quad \text{(D.14)}$$

$$\mathcal{H}_3 = \sin^2\alpha^{(0)}\cos 2\beta^{(0)} + \mu_2\sin^3\alpha^{(0)}\cos\beta^{(0)}\cos 2\beta^{(0)}\Big(\sin\alpha^{(0)}\sin\beta^{(0)}\mathcal{G}_2 + \cos\alpha^{(0)}\mathcal{F}_2\Big)$$
$$+ 2\mu_3\sin\alpha^{(0)}\cos\alpha^{(0)}\cos\beta^{(0)}\mathcal{F}_2, \quad \text{(D.15)}$$

### D.1.3 Functions defined in the transformed equation for the longitudinal velocity

As described in the main text, obtaining the functions $\mathcal{J}_0, \mathcal{J}_1$ requires the substitution of $\zeta^{(1)}$ and $\dfrac{\partial u^{(1)}}{\partial r}$ into (5.62), before substituting the resulting expression for $\sigma_{xx}^{(0)}$ into (5.60), using (5.61), and expanding. This yields

$$\frac{\partial}{\partial\lambda}\Bigg(\frac{R^{(0)^2}}{L}\frac{\partial u^{(0)}}{\partial\lambda}\int_0^1\Bigg(2+4\mu_3\cos^2\alpha^{(0)}+\mu_2\cos^2\alpha^{(0)}\Bigg(\sin\alpha^{(0)}\cos\beta^{(0)}\Big(\sin\alpha^{(0)}\sin\beta^{(0)}\mathcal{G}_1+ \cos\alpha^{(0)}\mathcal{F}_1\Big)+\frac{1}{2}\Big(3\cos^2\alpha^{(0)}-1\Big)\Bigg)+2\mu_3\sin\alpha^{(0)}\cos\alpha^{(0)}\cos\beta^{(0)}\mathcal{F}_1\Bigg)\gamma\mathrm{d}\gamma + R^{(0)^2}\mu_1\int_0^1\Bigg(\cos^2\alpha^{(0)}+\mu_2\sin\alpha^{(0)}\cos^2\alpha^{(0)}\cos\beta^{(0)}\Big(\sin\alpha^{(0)}\sin\beta^{(0)}\mathcal{G}_2+\cos\alpha^{(0)}\mathcal{F}_2\Big) + 2\mu_3\sin\alpha^{(0)}\cos\alpha^{(0)}\cos\beta^{(0)}\mathcal{F}_2\Bigg)\gamma\mathrm{d}\gamma\Bigg) - R^{(0)^2}\int_0^1 p^{(0)}\gamma\mathrm{d}\gamma=0, \quad \text{(D.16)}$$

therefore $\mathcal{J}_0;\mathcal{J}_1$ are

$$\mathcal{J}_0(\lambda,\tau)=\int_0^1\Bigg(2+4\mu_3\cos^2\alpha^{(0)}+\mu_2\cos^2\alpha^{(0)}\Bigg(\sin\alpha^{(0)}\cos\beta^{(0)}\Big(\sin\alpha^{(0)}\sin\beta^{(0)}\mathcal{G}_1+ \cos\alpha^{(0)}\mathcal{F}_1\Big)+\frac{1}{2}\Big(3\cos^2\alpha^{(0)}-1\Big)\Bigg)+2\mu_3\sin\alpha^{(0)}\cos\alpha^{(0)}\cos\beta^{(0)}\mathcal{F}_1\Bigg)\gamma\mathrm{d}\gamma, \quad \text{(D.17)}$$

$$\mathcal{J}_1(\lambda,\tau)=\int_0^1\Bigg(\cos^2\alpha^{(0)}+\mu_2\sin\alpha^{(0)}\cos^2\alpha^{(0)}\cos\beta^{(0)}\Big(\sin\alpha^{(0)}\sin\beta^{(0)}\mathcal{G}_2+\cos\alpha^{(0)}\mathcal{F}_2\Big) + 2\mu_3\sin\alpha^{(0)}\cos\alpha^{(0)}\cos\beta^{(0)}\mathcal{F}_2\Bigg)\gamma\mathrm{d}\gamma. \quad \text{(D.18)}$$

# APPENDIX

# BIBLIOGRAPHY


[1] S. G. Advani and C. L. Tucker III. The use of tensors to describe and predict fiber orientation in short fiber composites. *J Rheol* 31.8 (1987), pp. 751–784.

[2] A. Ahmed and A. N. Alexandrou. Unsteady flow of semi-concentrated suspensions using finite deformation tensors. *J Non-Newton Fluid* 55.2 (1994), pp. 115–136.

[3] M. Al Khatib. The stretching of a viscoplastic thread of liquid. *J. Fluids Eng.* 125.6 (2003), pp. 946–951.

[4] A. Alexandrou and E. Mitsoulis. Transient planar squeeze flow of semi-concentrated fiber suspensions using the Dinh–Armstrong model. *J Non-Newton Fluid* 146.1-3 (2007), pp. 114–124.

[5] M. Antman-Passig, S. Levy, C. Gartenberg, H. Schori, and O. Shefi. Mechanically oriented 3D collagen hydrogel for directing neurite growth. *Tissue Engineering Part A* 23.9-10 (2017), pp. 403–414.

[6] N. J. Balmforth, N. Dubash, and A. C. Slim. Extensional dynamics of viscoplastic filaments: II. Drips and bridges. *J Non-Newton Fluid* 165.19-20 (2010), pp. 1147–1160.

[7] N. J. Balmforth, I. A. Frigaard, and G. Ovarlez. Yielding to stress: recent developments in viscoplastic fluid mechanics. *Annu Rev Fluid Mech* 46 (2014), pp. 121–146.

[8] N. Balmforth and R. Craster. A consistent thin-layer theory for Bingham plastics. *J Non-Newton Fluid* 84.1 (1999), pp. 65–81.

[9] N. Balmforth and I. Hewitt. Viscoplastic sheets and threads. *J Non-Newton Fluid* 193 (2013), pp. 28–42.

[10] M. Barone and D. Caulk. Kinematics of flow in sheet molding compounds. *Polym Composite* 6.2 (1985), pp. 105–109.

[11] G. Batchelor. Slender-body theory for particles of arbitrary cross-section in Stokes flow. *J Fluid Mech* 44.3 (1970), pp. 419–440.

[12] G. Batchelor. The stress generated in a non-dilute suspension of elongated particles by pure straining motion. *J Fluid Mech* 46.4 (1971), pp. 813–829.

[13] G. Batchelor. The stress system in a suspension of force-free particles. *J Fluid Mech* 41.3 (1970), pp. 545–570.

[14] M. Ben Amar and L. Cummings. Fingering instabilities in driven thin nematic films. *Phys Fluids* 13.5 (2001), pp. 1160–1166.

[15] J. Buckmaster. The buckling of thin viscous jets. *J Fluid Mech* 61.3 (1973), pp. 449–463.

[16] J. Buckmaster, A. Nachman, and L. Ting. The buckling and stretching of a viscida. *J Fluid Mech* 69.1 (1975), pp. 1–20.

[17] D. H. Chung and T. H. Kwon. Improved model of orthotropic closure approximation for flow induced fiber orientation. *Polym Composite* 22.5 (2001), pp. 636–649.

[18] J. S. Cintra Jr and C. L. Tucker III. Orthotropic closure approximations for flow-induced fiber orientation. *J Rheol* 39.6 (1995), pp. 1095–1122.

[19] R. Courant, E. Isaacson, and M. Rees. On the solution of nonlinear hyperbolic differential equations by finite differences. *Communications on pure and applied mathematics* 5.3 (1952), pp. 243–255.

[20] J. Cousins, S. Wilson, N. Mottram, D. Wilkes, and L. Weegels. Squeezing a drop of nematic liquid crystal with strong elasticity effects. *Phys Fluids* 31.8 (2019), p. 083107.

[21] L. Cummings. Evolution of a thin film of nematic liquid crystal with anisotropic surface energy. *Eur J Appl Math* 15.6 (2004), pp. 651–677.

[22] L. Cummings and P. Howell. On the evolution of non-axisymmetric viscous fibres with surface tension, inertia and gravity. *J Fluid Mech* 389 (1999), pp. 361–389.

[23] G. Cupples, R. Dyson, and D. Smith. On viscous propulsion in active transversely isotropic media. *J Fluid Mech* 855 (2018), pp. 408–420.

[24] M. Darlington and P. McGinley. Fibre orientation distribution in short fibre reinforced plastics. *Journal of Materials Science* 10.5 (1975), pp. 906–910.

[25] S. M. Dinh and R. C. Armstrong. A rheological equation of state for semiconcentrated fiber suspensions. *J Rheol* 28.3 (1984), pp. 207–227.

[26] J. Donea, A. Huerta, J. Ponthot, and A. Rodríguez-Ferran. *Arbitrary Lagrangian–Eulerian Methods*. Wiley Online Library, 2017, pp. 1–23.

[27] P. Doshi and O. A. Basaran. Self-similar pinch-off of power law fluids. *Phys Fluids* 16.3 (2004), pp. 585–593.

[28] R. Dyson, J. Green, J. Whiteley, and H. Byrne. An investigation of the influence of extracellular matrix anisotropy and cell–matrix interactions on tissue architecture. *J. Math. Biol* 72.7 (2016), pp. 1775–1809.

[29] R. Dyson and O. Jensen. A fibre-reinforced fluid model of anisotropic plant cell growth. *J Fluid Mech* 655 (2010), pp. 472–503.

[30] J. Eggers and E. Villermaux. Physics of liquid jets. *Rep Prog Phys* 71.3 (2008), p. 036601.

[31] J. Engmann, C. Servais, and A. S. Burbidge. Squeeze flow theory and applications to rheometry: A review. *J Non-Newton Fluid* 132.1-3 (2005), pp. 1–27.

[32] J. Ericksen. Transversely isotropic fluids. *Kolloid Z* 173.2 (1960), p. 117.

[33] K. Ericsson, S. Toll, and J.-A. Månson. The two-way interaction between anisotropic flow and fiber orientation in squeeze flow. *J Rheol* 41.3 (1997), pp. 491–511.

[34] E. Evans-Hoeker, D. Pritchard, D. Long, A. Herring, J. Stanford, and A. Steiner. Cervical mucus monitoring prevalence and associated fecundability in women trying to conceive. *Fertil Steril* 100.4 (2013), pp. 1033–1038.

[35] F. Folgar and C. L. Tucker III. Orientation behavior of fibers in concentrated suspensions. *J Reinf Plast Comp* 3.2 (1984), pp. 98–119.

[36] M. A. Fontelos. Break-up and no break-up in a family of models for the evolution of viscoelastic jets. *Z Angew Math Phys* 54.1 (2003), pp. 84–111.

[37] I. Frigaard and C. Nouar. On the usage of viscosity regularisation methods for visco-plastic fluid flow computation. *J Non-Newton Fluid* 127.1 (2005), pp. 1–26.

[38] P. Gaskell, P. Jimack, M. Sellier, H. Thompson, and M. Wilson. Gravity-driven flow of continuous thin liquid films on non-porous substrates with topography. *J Fluid Mech* 509 (2004), pp. 253–280.

[39] L. Goettler, R. Leib, and A. Lambright. Short fiber reinforced hose—A new concept in production and performance. *Rubber Chemistry and Technology* 52.4 (1979), pp. 838–863.

[40] M. Goldin, J. Yerushalmi, R. Pfeffer, and R. Shinnar. Breakup of a laminar capillary jet of a viscoelastic fluid. *J Fluid Mech* 38.4 (1969), pp. 689–711.

[41] J. Green and A. Friedman. The extensional flow of a thin sheet of incompressible, transversely isotropic fluid. *Eur J Appl Math* 19.3 (2008), p. 225.

[42] I. Griffiths and P. Howell. Mathematical modelling of non-axisymmetric capillary tube drawing. *J Fluid Mech* 605 (2008), pp. 181–206.

[43] J. B. Grotberg. Respiratory fluid mechanics and transport processes. *Annu Rev Biomed Eng* 3.1 (2001), pp. 421–457.

[44] E. Hinch and L. Leal. The effect of Brownian motion on the rheological properties of a suspension of non-spherical particles. *J Fluid Mech* 52.4 (1972), pp. 683–712.

[45] E. M. Hinton, A. J. Hogg, and H. E. Huppert. Interaction of viscous free-surface flows with topography. *J Fluid Mech* 876 (2019), pp. 912–938.

[46] C. Holloway, R. Dyson, and D. Smith. Linear Taylor–Couette stability of a transversely isotropic fluid. *Proc. R. Soc. A* 471.2178 (2015), p. 20150141.

[47] C. R. Holloway, G. Cupples, D. J. Smith, J. E. F. Green, R. J. Clarke, and R. J. Dyson. Influences of transversely isotropic rheology and translational diffusion on the stability of active suspensions. *Roy Soc Open Sci* 5.8 (2018), p. 180456.

[48] C. R. Holloway, D. J. Smith, and R. J. Dyson. Linear Rayleigh–Benard stability of a transversely isotropic fluid. *Eur J Appl Math* 30.4 (2019), pp. 659–681.

[49] P. Howell. "Extensional thin layer flows". PhD thesis. University of Oxford, 1994.

[50] P. Howell. Models for thin viscous sheets. *Eur J Appl Math* 7.4 (1996), pp. 321–343.

[51] H. Huang, J. J. Wylie, R. M. Miura, and P. D. Howell. On the formation of glass microelectrodes. *SIAM J Appl Math* 67.3 (2007), pp. 630–666.

[52] H. E. Huppert. The propagation of two-dimensional and axisymmetric viscous gravity currents over a rigid horizontal surface. *J Fluid Mech* 121 (1982), pp. 43–58.

[53] G. B. Jeffery. The motion of ellipsoidal particles immersed in a viscous fluid. *P R Soc A* 102.715 (1922), pp. 161–179.

[54] M. Lam, L. Cummings, T.-S. Lin, and L. Kondic. Modeling flow of nematic liquid crystal down an incline. *J Eng Math* 94.1 (2015), pp. 97–113.

[55] L. J. Lee, L. Marker, and R. Griffith. The rheology and mold flow of polyester sheet molding compound. *Polym Composite* 2.4 (1981), pp. 209–218.

[56] M. Lee and H. Ockendon. A continuum model for entangled fibres. *Eur J Appl Math* 16.2 (2005), pp. 145–160.

[57] F. M. Leslie. Some constitutive equations for anisotropic fluids. *Q J Mech Appl Math* 19.3 (1966), pp. 357–370.

[58] G. Lipscomb II, M. M. Denn, D. Hur, and D. V. Boger. The flow of fiber suspensions in complex geometries. *J Non-Newton Fluid* 26.3 (1988), pp. 297–325.

[59] G. Lipscomb and M. Denn. Flow of Bingham fluids in complex geometries. *J Non-Newton Fluid* 14 (1984), pp. 337–346.

[60] J. Matta and R. Tytus. Liquid stretching using a falling cylinder. *J Non-Newton Fluid* 35.2-3 (1990), pp. 215–229.

[61] M. McClelland and B. Finlayson. Squeezing flow of highly viscous polymers. *J Rheol* 32.2 (1988), pp. 101–133.

[62] G. H. McKinley and T. Sridhar. Filament-stretching rheometry of complex fluids. *Annu Rev Fluid Mech* 34.1 (2002), pp. 375–415.

[63] A. Metzner. Rheology of suspensions in polymeric liquids. *J Rheol* 29.6 (1985), pp. 739–775.

[64] K. Moghissi. The function of the cervix in fertility. *Fertil Steril* 23.4 (1972), p. 295.

[65] N. F. Morrison and O. G. Harlen. Viscoelasticity in inkjet printing. *Rheol Acta* 49.6 (2010), pp. 619–632.

[66] K. W. Morton and D. F. Mayers. *Numerical solution of partial differential equations: an introduction*. Cambridge university press, 2005.

[67] T. Myers. Application of non-Newtonian models to thin film flow. *Phys Rev E* 72.6 (2005), p. 066302.

[68] J. A. Nuhn, A. M. Perez, and I. C. Schneider. Contact guidance diversity in rotationally aligned collagen matrices. *Acta biomaterialia* 66 (2018), pp. 248–257.

[69] C. O'Rourke, R. A. Drake, G. W. Cameron, A. Jane Loughlin, and J. B. Phillips. Optimising contraction and alignment of cellular collagen hydrogels to achieve reliable and consistent engineered anisotropic tissue. *Journal of biomaterials applications* 30.5 (2015), pp. 599–607.

[70] D. O. Olagunju. A 1-D theory for extensional deformation of a viscoelastic filament under exponential stretching. *J Non-Newton Fluid* 87.1 (1999), pp. 27–46.

[71] C. J. Petrie. Some results in the theory of melt spinning for model viscoelastic liquids. *J Non-Newton Fluid* 4.1-2 (1978), pp. 137–159.

[72] C. J. Petrie. The rheology of fibre suspensions. *J Non-Newton Fluid* 87.2-3 (1999), pp. 369–402.

[73] G. Pfingstag, B. Audoly, and A. Boudaoud. Thin viscous sheets with inhomogeneous viscosity. *Phys Fluids* 23.6 (2011), p. 063103.

[74] N. Phan-Thien and A. Graham. A new constitutive model for fibre suspensions: flow past a sphere. *Rheol Acta* 30.1 (1991), pp. 44–57.

[75] N. Phan-Thien and A. Graham. The squeezing flow of a model suspension fluid. *Rheol Acta* 29.5 (1990), pp. 433–441.

[76] D. Pritchard, B. R. Duffy, and S. K. Wilson. Shallow flows of generalised Newtonian fluids on an inclined plane. *J Eng Math* 94.1 (2015), pp. 115–133.

[77] D. Pritchard, S. K. Wilson, and C. R. McArdle. Flow of a thixotropic or antithixotropic fluid in a slowly varying channel: The weakly advective regime. *J Non-Newton Fluid* 238 (2016), pp. 140–157.

[78] M. Renardy. A numerical study of the asymptotic evolution and breakup of Newtonian and viscoelastic jets. *J Non-Newton Fluid* 59.2-3 (1995), pp. 267–282.

[79] M. Renardy. Self-similar breakup of a Giesekus jet. *J Non-Newton Fluid* 97.2-3 (2001), pp. 283–293.

[80] M. Renardy. Some comments on the surface-tension driven break-up (or the lack of it) of viscoelastic jets. *J Non-Newton Fluid* 51.1 (1994), pp. 97–107.

[81] O. Reynolds. IV. On the theory of lubrication and its application to Mr. Beauchamp tower's experiments, including an experimental determination of the viscosity of olive oil. *Philos T R Soc Lond* 177 (1886), pp. 157–234.

[82] N. M. Ribe. A general theory for the dynamics of thin viscous sheets. *J Fluid Mech* 457 (2002), p. 255.

[83] N. M. Ribe. Coiling of viscous jets. *P Roy Soc A-Math Phy* 460.2051 (2004), pp. 3223–3239.

[84] N. Ribe. Bending and stretching of thin viscous sheets. *J Fluid Mech* 433 (2001), p. 135.

[85] T. Rogers. Squeezing flow of fibre-reinforced viscous fluids. *J Eng Math* 23.1 (1989), pp. 81–89.

[86] A. Ross, B. Duffy, and S. Wilson. Thin-film flow of a viscoplastic material round a large horizontal stationary or rotating cylinder. *J Fluid Mech* 430 (2001), pp. 309–333.

[87] N. Roussel, C. Lanos, and Z. Toutou. Identification of Bingham fluid flow parameters using a simple squeeze test. *J Non-Newton Fluid* 135.1 (2006), pp. 1–7.

[88] R. K. Sawhney and J. Howard. Slow local movements of collagen fibers by fibroblasts drive the rapid global self-organization of collagen gels. *Int J Cell Biol* 157.6 (2002), pp. 1083–1092.

[89] M. Scaraggi and B. Persson. Theory of viscoelastic lubrication. *Tribol Int* 72 (2014), pp. 118–130.

[90] W. W. Schultz. Slender viscoelastic fiber flow. *J Rheol* 31.8 (1987), pp. 733–750.

[91] P. Shirodkar and S. Middleman. Lubrication flows in viscoelastic liquids. I. Squeezing flow between approaching parallel rigid planes. *J Rheol* 26.1 (1982), pp. 1–17.

[92] D. E. Sommer, A. J. Favaloro, and R. B. Pipes. Coupling anisotropic viscosity and fiber orientation in applications to squeeze flow. *J Rheol* 62.3 (2018), pp. 669–679.

[93] A. Spencer. *Deformations of fibre-reinforced materials*. 1972.

[94] A. Spencer. Fibre-streamline flows of fibre-reinforced viscous fluids. *Eur J Appl Math* 8.2 (1997), pp. 209–215.

[95] A. Spencer. Theory of fabric-reinforced viscous fluids. *Compos Part A-Appl S* 31.12 (2000), pp. 1311–1321.

[96] T. Sridhar, V. Tirtaatmadja, D. Nguyen, and R. Gupta. Measurement of extensional viscosity of polymer solutions. *J Non-Newton Fluid* 40.3 (1991), pp. 271–280.

[97] H. Stark. Physics of colloidal dispersions in nematic liquid crystals. *Phys Rep* 351.6 (2001), pp. 387–474.

[98] Y. M. Stokes, P. Buchak, D. G. Crowdy, and H. Ebendorff-Heidepriem. Drawing of micro-structured fibres: circular and non-circular tubes. *J Fluid Mech* 755 (2014), pp. 176–203.

[99] A. Tam, J. E. F. Green, S. Balasuriya, E. L. Tek, J. M. Gardner, J. F. Sundstrom, V. Jiranek, and B. J. Binder. A thin-film extensional flow model for biofilm expansion by sliding motility. *P R Soc A* 475.2229 (2019), p. 20190175.

[100] R. Törnqvist, P. Sunderland, and J. Månson. Non-isothermal process rheology of thermoplastic composites for compression flow moulding. *Compos Part A-Appl S* 31.9 (2000), pp. 917–927.

[101] F. T. Trouton. On the coefficient of viscous traction and its relation to that of viscosity. *P R Soc A* 77.519 (1906), pp. 426–440.

[102] B. Van De Fliert, P. Howell, and J. Ockenden. Pressure-driven flow of a thin viscous sheet. *J Fluid Mech* 292 (1995), pp. 359–376.

[103] V. Verleye et al. "Modelling the flow of fiber suspensions in narrow gaps". *Rheology Series*. Vol. 8. Elsevier, 1999, pp. 1347–1398.

[104] P. Wilmott. The stretching of a thin viscous inclusion and the drawing of glass sheets. *Phys Fluids A-Fluid* 1.7 (1989), pp. 1098–1103.

[105] S. L. Wingstrand, N. J. Alvarez, O. Hassager, and J. M. Dealy. Oscillatory squeeze flow for the study of linear viscoelastic behavior. *J Rheol* 60.3 (2016), pp. 407–418.

[106] D. Wolf, L. Blasco, M. Khan, and M. Litt. Human cervical mucus. IV. Viscoelasticity and sperm penetrability during the ovulatory menstrual cycle. *Fertil Steril* 30.2 (1978), pp. 163–169.

[107] J. Wylie, B. Bradshaw-Hajek, and Y. Stokes. The evolution of a viscous thread pulled with a prescribed speed. *J Fluid Mech* 795 (2016), pp. 380–408.